Synthesis and Characterization of $Pt_{1-x}Pd_x$ Nanoparticles and their Suitability for NH_3 Oxidation Catalysis

Martin Jensen

Master Thesis in Chemistry

60 credits

Department of Chemistry
Faculty of Mathematics and Natural Sciences

UNIVERSITY OF OSLO

October 2017

2017

Synthesis and characterization of $Pt_{1-x}Pd_x$ nanoparticles and their suitability for NH_3 oxidation catalysis

Martin Jensen

http://www.duo.uio.no/

Print: Reprosentralen, Universitetet i Oslo

Author Contribution

The candidate performed the following experiments and analyses:

- Synthesis of free standing nanoparticles
- Kinetics experiments including all SEM imaging
- Development of the polyol approach
- In-house XRD experiments with subsequent data analysis
- Preparation of samples for synchrotron X-ray diffraction experiments in Grenoble including data collection at the beam line
- Data analysis connected to the catalytic testing results including a visit at Yara International at Herøya to learn about the lab scale reactor test system for ammonia oxidation
- All data analysis for providing histograms for particle sizes from TEM BF images of PtPd NPs (as well as for PtRh NPs, which is not included in the current thesis).

The candidate was supported on the following experiments:

- Preparation of the in-house made catalysts, Pt/Al_2O_3, $Pt_{0.90}Pd_{0.10}/Al_2O_3$ and $Pt_{0.50}Pd_{0.50}/Al_2O_3$, which were performed by Dr. P. Dhak.
- TEM imaging of free standing NPs and catalysts, which were performed Dr. P. Dhak.
- "Whole Powder Pattern Fitting" of synchrotron X-ray diffraction data was performed by Dr. W. Slawinski, ISIS, UK
- Catalytic testing experiments at Yara were performed by Principal Eng. Dr. K. I. Skau
- High resolution HAADF-STEM-EDX analysis, which were performed by Prof. Patricia Kooyman, Cape Town University, South Africa.
- HAADF-STEM-EDX analysis which was performed by Dr. Phuong D. Nguyen

Acknowledgements

In the work of this Master thesis, I have been introduced to the exciting field of nanoscience. It has been a great experience from start to end.

I would especially like to thank my supervisor Prof. Anja O. Sjåstad for being a constant source of inspiration to me throughout this project. When times were tough the advice were plenty, and when times were good the acknowledgement was profound.

I would also like to thank:

Prof. Helmer Fjellvåg my co-supervisor, for solid guidance in times of need.

Dr. Prasanta Dhak for constructive input and general guidance.

Prof. Patricia Kooyman for showing me how magnificent the TEM could be.

Fabian L. M. Bernal for inspiring and educational conversations in the lab next door.

Morten Østigård for good times in the lab, and valuable conversations.

Dr. David Wragg for excellent guidance in the x-ray lab.

Kristian B. Lausund for training me on the SEM.

Dr. Wojciech Slawinski for helping out with data treatments, and educational talks.

Dr. Karl I. Skau for a nice tour at Yara, Herøya.

Dr. Phuong D. Nguyen for helping out at the TEM, and providing advice in this respect.

A thank you to my nearest:

My girlfriend Synne Myhre, for invaluable support in this period of hard work and challenging moments.

My mom and dad for always supporting me.

Martin Jensen

Abstract

In this master project, bimetallic nanoparticles with nominal composition $Pt_{1-x}Pd_x$ NPs ($0 \leq x \leq 1$) have been synthesized via a polyol method. PVP was used as the stabilizer/capping agent, $Pt(acac)_2$ and $Pd(acac)_2$ as metal precursors, and 1,4-butanediol as solvent. The precursors were reduced by a simultaneous reduction method. Using these chemicals, the following reaction conditions were established as *standard conditions*: Reaction temperature of 220°C, aging time of 2 hours, metal/PVP ratio of 1/10, a total amount of 0.2 mmol of metal in 20 mL of solvent.

Bimetallic $Pt_{1-x}Pd_x$ NPs with nominal compositions x = 0; 0.25; 0.50; 0.75; 1 were characterized by powder X-ray diffraction to determine phase purity. It was found that the NPs were phase pure. With respect to the unit cell dimensions, PXRD was not conclusive relative to type of element distribution. NPs with nominal composition $Pt_{0.50}Pd_{0.50}$ synthesized at standard conditions were studied in more detail with HAADF-STEM-EDX and synchrotron PXRD to determine the elemental distribution in these nanoparticles. It was proved that the elemental distribution was Pd@Pt.

Simple visual kinetics experiments, were performed on the $Pt(acac)_2$ and $Pd(acac)_2$ metal precursors to get a better understanding of the core@shell formation. Their relative difference in reaction kinetics for nanoparticle formation was investigated, and it was found that $Pd(acac)_2$ had a much faster reaction kinetics than $Pt(acac)_2$. The nanoparticle formation visually inspected by color change in suspension and documented with STEM-imaging.

Through these initial experiments, the conclusion was that the Pd@Pt core@shell elemental distribution is attributed to the large difference in reaction kinetics between the metal precursors. Therefore, a series of experiments were performed in an attempt to tune the relative reaction kinetics between $Pt(acac)_2$ and $Pd(acac)_2$ for nanoparticle formation. In this regard, the reaction kinetics of the precursors were screened in similar but different solvents (ethylene glycol, 1,4-butanediol, 1,2-butanediol, 1,3-propanediol), with two different metal/PVP ratios (1/10 and 1/100). Visual- and STEM-images were used for proving the formation of NPs. It was found that the relative reaction kinetics was not significantly changed by varying these parameters. Another approach was therefore chosen; modifying the standard polyol synthesis by utilizing a successive reduction method. Via this route, we successfully produced Pt seed-NPs with incorporation of Pd.

To see if an increased aging time would facilitate diffusion of atomic species in the Pd@Pt nanoparticles synthesized by the standard polyol method, an aging time of 24 hours was

selected. Whole Powder Pattern Fitting of synchrotron PXRD results point in the direction of solid solution, however stated with an uncertainty.

A general strategy for synthesis of bimetallic nanoparticles with tunable element distribution was developed based on our findings. Main ingredients are to explore the relative kinetics of the metal precursors, choice for successive or simultaneous reduction and to combine PXRD with HAADF-STEM-EDX for the structural analysis.

Metal-on-support $Pt_{1-x}Pd_x/Al_2O_3$ (x = 0, 0.10 and 0.50) catalysts have been characterized and evaluated in terms of suitability for NH_3 oxidation. The $Pt_{1-x}Pd_x$ NPs were synthesized by the standard polyol method, and deposited on γ-alumina supports. Nanoparticle size measurements were performed on the basis of BF-TEM images of the free-standing NPs. The composition, and metal loading in the catalyst was determined by ICP-MS, and the catalytic activity was measured by YARA International, Herøya. The TOF for the respective compositions was calculated, and it was found that the pure Pt/Al_2O_3 catalyst outperformed all other compositions. Further, it was shown that the presence of Pd had a negative effect on the selective oxidation of NH_3 to form N_2. Moreover, it was established that the characterization technique used for the prepared catalysts needs optimization, in relation to detection of supported noble metal NPs.

Abbreviations Used in this Thesis

NP: Nanoparticle

SEM: Scanning electron microscope

TEM: Transmission electron microscope

STEM: Scanning transmission electron microscope

HAADF-STEM: High angle annular dark field scanning transmission electron microscopy

BF (TEM): Bright field

DF (TEM): Dark field

HR (TEM): High resolution

STP: Standard temperature and pressure (0°C and 1 atm)

R.T.: Room temperature

NAFUMA: Nanostructures and functional materials

Comp.: Composition

PID (controller): Proportional integral derivative (controller)

No.: Number

Rxn: Reaction

Pre: Preheating (step)

Centr.: Centrifugation

FCC: Face centered cubic

BCC: Body centered cubic

HCP: Hexagonally close packed

CTAB: Cetyltrimethylammonium bromide

PVA: Polyvinyl alcohol

SE: Secondary Electron

BSE: Backscattered electron

Solid sol.: Solid solution

N.R.: Not reported

TTEG: Tetraethylene glycol

EG: Ethylene glycol

BD: Butanediol

Acac: Acetylacetonate

NIST: National institute of standards and technology

XRD: X-ray diffraction

PXRD: Powder X-ray diffraction

SCCM: Standard cubic centimetres per minute

Table of Contents

1 Introduction

The main topic of the current master project is to establish a protocol for synthesis and characterization of $Pt_{1-x}Pd_x$ nanoparticles together with exploring the potential the metallic nanoparticles has to act as catalysts for the oxidation of diluted ammonia concentrations at intermediate temperatures (200-500 ^oC) to nitrogen. This chapter starts with an introduction to some aspects connected to nanoparticles and the finite size effect when going from bulk materials to nanometer scale followed by a brief introduction to published literature on synthesis and characterization of $Pt_{1-x}Pd_x$ nanoparticles by means of the polyol approach. In the end some background information and principles connected to ammonia oxidation as an aid for NO_x abatement will be presented together with the motivation of the current master project.

1.1 From Bulk Materials to Nanoparticles

Nanoscience is formally defined as the field of engineering and science conducted at the nanoscale, where the prefix *nano* denotes 10^{-9} m. A different approach is to emphasize the fact that the *characteristic properties* of a bulk material changes when at least one of its dimensions approaches the nanometer scale. In this prospective, nanoscience can be understood as the study of these changes. Typically, the finite size effect is seen in the order of 1-100 nm, depending on the property- and material in question. Chemical reactivity, thermal, optical and electromagnetic properties of the nanomaterial can be distinctively different than their bulk counterparts would be per traditional scaling laws. For proper studies of these effects, it is necessary to have uniform particle sizes, control on faceting, chemical composition as well as atomic arrangement. Often, we request a *monodispersed* particle size distribution, and this is defined as standard deviation in particle diameter typically is less than 10% of the length.

In this section, some introductory aspects of metallic nanoparticles are reviewed. First size effects and elemental distribution in bimetallic nanoparticles will be reviewed, followed by a brief historical timeline of major achievements in the field of metallic nanoparticle synthesis [1, p.1],[2].

When the particle size decreases, the surface area/volume ratio increases, and when the nanometer size-range is reached, the number of surface atoms relative to bulk atoms can be very high. This is illustrated for cuboctahedral Pt NPs in Figure 1-1, where the percentage of

surface atoms is plotted against the particle size between 0.8-5.1 nm. The plot is based on a calculation shown in [1, p.5]. As surface atoms have *dangling bonds*, meaning they have positions in the lattice where they have fewer neighboring atoms than their bulk counterparts, they are often more reactive. I.e. reactivity is therefore expected to increase or change when the particle size is reduced.

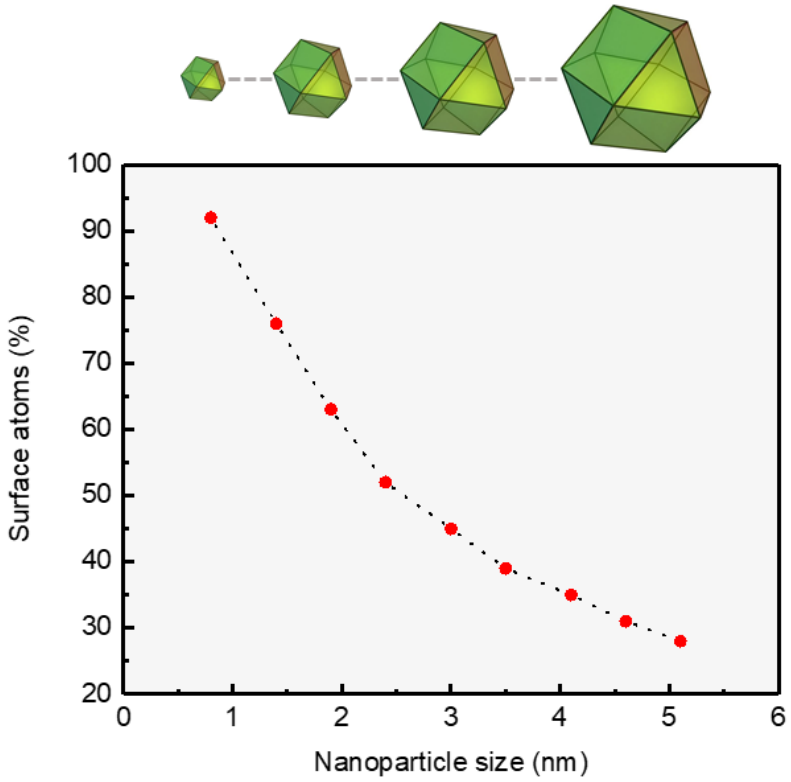

Figure 1-1: The number of surface atoms (percentage) in a cuboctahedral platinum nanoparticle plotted against its size [1, p.5]. Cuboctahedron figure: [3].

Another well-known effect of increased surface to volume ratio is the decrease in melting point when particle size is reduced to the nanometer scale. According to the Lindemann melting rule, a solid will melt when the root mean square of the amplitude of the atomic vibrations about the equilibrium lattice positions exceeds a threshold value. This might vary between 5 to 20%, depending on multiple factors such as magnitude of quantum effects, crystal structure (CN) and the nature of interparticle actions. Most often a value of ~15% is used [4].

With respect to optical properties, the electrons of the material dictate how that material interacts with photons. Photon absorption by semiconductors is only likely to occur if the photon's energy exceeds that of the bandgap. Since visible light often has a lower energy than the bandgap of a semiconductor, they appear transparent. However, when the dimensions of a

semiconducting material are confined to nanometer scale, a quantization of energy levels occur and the bandgap is increased as visualized in Figure 1-2.

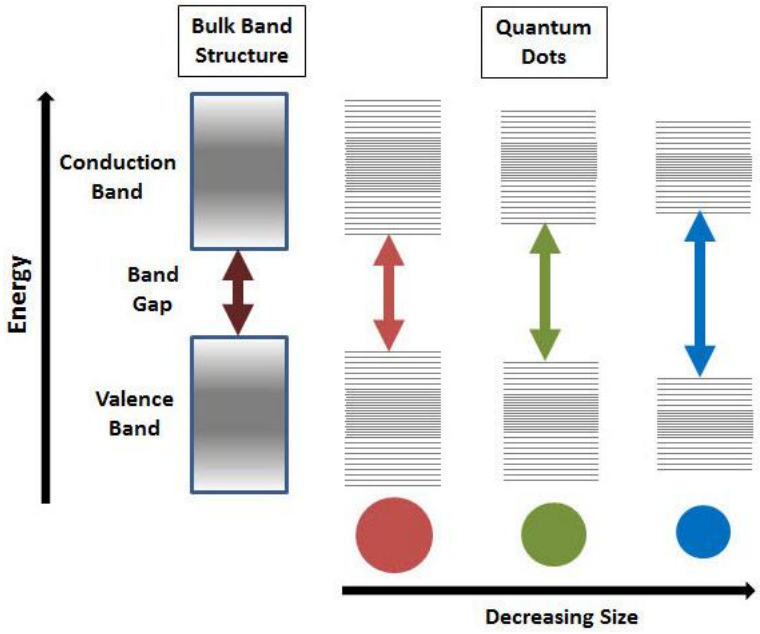

Figure 1-2: Splitting of energy levels in quantum dots due to the quantum confinement effect, the semiconductor bandgap increases with decrease in size of the nanocrystal [5].

This means that smaller nanoparticles will absorb electromagnetic radiation with shorter wavelengths. The corresponding absorption band is therefore blue-shifted. A schoolbook example of this is nanoparticles of CdSe, when irradiated with UV-light, can emit the entire visible range of colors depending on the nanoparticle size, see Figure 1-3 [6]. Metallic nanoparticles also give rise to color for similar reasons, however this becomes apparent first for particles in the size range of 1-2 nm. In the size range 5-50 nm, it is the so-called *plasmon resonance effect* that give metallic nanoparticles color.

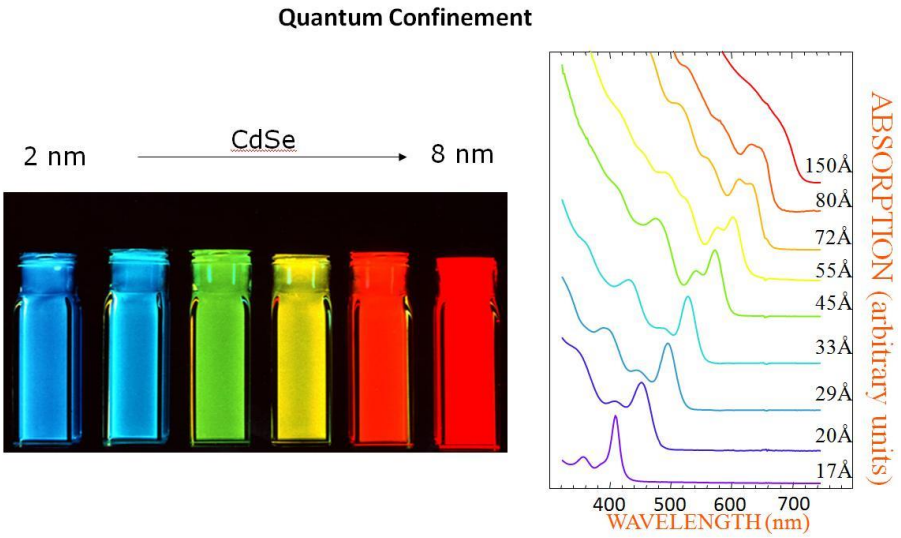

Figure 1-3: Fluorescence induced by exposure to ultraviolet light in vials containing various sized cadmium selenide (CdSe) quantum dots [6].

Another classic finite size effect is the transformation from ferro/ferrimagnetism to superparamagnetism. This effect arises when the nanoparticle size become smaller than the ferro/ferridomain size, and the whole particle is regarded as a single domain. This occurs when the particle diameter become smaller than 10-15 nm, and it is manifested through loss of hysteresis loop when collecting the magnetization (M) versus external magnetic field (H) curve, Figure 1-4.

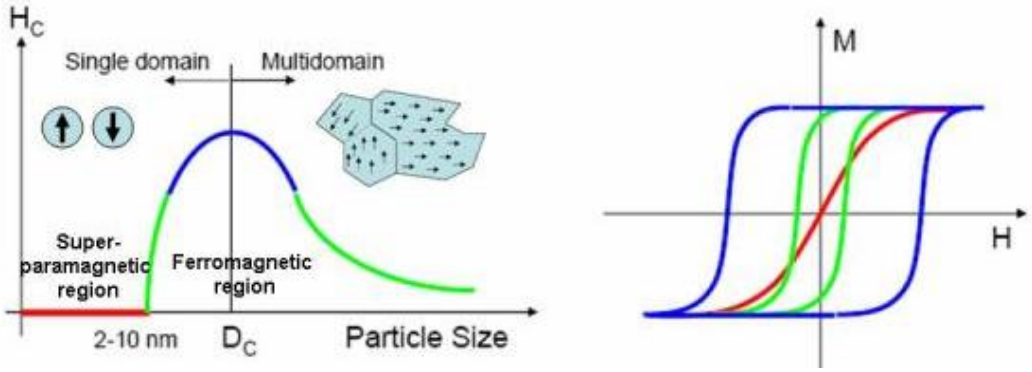

Figure 1-4: Left, remanent magnetization versus particle size, right: Hysteresis loop during magnetization (M) – external magnetic field (H) experiment [7].

Next to particle size, the atomic arrangement and faceting affects particle properties. For example, metals often crystallize as one of the three following structures: cubic close-packed (ccp), hexagonal close-packed (hcp) or body-centered cubic (bcc) [8]. However, metallic

nanoparticles may take other structures than their bulk counterparts. One example would be cobalt at ambient pressure, which is stable as hcp whereas in nanoparticles, the ccp form is found stabilized due to a finite size effect. Furthermore, Co NPs are reported to crystallize in the bcc structure or as ε-Co (β-Mn structure) [9]. Titanium dioxide, TiO_2, a common material for photo catalysis, can be used to exemplify how changes in structural arrangement can affect properties. TiO_2 can be found as multiple polymorphs, with rutile, anatase and brookite being the most common. Rutile is the most stable form in bulk. However, anatase has been shown to stabilize when forming nanoparticle or thin films. This is interesting as anatase shows better photocatalytic properties than rutile. Both rutile and anatase have tetragonal symmetry, but small differences in their atomic arrangement leads to Ti-Ti distance in anatase being shorter, giving a different distribution of mass and electrons, and effectively a different electronic band structure with a band gap of 3.21 eV compared to 3.00 eV in rutile [10].

Nanoparticles can have different faceting depending on what is the most thermodynamically stable situation. The exposed facets will in general be those with the lowest surface energies, i.e. those with the lowest Miller indices. However, the thermodynamic environment can be manipulated during synthesis to provide other facets. This is important as different facets provide different energetic landscapes and interatomic distances, which again facilitates different reaction products. A consequence of this is that the different morphologies show varying degrees of selectivity toward products during chemical reactions. A good example that shows the effect of shape selectivity is cubic and cuboctahedra Pt NPs used for benzene hydrogenation [11]. The cubic NPs favor cyclohexane formation; whereas the cuboctahedra particles, with two types of facets, give both cyclohexane and cyclohexene, see Figure 1-5.

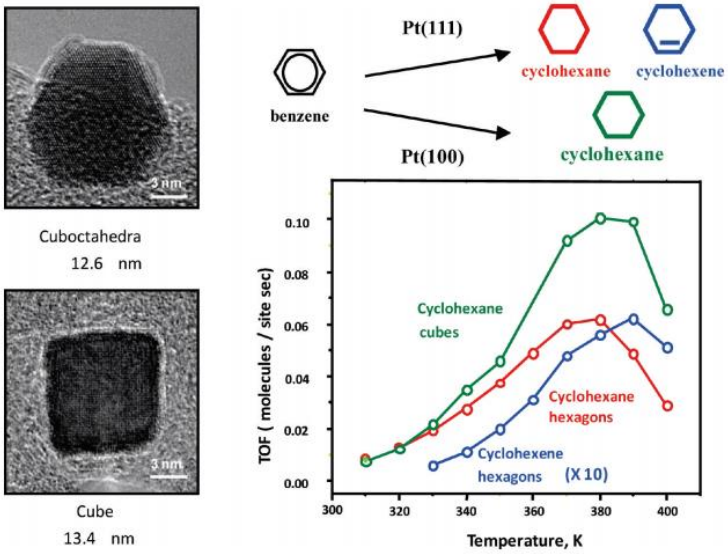

Figure 1-5: Variation in product selectivity with Pt nanoparticle faceting [11].

Finally, the chemical composition and element distribution in a bimetallic nanoparticle influences its properties. For example, by combining a metal with a second metal can be used to tune or promote particular effects such as catalytic activity and/or product selectivity. The improved properties may also be better than just the *combination* of the properties of the two metals, and display applicational potentials. When the combination of the two metals show improved properties toward a specific endeavor, relative to the properties of the monometallic contributions combined, it is referred to as *synergy* [1, p.75-76]. This adds another level of possibilities for engineering materials with desired properties.

In terms of the synergistic effect, not only does the *choice of elements* in the bimetallic nanoparticles matter, but also the *elemental distribution* [1, p.75-76]. Several types of atomic distributions are possible, and a selection of some of them are schematically illustrated in Figure 1-6. In this figure only NPs with distinctive, segregated phases of the two metals are depicted, but elemental distribution as a solid solution, where the elements are homogeneously mixed is also possible [1, p.76].

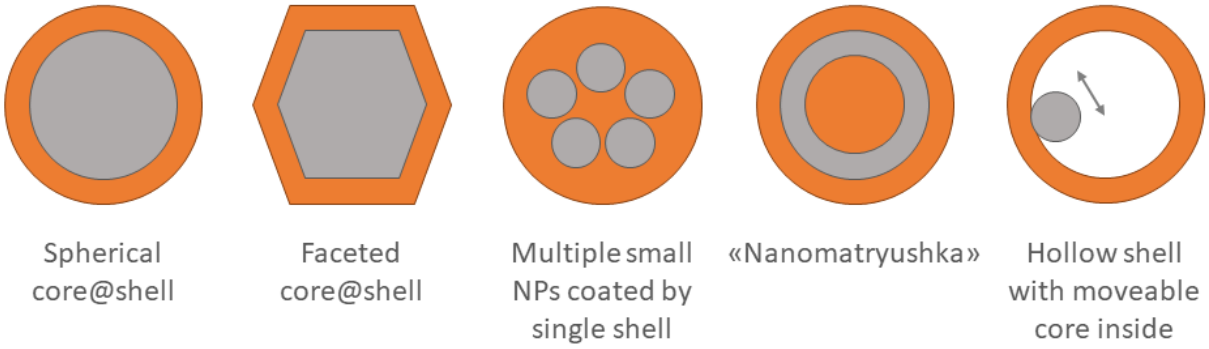

Figure 1-6: Selected types of elemental distribution in bimetallic nanoparticles. The figure is taken from the literature [12], with some modifications.

1.2 Previous Work on $Pt_{1-x}Pd_x$ Nanoparticles

The literature survey on the previous work in the $Pt_{1-x}Pd_x$ system is here limited to the production of nanoparticles via the *polyol method* (described in detail in section 2.2.2) with the polymer PVP (polyvinylpyrrolidone) as stabilizing/capping agent (see section 2.2.1 for more information), as this is the production method employed in the practical work of this thesis. A brief introductory review of selected works from the literature presented in Table 1-1 will follow, with focus on the reported nanoparticle characteristics of *element distribution* and *particle size* with respect to various synthesis parameters.

Table 1-1: Previous work in the $Pt_{1-x}Pd_x$ system with PVP as stabilizer/capping agent where the polyol method was used to produce the NPs. In this table, the following information is given: Nominal composition of the NPs, type of solvent, type of metal precursor(s), metal-to-PVP molar ratio (based on monomer of PVP), average molecular mass of PVP, reaction -temperature and -time, reported particle size, reduction method (for bimetallic systems) and reported element distribution in the product-NPs. See explanations to the respective alphabetical superscripts at the bottom of the table.

Reference	Nominal Composition	Solvent	Metal precursors	$\frac{\text{Metal}}{\text{PVP}}$	Average molecular mass [g/mol] (PVP)	Reaction temperature [°C]	Reaction time [min]	Particle size [nm]	Reduction method	Element distribution[a]
Bundli [13] (2016)	Pt	1,4-BD	$Pt(acac)_2$	$\frac{1}{10}$	10 000	220	120	16.21 ±5.19	—	—
Zhou et al. [14] (2016)	$Pt_{0.21}Pd_{0.79}$	EG	K_2PtCl_4 Na_2PdCl_4	$\sim\frac{2}{5}$	55 000	160	60	6.3 ±1.1 (edge)	Simultaneous	Pd@Pt
	$Pt_{0.21}Pd_{0.79}$	EG	K_2PtCl_4 Na_2PdCl_4	$\sim\frac{2}{5}$	55 000	160	60	6.1 ±0.9 (edge)	Simultaneous	Solid sol.[c]
Muri [15] (2015)	Pt	1,4-BD	$Pt(acac)_2$	$\frac{1}{10}$	10 000	220	30	12.3 ±3.6	—	—
	Pt	1,4-BD	$Pt(acac)_2$	$\frac{1}{10}$	10 000	220	60	13.8 ±4.3	—	—
	Pt	1,4-BD	$Pt(acac)_2$	$\frac{1}{10}$	10 000	220	120	14.3 ±6.0	—	—
	Pt	1,4-BD	$Pt(acac)_2$	$\frac{1}{10}$	10 000	220	180	16.7 ±6.2	—	—
Gupta et al. [16] (2014)	Pd	EG	Na_2PdCl_4	$\frac{17}{10}$	N.R.	100	60	~ 10[d]	—	—
Wang et al. [17] (2013)	Pd	TTEG	Na_2PdCl_4	$\sim\frac{1}{10}$	55 000	140	60	12.8 ±1.3[f]	—	—
	Pd	TTEG	$Pd(acac)_2$	$\sim\frac{1}{10}$	55 000	140	60	14.5 ±1.0[f]	—	—

Hei et al. [18] (2012)	Pt	EG	H_2PtCl_4	$\frac{1}{10}$	300 000	190	120	3.2-6.4[h]	—	—
	Pd	EG	H_2PdCl_4	$\frac{1}{10}$	300 000	190	120	3.2-5.3[h]	—	—
Lee et al. [19] (2011)	$Pt_{0.75}Pd_{0.25}$	H_2O, glycerol	H_2PtCl_6; Na_2PdCl_4	$\frac{4}{9}$	29 000	100	180	~ 11[f, d]	Simultaneous	Solid sol.
Lee et al. [20] (2011)	Pd	H2O, glycerol	Na_2PdCl_4	$\frac{2}{9}$	29 000	100	180	57.86[d]	—	—
Long et al. [21] (2011)	$Pt_{0.50}Pd_{0.50}$	EG	H_2PtCl_6; Na_2PdCl_4	$\frac{1}{6}$	N.R.	160	15[e]	6-10[d]	Simultaneous	Solid sol.
	$Pt_{0.50}Pd_{0.50}$	EG	H_2PtCl_6; Na_2PdCl_4	$\frac{1}{12}$	N.R.	160	15[e]	20-30[d]	Successive	Mix of Pt@Pd or[b] Pd@Pt and separate NPs of Pt; Pd; solid sol.
	$Pt_{0.50}Pd_{0.50}$	EG	H_2PtCl_6; Na_2PdCl_4	$\frac{1}{12}$	N.R.	160	15[e]	16-25[d]	Successive	Pt@Pd
	$Pt_{0.50}Pd_{0.50}$	EG	H_2PtCl_6; Na_2PdCl_4	$\frac{1}{12}$	N.R.	160	15[e]	10-16[d]	Successive	Pd@Pt
	$Pt_{0.50}Pd_{0.50}$	EG	H_2PtCl_6; Na_2PdCl_4	$\frac{1}{6}$	N.R.	160	360[e]	≤ 40[f, d]	Simultaneous	Solid sol.; Pt@Pd
	$Pt_{0.50}Pd_{0.50}$	EG	H_2PtCl_6; Na_2PdCl_4	$\frac{1}{6}$	N.R.	160	360[e]	18-25[d]	Simultaneous	Solid sol.; Pd@Pt
Long et al. [22] (2011)	Pt	EG	H_2PtCl_6	$\frac{1}{12}$	55 000	160	~10-30[e]	~ 8[f, d]	—	—

Papa et al. [23] (2011)	Pt	EG	H_2PtCl_6	$\frac{1}{10}$	8000	120	60	4.9[d]	—	—
Chen et al. [24] (2009)	Pd	TTEG	H_2PtCl_6	$\frac{1}{1}$	40 000	160	150	45 ±5	—	—
Li et al. [25] (2009)	Pd	EG	Na_2PdCl_4	$\frac{1}{40}$	360 000	120	2880	5-8[d]	—	—
	Pd	EG	Na_2PdCl_4	$\frac{1}{40}$	40 000	120	2880	17[f, d]	—	—
	Pd	EG	Na_2PdCl_4	$\frac{1}{20}$	360 000	120	2880	32[f, d]	—	—
	Pd	EG	Na_2PdCl_4	$\frac{1}{40}$	360 000	120	2880	31 ±2[f]	—	—
	Pd	EG	Na_2PdCl_4	$\frac{1}{60}$	360 000	120	2880	28[f, d]	—	—
	Pd	EG	Na_2PdCl_4	$< \frac{1}{100}$	360 000	120	2880	5[f, d]	—	—
	Pd	EG	Na_2PdCl_4	$\frac{1}{40}$	360 000	120	10	< 1[f, d]	—	—
	Pd	EG	Na_2PdCl_4	$\frac{1}{40}$	360 000	120	180	2-10[f, d]	—	—
	Pd	EG	Na_2PdCl_4	$\frac{1}{40}$	360 000	120	900	4-18[f, d]	—	—
	Pd	EG	Na_2PdCl_4	$\frac{1}{40}$	360 000	120	2400	28[f, d]	—	—
	Pd	EG	Na_2PdCl_4	$\frac{1}{40}$	360 000	100	2880	42[f, d]	—	—
	Pd	EG	Na_2PdCl_4	$\frac{1}{40}$	360 000	140	2880	15[f, d]	—	—

	Pd	EG	Na_2PdCl_4	$\frac{1}{40}$	360 000	150	2880	2-6[f, d]	—	—
Han et al. [26] (2008)	Pt	EG	H_2PtCl_6	$\frac{1}{9}$	29 000	180	60[e]	3.6[d]	—	—
Park et al. [27] (2008)	Pt	EG	H_2PtCl_6	$\frac{1}{20}$	24 000	185	90	9.5 ±0.8	—	—
Tao et al. [28] (2008)	$Pt_{0.5}Pd_{0.5}$	1,4-BD	$Pt(acac)_2$; $Pd(acac)_2$	$\frac{1}{10}$	N.R.	215	30	13-17[d]	Simultaneous	Pt@Pd
Song et al. [29] (2005)	Pt	EG	H_2PtCl_6	$\frac{1}{12}$	55 000	197[g]	5[e]	9.4 ±0.6[f]	—	—
	Pt	EG	H_2PtCl_6	$\frac{1}{12}$	55 000	197[g]	5[e]	9.1 ±0.6[f]	—	—
	Pt	EG	H_2PtCl_6	$\frac{1}{12}$	55 000	197[g]	5[e]	9.8±0.6[f]	—	—
Xiong et al. [30] (2005)	Pd	EG	Na_2PdCl_4	$\frac{1}{5}$	55 000	85[e]	270	8-28[d]	—	—

[a]Core@shell

[b]Not specified in source

[c]Addition of additional compounds affecting the NP-formation kinetics of the precursors

[d]Size distribution not reported

[e]Reactants were added step-wise for a prolonged period of time prior to the reaction time reported here

[f]Shape-directing agent was used

[g]Reported temperature was boiling point of EG

[h]By varying the metal precursor concentration relative to the solvent (with a fixed metal/PVP molar ratio)

Element Distribution

Long et al. [21] analyzed by means of TEM the element distribution of $Pt_{50}Pd_{50}$ NPs for batches obtained by varying several synthesis parameters. It was found that Pt@Pd core@shell NPs was the product when successive reduction of H_2PtCl_6 followed by Na_2PdCl_4 was done in ethylene glycol with a metal/PVP - ratio of 1/12, reaction time of 15 min (dwelling time) and reaction temperature of 160°C. In this case, the Pt-precursor that was first reduced formed Pt NPs which acted as seeds for the Pd to grow on and form the shell after the reduction of Na_2PdCl_4. TEM-images of the results are presented in Figure 1-7 (a-c). At the same synthesis conditions (as reported in Table 1-1), except with the opposite order of successive reduction; here with the Pd-precursor first reduced followed by the Pt-precursor, yielded Pd@Pt core@shell NPs. These NPs are shown in Figure 1-7 (d-f).

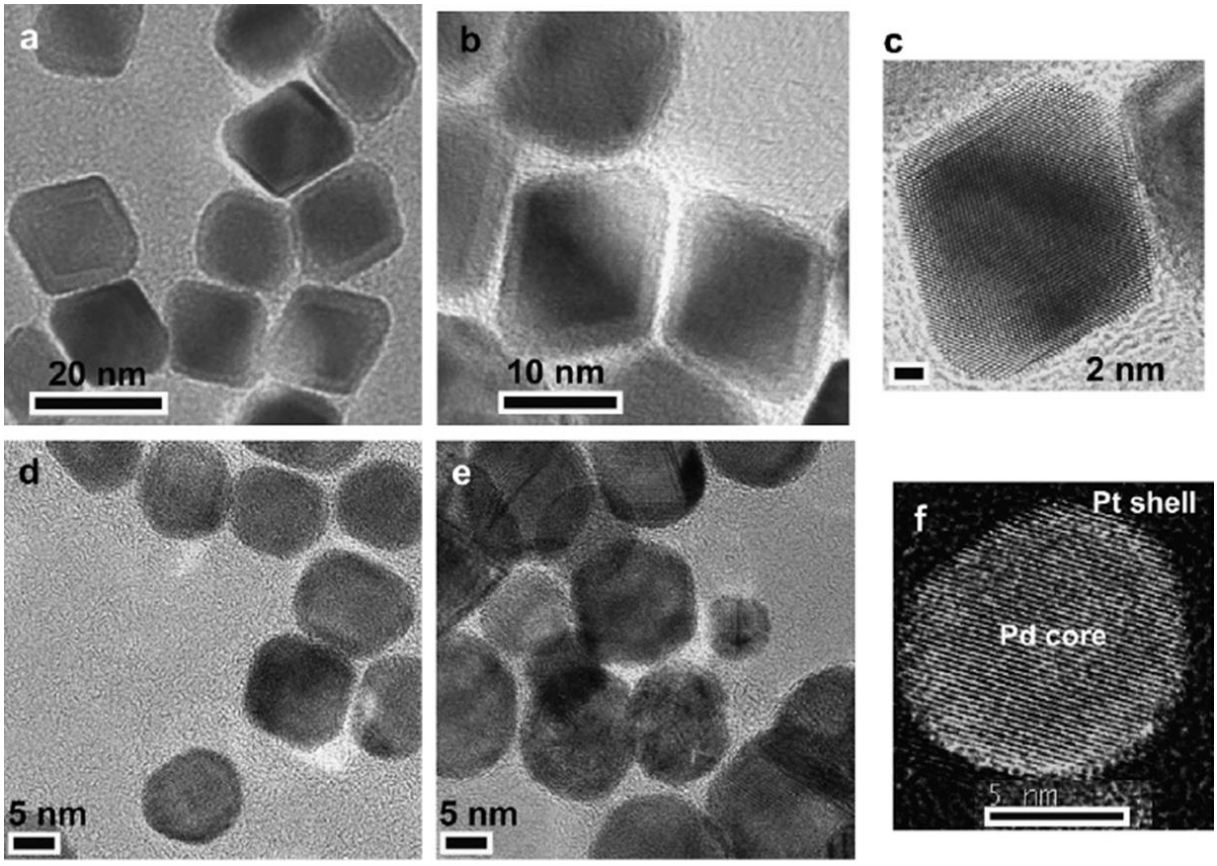

Figure 1-7: TEM and HR-TEM images of Pt@Pd (a-c) and Pd@Pt (d-f) core@shell $Pt_{0.50}Pd_{0.50}$ NPs as synthesized by Long et al. [21].

However, when the nanoparticles were produced by simultaneous reduction, the elements in the nanoparticle product were distributed as a solid solution. Note that the metal-to-PVP ratio in this synthesis was metal/PVP = 1/6, otherwise the synthesis parameters of temperature and reaction time were kept the same as for the core-shell synthesis. TEM-images of the NPs with solid solution distribution are shown in Figure 1-8.

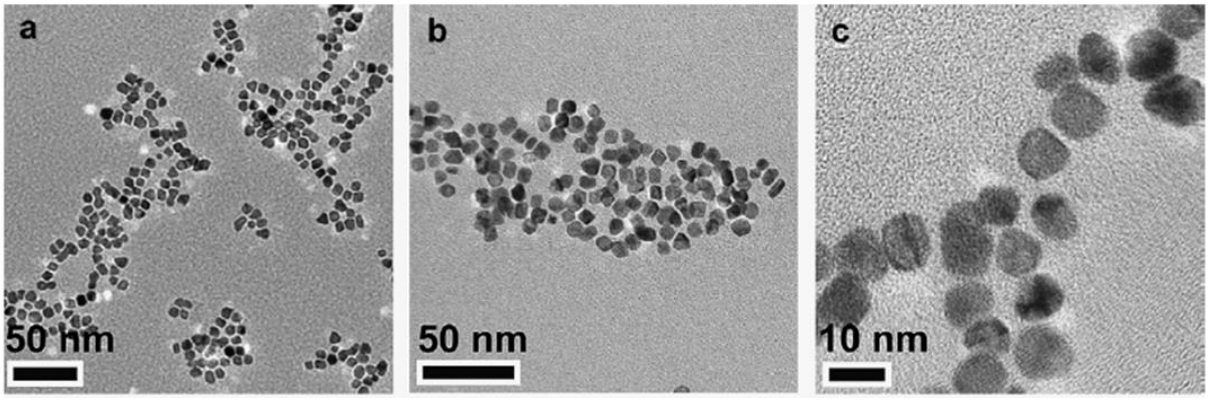

Figure 1-8: TEM-images of $Pt_{0.50}Pd_{0.50}$ NPs as synthesized by Long et al. [21] with elemental distribution as a solid solution.

The results by Long et al. [21] with respect to element distribution are consistent with the findings published in an article by Lee et al. [19], which synthesized $Pt_{0.75}Pd_{0.25}$ NPs by simultaneous reduction with the same types of metal precursors, but with a different molar ratio of metal-to-PVP (metal/PVP = 4/9) and solvent (aqueous glycerol), with reaction time and -temperature at 3 hours and 100°C. The elements were also in this case distributed as a solid solution, determined by EDX line scanning characterization. TEM-images of the nanoparticles and the EDX results are presented in Figure 1-9.

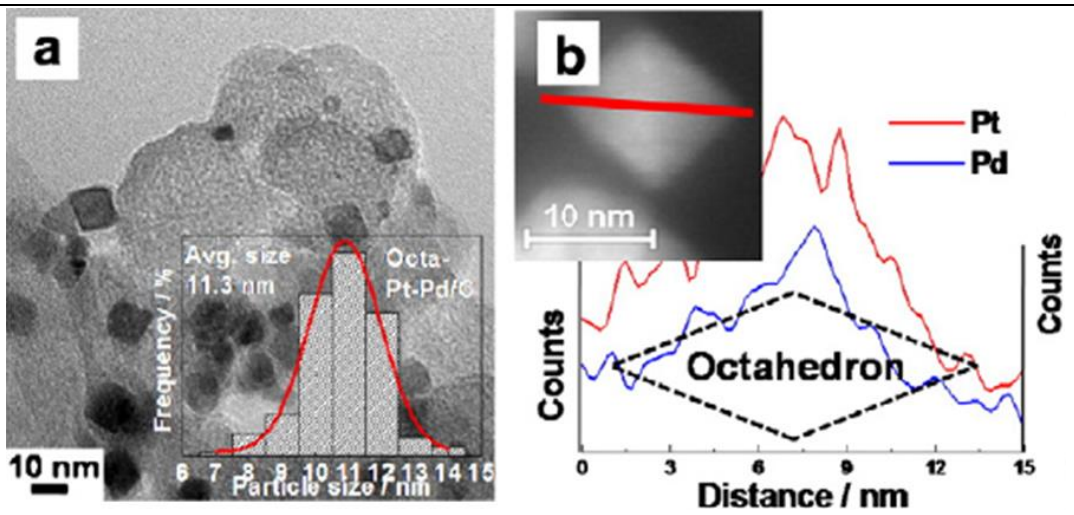

Figure 1-9: (a) TEM-image of $Pt_{0.75}Pd_{0.25}$ NPs. (b) Line scan (EDX) of a nanoparticle shows the element distribution is a solid solution. As synthesized by Lee et al. [19]

Zhou et al. [14] provide an example of this in a paper published in 2016. Using K_2PtCl_4 and Na_2PdCl_4 as metal precursors, reaction temperature and -time of 160°C and 1 h, and metal/PVP ratio of ~2/5 they synthesized two parallel batches of $Pt_{0.21}Pd_{0.79}$ NPs via simultaneous reduction. In one of the batches KBr was also added as an additive to control the formation kinetics of the metal precursors. It was found that without the addition of KBr, the elements were distributed as Pd@Pt because the Pd-precursor reacted much faster than the Pt-precursor, leading to an initial formation of Pd NPs followed by formation of Pt metal atoms. On the other hand, with KBr present during the reaction the elements were distributed as a solid solution because the difference in the formation kinetics of the two metal precursors was lowered. The element distributions were determined by HR-TEM and EDX mapping and -line scans. The results for the core-shell and solid solution distributions are shown in Figure 1-10 and Figure 1-11, respectively. This tells that although simultaneous reduction of the metal salts generally may promote solid solution distribution, and is used for this purpose throughout the literature, the formation kinetics of the metal precursors dictate whether the outcome of the reaction gives a solid solution or e.g. core-shell distribution.

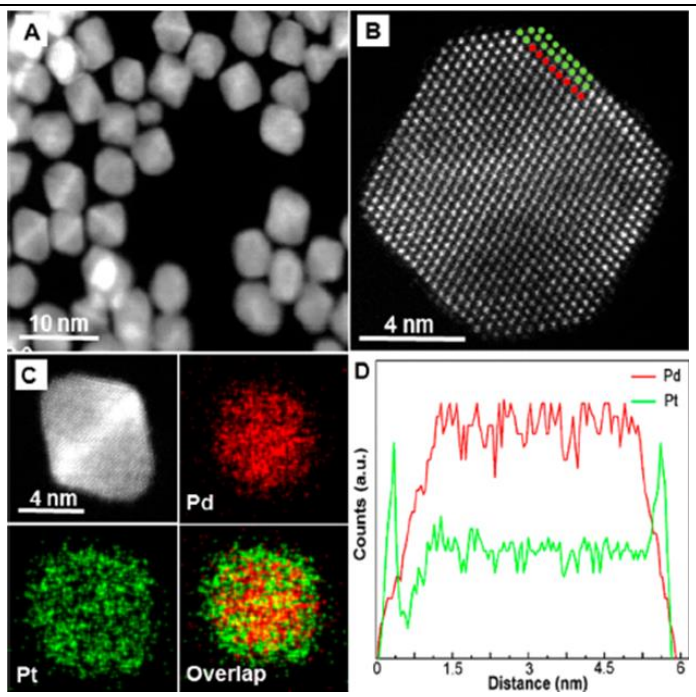

Figure 1-10: $Pt_{0.21}Pd_{0.79}$ Pd@Pt core@shell NPs as synthesized by Zhou et al. [14] and characterized by: (A) HAADF-STEM, (B) HAADF-STEM with atomic resolution: Red colored dots are Pd atoms, green dots are Pt atoms, (C) HAADF-STEM image and EDX element mapping, (D) EDX line-scans.

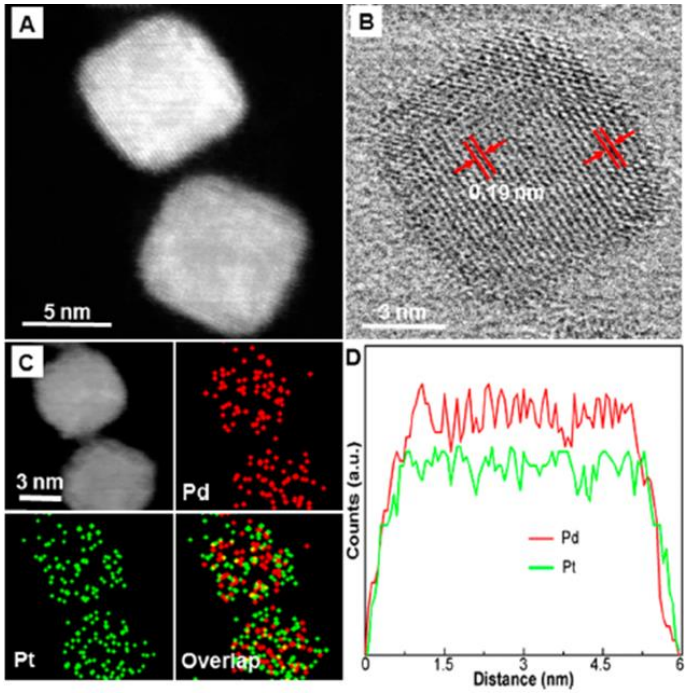

Figure 1-11: $Pt_{0.21}Pd_{0.79}$ solid solution-NPs as synthesized by Zhou et al. [14] and characterized by: (A) HAADF-STEM, (B) HAADF-STEM with atomic resolution, (C) HAADF-STEM image and EDX element mapping, (D) EDX line-scans.

Particle Size

The metal-to-PVP ratio is an important synthesis parameter that affects the particle size of the NP-product, as documented by Li et al. [25]. As listed in Table 1-1, they synthesized Pd NPs by reducing Na_2PdCl_4 in ethylene glycol at 120° with a reaction time of 48 hours. By tuning the metal/PVP -ratio they were able to control the particle size in the range from 5-32 nm. The conclusion they gave was that with increasing concentration of PVP relative to metal precursor in the synthesis, the higher coverage of polymer on the metal would result, and thus a more effective capping action, or inhibition of growth during the synthesis leading to smaller particle sizes. Similar results were also found by Hei et al. [18], where they synthesized Pt and Pd NPs in from H_2PtCl_6 and H_2PdCl_4 in ethylene with PVP at a temperature of 190°C and reaction time of 2 hours. Their findings are summarized in Figure 1-12. Note that the particle size was observed to *decrease* with increasing metal/PVP ratio below the ratio of 1/10.

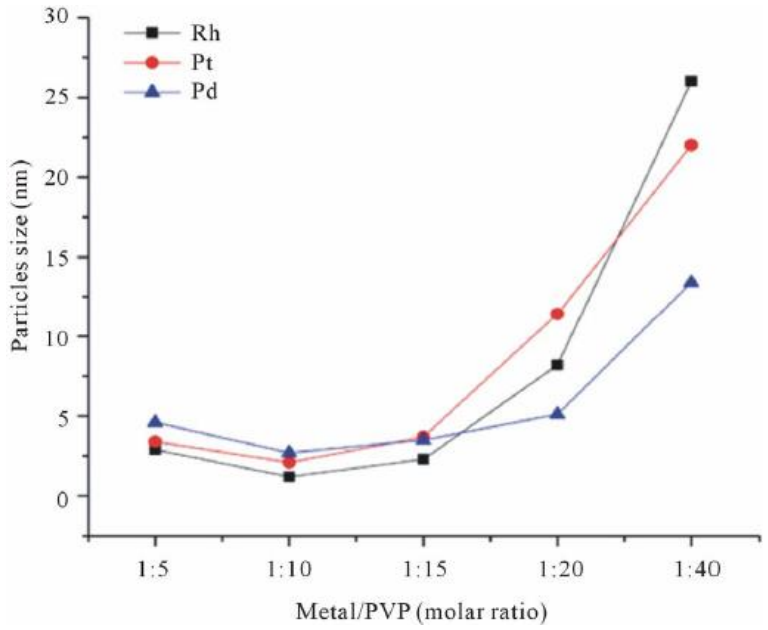

Figure 1-12: Particle size with respect to change in metal/PVP molar ratio for Pt; Pd; Rh. The figure is taken from reference [18].

Another interesting observation that was done by this group was that by using PVP with a lower average molecular mass, speeds up the reaction kinetics of the Na_2PdCl_4 precursor, and promoted smaller particle sizes. Under identical synthesis conditions with the exception of different average molecular masses of the PVP, they synthesized two batches of Pd NPs (see Figure 1-13) with different sizes.

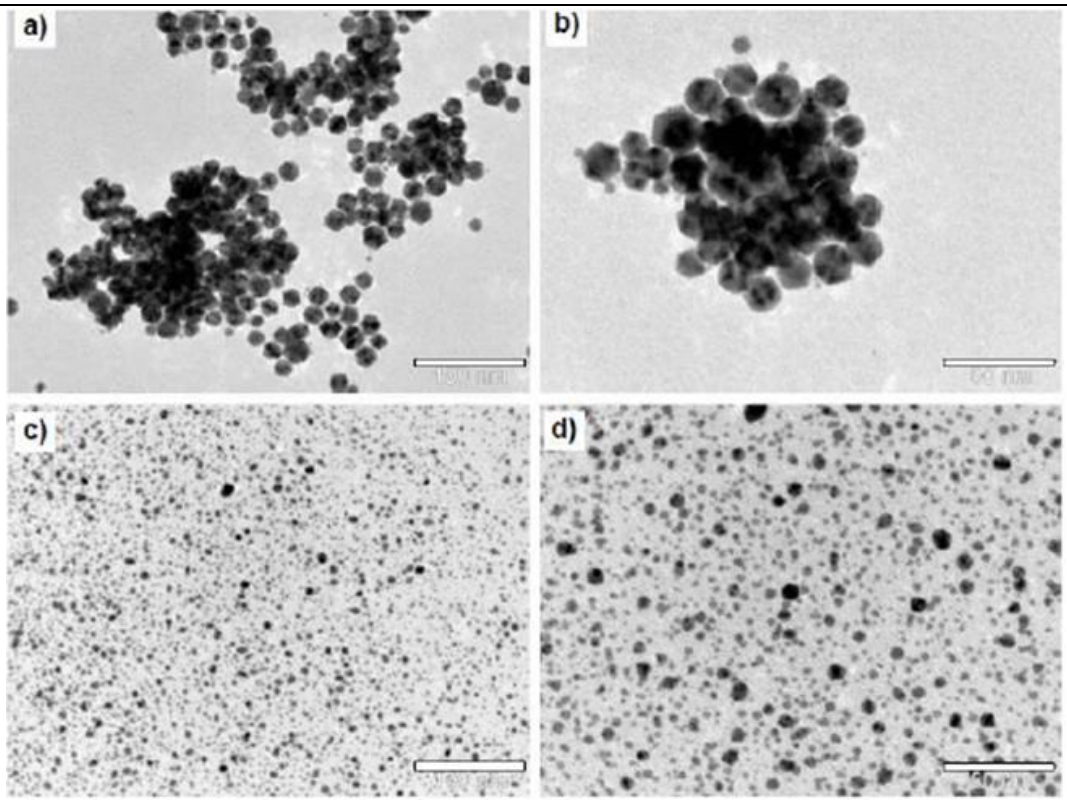

Figure 1-13: TEM-images of Pd NPs synthesized by Li et al. [25]. Visual comparison of NP-size with respect to change in the average molecular mass of PVP used in the synthesis. (a-b) Mass of PVP = 40 000 g/mol; (c-d) Mass of PVP = 10 000 g/mol. The scale-bar on TEM-image *a* and *c* is 100 nm, and on image *b* and *d* is 50 nm.

The reduction rate of the metal precursor is essential in terms of controlling particle size. This is also proven by Li et al. [25] where they synthesized four batches of Pd NPs under identical conditions except for varying the reaction temperature (see Table 1-1). TEM-images of the NPs at corresponding temperatures are shown in Figure 1-14, which clearly illustrate the trend that increasing the reaction temperature promotes smaller particle size by increasing the reduction rate.

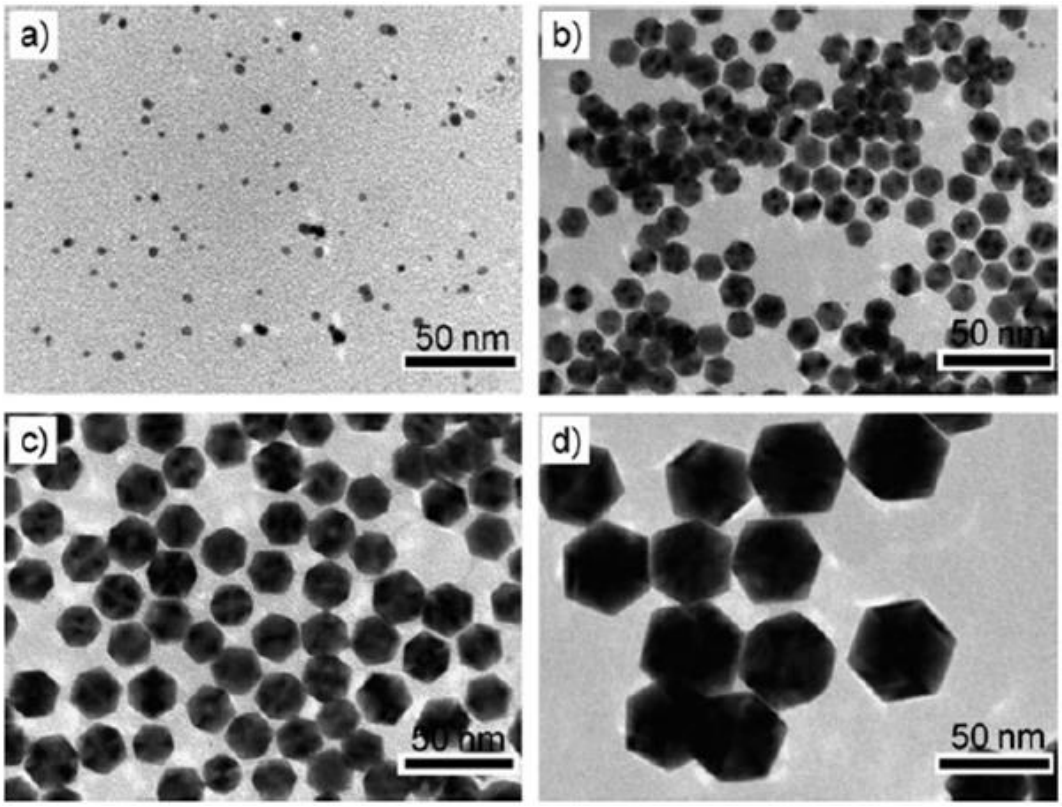

Figure 1-14: TEM-images of Pd NPs as synthesized by Li et al. [25] by reduction of Na_2PdCl_4 in EG with metal/PVP ratio of 1/40 and reaction time of 48 hours at the following reaction temperatures: (a) 150°C; (b) 140°C; (c) 130°C; (d) 100°C.

A series of experiments were performed by Hei et al. [18], where the effect of varying the metal precursor concentration was on particle size were explored. The chemical system was H_2PtCl_6 and H_2PdCl_4 as metal precursors, ethylene glycol as solvent, and PVP as capping agent/stabilizer. It was reported that with a fixed metal/PVP molar ratio, increasing the metal precursor concentration typically produced larger nanoparticles.

1.3 NO_x Abatement by a Two-Step Reduction-Oxidation Technology

NO_x is the collective name for the gases NO and NO_2, which are reported to cause acid rain, severe biological perturbation in lakes and rivers, and have a negative effect on lung infections and allergies in humans [31]. The fact that the emission of air pollutants like these gases need to be restricted, is well known to most people today.

NO_x gases are typically produced by combustion reactions, and mainly from sources like heavy transport, or stationary sources, that is e.g. industrial plants. Systems that can limit the emission of these harmful gases are employed today, but research is still needed to improve them, rendering them more effective [31].

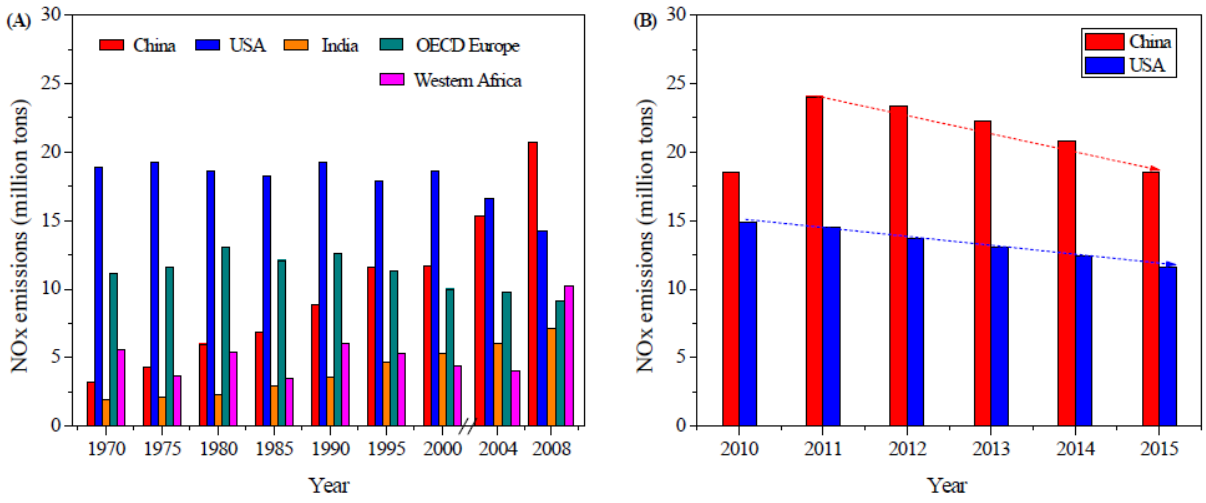

Figure 1-15: (A) NO_x-emission plotted against a timeline for various large nations and regions. (B) NO_x-emission evolution for China (red) and USA (blue) from 2010-2015. The figure is taken from the literature [31].

Several *combustion control* methods have been used to reduce NO_x-emissions in the past. The principle behind these approaches is to tune the combustion reaction conditions to reduce the total amount of NO_x produced. However, these methods generally fail to meet the emission restrictions. *Post-combustion processes* are another way of tackling the NO_x issue. The working principle here is elimination of the gases *after* the combustion processes by SCR (Selective Catalytic Reduction), SNCR (Selective Non-Catalytic Reduction) or hybrid-SNCR-SCR. The NH_3-SCR process is capable of yielding over 90% conversion of NO_x [31].

The standard SCR process is the elimination of NO_x through a catalytically driven reaction of the gas with ammonia (either anhydrous or aqueous) or urea. Removal of excess ammonia from

the previous step, can be applied as this also is a gas that have strict restrictions for emission due to pollution hazards. This is done by SCO (Selective Catalytic Oxidation) of NH_4 [31],[32]. The SCO reaction is often done between 200-500°C, and thereby frequently referred to as intermediate temperature ammonia oxidation.

The catalytically driven chemical reaction taking place in SCR with NH_3 is shown via reaction equations Rxn. eq. 1.1-2 [31]:

$$4NH_3(g) + 4NO\ (g) + O_2(g) \rightarrow 4N_2(g) + 6H_2O(g) \quad \text{(Rxn. eq. 1.1)}$$

$$4NH_3(g) + 2NO_2(g) + O_2(g) \rightarrow 3N_2(g) + 6H_2O\ (g) \quad \text{(Rxn. eq. 1.2)}$$

The chemical reaction with the presence of a catalyst for removal of excess ammonia by oxidation is shown in Rxn. eq. 1.3-6 [32]:

$$4NH_3(g) + 3O_2(g) \rightarrow 2N_2(g) + 6H_2O\ (g) \quad \text{(Rxn. eq. 1.3)}$$

$$2NH_3(g) + 2O_2(g) \rightarrow N_2O\ (g) + 3H_2O\ (g) \quad \text{(Rxn. eq. 1.4)}$$

$$4NH_3(g) + 5O_2(g) \rightarrow 4NO\ (g) + 6H_2O\ (g) \quad \text{(Rxn. eq. 1.5)}$$

$$4NH_3(g) + 7O_2(g) \rightarrow 4NO_2(g) + 6H_2O\ (g) \quad \text{(Rxn. eq. 1.6)}$$

The mission here is to limit the emission of pollutants; therefore, the goal is to optimize the catalyst in the ammonia oxidation step selectively towards water and nitrogen (Rxn. eq. 1.3) rather than laughing gas and nitrogen oxides (Rxn. eq. 1.4-6). In addition to this, the catalysts should have as high a catalytic activity as possible. The underlying inspiration behind the experimental work of this thesis is based on *controlling* the synthesis parameters in the production of these catalysts, for optimization towards this step. Typical suitable materials active for ammonia oxidation are noble metals including; Pt, Pd, Ru, Ag, Ir and Au, or transition metal oxides including; MoO_3, CuO, Fe_2O_3, TiO_2, Co_3O_4, V_2O_5 and MnO_2 [32].

1.4 The Pt-Pd System -Phase Diagram and other Properties

In Figure 1-16 the binary phase diagram of bulk $Pt_{1-x}Pd_x$ is shown. From the figure, it is clear that an *immiscibility dome* is present, that is an area in the phase diagram where the two metals cannot form a solid solution: For compositions between approximately 10-90% Pt in the bimetallic system, at temperatures between ~300-770°C (depending on the composition), Pt and Pd are not miscible. It should be noted that as several groups have successfully synthesized $Pt_{1-x}Pd_x$ NPs in the range of x = 0-1 (Table 1-1).

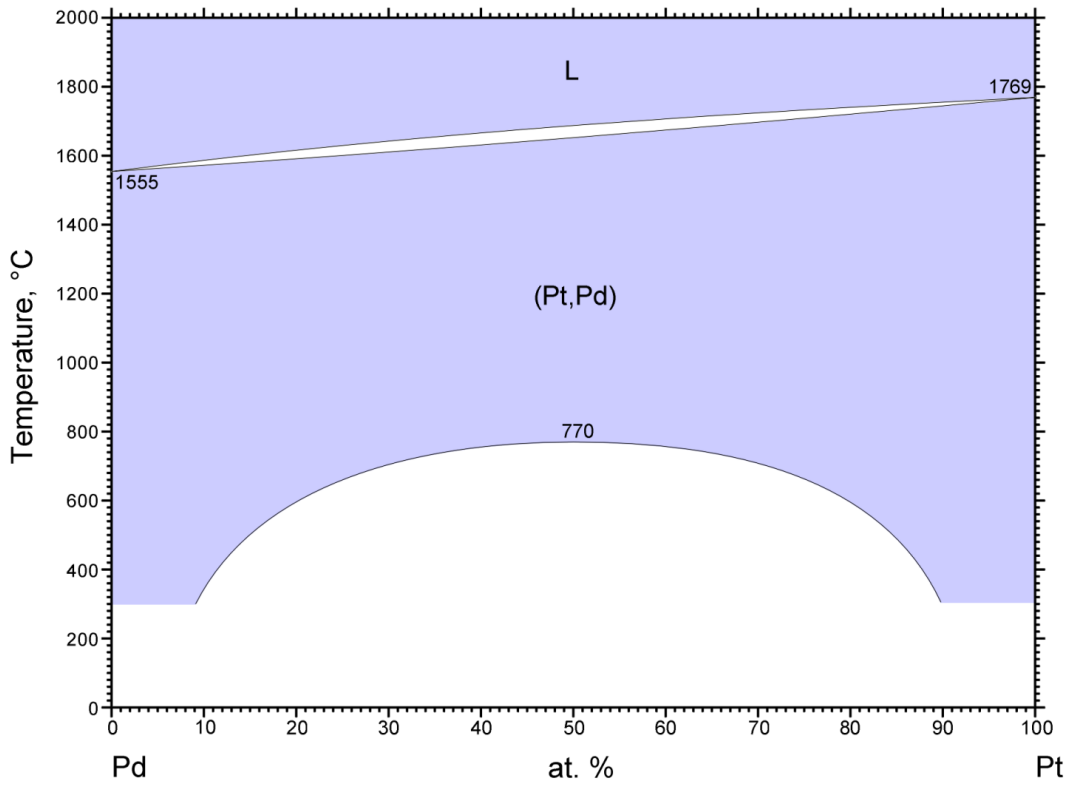

Figure 1-16: Pt-Pd binary phase diagram. The white and blue areas represent two-phase- and single-phase regions, respectively. Taken from the reference: [33].

Table 1-2: Reported a-axis values for bulk Pt, $Pt_{0.5}Pd_{0.5}$ and Pd.

Reference	Pt a-axis [Å]	$Pt_{0.5}Pd_{0.5}$ a-axis [Å]	Pd a-axis [Å]
Webelements [34],[35]	3.9242	—	3.8907
Gibaud et al. [36]	3.92	—	—
Manoun et al. [37]	3.924	—	—
Arblaster [38]	[1]3.9236 ±0.0006	—	—
Arblaster [39]	—	—	[2]3.8902 ±0.0006
Thiebaut et al. [40]	—	—	3.891
Moysan et al. [41]	—	3.903	3.890

[1]Mean value of 14 references ± one standard deviation

[2]Mean value of 19 references ± one standard deviation

Table 1-3: Reported a-axis values for Pt and Pd NPs

Reference	Particle size [nm]	Pt a-axis [Å]	Pd a-axis [Å]
Teranishi et al. [42]	2.16 - 3.31	3.9157 - 3.9366	—
Teranishi et al. [43]	2.22 - 4.89	—	3.9139 - 3.9752
Jeon et al. [44]	3-5[a]	—	3.94 ±0.01
Shinohara et al. [45]	5-30[a]	—	3.90
Bundli [13]	16 ±5	~3.92	—
Muri [15]	~7-22[a]	~3.91-3.92	—
Papa et al. [23]	~4.9	3.917	

[a]Whole size range, not based on mean particle sizes

1.5 Motivation

In the NAFUMA research group at Department of Chemistry, UiO we have a long tradition in exploring new materials by combining fundamental studies with application motivated research. For example, metallic nanoparticles fabricated with controlled size, faceting, atomic arrangement and chemical composition gives a huge space of opportunity with respect to controlling chemical- and physical properties, and thereby applications.

The ASCAT project, which is a joint effort between the NAFUMA group and industry, and with several PhD- and postdocs associated, focuses on understanding and exploring ammonia slip catalysts. The main objective in the ASCAT project is to develop a high-performance catalyst that quantitatively can remove an excess of ammonia (in trace amounts) that has deliberately been co-fed as the active reductant in NO_x abatement. The excess ammonia is subsequently removed by intermediate temperature (200-500°C) oxidation over a metal-on-support catalyst or an oxide based catalyst.

The motivation of the current master project is to perform an initial suitability screening of the bimetallic Pt-Pd system for NH_3 oxidation catalysis and provide recommendations on protocols on synthesis and characterization of free standing $Pt_{1-x}Pd_x$ NPs as well on catalytic performance relative to NH_3 oxidation.

In the first part of the master project, synthesis methods for producing colloidal $Pt_{1-x}Pd_x$ nanoparticles (NPs) will be established with basis in the so-called polyol approach. Phase pure NPs with tunable Pt-Pd element distribution is targeted for. In this connection the relative reactivity of the Pt- and Pd-metal precursors becomes critical. Selected samples will be studied in detail with respect to elemental distribution. $Pt_{1-x}Pd_x$ samples will also be utilized as model samples for implementation of new methodologies to the NAFUMA group on atomic scale element distribution characterization of nanoparticles.

The second part of the master work is devoted to understanding of the suitability of $Pt_{1-x}Pd_x$ nanoparticles for NH_3 oxidation. Synthesized nanoparticles from part one will be converted to metal-on-support catalysts and tested for NH_3 oxidation. The material characterization of the obtained catalysts and analysis of catalyst activity tests are foreseen to be key tasks in this subproject.

Methodologies used will be Schlenk-lines and glove box for inert synthesis of colloidal nanoparticles, powder X-ray diffraction in combination with Rietveld refinements for structural

characterization, high-resolution scanning electron microscopy (SEM) for imaging of nanoparticles, furthermore data obtained from transmission electron microscopy (TEM) and fixed-bed catalytic testing will be analyzed in-depth.

2 Methods and Theory

In this chapter, theory of nucleation and growth is given as an introduction to different aspects of nanoparticle synthesis which are described subsequently. Thereafter a brief description of the preparation of *metal-on-support catalysts* by the method utilized in this thesis follows. At the end of the chapter is the theory behind the various characterization techniques that are relevant in this work.

2.1 Nucleation and Growth

In this chapter, an introduction to the concepts of surface tension and surface energy are provided in order to understand the subsequent descriptions of mechanisms of nucleation and growth. The concept of *burst nucleation,* a process utilized to yield a monodispersed size distribution of the particles, is then defined through the description provided by La Mer [46, p.36]. At the end of the sub-chapter faceting of nanoparticles will be explained.

2.1.1 Surface Tension and Surface Energy

Surface tension (γ) can be defined in units of *force per unit length* or *energy per unit area.* See Figure 2-2 (*Top view*). Accordingly, the surface tension can be regarded a force acting along the length (L) of the moveable wire, on the surface film tending to minimize its area. This tendency to decrease the total surface area is there because the molecules constituting the surface have a lower number of interactions with neighboring molecules than those in the bulk (Figure 2-1).

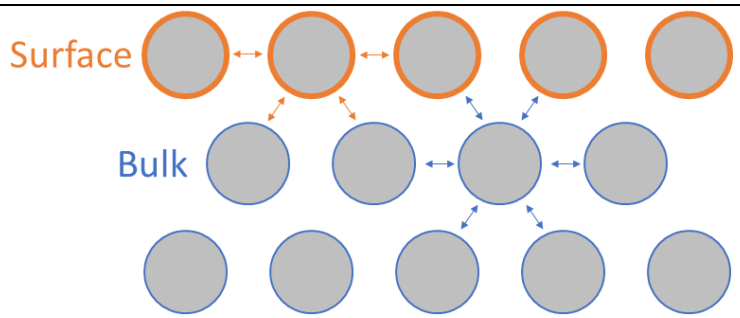

Figure 2-1: Interactions of neighboring molecules in the surface and bulk of a liquid. The purpose of this figure is only to show that there are a larger number of molecules surrounding the ones located in the bulk, than in the surface of the liquid. The arrows indicate the intermolecular interactions.

Thermodynamically, it is favorable to have the maximum number of interactions around the molecules. It can be seen from Figure 2-2 (*Side* view) that when the film is stretched more, a larger number of molecules of the total in the liquid are located in the surface, as opposed to when the film is stretched less. This is assuming a constant volume (and total number of molecules) in the film. Therefore, the tendency is that the surface area decreases to minimize the number of molecules with few neighboring interactions [47, p.251-252], [48, p.132-133].

In Figure 2-2 (*Top* view) the orange wire can move freely, and will do so in the direction which results in a decrease in the surface area of the film. Therefore, an opposing force (F) is required to keep the wire in a fixed position. In Eq. 2.1, the relationship between this force (F), the length of the wire (L), and the surface tension is given, keeping in mind that the film has an upper and lower side which explains the factor of two [47, p.252].

$$\gamma = \frac{F}{2L} \qquad \text{(Eq. 2.1)}$$

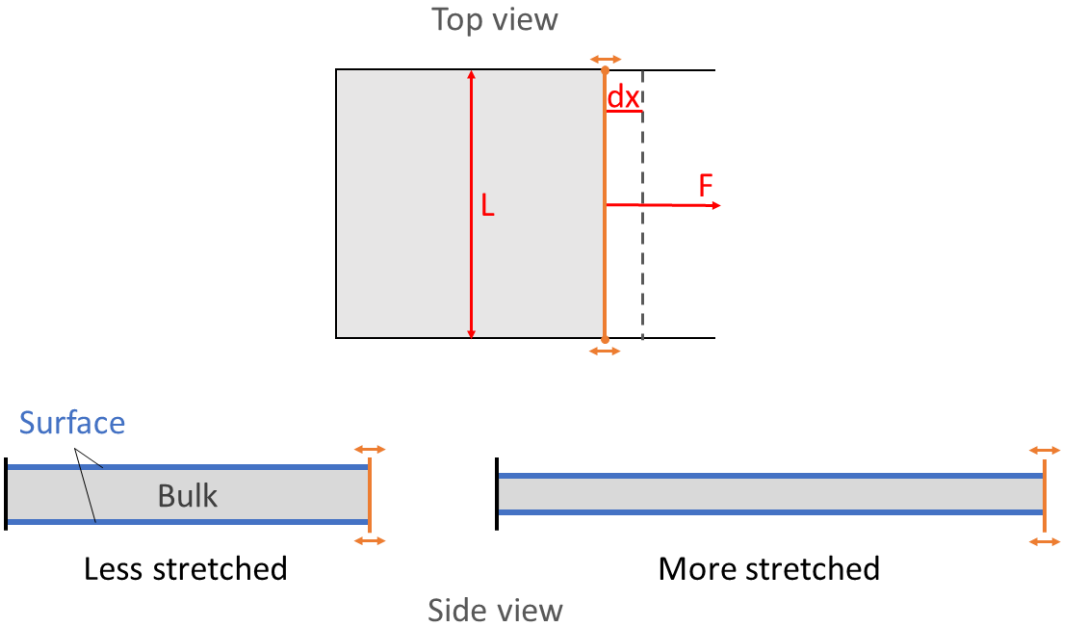

Figure 2-2: Top view: Phenomenological illustration of surface tension. The black U-shaped frame is rigid, and has a frictionless moveable (orange) wire attached to it. The apparatus can be dipped into a liquid such that it forms a film (gray area) between the boundaries of the frame and wire. The orange line can move in the directions labelled. The figure is made based on Fig. 6.2 (a) in the literature: [47, p.252]. Side view: The film is shown to have two surfaces (blue); an upper- and a lower- side.

The work (W) required to increase the area of the surface by the amount dA is stated in Eq. 2.2. Note that the product of 2L and dx is equal to dA. Following this description, it is clear through Eq. 2.2 that if the moveable wire is displaced a distance dx by a force infinitesimally greater than F, *work* is required [47, p.255].

$$W = Fdx = \gamma 2Ldx = \gamma dA \qquad \text{(Eq. 2.2)}$$

In other words, γ is here defined as the work required to form a unit area of new surface [47, p.255]. However, thermodynamics states that *work* is a path-dependent process [47, p.255]. Therefore, it is useful to take this a step further, and introduce the correlation between the surface tension and change in Gibbs free energy per change in unit area $\left(\frac{\partial G}{\partial A}\right)$ (Eq. 2.3), avoiding the path-dependent variable:

$$\gamma = \left(\frac{\partial G}{\partial A}\right)_{T,p} \qquad \text{(Eq. 2.3)}$$

The relation in Eq. 2.3 assumes a reversible process at constant temperature and pressure [47, p.256,257].

The surface energy can also be expressed according to Eq. 2.4, which shows that γ is equal to the *excess Gibbs free energy per unit area* of the surface (G^s), and that the relationship between G, H and S also are applicable in relation to γ [47, p.257].

$$\gamma = G^s = H^s - TS^s \quad \text{(Eq. 2.4)}$$

An alternative phrasing of this could be that the *excess surface energy* of a material is associated with the extra energy of the atoms constituting its surface, due to their dangling bonds [49, p.313]. Conventionally, the term "surface energy" is used in reference to solid materials, whereas the term "surface tension" is used when dealing with liquids [49, p.311].

2.1.2 Nucleation

Nucleation is the process leading to the formation of small clusters of a growth species, which subsequently can continue to grow in a growth process. These clusters can for example be a collection of some very few metal atoms, in production of metallic NPs. During the formation of the nuclei, the metallic atoms arrange themselves into their respective crystal structures [1, p.55]. The nucleation process can occur in gas-, liquid- and solid- phase [1, p.56], but along the scope of this thesis the focus is on the *liquid phase*. In the liquid phase, nucleation can only occur if the solution is *supersaturated* [50, p.526].

Nucleation will here be categorized as sketched in Figure 2-3. *Primary* nucleation covers the subordinate terms *homogeneous*- and *heterogeneous* nucleation. These terms respectively refer to spontaneous nucleation, and nucleation that are induced by the presence of *foreign particles* and whereof the new phase forms on the surface of these [51, p.181], [1, p.63]. *Secondary* nucleation is defined by Mullin et al. as nucleation taking place on crystals of the *same* substance as the nucleating phase. Note that these seed crystals are added to the system prior to the initiation of the nucleation process [51, p.195].

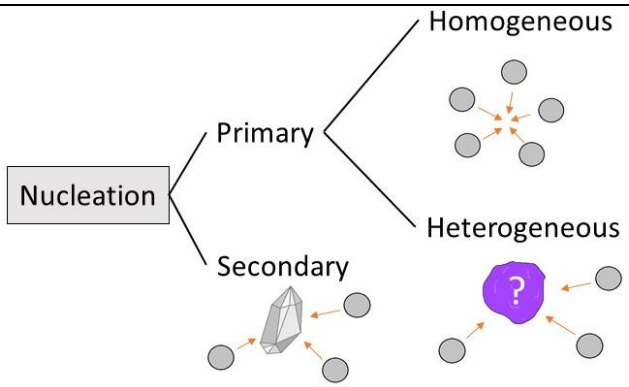

Figure 2-3: Terminology related to different conditions for nucleation.

Homogeneous Nucleation

In view of thermodynamic considerations, homogeneous nucleation is given as the sum of two energy contributions; ΔG_S and ΔG_V. This is shown in Eq. 2.5, which expresses the total excess free energy (ΔG_N) for nucleation of a cluster with a spherical shape and radius (r). The subscripts *N, S* and *V*, refer to *Nucleation, Surface* and *Volume* in this respective order [7, p.183], [8].

$$\Delta G_N = \Delta G_S + \Delta G_V = 4\pi r^2\gamma + \frac{4}{3}\pi r^3 \Delta G_{tpv} \qquad \text{(Eq. 2.5)}$$

ΔG_S refers to the excess free energy difference between the surface of a particle and its bulk phase, while ΔG_V is the energy difference associated with the formation of a *bulk phase* from the solute in solution. The quantity ΔG_{tpv} is the free energy change of *transformation per volume*, where the transformation refers to the formation of the new phase. γ is the interfacial tension between the surface of the new phase and the supersaturated solution from which it occurred [51, p.183]. The surface energy contribution (ΔG_S) to Eq. 2.5 has a positive value as it is associated with the formation of a new surface, see section 2.1.1. The energy contribution corresponding to the bulk phase (ΔG_{tpv}) has a negative value in supersaturated solutions ($C > C_0$ in Eq. 2.6). In Figure 2-4 the two energy contributions and their sum are sketched schematically.

$$\Delta G_{tpv} = -\frac{kT}{\Omega \ln\left(\frac{C}{C_0}\right)} \qquad \text{(Eq. 2.6)}$$

Eq. 2.6 expresses the change in Gibbs free energy per volume of solid phase. Ω is the volume occupied by one molecule, C is the concentration of the solute, C_0 is the equilibrium concentration of the solute in solution, k is the Boltzmann constant, and T is the temperature.

In the production of metallic NPs, the *solute* refers to the metal monomers in solution which are the building blocks of the nuclei [1, p.56].

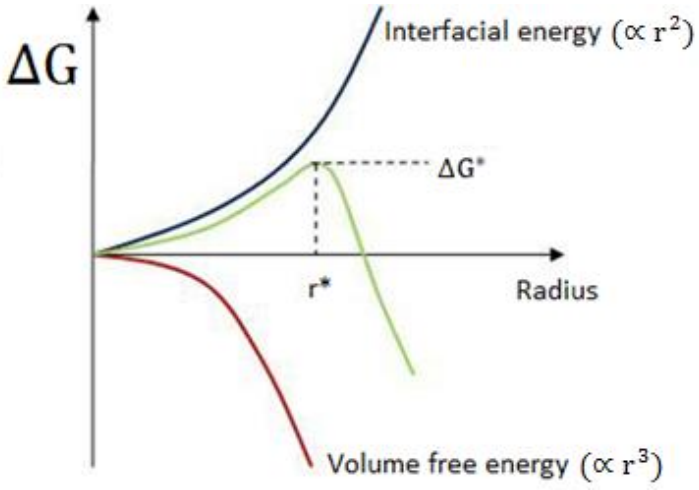

Figure 2-4: Energy contributions to the total free energy in the process of nucleation [52].

Since the energy contribution related to the surface scales with r^2, and the contribution associated with the bulk phase scales with r^3, ΔG_N passes through a maximum (ΔG^*). This extremal value of the total free energy corresponds to a *critical radius* (r^*) of the nucleus. This is the smallest size that the nucleus can have, and be thermodynamically stable. From Figure 2-4, this is easy to see. For values of r smaller than r^*, ΔG_N decreases by *redissolving* the particle. In the case where r is larger than r^*, ΔG_N decreases by *growing* it larger. The energy barrier needed to be overcome in order to form the stable nucleus (ΔG^*), can be realized in local regions of higher energy in the system. This can be described with a statistical foundation by the well-known Arrhenius (Eq. 2.7) [51, p.183-184]:

$$J = A \exp\left(-\frac{\Delta G^*}{kT}\right) \qquad \text{(Eq. 2.7)}$$

Eq. 2.7 expresses the rate (J) of a process that is thermally activated. A is the frequency factor related to collisions of the involved entities and their orientation, k is the Boltzmann constant, T is the temperature [7, p.184], [9]. In a supersaturated system, the *rate of nucleation* mainly depends on the *temperature*, *degree of supersaturation* and the *interfacial tension* between the solution and nucleated phase. Mullin et al. provide an expression (Eq. 2.8) that shows this [51, p.183-185]:

$$J = A \exp\left(-\frac{16\pi\gamma^3 V_m^2}{3k^3T^3(\ln S)^2}\right) \quad \text{(Eq. 2.8)}$$

Eq. 2.8 is based on Eq. 2.7, and in the prior J is the rate of nucleation in units of *number of formed nuclei per unit volume per unit time*, V_m is the molar volume, and S is the supersaturation ratio. S is defined as the ratio between the actual concentration in the solution and the equilibrium saturation at a specific temperature [51, p.125, 184-185].

Heterogeneous Nucleation and Seeding

Foreign solid particles that are present in the reaction mixture during the nucleation process can lead to an altered nucleation rate as compared to homogeneous nucleation. These particles are always present in an unfiltered system [51, p.192].

The free energy change in formation of a critical nucleus in heterogeneous nucleation is lower than for homogeneous nucleation [51, p.192-193], see Figure 2-5.

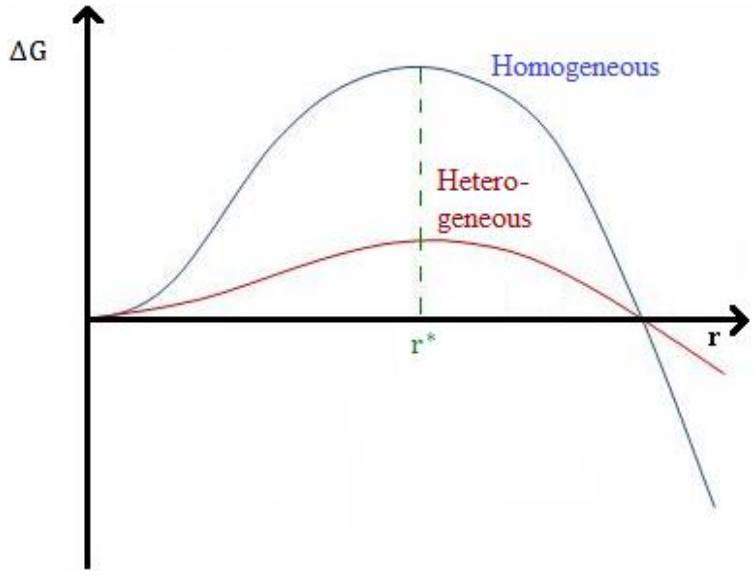

Figure 2-5: Comparison of change in free energy in the formation of a critical nucleus between the homogeneous and heterogeneous nucleation processes. Drawing is taken from reference [53].

The difference in change of free energy between the two processes can also be described according to Eq. 2.9, by a factor ϕ which depends on the interactions between the newly formed crystalline phase and the foreign particle surface on which it was deposited. The value of ϕ can range between 0 and 1. The two values of free energy change with subscripts *hetero* and

homo refer to the energy change in the formation of a critical nucleus in the processes of heterogeneous and homogeneous nucleation, respectively [51, p.193-194].

$$\Delta G^*_{hetero} = \phi \Delta G^*_{homo} \quad \text{(Eq. 2.9)}$$

Secondary nucleation occurs typically at lower levels of supersaturation than the prementioned nucleation processes [51, p.193-195]. Although, the material used as a promotor for nucleation (the *seed crystal*) does not have to be composed of the exact same material as the one being formed in the process. Seeds that are isomorphous in relation to the material being crystallized are also effective promotors [51, p.197-198]. These seeds can serve as *templates* for producing monodispersed NPs with predetermined shapes. That is if the seeds themselves are monodispersed and have uniform shapes [1, p.63].

2.1.3 Growth of Nanoparticles

The growth process of NPs in solution can be controlled by *diffusion*- or by *surface processes.* Camargo et al. describe the growth process by dividing it into four steps [1, p.59-60] (see Figure 2-6). *Step 1* corresponds to the formation of a *growth species*, which subsequently *diffuses* to the surface of the particle from the bulk of the solution (*step 2*). It then *adsorbs* on the surface (*step 3*), before it *incorporates* to it (*step 4*). *Steps 1-3* are regarded as *diffusion*, while *step 4* is the actual growth (by *surface processes*).

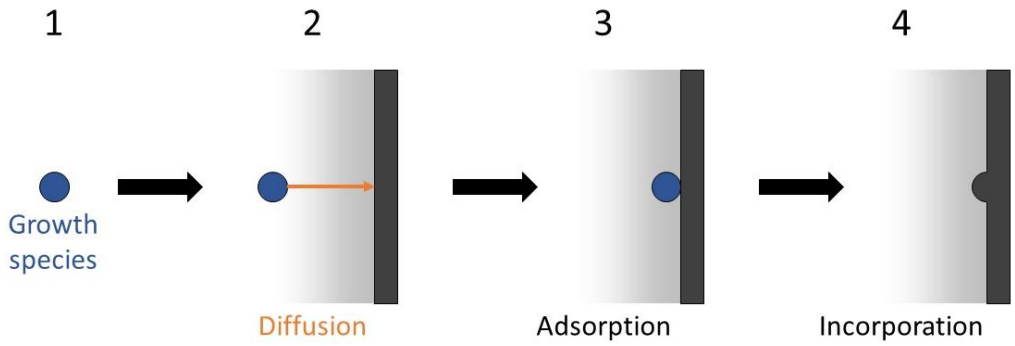

Figure 2-6: Four steps in the growth process as outlined by Camargo et al. The figure is taken from reference [1, p.60].

If diffusion is the rate limiting step in the growth process, it is referred to as *diffusion controlled growth.* Experimentally, this type of growth mechanism can be promoted if the concentration

of growth species is low as then the diffusion distance is large. It is also possible to obtain a diffusion limited growth by limiting the amount of growth species to the growth surface. A solvent with a high viscosity will also favour this growth mechanism. Polymers employed to sterically stabilize the particles, as elaborated in section 2.3.2, can also act as a *barrier* which the growth species need to diffuse through in order to reach the growth surface. Therefore, using these kinds of stabilizing agents also favours diffusion limited growth [1, p.60-61].

The growth process needs to be *controlled* in some way to achieve monodispersed NPs with correspondingly tuneable sizes and shapes. The use of *capping agents* is a means to an end in this regard. For more details see section 2.1.5

Ostwald Ripening and Coalescence

One can speak about a *solubility of NPs* in a liquid system where they are produced in solution. What is meant by this is that they can *redissolve* depending on their size, as mentioned in section 2.1.2. The process where smaller particles redissolve to "feed" the larger ones such that they further increase their size is referred to as *Ostwald ripening.* This process can cause the size distribution of the NPs to narrow [51, p.320]. The size-dependent solubility of the particles is given in Eq. 2.10, and shows that the solubility increases as the particle size decreases. This is the so-called *Kelvin equation* applied to a crystal in solution. Here, C(r) is the solubility of a NP with the radius r, and C_0 is the solubility of the bulk solid composing the particle. V_m is the molar volume of the solid, γ is the interfacial tension between the particle and the solvent [48, p.144-145].

$$\ln\left(\frac{C(r)}{C_0}\right) = \frac{2\gamma V_m}{rRT} \qquad \text{(Eq. 2.10)}$$

The processes of Ostwald ripening and coalescence are illustrated schematically in Figure 2-7.

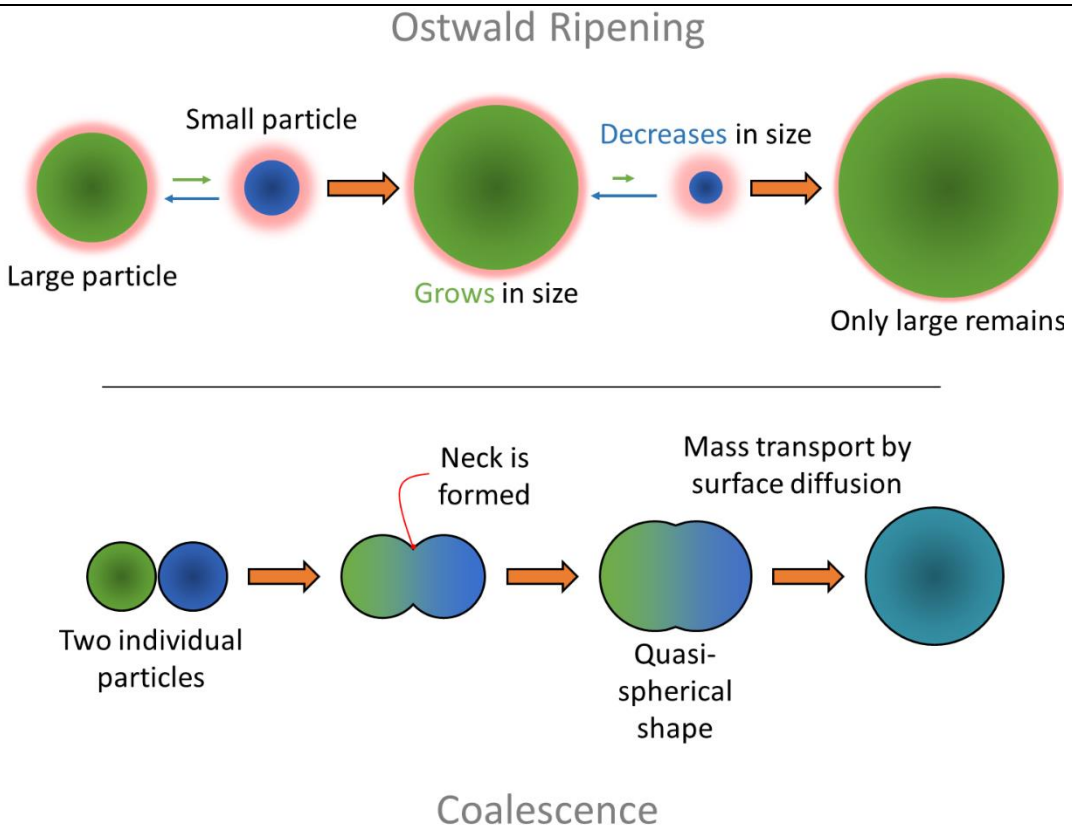

Figure 2-7: Schematic illustration of Ostwald ripening and coalescence. Ostwald ripening: The large (green) particle has a lower solubility than the smaller one (blue). The lengths of the green and blue arrows indicate this. In the end, only the large particle remains. Coalescence: Two (or more) particles collide, and a neck is formed, joining them together. Mass transport occurs through surface diffusion (below the melting point), and a quasi-spherical shape results from the reduction of surface energy [54].

Whereas Ostwald ripening is growth of large particles on the expense of small ones through dissolution, *coalescence* is growth of particles by *combination* of more small particles. This means that particles of equal size also can combine to result in a particle of bigger size [49, p.324-325].

2.1.4 La Mer Theory - Burst Nucleation

In the production of nanoparticles, the particle growth must be separated in time from the initial nucleation during the formation process. By doing this, products with monodispersed size distributions are possible to achieve. In other words, the history of each individual particle are the same in terms of growth and nucleation [55, p.659]. This temporal separation of nucleation and growth is achievable through the initial formation of a large number of stable nuclei within a narrow time window, followed by growth without nucleation occurring. This is possible due

to the activation-energy barrier associated with the crystallization process. If this barrier is rapidly surpassed in a single jolt of action by pushing the chemical system into a highly non-equilibrium state, homogeneous nucleation will readily happen to form a large number of nuclei. Equilibrium is restored by the progression of this process, which implies that the system will be less prone to further nucleation [55, p.659-660]. This is conceptualized in the literature of nanoparticle synthesis as *burst nucleation* [1, p.56].

A qualitative illustration of the concept of burst nucleation is shown in Figure 2-8. The concept was established by La Mer and Dinegar in 1950, and shows how the concentration of monomer varies with time through the process [46, p.36].

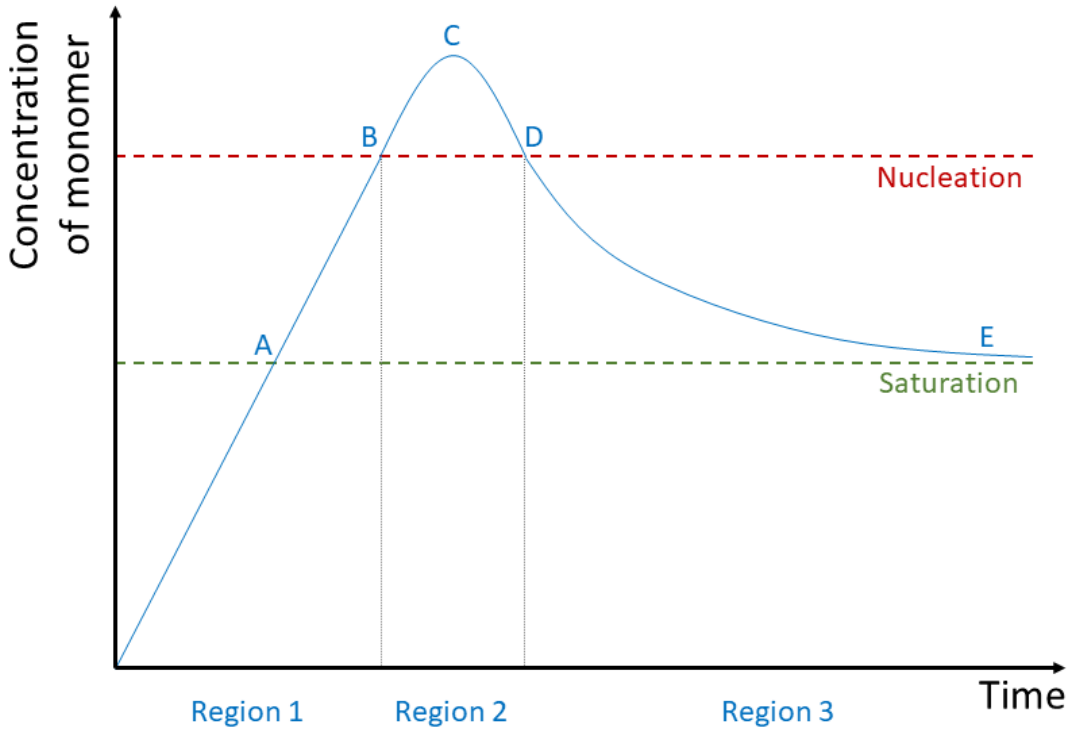

Figure 2-8: The La Mer diagram. The figure is made based on the literature found here: [50, p.527].

The process is divided into three *time-regions* (Figure 2-8). In *Region 1* the concentration of monomers in solution increases as time progresses. In the synthesis of metallic NPs, the term *monomer* refers to zerovalent metal atoms which can be produced through a continuous chemical reaction. Examples are chemical reduction reactions, or thermal decomposition reactions (for more details see section 2.2.1). Point "A" denotes the concentration where the system is *saturated*. Entering *Region 2*, point "B" is reached, and the concentration at this point

leads to the initiation of a *self-nucleation* process, in which monomers collide and combine to produce *nuclei*, or *embryos* [46, p.37]. Between point "B" and "C", the nucleation rate increases rapidly [50, p.527]. Point "C" is referred to as the *critical limiting supersaturation*. A decrease in monomer concentration is observable from point "C" to "D", and as a result of the formation of nuclei [46, p.38]. The nucleation process is occurring very fast, and is confined within *Region 2*, as the process is terminated after point "D", as it crosses the lower concentration limit for nucleation to occur. Point "D" to "E" comprise *Region 3*, in which the concentration decreases because of *growth* of the newly formed nuclei *by diffusion* of monomer onto the surface of the nuclei. This occurs since the system is still in a supersaturated state [50, p.527]. More details on growth mechanisms are provided in section 2.1.3.

It is worth pointing out that the La Mer model only describes that the nucleation process is followed by a growth step, but it cannot predict specific details regarding the development of the NP size distributions during the growth process [56].

2.1.5 Faceting of Nanoparticles

The various crystallographic planes that are present in a crystal can have different chemical and physical properties. The reason for this is that these different planes, have different atomic arrangements. This means that there is also a variation in the chemical and physical properties affiliated with these respective planes. Different geometrical shapes (morphologies) that crystals can have, affects which of these planes that are on their surface, and the ability to control the size and shape of NPs through their synthesis can grant an opportunity to *tune* these properties. Within the relevance of this thesis, *catalytic activity* is one of the most important properties that are shown to be strongly dependent on the morphology of the NPs [57].

Spheres, cubes, rods, wires, dumbells, decahedra, icosahedra, tetrahedra, octahedra, prisms, pyramids, stars and multipods are some examples of morphologies of nanoparticles that are already produced. However, there is no limit to what is possible to create in this regard as long as the processes of nucleation and growth in the respective system are thoroughly understood. Sau et al. [57] has classified NPs with anisotropic morphologies in three categories of different growth dimensionality; 1D, 2D and 3D. 1D NPs are defined to grow in only one direction. Examples of NPs with this kind of morphology are nanowires, nanorods and nanotubes. 2D NPs characterize particles with growth in two dimensions, with nanoplates, nanodiscs and

nanobelts as examples. Finally, 3D NPs are particles that has growth in all dimensions of space, e.g. tetrahedra, octahedra and cubes.

Gibbs-Wulff Shape

Nucleation and growth are the processes responsible for the formation of the nanoparticles, hence the morphology of these particles depend on how these processes proceed. More specifically, considering the formation of *nuclei* in the nucleation process, the *morphology* and *growth rate* of these entities determine the morphology characterizing the product-NPs. Under equilibrium conditions, and assuming homogeneous nucleation, the shape that these nuclei attain can be predicted based on the tendency for a reduction in the total surface energy in the system. The reduction in the total surface energy of crystalline material is in this case balanced between *two* contributions: Firstly, the total *surface area* of the crystal is minimized, and secondly which *(hkl)-plane* (see section 2.5.2) the surface facet lies in. This leads to a crystal shape that has facets with surface energies (γ) as low as possible, and with *truncation* (a kind of "rounding" of the shape, approaching spherical morphology) for minimalization of the total surface area. This shape is a polyhedron in systems of crystalline solids where the surface energy is *anisotropic* (not equal in all directions, e.g. in crystalline solids with different crystallographic planes of different γ). In systems where γ is *isotropic* (equal in all directions, e.g. in liquids), the equilibrium shape is a sphere. This shape, which corresponds to the lowest total surface energy, is referred to as the *equilibrium shape*, or the *Gibbs-Wulff shape*. Pd and Pt crystallizes in the fcc structure, and the Gibbs-Wulff shape for a macroscopic crystal with this structure is a *truncated octahedron*, as shown on the right-hand side in Figure 2-9. When the size of the crystal approaches the nano size-regime, the Gibbs-Wulff shape is an *octahedron*, shown on the left side in Figure 2-9. Note that deviation from the equilibrium shape occurs at temperatures above absolute zero, because the anisotropy in surface energy decreases with temperature. This deviation involves a *rounding* of the sides in the shape [57].

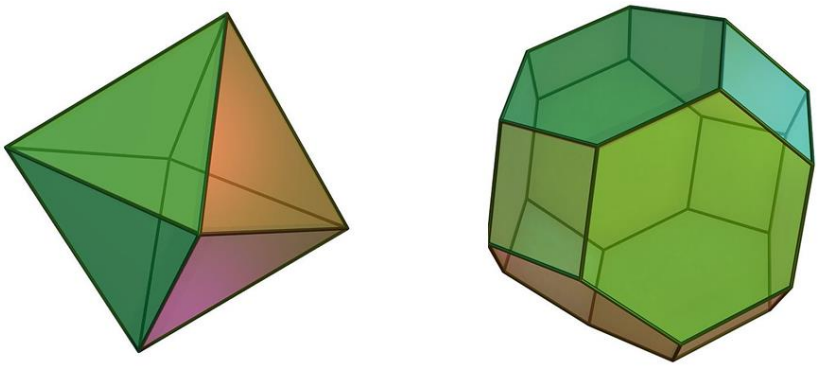

Figure 2-9: On the left hand-side is an octahedron, and to the right is a truncated octahedron shown [58], [59].

The truncated octahedron shape has 8 hexagonally shaped (111)-facets, and 6 square-shaped (100)-facets, while the (100)-facets is not present in the octahedron shape. These low-index facets possess different surface energies, because creating a surface in an fcc type structure generates a different number of dangling bonds with respect to which crystallographic plane the surface is created in. If a surface is generated in the (111)-plane, only three bonds will be broken, and if it is created in the (100)-plane 4 bonds is broken. A surface is made in the (110)-plane generates 5 broken bonds. This is shown in Figure 2-10.

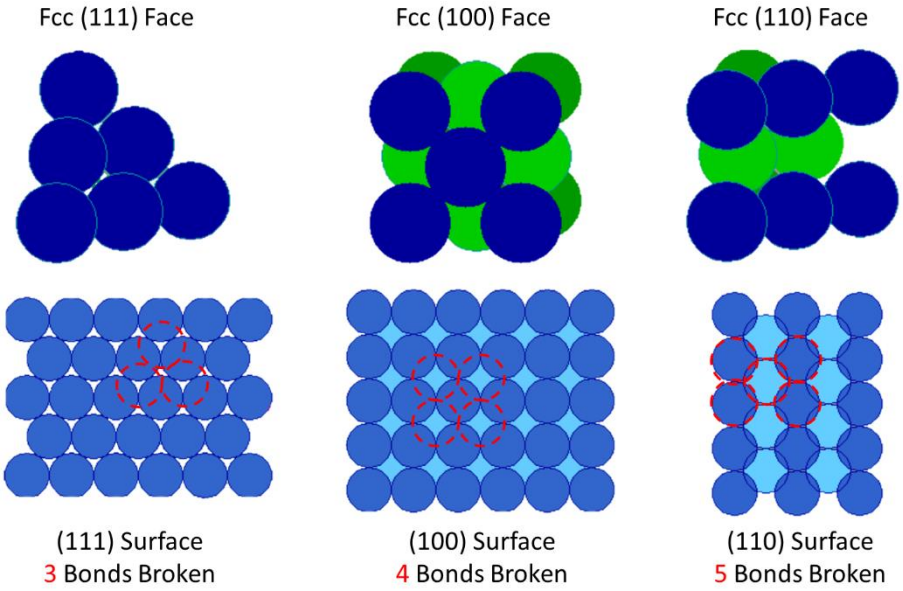

Figure 2-10: Illustration of the number of bonds broken per atom creating a new surface in the crystal planes (111), (100) and (110) in a fcc type structure. The red stippled circles indicate the lost atomic interactions when the surface is created [60].

Therefore, the surface energy of these respective crystallographic planes is in order of increasing energy: $(111) < (100) < (110)$ [57].

In the case of heterogeneous nucleation, the resulting equilibrium shape of a supported macroscopic crystal depends on the surface energies of the facets *and* the adhesion energy with the support. The relative magnitudes of the facet surface energies and the adhesion energy can affect the degree of truncation in the shapes of the crystals. Also, a lattice-mismatch between the support and the crystal that is depositing on it can affect the morphology of the final crystals. This is because of the *strain* that is occurring in the interface between the support and depositing crystal [57].

Modification of Nanoparticle Morphology

First, it should be stated that the mechanisms that lead to the various morphologies seen in NP-products are not yet fully understood, but the baseline is that the kinetic conditions in the syntheses of NPs with controlled morphology must be tuned in such a way that specific facets grow at different rates in the crystal. The shapes of *nanoparticles* are often seen to be in disagreement with the Gibbs-Wulff shapes. This is because several other contributing factors to the total surface energy increase become significant as the size of the crystal reduces into this regime. These factors are *increased proportion of edge atoms, increased edge-energies, high surface energy, high surface stress, alternative stable shapes.* A detailed description of them will not be included here. In practice, tuning the morphology of NPs, can be done by changing the surface energy of specific facets by adsorbing various additives such as surfactants, polymers, ions, ligands or impurities to them at varying concentrations. Examples of these additives are given in Table 2-1. It is also known that the type of the *solvent* may affect the morphology of the NPs, for example causing certain facets to be more favorable than others [57].

Table 2-1: Additives that can modify the morphology of NP [57]s.

Additive	Examples	Function related to the alteration of morphology
Surfactants	CTAB, sodium dodecyl sulfate	Facet selective growth rate suppression by respective selective adsorption of the capping agent onto these specific facets.
Polymers	PVP, PVA	
Ligands	Inorganic ions, thiols, amines	
Ions	Ag^{+}, Cu^{2+}, Cl^{-}, Br^{-}, I^{-}	Selective adsorption onto certain facets stronger than others, resulting in anisotropic growth. Generation of defects in nuclei.

In Practice

In the work of synthesizing NPs with control of the morphology e.g. the *preformed-seed-mediated growth method* can be used [57]. This method is described here because it is applicable to the methods used in the practical work of this thesis.

Preformed-Seed-Mediated Growth

When producing noble metal NPs small metal particles (seeds) can be added to a solution of metal ions together with the other necessary additives. These seeds can be used to control the morphology of the NPs. In the solution, the growth species can heterogeneously nucleate on the seeds, followed by their growth (see section 2.1.2 and 2.1.3). The composition of the seed can be identical to, or different from the growth species. The *concentration*, *crystal structure*, *facets*, *composition* and *size* of the seed are what govern the sizes and shapes obtained in the NP-product [57].

2.2 Nanoparticle Synthesis Methods

Nanoparticle synthesis methods will be presented in this chapter. As the main route in this thesis are solution based synthesis methods, they will lie in the focal point of this text.

Methods by which nanoscale materials can be prepared are typically classified into two approaches; *top-down* and *bottom-up*, see Figure 2-11. The top-down approach concerns methods and techniques that involve the size reduction of matter from bulk into the nano-range through mechanical, physical or chemical processes [49, p.179]. Therefore, these are said to be *subtractive*. In other words, they involve the actions of subtraction, removal, division and reduction of the bulk material to get it into smaller pieces. These progressively smaller pieces is finally the end-product, which is a material with at least one dimension of size in the nano-scale [49, p.193]. The bottom-up approach on the other hand, is based on the combination of atoms from ground up in a specified manner, and is therefore denoted as *additive* [49, p.210]. This approach is based on controlling interactions of covalent, ionic, metallic character, or hydrogen bonding, van der Waals, electrostatic, $\pi - \pi$ interactions, hydrophilic-hydrophilic, and hydrophobic-hydrophobic interactions [61]. Controlling the thermodynamics, and utilization of mechanisms like self-organization and self-assembly are essential in the bottom-up approach [62, p.119].

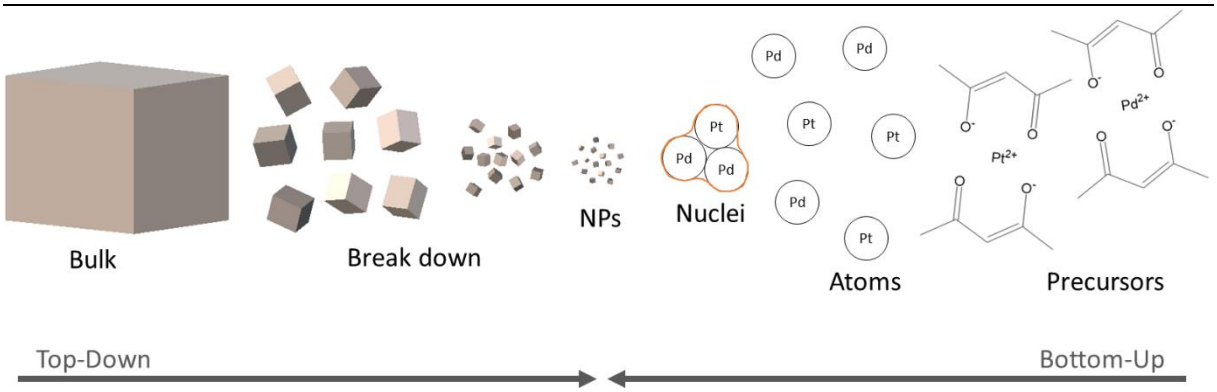

Figure 2-11: Schematic illustration of the top-down and bottom-up approaches.

Top-Down

Hornyak et al. [49, p.180-185] have organized top-down preparation routes of nanomaterials into different categories depending on type of fabrication method, see Table 2-2. A more detailed description of these techniques is omitted here as they fall well outside the scope of this thesis.

Table 2-2: Summary of top-down fabrication methods.

Fabrication method	Examples
Mechanical-energy	Ball milling, rolling or beating of sample
Thermal	Sublimation, combustion
High-energy	Arc discharge, solar power
Chemical	Chemical etching, CMP (Chemical-Mechanical Polishing)
Lithographic	Optical lithography, XRL (X-Ray Lithography)

Bottom-Up

In this section bottom-up synthesis methods for nanoparticles are covered. *Gas-phase* and *solution based* methods are among the most widely used in the production of monodispersed nanoparticles [55, p.659]. Solution based methods in relevance for this thesis, are used as representative examples within the bottom-up category. Also in line with the scope of the thesis,

the focus is placed on the preparation of *metallic* nanoparticles in the exemplifications of the presented methods.

2.2.1 Solution Based Methods

The manufacture of nanoparticles via a solution-based route provides independent controllability of parameters like reaction temperature, precursors, surfactants and shape-directing agents. All of this can lead to a viable means of producing highly monodispersed nanoparticles with uniform shapes, and tunable compositions with targeted nanostructuring [1, p.10],[63]. It should be noted that taming the processes involved, has long been a great challenge [1, p.11]. Although variations appear in the different synthesis methods, there are some stages that are characteristic of solution-based syntheses in general. These are illustrated in Figure 2-12, as described by Atkins et al. [55, p.659].

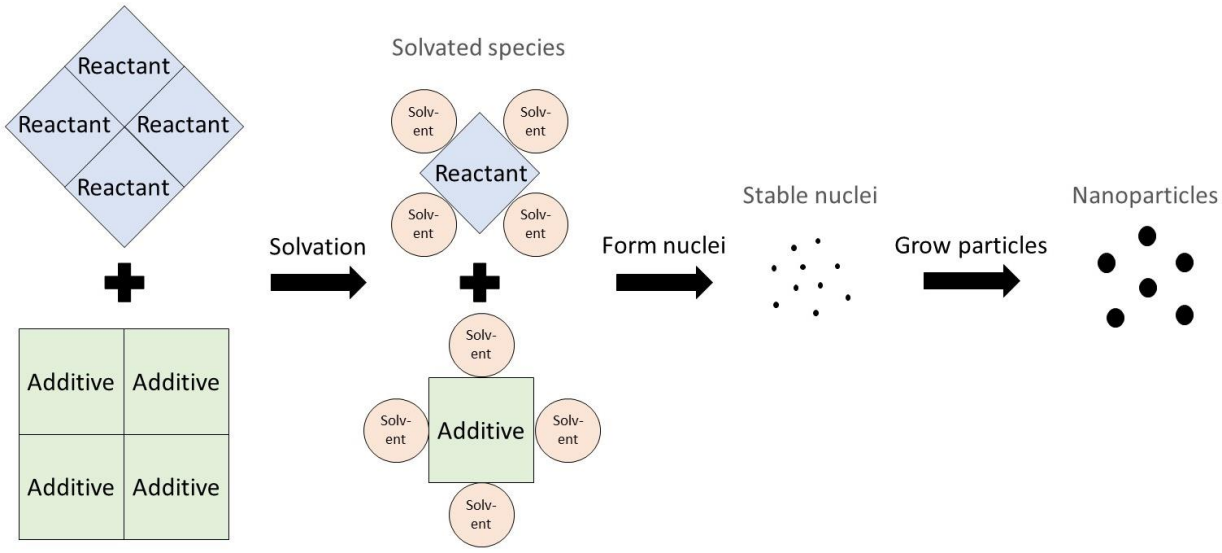

Figure 2-12: Illustration of different general stages in solution-based chemistry. The first step involves solvation of the reactants and additives by a suitable solvent. The reaction in the solvent progresses to form stable solid nuclei. Formation of nanoparticles occur as a last step by a growth process, and progresses until the reactants are consumed [55, p.659].

Solution-based synthesis methods involve initial solvation of the reactants and potential additives by a solvent of choice, followed by mixing to obtain a homogeneous solution at the atomic level. This implicate that typically, the diffusion distances between the reactant molecules are short, which favors a fast reaction. The system therefore does not have to be kept

at very high temperatures during the reaction, compared with the reaction temperatures needed in the *direct reaction* of bulk solids. Comparatively, thermodynamically driven particle growth can also therefore be reduced using a solution based route, enabling the formation of materials in the nanometer-size range [55, p.659]. A wide variety of inorganic solid bulk materials can be synthesized by the *direct reaction* of the solid reactants, meaning they are kept at high temperature (typically $500 - 1500°C$) for some extended period of time [55, p.602]. This is not very applicable to nanoparticle synthesis, because the high temperatures facilitates particle growth and large crystallite sizes in the product [55, p.659]. This is avoided with the moderate temperatures feasible for solution-based synthesis routes.

Two examples of solution based methods that can be employed to initiate burst nucleation are presented here. The *heat-up method (alternatively the non-injection method)*, and the *hot-injection method.* These have some features in common, but there are also some distinctions between them. Historically, the hot-injection method is the most commonly used procedure for production of nanoparticles with narrow size distributions. Unfortunately, this methodology is not easily scalable in terms of achieving large quantity production. On the other hand, according to Embden et al. the heat-up method is more suited for large scale production purposes [64]. In the following, the two concepts will be described together with known challenges and benefits related to them.

The Hot-Injection Method

In the hot-injection method, burst nucleation occurs through injection of the dissolved precursor(s) into a hot liquid phase, with a stabilizing agent present [1, p.11], as illustrated in Figure 2-13.

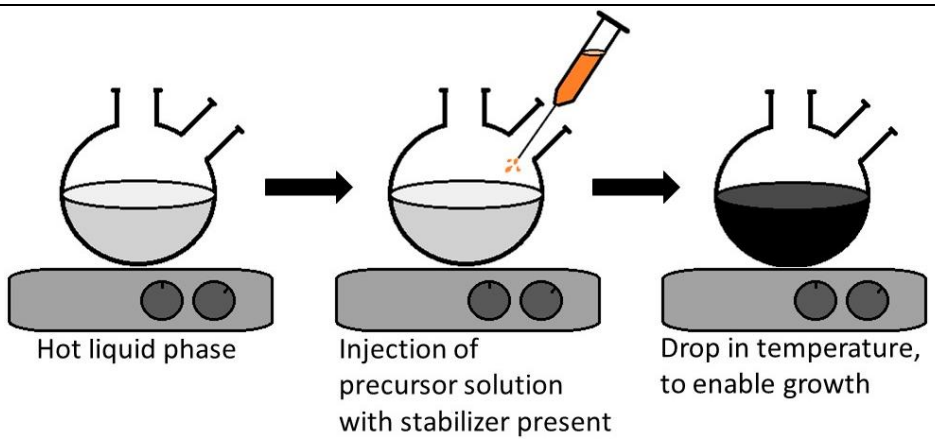

Figure 2-13: The hot-injection method. A hot liquid medium is shown in the left-hand side of the figure, illustrated as a reaction vessel on a heating plate. The synthesis is performed in organic solvents. The precursor solution (orange liquid in syringe) is injected into the hot liquid phase, after which the reaction process starts. The solution becomes supersaturated, and nuclei are formed in the presence of a stabilizing agent. The right-hand side of the figure shows the last step of the process, where the temperature is lowered to suppress the formation of new nuclei, while allowing the already formed ones to grow.

A key aspect of this method is that the fast injection results in supersaturation and subsequent formation of nuclei (see Figure 2-8). The initial nucleation process can be constricted in time by a drop in the temperature, which suppresses the nucleation. The lower temperature is chosen so that the already formed nuclei are able to grow. In this way, the nucleation process is temporally separated from the growth process [65, p.332]. The crucial point here, is that the process of nucleation occurs very fast, and lasts for a short time, while the growth process is more extended in time [64].

The hot-injection method can generate nanoparticles with various shapes, compositions, and sizes with monodispersed distributions [64]. Embden et al. claims that upscaling the hot-injection method for production of a large quanta of nanoparticles is not easy, based on the following arguments. As the production volume of the synthesis increases, so does the injection volume of precursor solution correspondingly. As a result of this, the mixing time needed to reach a homogeneous state of the system increases. In this way control of the nucleation process decreases, as it depends on fast mixing of the reagents at a high temperature. In addition, the batch-to-batch product similarity would depend on the quantum produced. The reason for this is that the cooling rate of the solution does not scale linearly with its volume. This will affect the suppression of nucleation in that the temperature drop would occur at different time values depending on the volume. An argument of practicality is also given, and states that the injection of very large volumes (given injection volume is 25-50% of mother solution volume) is not

very practical. As a last point, Embden et al. suggest that the injection time between batches, as well as from one user to another, is time dependent also. This could also to a small degree contribute to deviations between batches [64].

Reproducibility of the synthesis in terms of obtaining a product with a *specific particle size* can only be achieved through careful control of the synthesis parameters. In the production of cobalt NPs with the hot-injection route, Zacharaki et al. [9] performed elaborate studies on the topic of reproducibility in this regard. It was found that the two most important parameters for tuning the particle size were the *metal to surfactant molar ratio* and the *injection temperature.* The particle sizes were shown to increase with this ratio, and decrease with increase in injection temperature. It was also mentioned by Zacharaki et al. that reproducible experiments are only achieved by applying the same experimental set up each time, carefully controlling temperature and maintaining equal insulation of the reaction vessel from one experiment to the next.

The Heat-Up Method

In this method, all reaction ingredients are mixed and kept in the same vessel while the temperature is set to increase. The temperature is ramped with a heating rate of typically 10-15°C/min to the targeted temperature, and nucleation and growth occurs with a temporal overlap. The burst nucleation is initiated by means of this gradual heating. This is in contrast to the hot injection method where the injection of precursor(s) is done into a suspension already stabilized at the targeted reaction temperature. However, the mechanism by which the NPs is formed in the heat-up method, is principally equivalent to that of the hot-injection method [64]. A schematic representation of these key aspects of the procedure is illustrated in Figure 2-14.

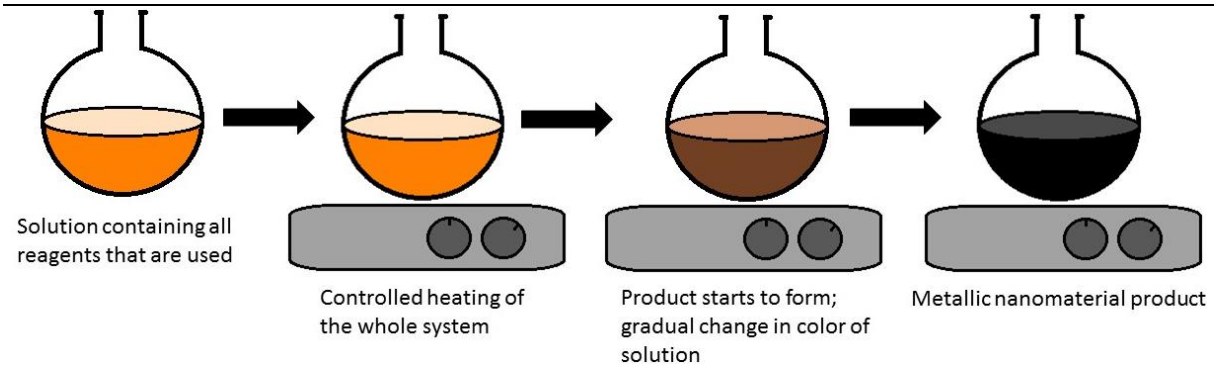

Figure 2-14: Burst nucleation initiated by the heat-up method. The solution includes the solvent (which can also act as the reducing agent), the precursor(s), the stabilizer, and potential additives. The orange solution on the left-hand side in the figure illustrates a homogeneous solution of the components. Next, the whole system is heated on a hotplate. This results in a gradual transformation into the black liquid, shown to the far right, representing the metallic nanoparticles.

Generally, in one important aspect the heat-up method differentiates itself from the hot-injection method, and that is in how long the nucleation and growth processes last in time. In the heat-up method the duration of the nucleation- and growth process are approximately equal, and with strong overlap. This is a result of the gradual increase in temperature of the system. Because the temperature is increasing gradually, it becomes harder to separate the nucleation and growth, and thus adds complexity to the production of nanoparticles with very narrow size distributions. The choice of precursor(s) and a suitable *heating rate* are crucial in heat-up syntheses; the precursor kinetics for conversion to product should match the heating rate such that burst nucleation is achieved. The heating rate can affect the particle size of the product-NPs. Small particles are produced if the heating rate is high enough to convert precursor to monomer at a much higher rate than the growth of the nuclei. In this way, the monomers will be consumed to produce a large number of nuclei. Conversely if the heating rate is low enough, the rate of precursor conversion is slower than the growth of the nuclei. In this case the level of supersaturation decreases after nucleation occurs, and the monomer that are continuously produced feed the growth process instead of the nucleation. This means that the particle size will be larger. Increasing the number of reactants, by for instance working with bimetallic systems, adds another layer of complexity to the methodology. In this case, the kinetics of the two precursors *relative* to each other must also be accounted for. This is however important in both the heat-up- and hot-injection method [64]. The formation of monomer in the hot-injection- and heat-up method can be realized through chemical reduction- and thermal decomposition reactions. A description of these types of reactions are described in the following.

Chemical Reduction and Thermal Decomposition

Nanoparticles composed of for example noble metals like Pt, Pd, Rh, Au and Ag are possible to synthesize utilizing a chemical reduction method route. In line with the *general stages* of solution-based chemistry as described previously in this sub-chapter, the metal *nuclei* are formed as a product of a reduction reaction. In general, there are at least four crucial components to control for producing well-defined nanoparticles [1, p.11, 29]:

1. **Solvent**
2. **Precursor**
3. **Reducing agent**
4. **Stabilizer**

The Solvent

The solvent is the reaction medium of the chemical system. In e.g. the polyol process (see section 2.2.2), switching from one solvent to another can alter the monodispersity of the nanoparticles. Different level of dilution of the precursor can affect the mean particle size of the NPs. Well educated combinations of these parameters can enable production of monodispersed nanoparticles with tunable sizes [66].

The Precursor

The precursor is the metal source. If the goal is to synthesize monometallic materials, one precursor containing the target element is used. If the goal is to produce bimetallic products, normally two precursors would be used. By mixing precursors in a specific ratio the end-product composition can be tuned [1, p.90-93].

Using a simulation to show the effect of precursor reactivity on the evolution of particle formation in a typical heat-up method, Embden et al. compares precursors with three levels of reactivity; *high, intermediate* and *low*. *High reactivity* corresponds to precursors with an activation energy of E_A = 60 kJ/mol, *intermediate reactivity* refers to E_A = 80 kJ/mol, and *low reactivity* corresponds to E_A = 110 kJ/mol.

It is reported that precursors with high reactivity results in broad particle size distributions and rapid *simultaneous* nucleation and growth. Typical precursors of this reactivity are organometallic precursors like bis(trimethylsilyl) chalcogenides and short chain alkyl metal complexes [64]. They furthermore report that precursors with an intermediate reactivity will generate narrow particle size distributions. This reactivity is similar to that of phosphine

chalcogenides and metal precursors derived from carboxylic acids. Utilization of precursors with intermediate reactivity is stated to promote better quality in the products, in terms of yield and narrow size distribution. This is enabled through the suitable separation of the nucleation and growth processes in time [64]. Lastly, precursors with low reactivity, corresponding to phosphonic- or phosphinic- acid derived metal precursors, is reported to result in broad size distributions, and large particles [64].

The Reducing Agent

The purpose of the *reducing agent* in the chemical reaction is to reduce the metal salts by itself being oxidized, forming the metal atoms that will compose the metallic nanoparticle product. Examples of reducing agents that are often used are sodium borohydride, hydrazine, hydroxylamine, hydrogen, carbon monoxide, sodium citrate, sugars, (poly)alcohols, aldehydes, amides and amines [1, p.11]. A reducing agent can be added to the chemical system as an independent component [1, p.11], or one can exploit that in some cases the solvent accommodate reducing capabilities, and can thus act as both the solvent and the reducing agent in the system [1, p.29], e.g. polyalcohols (section 2.2.2).

The Stabilizer/Capping Agent

Some form of *stabilizer* must most often be included to prevent aggregation of the metal NPs. The same compound may also serve to selectively control the growth of the particles (see 2.1.5), in which case it is referred to as a *capping agent.* Frequently used stabilizers are polymers or surfactants that are able to adsorb onto the surfaces of the particles [1, p.11]. Stabilizers are one of the before mentioned *additives* which can be included in the solution mixture, and should be added in order to achieve a monodispersed product [55, p.659]. If they are not added, *Ostwald ripening* (section 2.1.3) will readily cause smaller particles to dissolve of the expense of growing larger ones. This occurs because of the reduction in surface energy associated with the increase in particle size, and is the driving force of the process. It is however not a benefit in the production of nanoparticles, as it leads to particles with non-uniform sizes, or in other words a broad size distribution [49, p.324]. The stabilizers serve to prevent the dissolution of smaller particles and the growth of larger ones, or namely *stabilize* them.

Additional Additives

Another component can be added for increasing the control of the particle morphology, or faceting. These additives are referred to as *shape-directing agents*. The functionality of the shape-directing agents is that they may alter the kinetics of the chemical reaction, or interact with specific facets of the nanostructure during its formation process. For more details, see section 2.1.5.

Thermal Decomposition

Typically, a thermal decomposition process is performed via a hot-injection method where an organometallic precursor is injected into a hot solvent with a stabilizer present. The precursor will decompose, forming the metallic NPs [1, p.11]. More reactive metals like Fe, Co and Ni are not possible to be reduced with typical reducing agents. In this case, it is more common to thermally decompose the organometallic precursor e.g. $Co_2(CO)_8$ to form, in this case Co NPs. In our research group carbonyl-based precursors are frequently used when using this route [9].

Bimetallic considerations

The production of bimetallic nanoparticles via a chemical reduction route is typically realized either by *simultaneous*- or *successive reduction* of metal ions from two different metals. Simultaneous reduction is the case where ions from two metals are homogeneously mixed and subsequently reduced to form metallic NPs, in the same manner as for monometallic NPs except for the different number of metal precursors. In the successive reduction technique, ions of one of the two metals are initially reduced to form metallic NPs, followed by addition of ions from the second metal to the solution. The second metal ions are then reduced such that growth of the second metal occurs on the surface of the pre-formed NPs. Typical outcomes of the simultaneous- and successive reduction methods are respectively solid solution- and core-shell distributed NPs, but this is absolutely not always the case. To illustrate this, some possible formation routes for core-shell distributed NPs via simultaneous reduction with presence of PVP as stabilizing agent are shown in Figure 2-15, as suggested by [67, p.481-485]: The starting point is a solution of the two metal ions (M_1^+ and M_2^+) with PVP present. The ions will then coordinate with the polymer by weak interactions (*step 1*). If e.g. the reduction potential of M_1^+ is higher than that of M_2^+, it first promotes reduction of M_1^+ (*step 2*). Two different paths (*step 3'-4'* or *step 3''*-4'') are suggested as possible in the progression of the reaction. *Step* 3': The

zero-valent M_1 atoms can proceed to aggregate forming a nanoparticle with ions of the second metal (M_2^+) still coordinated to the surrounding polymer. Then, in *step 4'* the M_2^+ ions are reduced to zero-valent M_2 atoms that are coordinated to the PVP surrounding the M_1 nanoparticle. Following the other path, *step 3''* involves reduction of the M_2^+ ions such that zero-valent atoms from both M_1 and M_2 are coordinated to the polymer without any aggregation and NP-formation. *Step 4''* follows, where one of the metals (e.g. M_1) can aggregate to form a nanoparticle surrounded by PVP with atoms of M_2 still coordinated to the polymer. Which metal that aggregates in this step depends on the interaction strength with the polymer. Both of these two pathways lead to *step 5*, where the atoms of M_2 can aggregate to form a shell on the M_1 NPs [67, p.481-483].

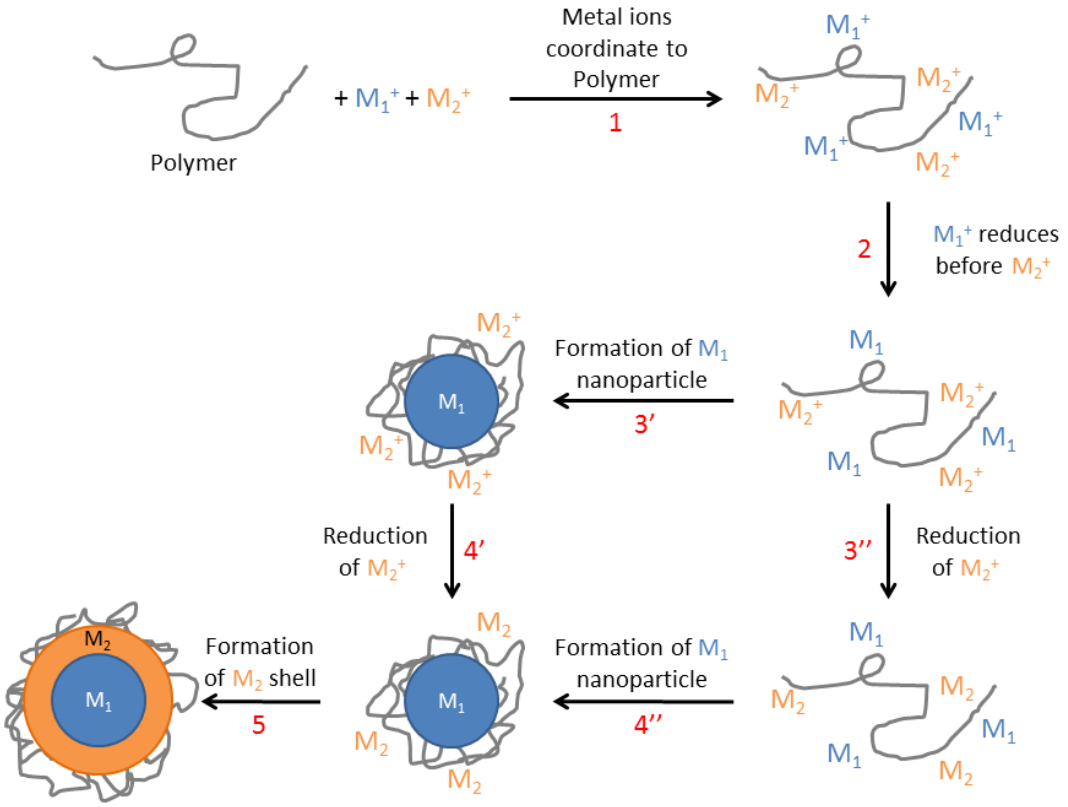

Figure 2-15: Formation of core@shell NPs by simultaneous reduction. The figure is based on the literature found here [67, p.483]

2.2.2 The Polyol Process

The *polyol process* is a synthesis route that utilizes polyalcohols as the solvent to produce nanoparticles. In 1989, Fievet et al. [68] coined the term *polyol process*, or analogously *polyol synthesis*. In the literature, this term is most often used and will therefore be used here in the description of the method. Fievet et al. were the first to report the use of polyols for small particle production purposes. Metal particles composed of Co, Ni, Cu and Pt were produced in the early era. The first syntheses yielded particles in the micron- to sub-micron size range. Syntheses of metals like Re, Ru, Rh, Au and Sn, and alloys as $Co_{20}Ni_{80}$, FeNi, Co_xCu_{1-x}, FeCoNi were later produced. Today, the process is widely adopted to produce high quality nanoparticles with a wide range of compositions, sizes, predeterminable shapes and atomic distributions [69]. The polyol process is a solution based synthesis route, and the chemical process can be regarded a *one-pot reaction* because several features occur simultaneously in the process. In the synthesis, a polyol can be used as the solvent as well as the reducing agent, because of its reducing capabilities at elevated temperatures. The *polyol* is the liquid medium in which the chemical reaction takes place, and Dong et al. divides the polyols into three series of molecules: (I) Molecules based on ethylene glycol, including this, and the resulting molecules when adding functional groups up to polyethylene glycol. (II) Diols, including propanediol, butanediol, etc. (III) Other chemicals belonging in the polyol category. These are here put into groups (I-III), as shown in Table 2-3. In preparation of NPs, ethylene glycol, diethylene glycol, glycerol and butanediol are among the polyols that are most used [69].

Table 2-3: Examples of commonly used polyols. Group I include polyols based on ethylene glycol, with increasing number of functional (OH) groups up to polyethylene glycol. Group II include typical diols whereas Group III designate other solvents that is categorized as polyols. This table is based on: [69].

Group	Polyol	Name	Boiling point/°C
I	$HO-CH_2-CH_2-OH$	Ethylene glycol	197
I	$HO-CH_2-CH_2-O-CH_2-CH_2-OH$	Diethylene glycol	244
I	$HO-(CH_2-CH_2-O)_2-CH_2-CH_2-OH$	Triethylene glycol	291
I	$HO-(CH_2-CH_2-O)_3-CH_2-CH_2-OH$	Tetraethylene glycol	314
I	$HO-(CH_2-CH_2-O)_n-CH_2-CH_2-OH$	Polyethylene glycol	>350[1]
II	$HO-CH_2-CH_2-CH_2-OH$	Propanediol	213
II	$HO-CH_2-CH_2-CH_2-CH_2-OH$	Butanediol	235
II	$HO-CH_2-CH_2-CH_2-CH_2-CH_2-OH$	Pentanediol	242
III	$HO-CH_2-CH_2(OH)-CH_2-OH$	Glycerol	290
III	$C(CH_2OH)_4$	Pentaerythritol	276

[1]Decomposes

As reported by Dong et al. [69], there are many beneficial attributions of the polyol synthesis route for NP production. The polyols have comparable *solubilizing capabilities* to that of water. This enables a wide range of precursors to be used, as very many of them are able to dissolve in the polyols. In addition, polyols have *higher boiling points than water*, which implies that the synthesis can be performed in liquid-phase, at atmospheric pressure, and still allow for the formation of crystalline NPs. This comparable capability to solubilize compounds in relation to water, comes from the *chelating effect* seen in polyols. Even if water is more polar than the polyols, the solubility is indemnified by the chelating effect. The effect also contributes to *stabilization* of the particles in solution (for oxides in particular), and helps to control the nucleation and growth processes during the synthesis. Although the polyol in some rare cases are able to stabilize NPs to form a colloidal suspension, additional stabilizers is most often added [69].

Redox Reactions in the Polyol Route

The reducing agent (solvent) needs to donate electrons to the metal ion in solution to generate zero-valent metal monomers. In the case of noble metals, their high reduction potentials make them relatively easy to reduce, and thus typically do not require strong reducing agents. However, it should be noted that kinetic factors play an important role on the temperature at which the reduction reaction can take place. In the polyol process where polyalcohols are used as the solvent and reducing agent (and in some cases stabilizer), the reaction mechanism of solvent oxidation depends on the reaction conditions and placement and type of functional OH-groups. If the OH-groups are not terminal groups (secondary alcohols), the polyalcohols are generally oxidized according to Figure 2-16 [70]:

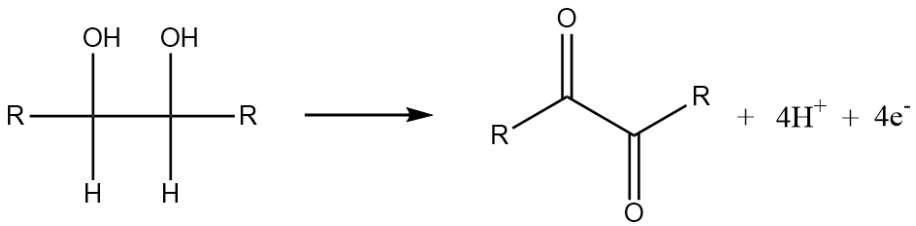

Figure 2-16: Oxidation of a secondary polyalcohol.

As an example of oxidation of polyalcohols with terminal functional OH-groups (primary alcohols), the oxidation of ethylene glycol is shown as reported by Bock et al. [71] in Figure 2-17.

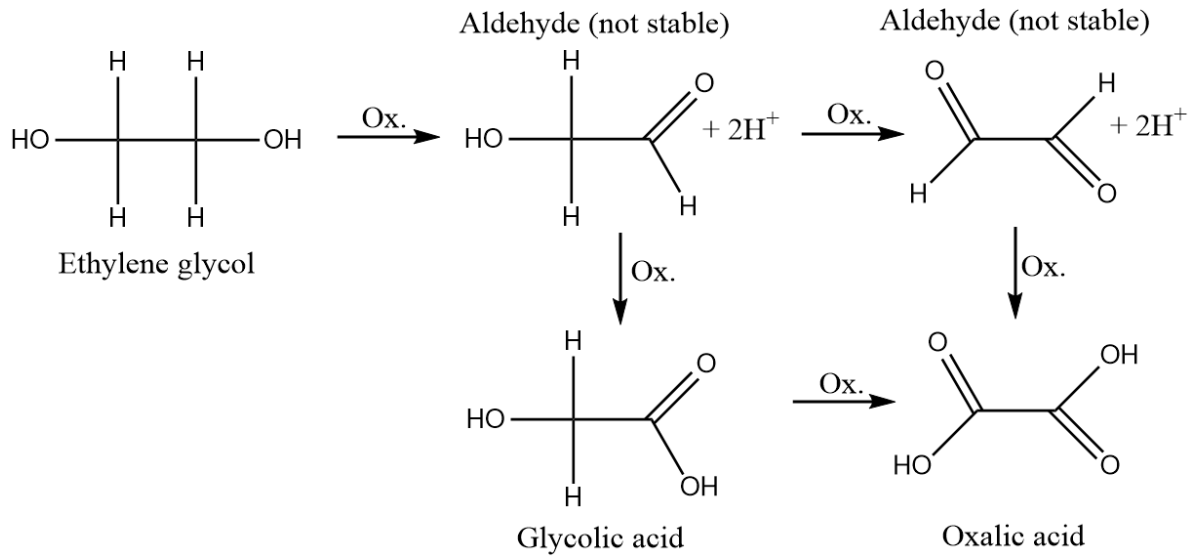

Figure 2-17: Oxidation of ethylene glycol. The functional OH-groups of ethylene glycol interacts with the metal ions to form unstable aldehydes by an oxidation reaction. The aldehydes readily form glycolic acid or oxalic acid depending on the type of aldehyde, as shown [71].

The metal ions are reduced by means of the electrons donated from the oxidation of the polyalcohol according to Rxn. eq. 2.1, and in this way the zero-valent metal atoms are produced.

$$M^{n+} + ne^{-} \rightarrow M \qquad \text{(Rxn. eq. 2.1)}$$

2.3 Colloidal Suspensions

Hiemenz et al. defines a *colloid* to be a particle with some dimension of length within the size range of $10^{-9}\ m - 10^{-6}\ m$ [47, p.1]. It is further specified that the terminology also includes macromolecules. In the case of the macromolecular colloids, these are *solutions*, in the thermodynamic definition of the term, and can be referred to as *lyophilic colloids* (translates to *"solvent loving" colloids*). In a colloidal system, a *dispersed phase* and a *continuous phase* are distinguished. Regarding colloidal metallic NPs, for instance, these colloids form a system of at least two phases, including the NPs (*dispersed phase*) and the dispersing medium or solvent

(*continuous phase*). These particles can be referred to as *lyophobic colloids* (from *"solvent fearing"*) [47, p.10].

Several terms are synonymously used to designate a system of solid NPs (dispersed phase) in a liquid phase (continuous phase). For the purpose of clarification, this can be referred to in the literature as *sol, colloidal solution,* or *suspension* [47, p.10].

2.3.1 Colloidal Stability

The basic underlying forces that govern the stability of sterically stabilized colloidal suspensions are reviewed in this section. As the theory of colloidal stability are a large topic to cover, only steric stabilization by the use of non-polar polymers are covered here to fit the scope of this thesis.

In a colloidal system consisting of a solid dispersed into a liquid continuous phase, the total surface energy (γ) increases with the decrease in particle radius given that the amount of the dispersed solid remains constant. The resultant increase in surface energy can be realized through the material dependent property of *surface tension*, see section 2.1.1. As an increase in surface area of the system is not a spontaneous process, one can assume that it has an intrinsic *thermodynamic* tendency to promote destabilization (the particles separate out of the continuous phase). Accordingly, the process of subdividing the material into progressively smaller pieces is associated with a rise in Gibbs free energy [47, p.14-15]. This is illustrated in Figure 2-18, where the total surface area (and surface energy) of the dispersed solid phase in *Suspension 1* is lower than in *Suspension 2*, although they have the same volume.

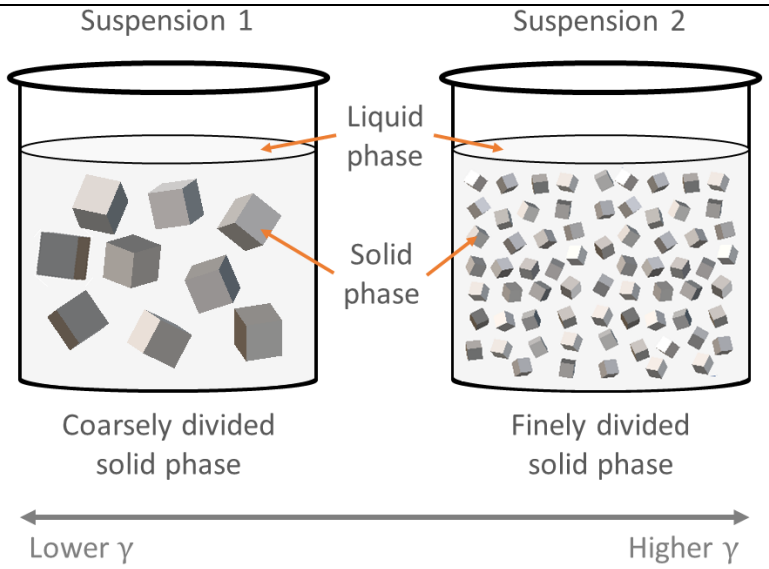

Figure 2-18: Schematic illustration of two colloidal suspensions with different coarseness in the suspended particles. Assume that the total volume of solid phase is equal in *Suspension 1* and *2*.

However, the *kinetics* of the system is not dictated by the *equilibrium thermodynamics* and colloidal systems can possess kinetic stability, without being thermodynamically stable. This implies that the colloidal solutions can stay unchanged for prolonged time periods, without particles separating out of suspension. When the term *colloidal stability* is used in literature, *kinetic* stability is implied. It refers to the extent to which the dispersed phase stay distributed in a uniform manner throughout the continuous phase [47, p.15]. Also, the more kinetically stable a suspension is, the more resilient it is toward *aggregation* or *coalescence* (see section 2.1.3). The aggregate moves like a single particle, but it is not a new particle, but rather a *cluster* of particles. Note, the total surface area of the system is not reduced during aggregation (neglecting the blocked sites on the particles where they are in contact). However, when a new particle is formed due to *coalescence*, the surface area of the system *is* reduced. It should be pointed out that the system can possess kinetic stability towards coalescence, but not to aggregation [47, p.15-16].

Aggregation occurs as a result of *attractive forces* between the particles in suspension, pulling them together [47, p.465]. These attractive forces are referred to as upscaled van der Waals forces, and they apply to macroscopic bodies such as colloidal NPs. Without going into too much detail, the upscaling of the van der Waals forces is based on the summation of all combinations of pair-wise intermolecular attraction between the two particles, and it depends on their geometry [47, p.483,485]. The summation of the attractive interaction between the two

particles leads to a longer effective range of the forces as compared with van der Waals forces between atoms and molecules. This upscaled version is referred to as *long range van der Waals force,* or *Hamaker force.* The latter term stems from the name of the person that researched it. If d is the distance of separation between two interacting *atoms,* e.g. the London (dispersion) force decreases with $1/d^6$. In the case of the long range van der Waals force between spherical *particles* of equal radii, it decreases approximately with $1/d$ [48, p.269],[47, p.486]. Repulsive forces between the particles are also present in the system, and these need to be harnessed in order to appropriately stabilize the colloidal system. Without these repulsive forces the particles would coagulate immediately. Stabilization of the system is usually realized with one of three strategies; the utilization of either *electrostatic, steric* or *electrosteric forces*. The electrostatic repulsive forces come from overlap of *electrical double layers* around the particles, resulting from the fact that typically the surfaces of particles in suspension are charged. The repulsive action comes from an osmotic pressure due to the increased concentration of charges affiliated with the double layer. Steric stabilization is the adsorption of e.g. polymers to the surfaces of the suspended particles such that the attractive forces are *masked,* by steric hindrance. The electrosteric forces are a combination of the two latter [47, p.465], [47, p.575]. The balance of the attractive and repulsive forces dictates the stability of the colloidal system. This can be described with *potential energy curves* (see Figure 2-19). The potential energy of the particle in this context can be considered as the sum of attractive and repulsive energies, which depend on distance between particles as illustrated in Figure 2-19. The repulsive and attractive energy contributions are conventionally defined to be positive and negative, respectively [47, p.465-467].

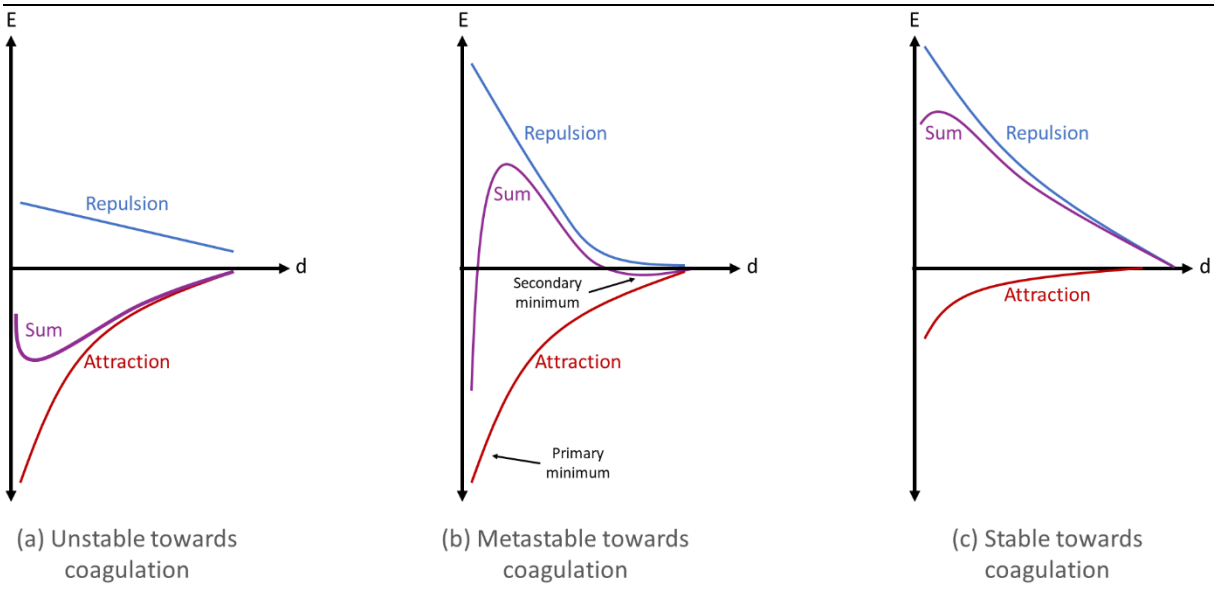

Figure 2-19: Potential energy curves for the interaction between two spherical particles in colloidal suspension. The y-axis is the interaction energy (E), and the x-axis is the distance of separation (d) between the particles. The potential energy of attraction is defined to be negative, and positive for repulsion [47, p.465-466]. (a) The repulsion is less than the attraction in magnitude. (b) The repulsion and attraction are comparable in magnitude and range. (c) Attraction is less than the repulsion. The figure is based on the literature [47, p.466].

As evident from Figure 2-19, when the distance between the two particles increases, both the potential energy associated with attraction and repulsion decrease. At long separation distances, the particles cease their interaction with each other, and this can be seen by the decrease in potential energy with distance. Note that the shape of curves like these depend on both the *physical properties* of the system as well as *geometrical properties* [47, p.465-466]. The geometry of the particles is assumed to be spherical here for simplification.

Section (b) in Figure 2-19 represents a *kinetically stable* but *thermodynamically unstable* system, which imply aggregation will occur, but slowly. The solid curve in (b) shows what is labelled a *secondary minimum* at larger distances of separation, and namely a *primary minimum* located at small distances of separation, as well as a *maximum* of potential energy in between. The primary minimum is associated with coagulation of the particles. This coagulation will however not take place unless first the maximum in energy is overcome. As such, the system is said to be *metastable*, or kinetically stable [47, p.467]. If the primary minimum is reached, the aggregation process that transpires is *irreversible.* If the particles enter the secondary minimum on the other hand, they are said to be *flocculated*. The flocculation process is *reversible*, and by agitation the particles can be redispersed [72, p.716].

2.3.2 Steric Stabilization

In this section, steric stabilization is reviewed with focus on *polymers*. This is referred to as *polymer induced stabilization* [47, p.575].

Polymers can stabilize the suspension by adsorbing to the particles to form a layer, such that the attractive migration between them is disrupted. In other words, the particles are kept at separation distances exceeding that of the attractive forces [47, p.575]. It should be noted that a polymer can either attach to the particle surface by *anchoring* or *adsorbing* to it. The former term involves a *binding* of one of the polymer ends to the surface, and the latter means that the polymer interacts *weakly* between its chain and the surface [1, p.54]. An adsorbed polymer resides partially in solution with its *tails* and *loops*, and on the surface of the particle, as illustrated in Figure 2-20 [47, p.606].

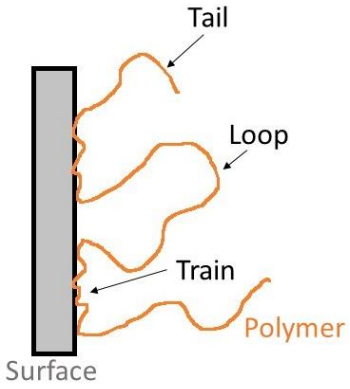

Figure 2-20: Illustration of a polymer chain that is adsorbed on a surface, depicting what is meant by a *tail*, *loop* and a *train*. The figure is constructed based on the figure found here: [47, p.606].

The adsorbed layer of polymer can be regarded as a *polymer solution* with an average thickness of δR_s, as shown in Figure 2-21, and contains an average *volume fraction* of polymer [47, p.607]. Note that the particles in the suspension are here defined to consist of two components; an *adsorbed polymer layer* and the *core particles*. What is meant by the latter is the *naked* particles, without any adsorbed polymer [47, p.614].

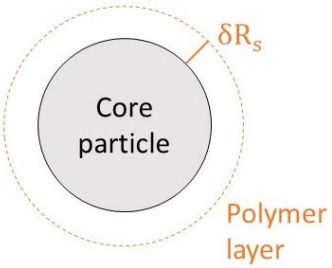

Figure 2-21: Illustration of thickness of adsorbed polymer layer. The thickness of the layer is δR_s.

In a sterically stabilized suspension, a thermodynamic quantity ΔG_R can be defined (see Figure 2-22). It corresponds to the *repulsive* free energy contribution felt by two approaching particles as a result of the steric interactions between them. An increase in ΔG_R means that the interaction energy between the particles is raised, and promotes stabilization of the suspension. Conversely, a decrease in ΔG_R implies that aggregation is spontaneous [47, p.607,609].

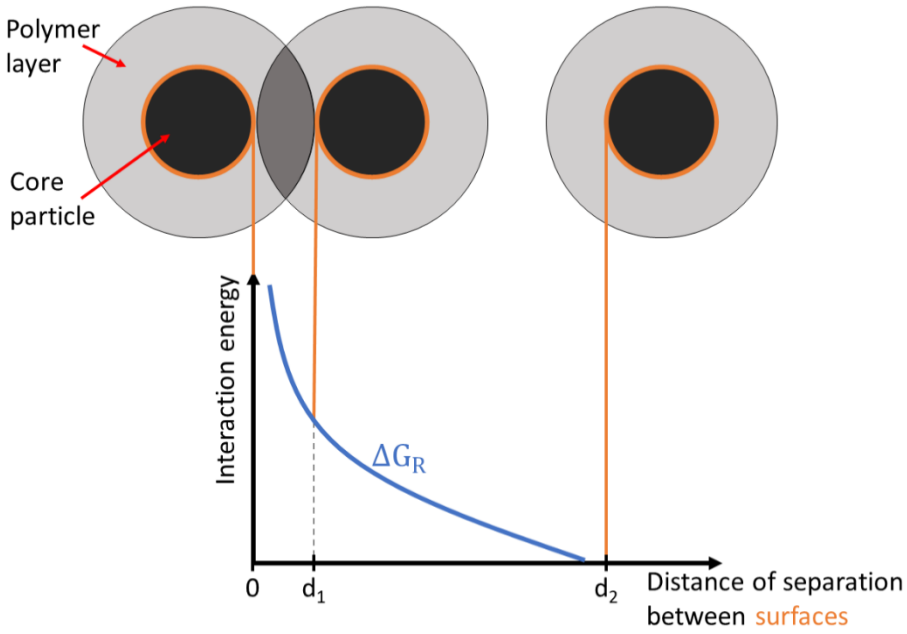

Figure 2-22: Illustration of the dependence between ΔG_R and separation distance between to polymer coated particles in suspension. The figure is based on reference [47, p.608].

The increase in ΔG_R as the distance between the particles decreases can be attributed to the decrease in entropy associated with the densification of polymer in the volume between them [56]. This is evident from Eq. 2.11, where ΔG_R expressed by repulsive enthalpy and entropy

contributions in relation to the polymer layer overlap. It is worth mentioning that the enthalpy or entropy contribution to ΔG_R can be the dominant term, and ΔG_R can change its sign with temperature. In this way, the colloidal stability can also depend on temperature [47, p.609].

$$\Delta G_R = \Delta H_R - T\Delta S_R \quad \text{(Eq. 2.11)}$$

Practical Approaches for Controlling Stability of Sterically Stabilized Suspensions

In this sub-chapter, practical approaches that can be taken to tune the stability of sterically stabilized colloidal suspensions will be reviewed in light of a theoretical model provided by Hiemenz et al. [47, p.614-619]. This model describes the initial approach of two particles with adsorbed polymer layers in suspension.

In this model, ΔG_R related to the distance between the two particles is considered. As the two particles approach each other, their adsorbed layers of polymer are the first entities to interact. As the core particles reduce their distance of separation the layers overlap. ΔG_R is equal to zero when there is no overlap (see Figure 2-22) [47, p.609]. As the layers start to overlap, the concentration of polymer increases in this region (Figure 2-23). Increasing the concentration in this way is not a spontaneous process, hence ΔG_R increases with the overlap [47, p.616].

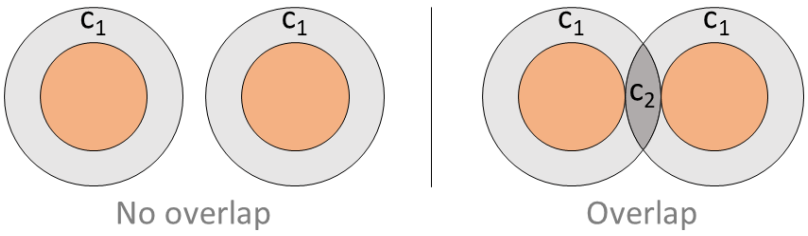

Figure 2-23: Concentration effects associated with overlap of polymer layers. The concentration (c) of the polymer layer with no overlap is c_1, and the concentration of polymer in the overlapping region is c_2. It is clear that $c_2 > c_1$ [47, p.616].

Two factors determine the behavior of ΔG_R; one associated with the *concentration* effect, and another with the volume of the region of overlap [47, p.616]. The model by Hiemenz et al. is based on Flory-Huggins theory. A very important parameter to be aware of from this theory, is the dimensionless *Flory-Huggins interaction parameter* (χ). This parameter is essential in determining the colloidal stability of a suspension. This is what determines the *sign* of ΔG_R [47,

p.617-618]. This parameter is related to the interaction between the solvent and the polymer in a polymer solution [73]. In the theoretical model, it is shown that ΔG_R is related to χ as shown in Eq. 2.12 [47, p.617].

$$\Delta G_R \propto \left(\frac{1}{2} - \chi\right) \quad \text{(Eq. 2.12)}$$

If $\chi < 1/2$, it means ΔG_R has a *positive* value, and this promotes repulsion between the particles. This situation is also referred to in literature as *good solvent conditions*, which involves a swelling of the polymer that is adsorbed on the particle surface. In this case the solvent has an affinity for the polymer, and therefore incorporates to it.

In the case where $\chi > 1/2$, ΔG_R has a *negative* value. This is referred to as *poor solvent conditions*. What is meant by this is that the polymer that is adsorbed will shrink in size, because the solvent does not have affinity for the polymer.

Note that the *goodness* of the solvent also depends on temperature and increases with temperature [47, p.125-126, 617-618].

In practice, this means that when the aim is to optimize the stability of suspensions stabilized by polymers, tabulated values of χ for the relevant polymer-solvent system can be looked up and used as a guide.

Polymer Concentration Effects

The suspension is not necessarily *stabilized* by the addition of a polymer. Adding it can also lead to *destabilization* of the suspension. What happens depend on the polymer-solvent and polymer-particle interactions [47, p.605].

Addition of polymer to a suspension can lead to different phenomena which are briefly mentioned in this section. Figure 2-24 summarizes some of the various effects related to the increase in concentration of polymer in a suspension [47, p.605].

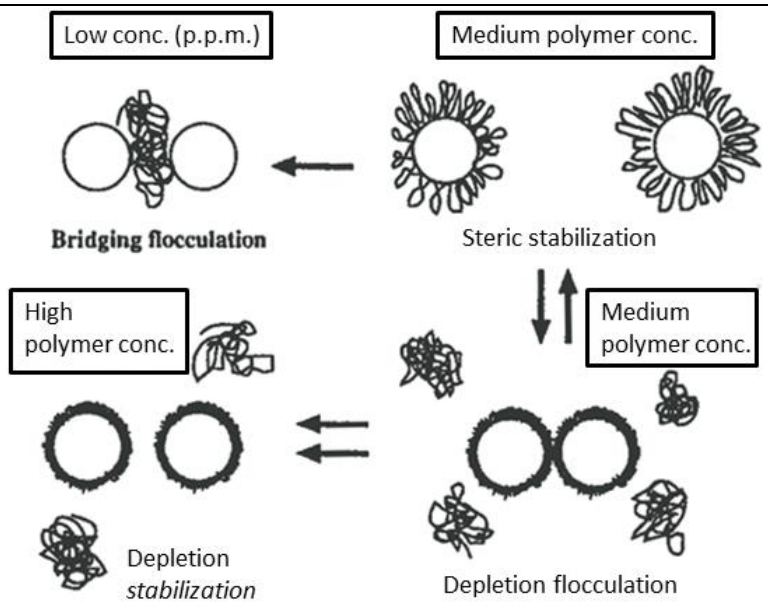

Figure 2-24: Phenomena related to different polymer concentrations in a suspension. The figure is copied from this source [47, p.605] (the color and size of the text in the figure was edited for clarification).

Bridging flocculation occurs at low concentrations, and implies that a polymer chain forms a bridge between two particles or more in suspension. *Brushes* or *brush-like layers* are formed on the particles at higher concentrations as the polymer chains adsorb on the particles. The size of extension of these brushes render them capable of *masking* the attractive forces in the system. This means the system is sterically stabilized. *Depletion flocculation* is an osmotic effect that occurs as the distance between the particles are very small (with the distance of separation approximately equal to, or less than R_g, the radius of gyration of the polymer chains). This causes a depletion of free polymer in between the particles, leading to a decreased osmotic pressure in this location, compared to the other sides of the particles, thus forcing them together. *Depletion stabilization* is another form of stabilization than *steric stabilization* per definition, and occurs when the polymer concentration is *high*. The previously described depletion occurs by demixing of the polymer and solvent, which in good solvent conditions is energetically unfavorable, and therefore the suspension remains stable [47, p.605,614].

Poly(vinyl pyrrolidone)

Poly(vinyl pyrrolidone) (PVP) is used in this thesis as stabilizer in the production of colloidal NPs. It is a non-ionic polymer with functional groups; C=O, C–N and CH_2 (see Figure 2-25). The polymer is widely used in nanoparticle synthesis, and can act as a stabilizer, capping agent, and also a reducing agent. The pyrrolidone part of the molecule is very hydrophilic, whereas the alkyl part is hydrophobic. In noble metal synthesis, the interaction between PVP and the metal occurs via the carbonyl group and nitrogen atom in the pyrrolidone component [74].

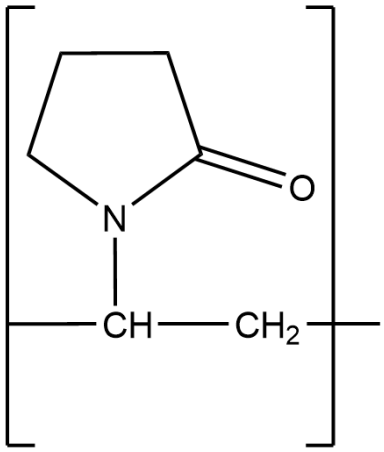

Figure 2-25: Repeating unit of PVP.

This compound decomposes at 400°C in air in pure form, but if it is bound to metal particles, the decomposition temperature may vary. For silver NPs, the temperature can be between 200-400°C [74].

2.4 Metal-on-Support Catalyst Preparation

A catalyst can lower the activation energy barrier in a chemical reaction by altering the reaction path resulting in an increased rate of product formation. The definition of a catalyst is a substance that accelerates a reaction without being chemically changed in the process. Catalysts are categorized into *homogeneous* and *heterogeneous* types. A homogeneous catalyst is working in the same phase as the reaction mixture, while a heterogeneous catalyst is of a different phase than the mixture [72, p.840]. It is important that the catalyst is stable over long periods of time, and has a high catalytic activity, however another critical factor is its *selectivity*.

What lies in this latter term is the ability of the catalyst to promote conversion of the reactants into *specific* products [75, p.2].

Nanoparticles of metals typically from group 8-11 in the periodic table can be used as *metal-on-support* catalysts. What is meant by this is that the NPs (typically 0.1-20 wt.%) are dispersed on a support material to avoid coalescence during use of the catalyst. Common support materials are oxides with a high surface area per unit mass such as alumina, silica and titania. The support material should be chemically stable, and its large surface area permits a good dispersion of the metal nanoparticles such that as much as possible of the catalytically active metal surface is accessible to the reactants during the reaction. Generally, by reducing the particle size of a non-porous support material, the highest surface areas that can typically be achieved are 50-200 m^2/g. To reach higher values, the support material needs to be porous.

Metal-on-support catalysts can be prepared via e.g. methods of *impregnation, adsorption from solution* and *ion-exchange*. In the latter case, an ion is introduced to the support material and then reduced. Another approach can be the method where a compound containing the catalytically active metal is deposited on the support in solution, followed by calcination and reduction. Further, another method is to first synthesize the nanoparticles, followed by deposition of the preformed NPs on the support [76, p.320-321], [77]. The latter method is the one employed in this thesis.

The support material used in this thesis is γ-Al_2O_3, and this oxide is also widely used elsewhere [76, p.326]. From Figure 2-26, it can be seen that this modification of alumina can be prepared from e.g. the aluminum hydroxide boehmite by heat treatment at ~500-750°C, dehydroxylating it to form γ-Al_2O_3.

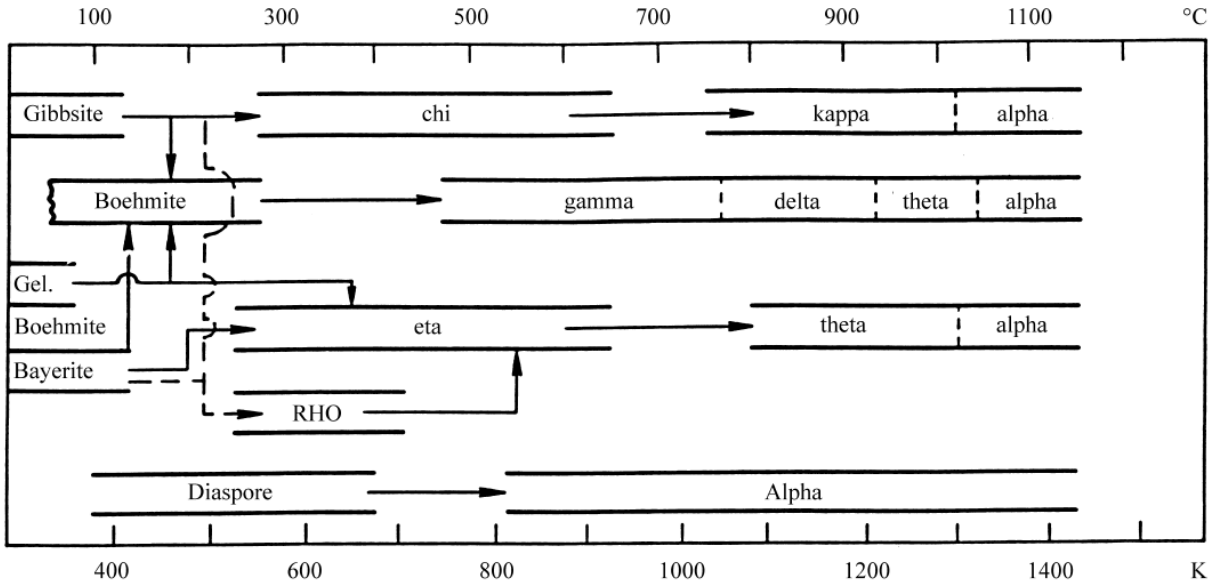

Figure 2-26: Transformations of aluminum hydroxides to *transition aluminas* (designated by Greek letters) at different temperatures [78].

2.4.1 Preparation of Metal-on-Support Catalysts via Deposition of Colloidal Free-Standing Nanoparticles

As the catalysts in this thesis are prepared via deposition of free standing nanoparticles on the support material, this technique is described in detail in this section.

In this method, free-standing metal nanoparticles are first produced via a colloidal synthesis route. These colloidal NPs are then introduced to a suspension of the support material followed by mixing to deposit the NPs on the support. The mixture is then dried in either air, vacuum or by freeze drying to remove the solvent and keep the distribution of NPs on the support. The catalyst is then typically calcined for removal of the stabilizer that was used in the synthesis. The reason for the removal is that the presence of the stabilizer can severely affect the catalytic activity of the catalyst. Depending on the material, the calcination should not be performed at too high temperatures, as it can cause the nanoparticles to sinter, meaning loss of surface area [77].

2.4.2 Calculation of Turnover Frequency

Metal-on-support catalysts consist of nanoparticles as the catalytically active ingredient because they have very large surface areas (for details on particle size and surface area see section 1.1). The catalytic activity of the particles depends on the surface area, as this is where the catalytic processes occur. When research is done to explicate differences in the catalytic activity between particular materials, the turnover frequency (TOF) is used as a means of measure. It is the number of reactant molecules converted to products at one active catalyst site per second (see Figure 2-27).

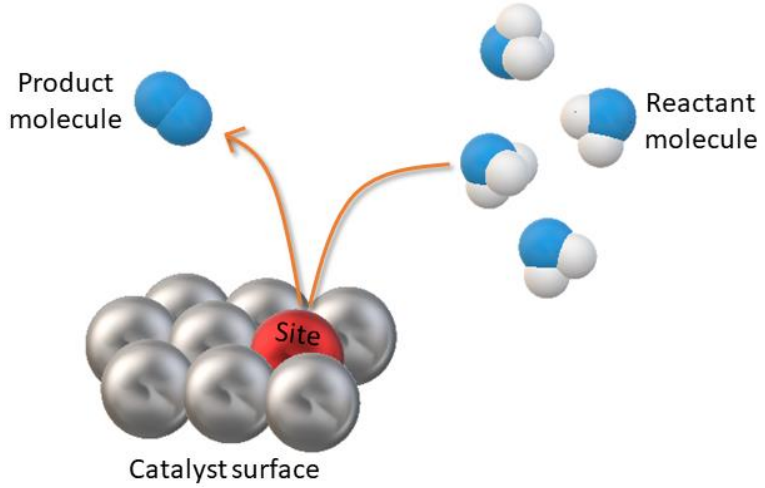

Figure 2-27: Schematic illustration of active catalyst site, reactant molecules and product molecule.

In this thesis, Pt and Pd are used as catalyst materials for conversion of ammonia, and each Pt atom in the surface of each nanoparticle is assumed to be catalytically active, corresponding to an active site. Further, the particle shape is assumed to be spherical. The TOF can be calculated as follows:

$$m_{Pt} = m_{cat} \cdot \frac{wt\%Pt}{100} \quad \text{(Eq. 2.13)}$$

$$V_{tot,Pt} = \frac{m_{Pt}}{\rho_{Pt}} \quad \text{(Eq. 2.14)}$$

$$V_{NP,Pt} = \frac{4}{3}\pi\left(\frac{\bar{D}}{2}\right)^3 \quad \text{(Eq. 2.15)}$$

$$S_{Pt} = \left(\frac{V_{tot,Pt}}{V_{NP,Pt}}\right) \cdot 4\pi\left(\frac{\bar{D}}{2}\right)^2 \quad \text{(Eq. 2.16)}$$

$$N_{A,Pt} = \frac{S_{Pt}}{S_{spec,Pt}} \quad \text{(Eq. 2.17)}$$

Where m_{Pt} is the mass of platinum in the catalyst, m_{cat} is the mass of the catalyst, $V_{tot,Pt}$ is the total volume of Pt in the catalyst, ρ_{Pt} is the density of Pt, $V_{NP,Pt}$ is the volume of a single Pt nanoparticle based on particle size measurements where $\overline{D}$ is the mean particle diameter. S_{Pt} is the exposed surface area of all Pt NPs, $N_{A,Pt}$ is the number of exposed surface sites and $S_{spec,Pt}$ is the surface area of one Pt-atom.

The TOF can be calculated by Eq. 2.18:

$$\text{TOF } (s^{-1}) = C \cdot F \cdot \frac{A}{N_{A,Pt}} \qquad \text{(Eq. 2.18)}$$

Where C is the ammonia conversion, F is the gas flow [mol/s] of ammonia over the catalyst, and A is Avogadro's number.

2.5 Characterization

In this section various characterization techniques of relevance in this thesis is reviewed.

2.5.1 Electron Microscopy

When a high-energy electron beam interacts with matter, a variety of signals are produced (see Figure 2-28). Many of these can be detected with different types of TEM [79, p.7-8]. In an SEM secondary electrons (SE) and back scattered electrons (BSE) are used to generate an image [49, p.125-126]. In both SEM and TEM (STEM), the characteristic x-ray signals are utilized in EDX (Energy-Dispersive X-ray spectroscopy) for quantitative analysis of the distribution of elements in the specimen [79, p.7-8]. In this sub-chapter the SEM-, TEM- and STEM- instruments are illustrated schematically in individual subsections, followed by a description of the principle behind image formation. Lastly, the theory and application of the EDX technique are reviewed.

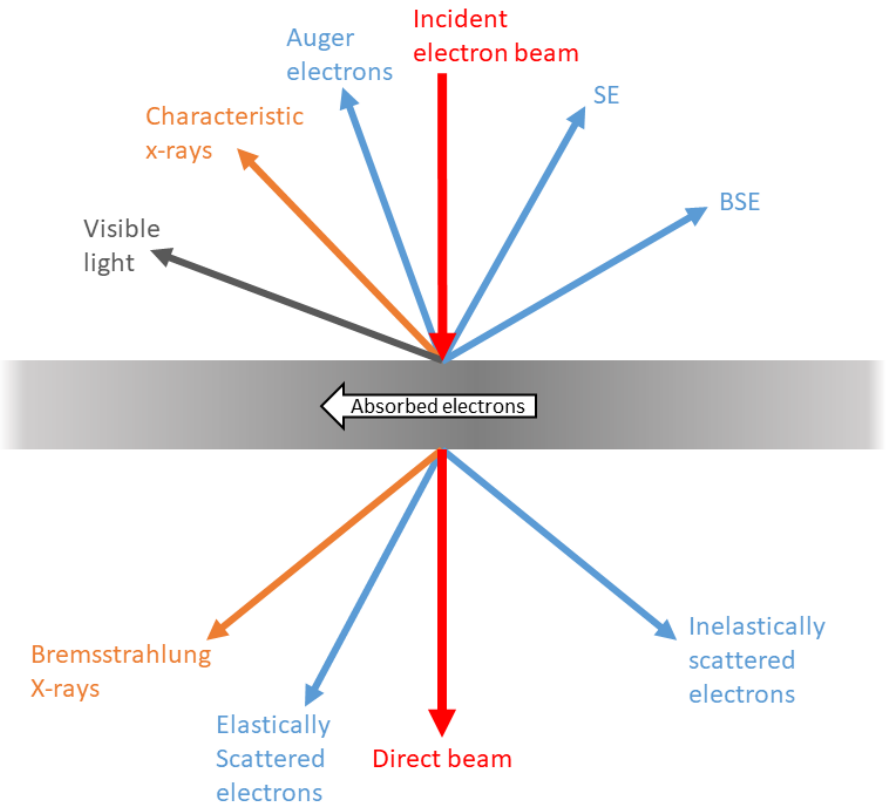

Figure 2-28: Signals generated from a specimen as a result of interaction with an incident electron beam [79, p.7].

Secondary Electrons (SE) and Backscattered Electrons (BSE)

Secondary electrons are electrons that are ejected from the valence shell of atoms in the specimen from inelastic scattering of the incident electron beam. This is schematically illustrated on the left-hand side in Figure 2-29 [80]. Only a part of the energy is transferred to the secondary electrons. The energy that is transferred is less than 50 eV, and therefore the SEs generated deeper than ~10 nm below the surface of the sample does not have enough energy to escape it, and will not be detected. Thus, it is clear that an image based on the collection of only secondary electrons contain topographical information from the specimen, which means the technique is *surface sensitive* [81]. It should however be noted that the *scattering range* depends on a number of factors; the energy of the scattering electron, the atomic number and density of the specimen [80].

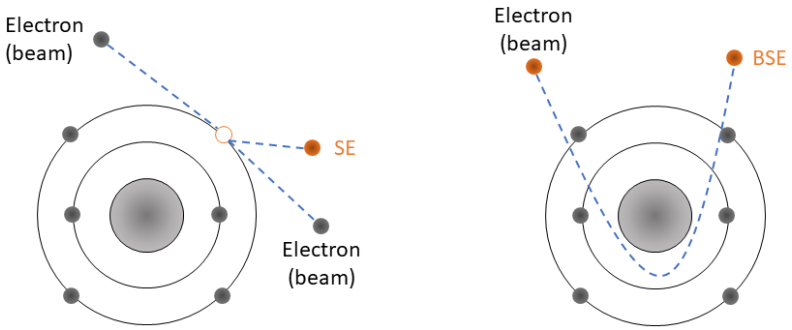

Figure 2-29: Illustration of secondary electrons (left) and backscattered electrons (right) [80].

The magnitude of SE emission depends on the angle of incidence of the electron beam, where it increases with an angle going from 0-90°. Sharp edges on the surface of the sample can result in a phenomenon that is referred to as the *edge effect.* If the surface has edges or roughness, a higher intensity of SEs contributes to the contrast in these areas, and appear as bright edges [81]. This effect is illustrated in Figure 2-30.

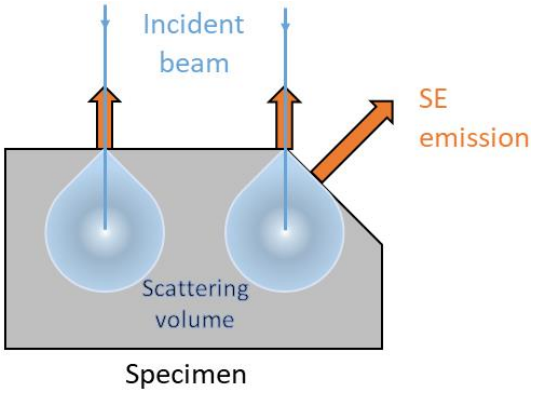

Figure 2-30: Illustration of the edge effect [80].

The generation of backscattered electrons is illustrated on the right-hand side in Figure 2-29, and shows that BSEs are electrons from the incident beam that are elastically or inelastically scattered back into the vacuum, or in other words *reflected* back [81]. The intensity of these electrons is strongly atomic number dependent; heavier atoms scatter more strongly, resulting in a higher intensity. The intensity also depends on the direction incidence and reflection (Figure 2-31), and the orientation of the crystals in areas of identical composition [80]. Therefore, images based on the BSEs can be utilized to differentiate between areas with different compositions, analyze the topography, and investigate crystal orientations. The energy of the BSEs is higher and therefore the scattering range is larger than that of the SEs, and information from a deeper penetration depth in the specimen is contained in the BSEs.

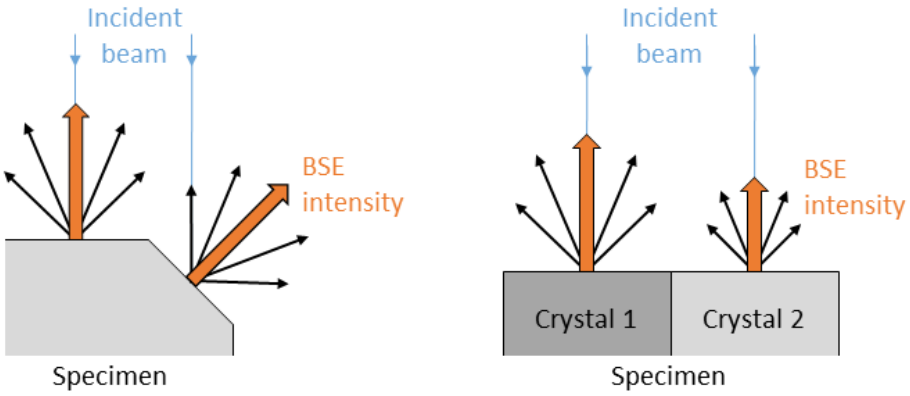

Figure 2-31: Left: Illustration of the dependence between BSE intensity and the angle of incidence from the electron beam on the specimen. Right: The dependence between the orientation of the crystals (*Crystal 1* versus *Crystal 2*) and the BSE intensity.

A rough schematic illustration of the SEM and its components are shown in Figure 2-32.

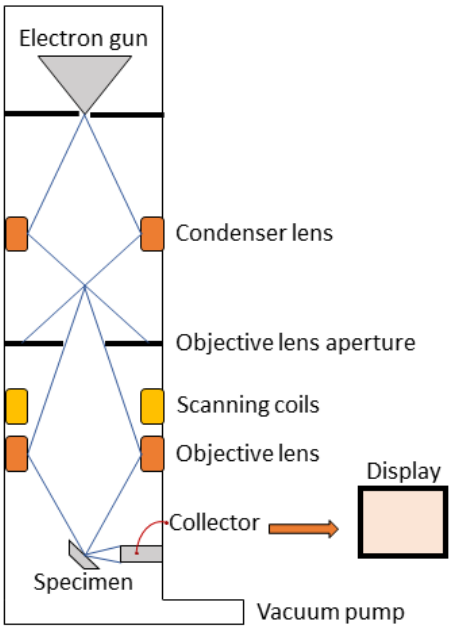

Figure 2-32: Basic components of an SEM instrument with two lenses.

Electron Sources

In an SEM, the electron gun is the source of electrons that are used to generate an electron beam which is subsequently focused onto a specimen, scanning it. Examples of types of such sources are *cold field emission gun (cold FEG), Schottky FEG, LaB_6 and tungsten (W) filaments.* What separate these different electron emission sources from each other are factors like lifetime, required level of vacuum when used, brightness (β), spread in energy (E), their work function (ϕ), emission current stability and operating temperature [79, p.73-87]. Some of these factors are summarized in Table 2-4.

Table 2-4: Commonly used electron emission sources in electron microscopy. Based on table [79, p.74].

Electron emission source	ϕ/eV	β[1]/[A/m²sr]	Spread (in E)[1]/[eV]	Vacuum/[Pa]	Lifetime/[hours]
Tungsten (W)	4.5	10^{10}	3	10^{-2}	100
LaB_6	2.4	$5 \cdot 10^{11}$	1.5	10^{-4}	1000
Schottky FEG	3.0	$5 \cdot 10^{12}$	0.7	10^{-6}	>5000
Cold FEG	4.5	10^{13}	0.3	10^{-9}	>5000

[1]At 100 kV

This sub-section is based on literature from Jeol Ltd. [80]. The lenses situated in an SEM are made from coiled wires with current flowing through them, which generates a *magnetic field*. Charged particles generally respond to a magnetic field, and the lenses are thus capable of deflecting the electrons in the electron beam supplied from the gun. They are deflected convergently. The strength of the magnetic field can be varied by changing the electric current flowing through the coils, and by this also the degree of the convergence of electrons, as illustrated in Figure 2-33.

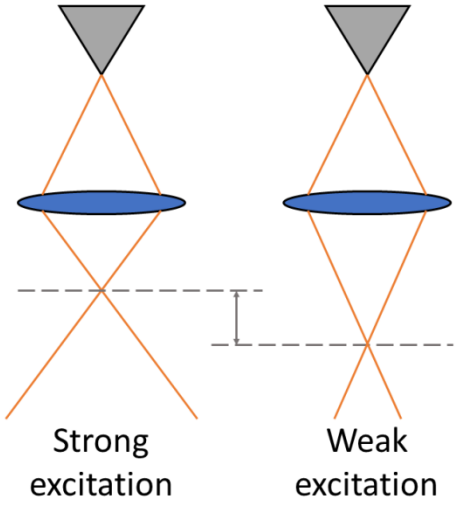

Figure 2-33: Effect of strong versus weak excitation of a magnetic lens on the convergence of the electron beam passing through. The gray triangles resemble the electron guns, the orange lines are the electron beams, the lenses are the blue ovals. The distance from the lens to the point where the beam converges into the smallest point is marked with a stippled gray line, and the arbitrary difference in this distance between the strong and weak excitation examples is shown with an arrow.

In this instrument, the specimen is illuminated by a very small *electron-probe,* that is a focused electron beam. In order to focus the beam, two lenses are employed; a *condenser lens* and an *objective lens.* These lenses are situated below the electron source, as shown in Figure 2-32. As seen from Figure 2-32, the *objective lens aperture* is situated below the condenser lens, and above the objective lens in the SEM. The *probe current* and the *probe diameter* can be controlled through the use of this aperture and the condenser lens. In this context, the probe current is referring to how many electrons hits the objective lens. By converging the beam to a large extent by the use of the condenser lens, more of the electrons would be blocked by the

aperture, resulting in a lower probe current (Figure 2-34). Conversely, a lower excitation of the condenser lens would result in a higher probe current.

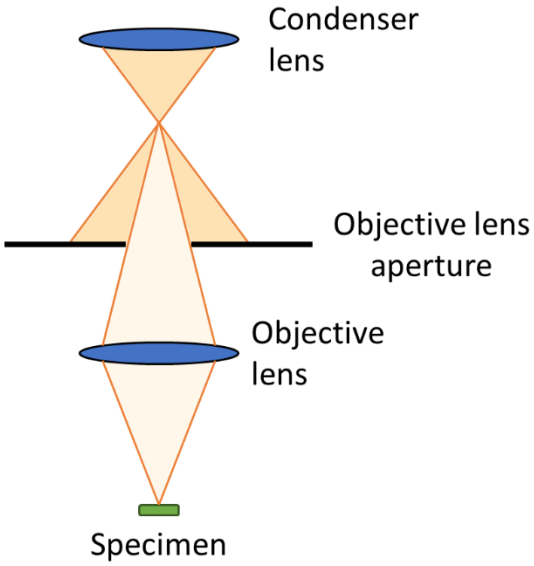

Figure 2-34: Illustration of the objective lens aperture and how it partially blocks the electron beam (orange lines and area) from entering the objective lens. This aperture is simply made of a metal plate with a small hole through it.

The size of the final electron-probe that illuminates the specimen is determined by the objective lens, therefore this lens is very important in determining the *resolution* of the images one can collect with the instrument. The *resolution* of an SEM-image is defined as the minimum distance between two distinguishable points in the image. In other words, if the distance between these two points are less than this minimum distance, the points will be indistinguishable. This is illustrated in Figure 2-35 with respect to two examples of different foci.

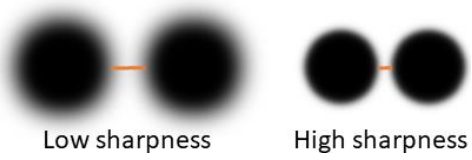

Figure 2-35: Poor resolution (left) versus better resolution (right), illustrating the minimum distance (orange line) of separation.

Magnification

Magnification in the SEM is given by Eq. 2.19 along with Figure 2-36 the definition of the variables [80]:

$$M = \frac{D}{d} \qquad \text{(Eq. 2.19)}$$

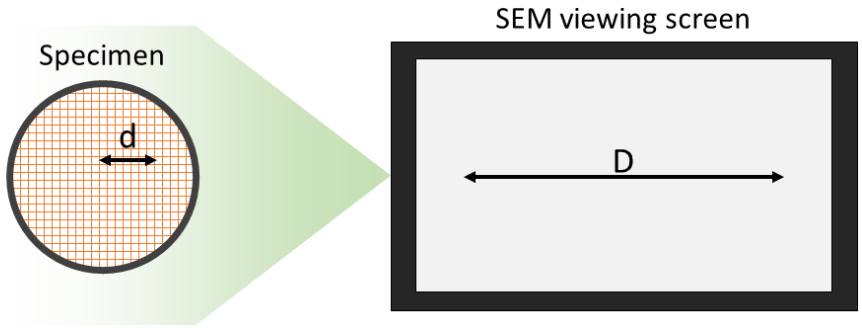

Figure 2-36: Definitions of variables in equation for magnification in the SEM. The distance *d* is the distance that is scanned by the electron probe in the microscope, and *D* is the length of the scanned section as viewed on the viewing screen. As the size of the screen is constant, different magnifications are achieved depending on the width of the electron probe [80].

If the electron probe size is decreased, the scanned area is smaller but because the size of the viewing screen is the same, the magnification is increased.

Aspects of Optimizing the Quality in the Images

The way the lenses work in an electron microscope is that they converge the electron beam passing through it, but the degree of convergence of the electrons in the beam is dependent on *where* they hit the lens. These lenses converge the electrons hitting them near the *optical axis* (see Figure 2-37) less than those that hit them far from it. This is referred to as *spherical aberration.* The energy of the electrons also affects the degree of convergence through the lens, as electrons with higher energy converges to a less degree than those of lower energy. This is known as *chromatic aberration* [79, p.103-106]. These aberrations, affect the diameter of the electron-probe in the SEM, and thus also the resolution in the images.

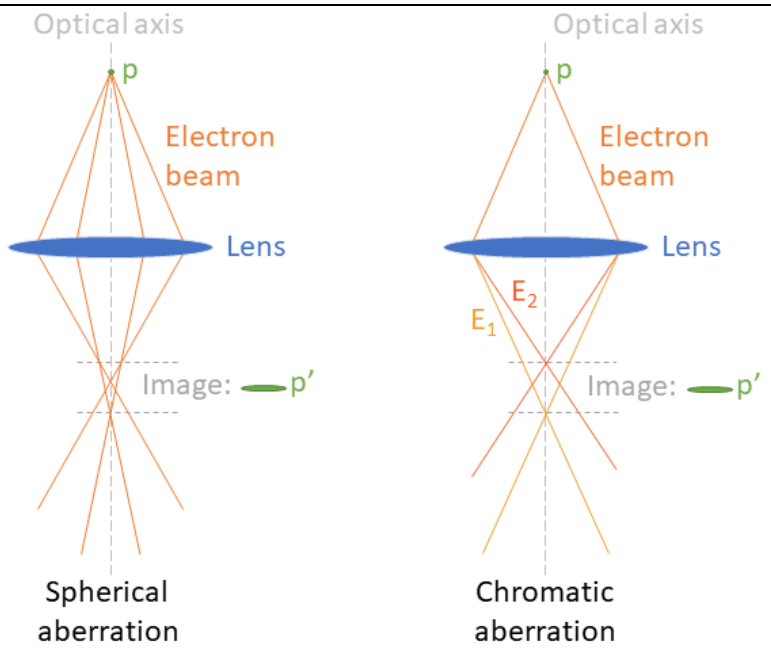

Figure 2-37: A disk (p') is perceived in the image plane when the real object is a point (p), and it is under the influence of spherical- or chromatic- aberration.

In Figure 2-38 are some effects related to the variation in acceleration voltage used when examining a specimen.

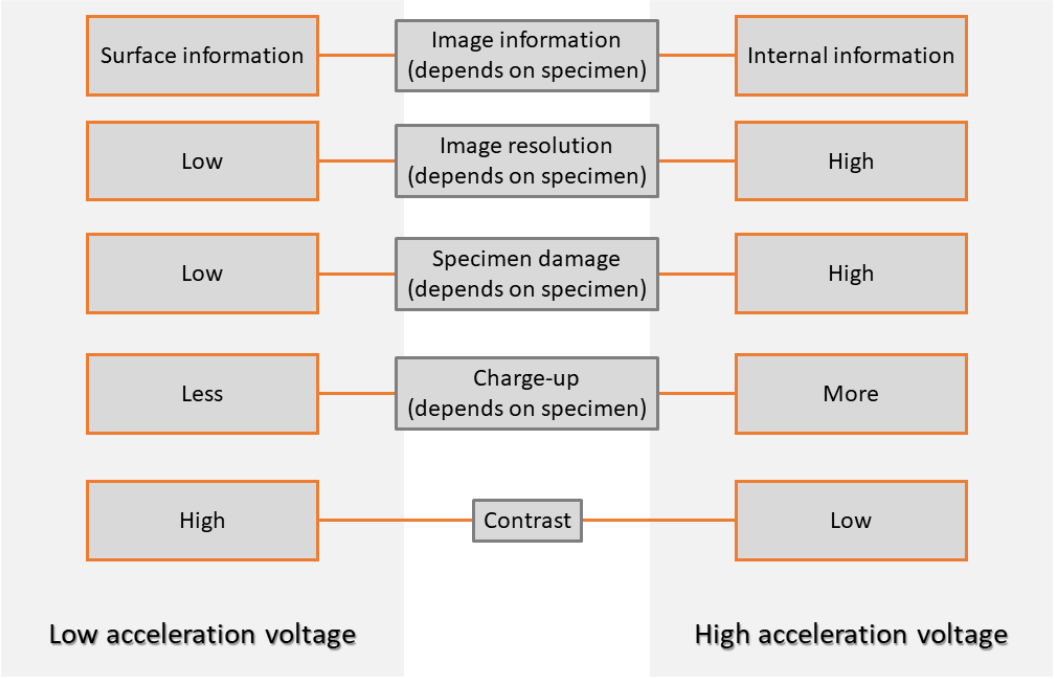

Figure 2-38: Effect of acceleration voltage on various attributes related to image quality using an SEM [81].

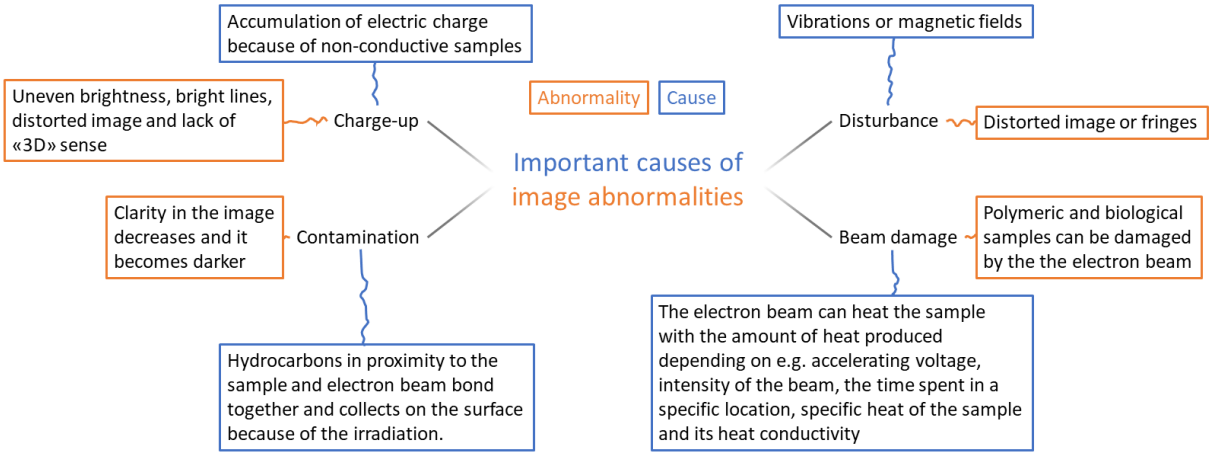

Figure 2-39: Some important SEM-image abnormalities and causes of these [81].

Transmission Electron Microscope and Scanning Transmission Electron Microscope

In this section, details regarding the components in the TEM instrument are first reviewed. Next, how magnification works in the TEM is explained, followed by a clarification of imaging types typically used in the instrument. A selection of modes for operating the TEM were made, based on the ones that are employed for the results in this thesis, and they are briefly described here. This include BF-TEM (Bright Field TEM), DF-TEM (Dark Field TEM), HR-TEM (High Resolution TEM) STEM (Scanning TEM) and HAADF-STEM (High Angle Annular Dark Field TEM).

The electron source typically used in TEMs are of the same types as those mentioned in Table 2-4, which are used in SEMs, but typical acceleration voltages that are used range between 100-400 kV. This enables atomic level resolution (<0.5 nm) [82, p.364], and by converging the electron beam into a small probe (which is also possible in many TEMs, like the SEM), referred to as STEM, chemical analysis can be performed in very small areas in the specimen. The STEM-mode will be described in detail at the end of this section [82, p.363-364]. An important note to make, is that all specimens to be examined in a TEM must be *electron transparent.* That is, the specimen must be thin enough for the electrons to be able to transmit through it [79, p.173]. The specimens prepared in this thesis are prepared on copper grids (diameter = 3 mm),

as this is a common technique [79, p.175]. A plasma cleaner is often used on the samples in the TEM, as well as in the SEM [79, p.132].

The main components of the TEM can be subcategorized into the *illumination system, objective lens/stage,* and the *imaging system* (see Figure 2-40) [79, p.141]. Like in the SEM, it is also important here to properly evacuate the column to avoid contamination, and ion pumps are commonly used for this purpose [82, p.364].

Like in the SEM, spherical and chromatic of aberrations are responsible for lower resolution in the TEM. In modern TEMs, aberration correction is common, and they can have resolutions down to less than 0.1 nm [79, p.6].

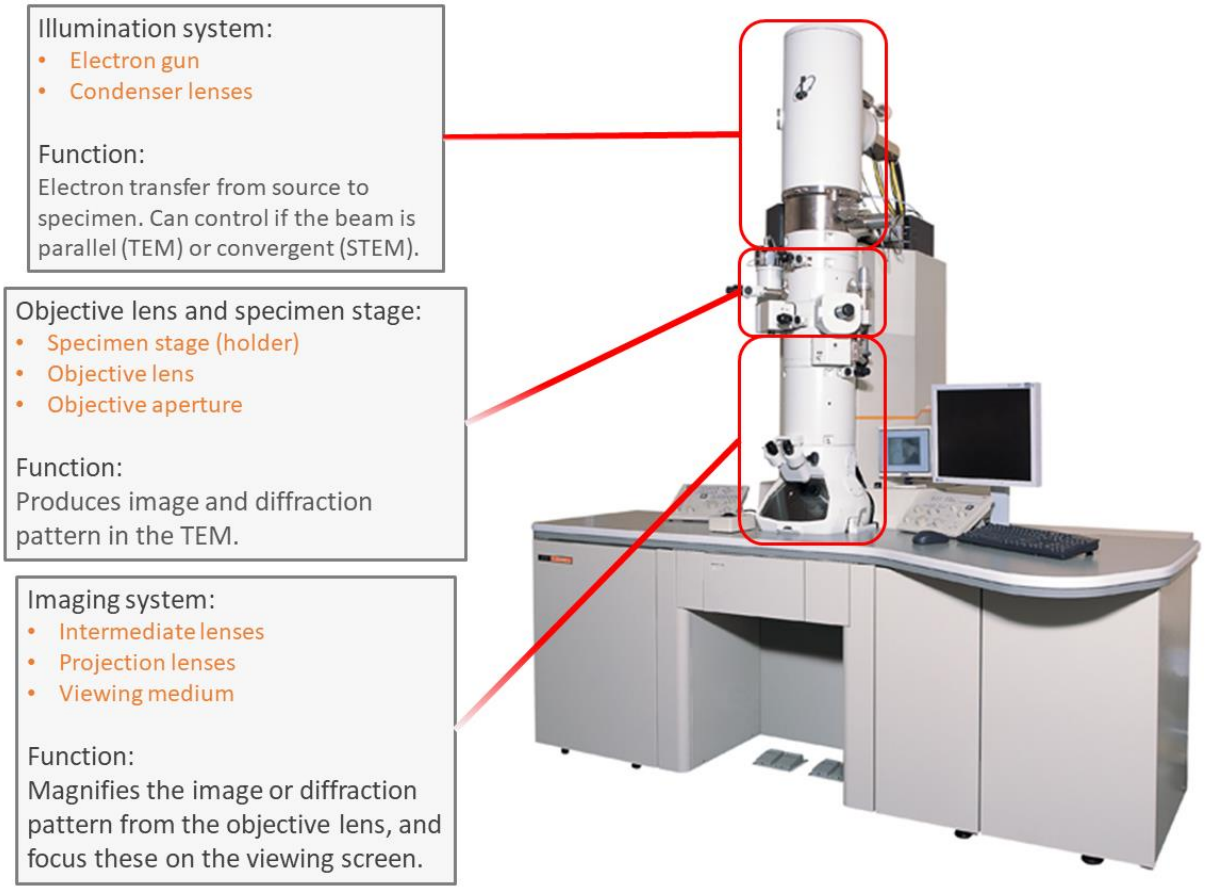

Figure 2-40: A rough overview of the different components and their functions in a TEM in imaging mode [79, p.141]. Image of TEM is taken from reference [83].

An equation for magnification (M) in the TEM (Eq. 2.20) is given here, and the two variables (d_i and d_0, where i = a; b) are defined in Figure 2-41 [79, p.95].

$$M = \frac{d_i}{d_0} \qquad \text{(Eq. 2.20)}$$

It can be seen from Figure 2-41 and Eq. 2.20 that if the excitation of the lens is strong, the result is a lower magnification, as d_i is then short, as with d_a. On the other hand, if the strength of the lens is weaker, the image plane is formed at a greater image distance (d_b), and thus would yield a higher magnification.

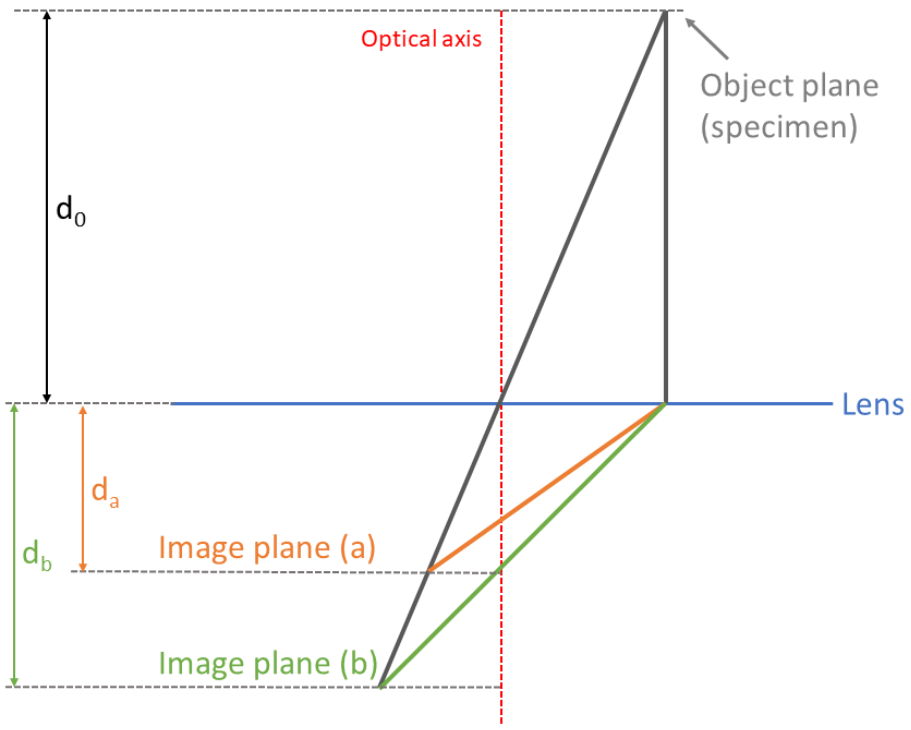

Figure 2-41: Magnification in the TEM. Two beams coming from the specimen in the object plane hit the lens. The orange beam represents a change in direction due to a more strongly excited lens than the green beam. An image is formed in plane (a) and (b) from the strong and weak excitation respectively, at different image distances (d_a and d_b). The longer this distance (d_i) is, the higher the magnification [79, p.95].

The condenser lenses in the illumination system control the convergence of the beam emerging from the electron source; if it is in the form of an electron probe (STEM) or parallel beam (TEM). Figure 2-42 shows a ray diagram displaying the progression of the beam through the objective lens and imaging system, after interaction with the specimen. The objective lens forms a diffraction pattern in the *back focal plane* (positioned where the *objective aperture* is in Figure 2-42), and an image (marked as *intermediate image 1*). The excitation of the intermediate lenses control if the diffraction pattern or the image is projected by the projector lens to the viewing medium (viewing screen, or PC-monitor) [79, p.152-153].

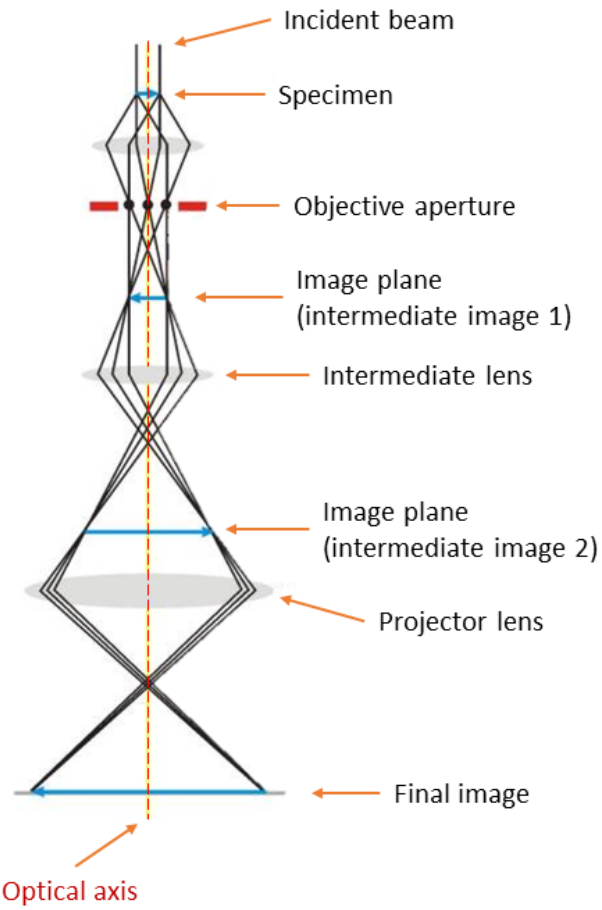

Figure 2-42: Schematic illustration of the TEM (image mode) below the specimen [79, p.153]. The figure was taken from the reference [84], and modified.

Two types of contrast are distinguished between in the TEM; *amplitude-* and *phase contrast*. Amplitude contrast can be further classified into *mass-thickness-* and *diffraction contrast*. Mass-thickness contrast arise when the transmitted electron beam travels through material with variations in density or thickness, as a dense or thick material region cases the electrons to be

scattered more strongly. Diffraction contrast is due to the presence of crystals which scatter electrons away from the direct beam path by Bragg reflections, giving rise to image contrast [85, p.53-54].

Two common methods for producing amplitude contrast is by operating the TEM in BF (Bright Field), or DF (Dark Field) mode. The difference between these modes are schematically illustrated and explained in Figure 2-43. From inspection of this figure, BF-mode can be selected by using an objective aperture to block out all of the scattered beams. Only the direct beam will then contribute to the image formation, and objects that scatter the electrons away from the optical axis appear dark, while the vacuum appear white in the final image. DF-mode is achieved by tilting the incident beam such that the diffracted beam is on-axis (along the optical axis), and only this beam contributes to the image. In this case, vacuum will appear dark, and the material that scatter the electrons looks white [79, p.372-373].

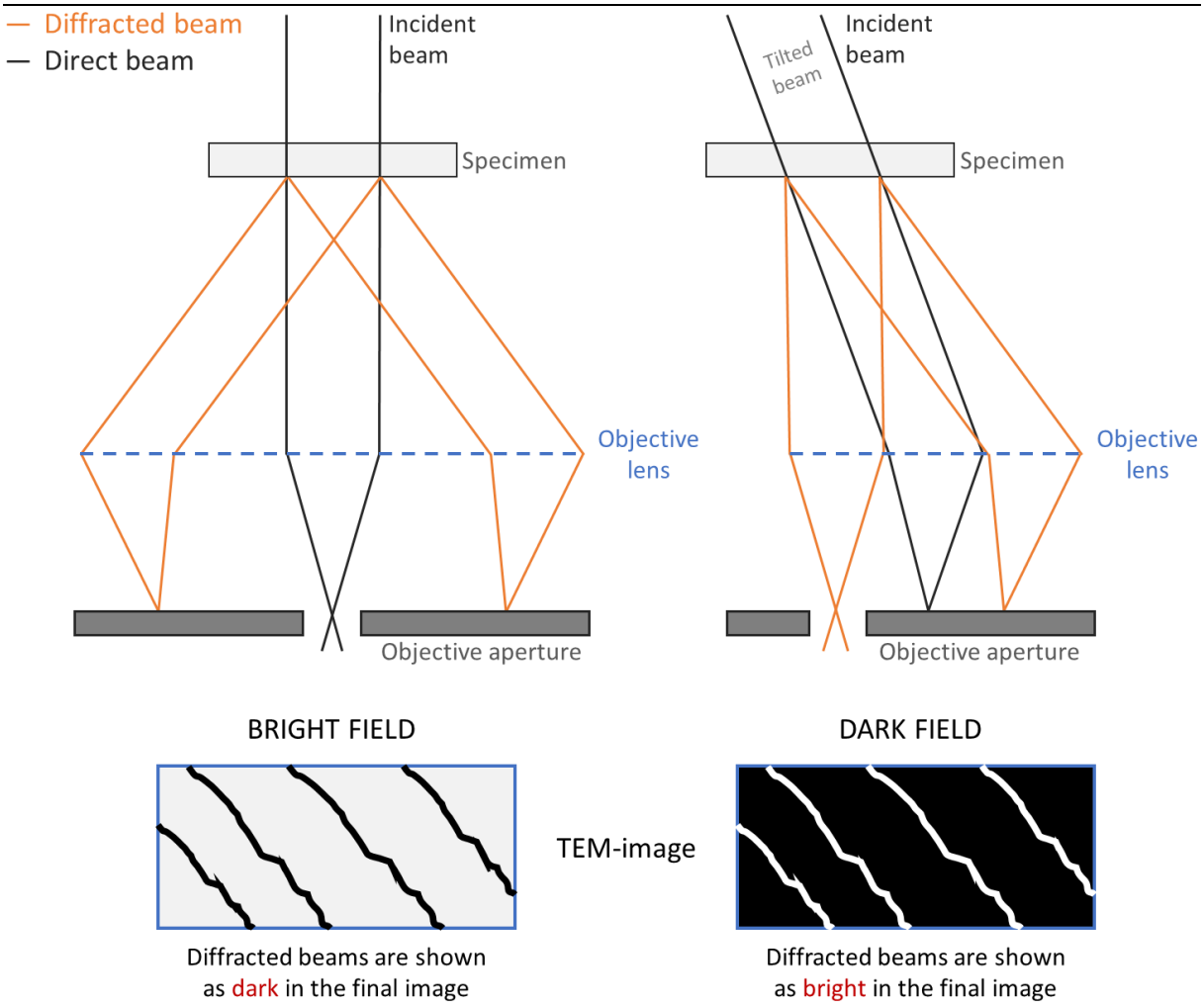

Figure 2-43: Bright field (left) versus dark field (right) modes in the TEM. In bright field the diffracted beams (orange) are blocked by inserting an objective aperture and they are not part of the image formation. On the other hand, in dark field mode, one of the diffracted beams are selected, and *only* this beam is involved in the final image formation. This can be achieved by tilting the illumination, as indicated. The differences in the final images from each respective mode is schematically illustrated at the bottom, where in bright field the diffracted beams remove intensity form the final image, and opposite in dark field [82, p.367-369].

If more than one beam is contributing to the image, it produces phase contrast which is the result of interference between waves. This contrast is what is used to produce the high-resolution images in HR-TEM. This type of contrast is, however present in most TEM images at almost all magnifications.

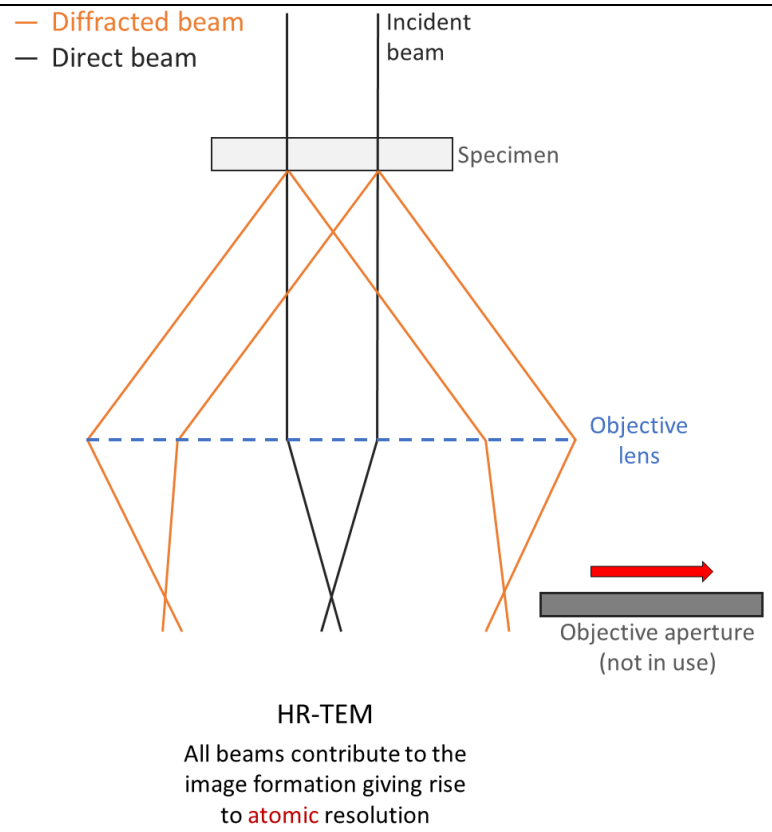

Figure 2-44: Phase contrast is used in HR-TEM by using all beams from the specimen, including the direct beam and diffracted beams. The figure shows the interaction of the incident beam with the specimen and upon transmission, the direct- and diffracted beams entering the objective lens. The objective aperture is not used, which means all beams from the sample are used in generating the image (by phase contrast) [79, p.389].

Scanning Transmission Electron Microscopy

If the condenser lenses are used to converge the beam into a small probe (STEM), instead of using apertures for selecting BF- or DF-mode, different types and placements of detectors are used. The BF-, ADF (Annular Dark Field)-, and HAADF (High Angle Annular Dark Field)-detectors are positioned relative to each other as illustrated in Figure 2-45. In this way, the placement of the detector determines which electrons are collected. The image contrast produced when the detector is located at high angles (HAADF) is *Z-contrast.* This contrast depend on the atomic number(s) of the species that make up the material in the specimen [79, p.379-380].

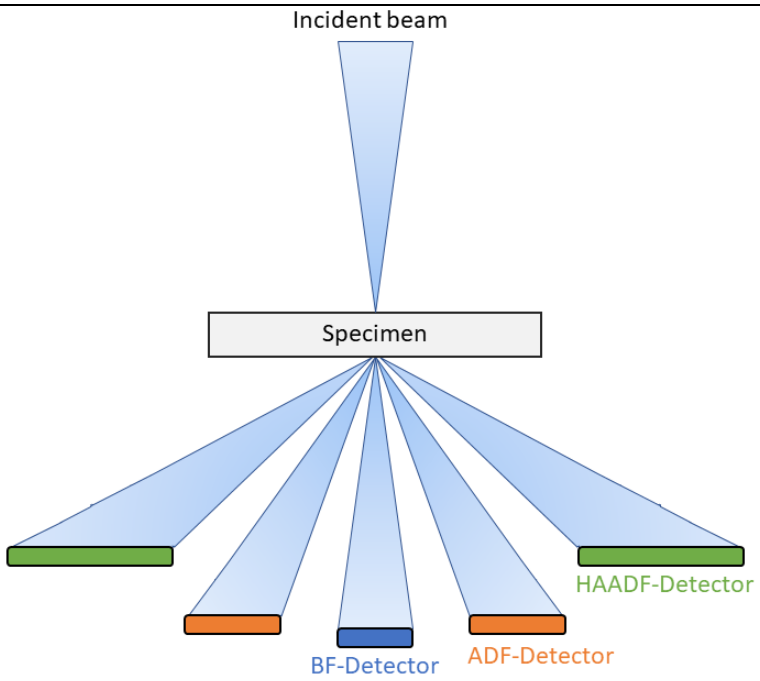

Figure 2-45: The blue "cones" are illustrating the convergent electron beam (on top of the specimen), and the scattered electrons at three different angles corresponding to the placement of the detectors; BF, ADF, and HAADF in the order of increasing angle [79, p.380].

Energy Dispersive X-ray Analysis

Characteristic x-rays are generated in the specimen by interaction with the electron beam, according to the process described in section 2.5.2. If these x-rays are detected and coupled to a specific area selected and observed by the (S)TEM or SEM [80], chemical information about this area is obtained [79, p.581-584]. This technique is referred to as EDS (Energy Dispersive x-ray Spectroscopy)/EDX/XEDS.

Voltage pulses are generated by the EDS-detector that is proportional to the energy of the detected x-ray signal. These signals are processed in a computer to give the number of *counts* (pulses) dispersed according to their energy in a spectrum, or in the configuration of an visual *EDS-map* which show where the counts of specific energy (corresponding to different species) originated from.

2.5.2 Powder X-Ray Diffraction

Powder x-ray diffraction (PXRD or PXD) has many applications, e.g. qualitative phase identification, quantitative analysis of the concentrations of the phases and unit cell parameter determination (size and shape) [86].

Unit Cells and Miller Indices

A unit cell is defined as the simplest unit of three-dimensionally arranged lattice points which, when repeated, reproduces the whole crystal lattice [87, p.86]. The unit cell can be defined in terms of the *unit cell parameters a, b, c, α, β* and *γ* (see Figure 2-46). The parameters a, b and c denote the edge length of the unit cell, in the respective spatial dimension, whereas α; β; γ specify the angles between the axes b and c; a and c; a and b, respectively. All possible three-dimensional lattices can be specified through only 7 combinations of these parameters, and they are referred to as *cubic, tetragonal, orthorhombic, monoclinic, triclinic, hexagonal* and *rhombohedral* unit cells. 14 *Bravais lattices* can be made from these 7 types of unit cells, as the atoms can be positioned e.g. in the corners and middle of the cell (body centered cubic) or in the corners and on each face (face centered cubic). Platinum and palladium crystallize with cubic close packing [35],[34] having an FCC (Face Centered Cubic) unit cell (see Figure 2-46). This cubic unit cell can be completely described by the lattice parameter *a*, because a = b = c in the cubic system, and all of the angles (α, β, γ) are 90°[88, p.101-103].

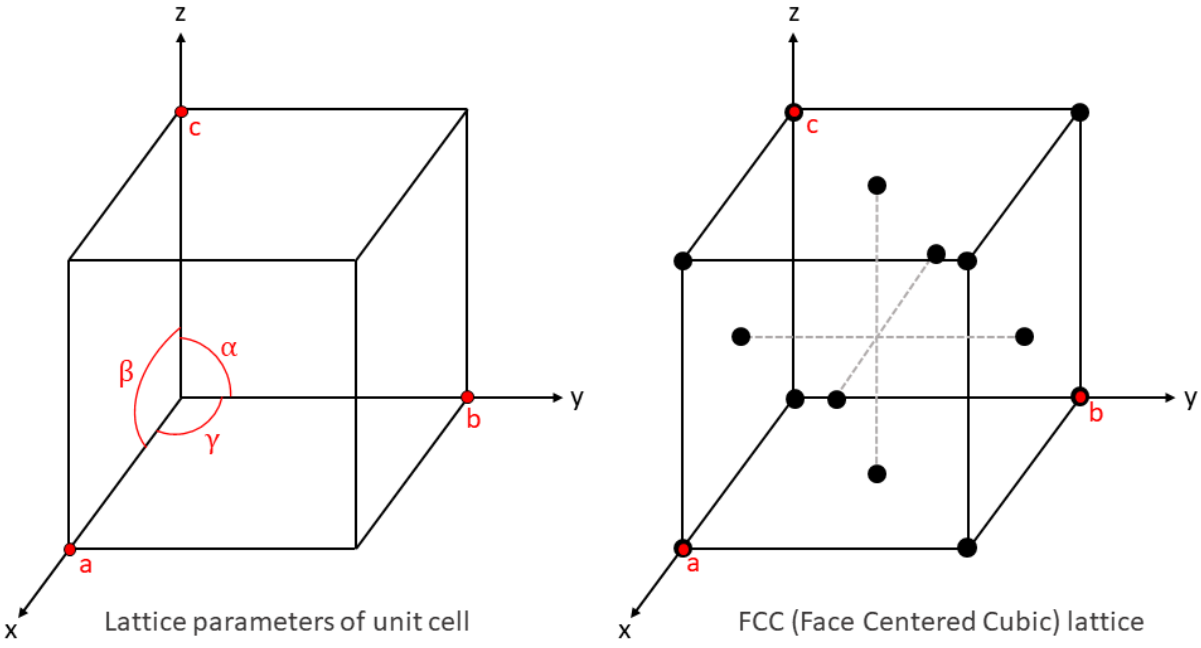

Figure 2-46: Left: Definition of lattice parameters a, b, c, α, β and γ in a unit cell. Right: The FCC lattice. Reference: [88].

Miller indices (hkl) are used to specify the interatomic planes in crystal structures. The (hkl) indices are the family of planes that intersect reciprocal values of fractions of the a, b and c unit cell parameters respectively. This is shown for three (hkl)-planes in the general unit cells in Figure 2-47 [88, p.107].

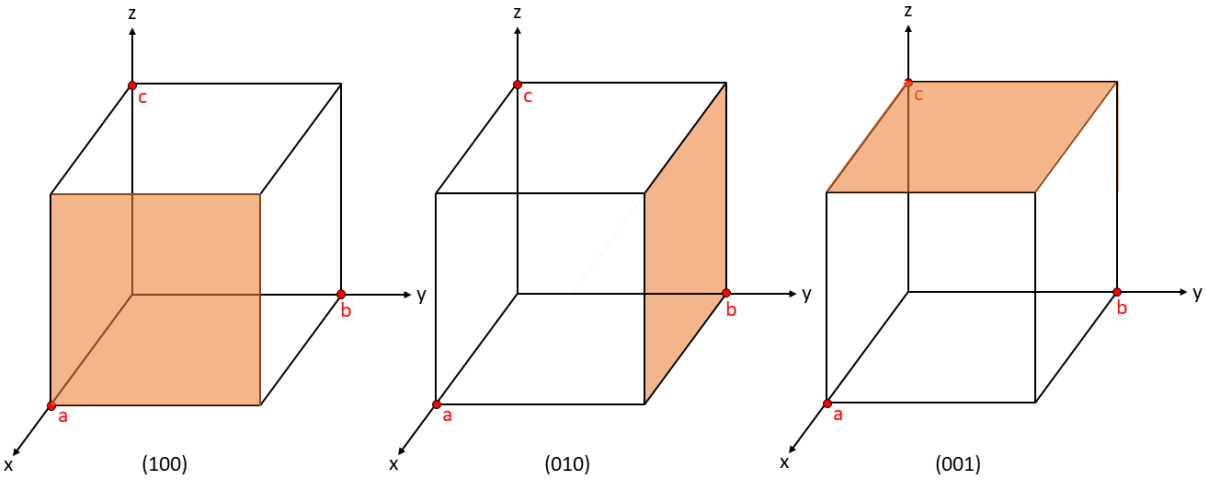

Figure 2-47: Three different crystallographic planes. (100): The plane intersects the a-axis at 1; (010): The plane cuts the b-axis at 1; (001): Intersection of the c-axis at 1. Reference: [88, p.106-107].

X-ray Diffraction

X-rays are used to determine the characteristics described in the introduction of this sub-chapter. The basic principle of material characterization with x-rays works because of the specific interaction this type of radiation has with crystalline matter. X-rays diffracts when it interacts with the specimen, because the periodic array of atoms that compose it acts like a diffraction grating. For diffraction to occur from the interaction of an electromagnetic wave with the periodic atomic arrangement in a crystal, the wavelength must be very short. X-rays fits this criterion ($\lambda \approx 0.07$-0.2 nm), and will diffract when they hit a crystalline specimen. If the *Bragg condition* is satisfied (see Figure 2-48), constructive interference give a maximum in intensity, which depend on the angle of incidence (2θ), the spacing between atomic the planes (d) and the wavelength of the beam (λ). In a typical powder x-ray experiment the wavelength of the radiation is known, the angle (2θ) is varied (and thus known), and by recording the resulting peaks in intensity versus the angle in a *diffractogram*, the d_{hkl}-spacing (distance between interatomic hkl-planes) can be determined [86]. In other words, the peak positions in the diffractogram can be utilized to determine the unit cell dimensions of the material [88, p.115].

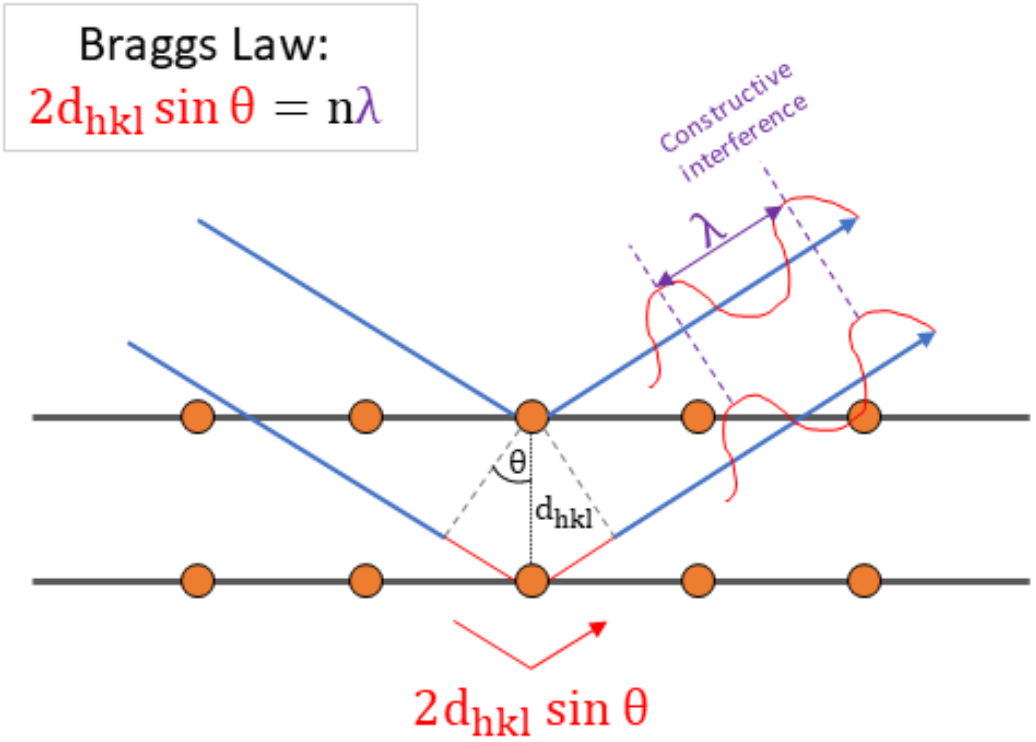

Figure 2-48: Braggs law. The orange circles represent atoms in atomic planes (gray lines). Two incident x-ray beams (blue lines) are diffracted by the atoms. For the two beams to still be in phase at the purple stippled markings, the minimum extra distance the lower beam must travel is $(2d \sin\theta)$ farther than the upper one, as indicated by the red arrow. Constructive interference causes diffraction maxima for all values of $(2d \sin\theta) = n\lambda$ [82, p.77-78].

Vegard's Law

In a bimetallic solid solution system where the two constituent metals have similar structures, PXRD can be used to determine the composition in the specimen. Vegard's law states that there is a linear relationship between the lattice parameter found for the solid solution and the substitution grade of each component (see Eq. 2.21) [88, p.115-116].

$$x = \frac{a_{ss} - a_1}{a_2 - a_1} \qquad \text{(Eq. 2.21)}$$

Here, a_1 and a_2 are the lattice parameters of metal 1 and 2, respectively, and a_{ss} is the lattice parameter of the solid solution. The composition is determined from x, which is the mole fraction of metal 2.

X-rays can be generated by shooting electrons at a target material, usually a metal, ionizing its surface atoms. An inner shell-electron in the target material is kicked out by the incident electron, causing an outer shell-electron to fill the hole. The energy difference between the outer- and inner shell-electrons corresponds to the energy of the emitted x-ray radiation. The transition could for instance be an electron from the L-shell filling a hole in the K-shell, and the radiation emitted is then referred to as K_α (see Figure 2-49) [82, p.88], [89].

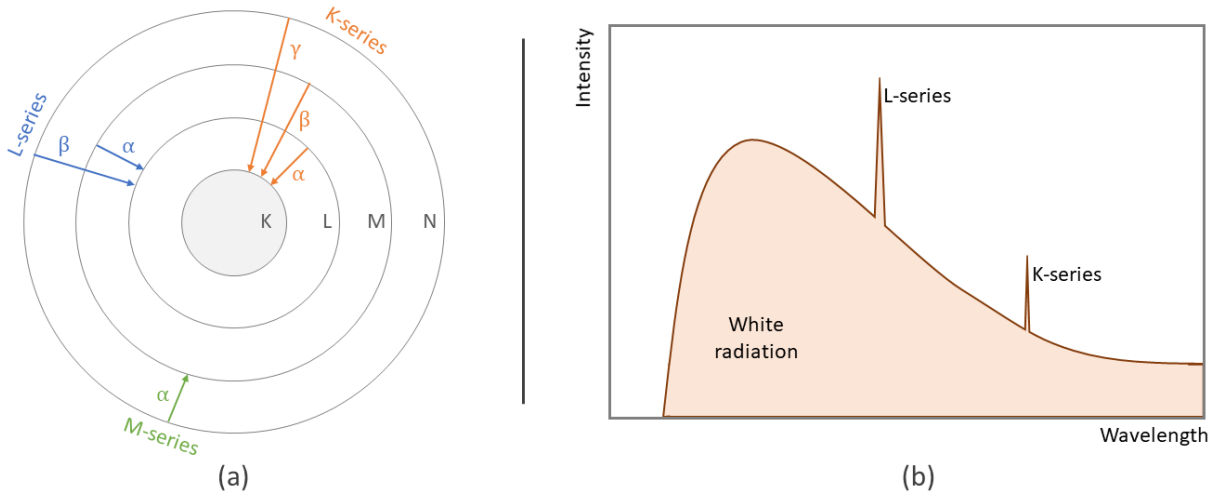

Figure 2-49: (a) Definition of notation for characteristic x-rays generated when an electron is kicked out of the respective shells (K, L, M and N). (b) Typical characteristic peaks for transitions in L-, and K-series superimposed on the background radiation. This *white radiation* is caused by deceleration of the incident electrons [82, p.88-89],[89].

The most common laboratory x-ray radiation is CuK_α (λ = 0.15406 nm) [86]. Other sources are also used, e.g. Cr, Fe, Co or Mo. The choice of x-ray source material can depend on whether the sample fluoresces from the characteristic radiation emitted by the material. Fluorescence originates from absorption of x-rays which excite electrons in the sample, when these electron holes are yet again filled, x-rays are emitted. This contributes to an increased background noise in the diffraction pattern, as these x-rays are scattered in all directions [90, p.319].

In this thesis powder x-ray diffraction is performed in an instrumental setup with $\theta - 2\theta$ Bragg-Brentano geometry (see Figure 2-50). In this configuration, the sample is rotated through the angle θ, as the detector is moved through 2θ. A monochromator is used to select specific characteristic wavelengths. If not, the diffractogram would be filled with several maxima arising from various transitions while rotating through 2θ [86]. Typical monochromators employed are based on crystals, which transmit specific wavelengths. Using the Cu-anode as

an example, a monochromator is able to filter the radiation such that Cu $K_{\alpha 1}$ and $K_{\alpha 2}$wavelengths are mainly left to strike the sample [90, p.320].

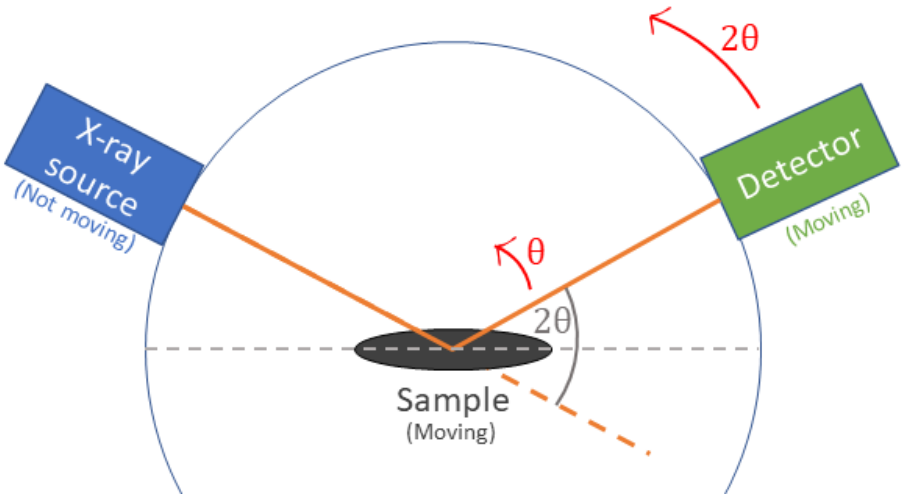

Figure 2-50: Schematic illustration of the θ − 2θ Bragg-Brentano geometry. The x-ray source is in a locked position, while the detector rotates through an angle of 2θ while the sample rotates through θ [86].

The sample in powder XRD experiments only gives a true representative diffraction pattern if it contains a very large number of randomly oriented crystallites. In fact the *real* pattern is only achieved by an infinite number of crystallites oriented in an infinite number of ways [90]. If they are not, it can give rise to what is referred to as *preferred orientation*. This is when the crystallites are not oriented randomly, giving rise to higher observed intensities at certain angles in the experiment. In Bragg-Brentano geometry displacement of the sample may cause shifts in peak positions, this is however possible to account for, as it is a systematic error, and can be *refined* as a parameter in the Rietveld refinement (see further down in the text) [90, p.301-314].

The *step scan mode* was used to record the diffraction patterns in this thesis. This means the movement of the moving parts in the measurement experiment is incremental. The x-ray intensity is measured when the moving part are at rest. In this mode there are two main parameters which are user defined; the *step size*, and the *counting time*. The step size refers to how many degrees (2θ) are changed per step, and the counting time is the time spent at each step in the measurement. A general rule of thumb is that for very broad peaks (nanoparticles), and for fast experiments, large step-sizes should be chosen. Smaller step-size should be selected

for materials with high crystallinity with narrow peaks. Smaller size also improves the resolution in the measurement [90, p.331-334].

Rietveld Refinements

The Rietveld method is a well-established approach for determination of a range of characteristics of a sample. In short, in this method the full diffraction pattern is calculated based on structural and instrumental parameters which are fitted to an experimentally obtained diffraction profile by the method of least squares [90, p.524]. In this section, a brief overview of the method is given, without diving too deep into the mathematics. A schematic illustration that lists the various parameters that may act as variables in the refinement is given in Figure 2-51. Furthermore, the figure describes some principles of the refinement, the type of information that can be obtained, as well as some challenges to consider.

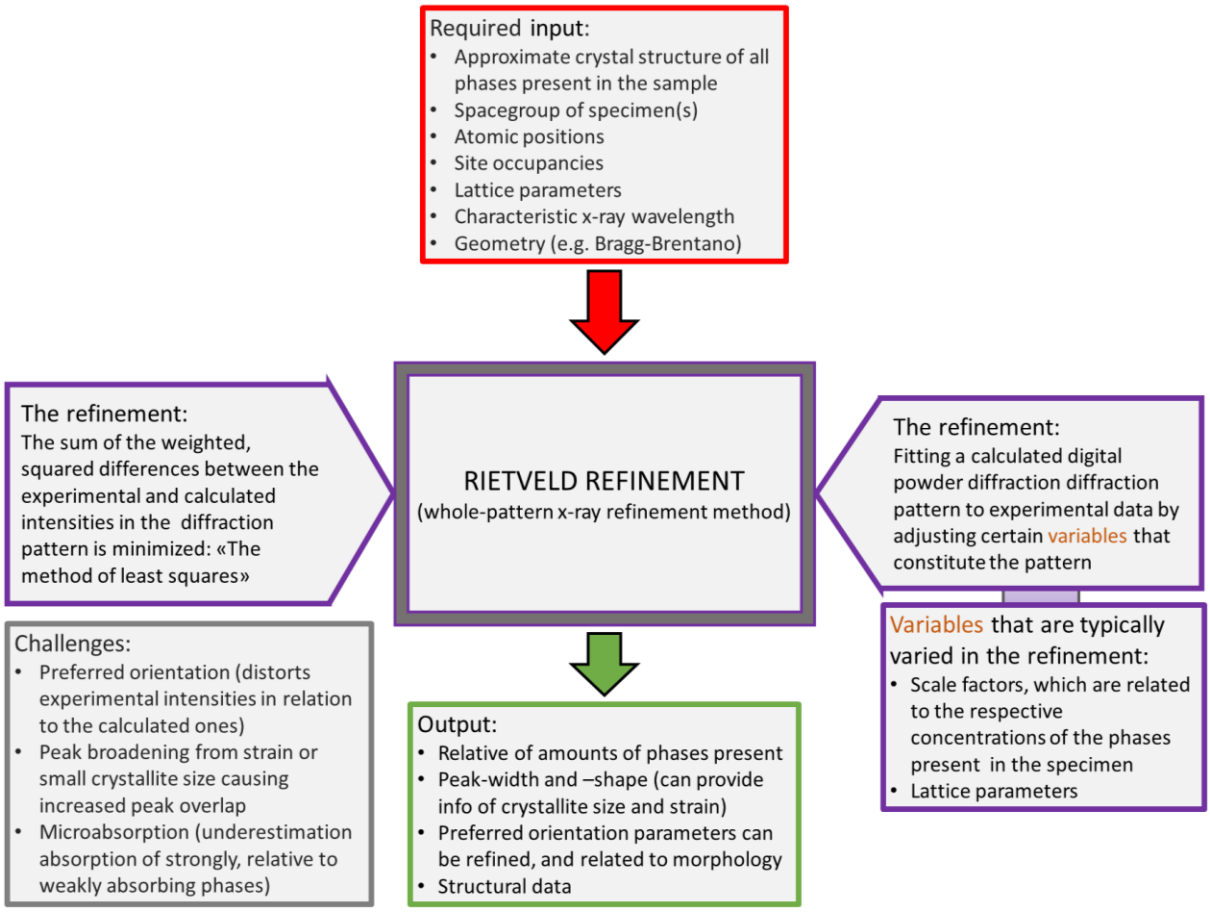

Figure 2-51: An overview of the Rietveld method. The upper red box indicate what parameters that are needed for the refinement, the purple boxes in the middle explain details about the refinement, the lower green box summarizes some important output data, and lastly the grey box on the lower left-hand side contains information of common challenges related to the method [86], [91, p.285-286].

The mathematical background for the Rietveld refinement is based on the least squares method. This requires a set of approximate starting values for the various variables, e.g. peak-shape parameters, unit cell dimensions, and atomic coordinates (and hence also the approximate space group). Further, the background, scale factors, atomic displacement parameters are examples of parameters that are refined, such that the calculated fit relative to the observed pattern converges to a global minimum. The approach is to refine the variables (parameters) that are chosen as free such that the difference between the experimental and calculated diffraction pattern is at minimum and approaches zero [90, p.524-526]. In the current work with focus on nanoparticles with very broad reflection profiles, a NIST Si-standard is used as a highly crystalline reference material to correct for *sample displacement*, and thereby assure determination of correct unit cell dimensions in the refinements.

Mathematically, the least squares method can be explained in terms of a *minimization function (ϕ)*:

$$\phi = \sum_{i=1}^{n} w_i \left(Y_i^{obs} - Y_i^{calc}\right)^2 \qquad \text{(Eq. 2.22)}$$

Y_i^{obs} and Y_i^{calc} is the experimental and calculated intensity at a point i in the diffraction pattern. The total number of experimental data points are given by the number *n*. The *weight* assigned to data point i is given by w_i [90, p.527-528].

3 Experimental

In this section, all the experimental procedures that have been used in this thesis is presented.

3.1 Chemicals Used in the Experimental Work of this Thesis

In Table 3-1 is an overview of all chemicals used in the current work listed. All chemicals were used as received.

Table 3-1: Overview of the chemicals that were used in the experiments in this thesis.

Chemical name and (CAS number)	Abbreviated designation	Chemical formula	Molar mass [g/mol]	Supplier	Purity [%]
Platinum(II) acetylacetonate (15170-57-7)	$Pt(acac)_2$	$Pt(C_5H_7O_2)_2$	393.29	Sigma Aldrich	97
Palladium(II) acetylacetonate (14024-61-4)	$Pd(acac)_2$	$Pd(C_5H_7O_2)_2$	304.64	Sigma Aldrich	99
Polyvinylpyrrolidone (9003-39-8)	PVP, (PVP10)	$(C_6H_9NO)_n$	10 000[1] 111.14[2]	Sigma Aldrich	—
Ethylene glycol (107-21-1)	EG	$HOCH_2CH_2OH$	62.07	Sigma Aldrich	99.8
1,4-Butanediol (110-63-4)	1,4-BD	$HO(CH_2)_4OH$	90.12	Sigma Aldrich	99
1,2-Butanediol (584-03-2)	1,2-BD	$CH_3CH_2CH(OH)CH_2OH$	90.12	Sigma Aldrich	98
1,3-Propanediol (504-63-2)	1,3-PD	$HO(CH_2)_3OH$	76.09	Sigma Aldrich	98
Argon	—	Ar	39.95	Praxair	99.999
Acetone (67-64-1)	—	CH_3COCH_3	58.08	VWR	—
Ethanol (64-17-5)	Et-OH	CH_3CH_2OH	46.07	VWR	—
Methanol (67-56-1)	Met-OH	CH_3OH	32.04	Sigma Aldrich	99.8
Chloroform (67-66-3)	—	$CHCl_3$	119.38	VWR	—
Reference Pt (catalyst)	—	—	—	Provided by YARA	—

[1]Average mol. mass; [2]Monomer

3.2 Synthesis of $Pt_{1-x}Pd_x$ NPs via the Polyol Heat-Up Method

All $Pt_{1-x}Pd_x$ ($0 \leq x \leq 1$) NPs in the current project were synthesized through a polyol process applying the heat-up method (sections 2.2.2).

In a typical synthesis, 20 mL solvent was first introduced into a three-neck 250 mL round flask with an automatic pipette. The metal precursors $Pt(acac)_2$ and $Pd(acac)_2$, as well as the capping agent PVP10 were then weighed out in the molar ratio metal/PVP of 1/10, and transferred to the round flask along with a small magnetic stirrer. Note that the PVP that was used had an average molecular mass of 10 000 g/mol, and is therefore referred to as *PVP10*. The molar ratio of metal and PVP10 is based on the number of moles of *monomer* of PVP. The number of moles of metal in the synthesis was kept at 0.2 mmol. A gas-adapter was connected to the round flask, supplying an Ar flow (0.2 atm) to maintain inert conditions. The temperature in the reaction mixture was monitored by a K-type *Fluke 54 II B* thermocouple inserted into a custom-made *glass liner*, located at a fixed position in the round flask during the reaction, Figure 3-1 (a and b). A close up of the thermocouple and the glass liner is provided in Figure 3-1 (c). The bent shape of the glass liner is introduced to give flexibility in how deep the thermocouple goes into the solution; i.e. at too shallow depth, the readout temperature would not display the true temperature in the solution.

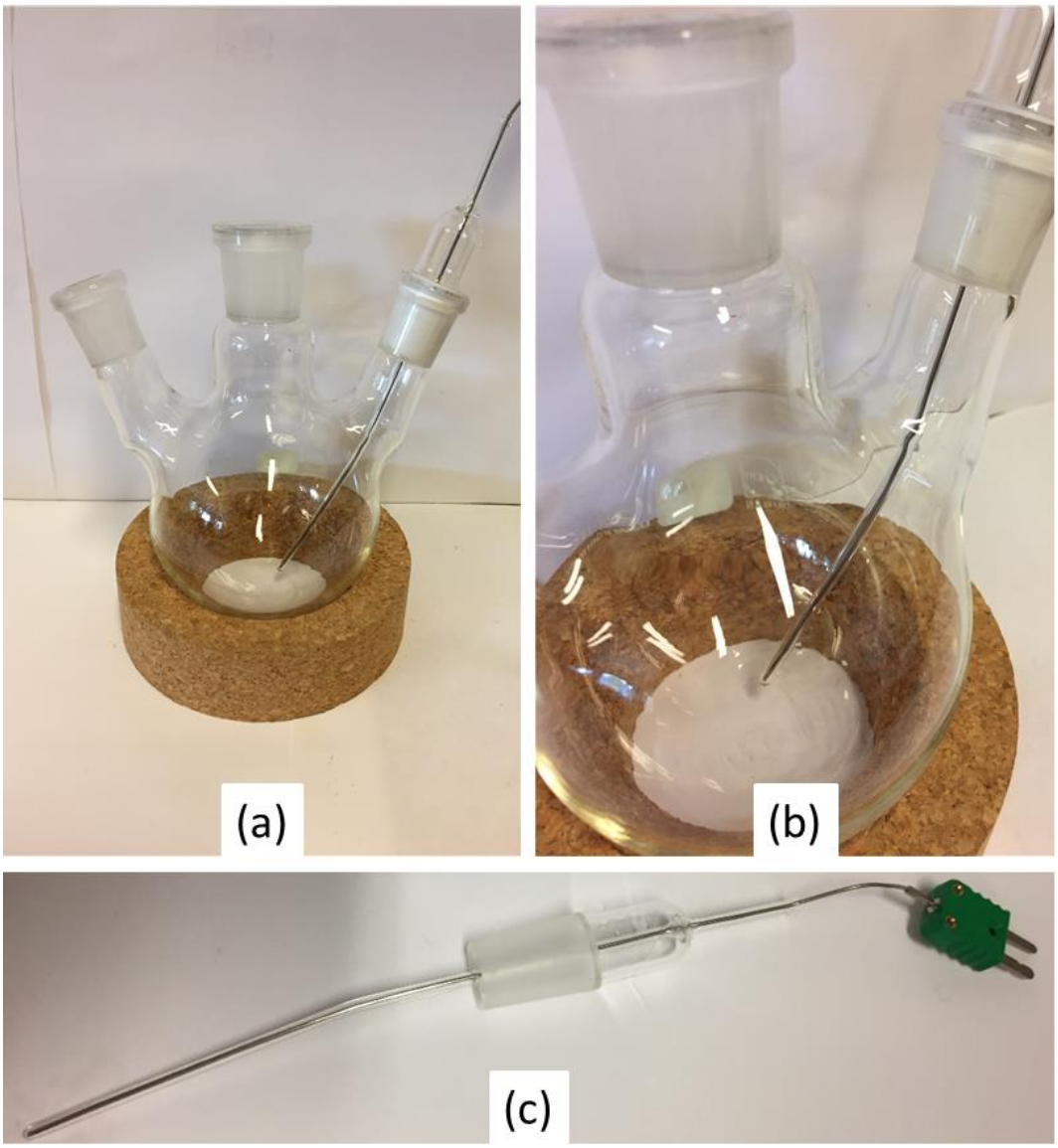

Figure 3-1: (a) Thermocouple with glass liner inserted in the three-neck round flask. (b) Close-up of bent thermocouple glass liner. (c) Showing only the glass liner. In all glass-to-glass connections Teflon tape was used to keep a secure seal and avoid friction.

The round flask was then placed on a heating block fixed on a *KIA RCT basic* heating plate pre-heated to 150°C, with stirring at 1500 rpm. To maintain stable temperature the glassware was isolated using quartz wool wrapped in aluminum foil, see Figure 3-2. The flask remained at 150°C for 15 minutes to outgas oxygen, evaporate water, and to thoroughly mix the reactants. This is in this thesis referred to as the *preheating step.*

After the preheating step, the round flask was transferred to a hotter (typically fixed at 220°C) heating block, and a 400-mm condenser was connected to avoid evaporation of the solvent (Figure 3-2). The reaction mixture remained at this higher temperature for a given time between

2 and 24 hours giving a viscous, dark brown colloidal suspension. The colloidal suspension was cooled to below 50°C before it was handled outside of the fume hood. The magnetic stirrer was then removed and the NP product was ready for the *washing procedure*, which was performed three times to wash away any residual compounds from the reaction, and to separate out the pure NP product. The washing procedure was done by first pouring ~3 mL colloidal suspension into six 15 mL sized centrifuge tubes. Flocculation was achieved by adding ~10 mL acetone to each of the tubes and shaking them well to homogenize the mixtures. After homogenizing, the tubes were centrifuged in an *Allegra X-22R* centrifuge (4500-9000 rpm; 5 minutes) to sediment the NPs. The NPs were thereafter separated from the eluent and the procedure was repeated two more times. If the further treatment of the NPs required them to be in the state of a stable suspension, they were re-dispersed in a suitable solvent (chloroform; ethanol; methanol; ethylene glycol).

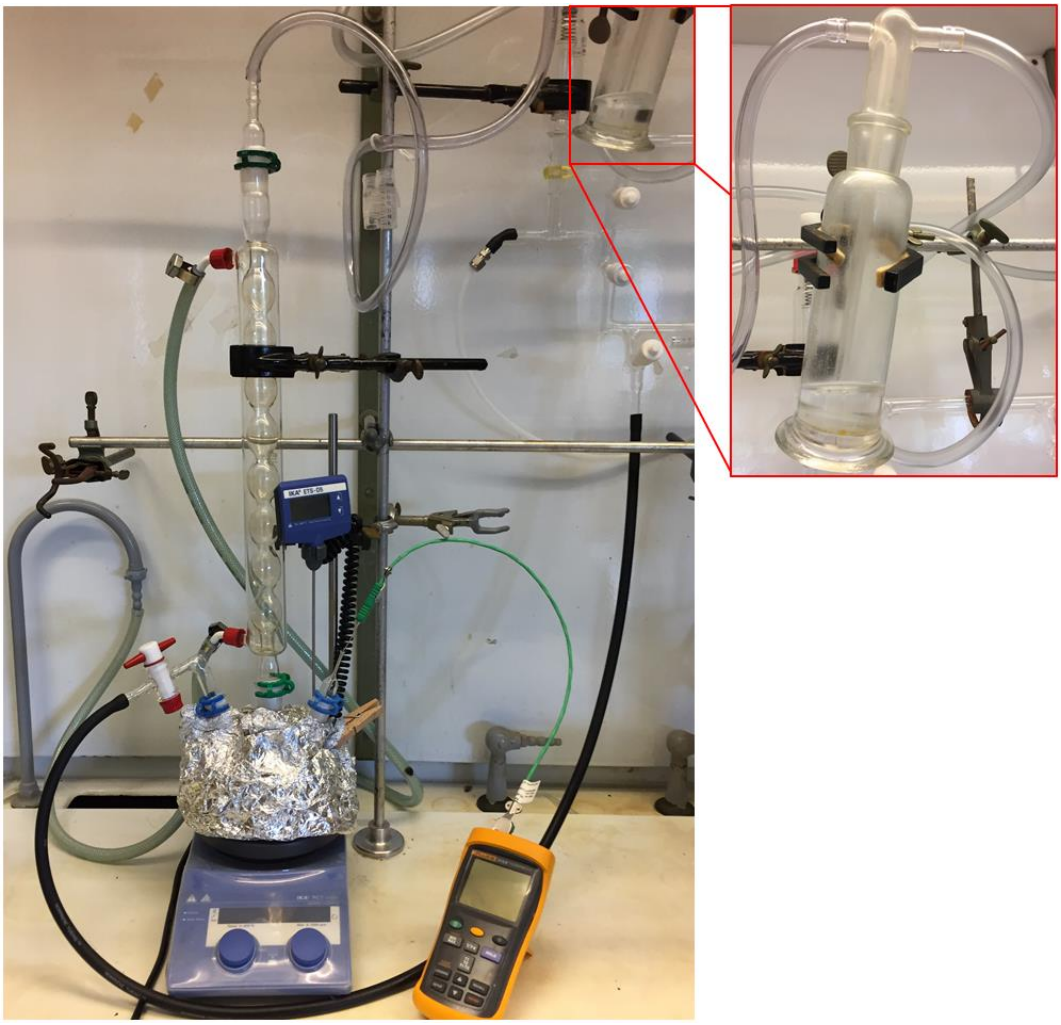

Figure 3-2: The synthesis setup during the reaction. In the preheating step, the condenser was not connected. The red insert is showing the bubbler which is used to visually see whether there are any leaks in the system.

3.3 Kinetics Experiments

The description of the procedural details regarding the kinetics experiments performed in the thesis is given in this section.

3.3.1 $Pt_{1-x}Pd_x$ Nanoparticle Formation Reaction Kinetics in 1,4-Butanediol – Standard Synthesis

The relative reduction kinetics of respectively $Pt(acac)_2$ and $Pd(acac)_2$ into Pt and Pd NPs and the propagation of $Pt_{1-x}Pd_x$ NP formation in 1,4-butanediol were investigated by means of some simple experiments. The experiments were conducted by performing the synthesis as outlined in section 3.2 either at 200 or 220°C as main reaction temperature. During the propagation of the reaction, small samples were withdrawn from the reaction mixtures at specific reaction times from the neck adjoining the thermocouple using a clean glass pipette. The small samples were photographed for examination of their colors at these time points, and the particle sizes were analyzed using SEM (see section 3.5.1). The same camera was used for taking all the pictures, and the ambient lighting was held constant. Typically, two paths were followed regarding collection of small samples from the reaction mixtures; see illustration in Figure 3-3.

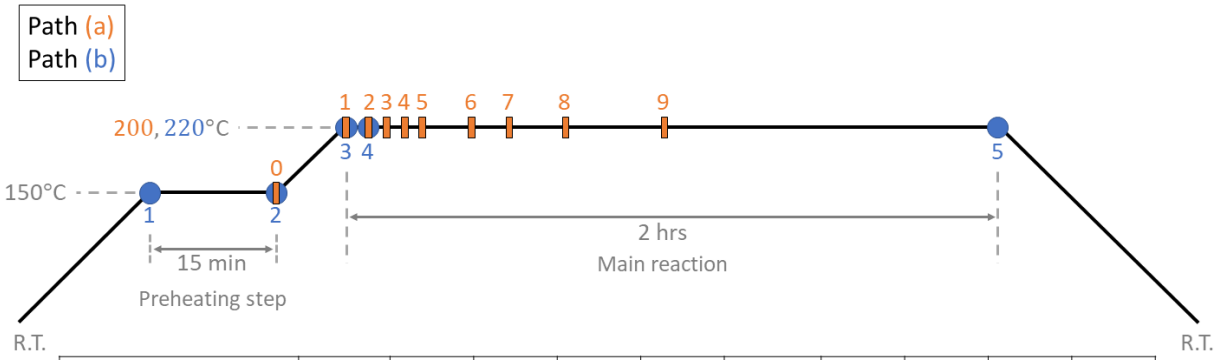

Sample	0	1	2	3	4	5	6	7	8	9
Synthesis step (a)	Preheat	Main reaction								
Reaction time (a) [mm:ss]	15:00	00:00	03:30	06:00	10:00	15:00	22:30	30:00	40:00	55:00
Synthesis step (b)		Preheat		Main reaction						
Reaction time (b) [mm:ss]		00:00	15:00	00:00	10:00	120:00				

Figure 3-3: Schematic illustration of sample collection strategy (a) and (b). The nine orange and five blue points refer to the samples collected during path (a) and (b) respectively.

3.3.2 Tuning the Reduction Kinetics of $Pt(acac)_2$ and $Pd(acac)_2$

The effect of synthesis parameters such as type of polyalcohol and metal precursor/PVP molar ratio have on the reduction reaction- and NP formation- kinetics of $Pt(acac)_2$ and $Pd(acac)_2$ were explored in detail following the concept described in section 3.3.1. Small samples from the synthesis batch were pulled out and subsequently analyzed with respect to color and nanoparticle size distribution. The experiments were designed in such a way that each parameter was explored for both $Pt(acac)_2$ and $Pd(acac)_2$ individually. Small modifications to the polyol heat-up method as it is reported in section 3.2 with respect to the choice of preheating temperature and at what point in the procedure the metal salt was dissolved were implemented. Relevant details regarding these experiments are listed in Table 3-2.

To know at which temperature the reduction of the metal precursor started, each experiment was performed twice. In the first run the temperature was increased with large increments to map very approximately at what temperature the color change would appear. The second experiment was performed more carefully, increasing the temperature with smaller increments to get a better resolution in the change of color with respect to temperature. This is illustrated schematically in Figure 3-4. An important aspect to consider in this set-up was also the elapsed *time* between each sample that was pulled. It was kept fairly constant between each experiment.

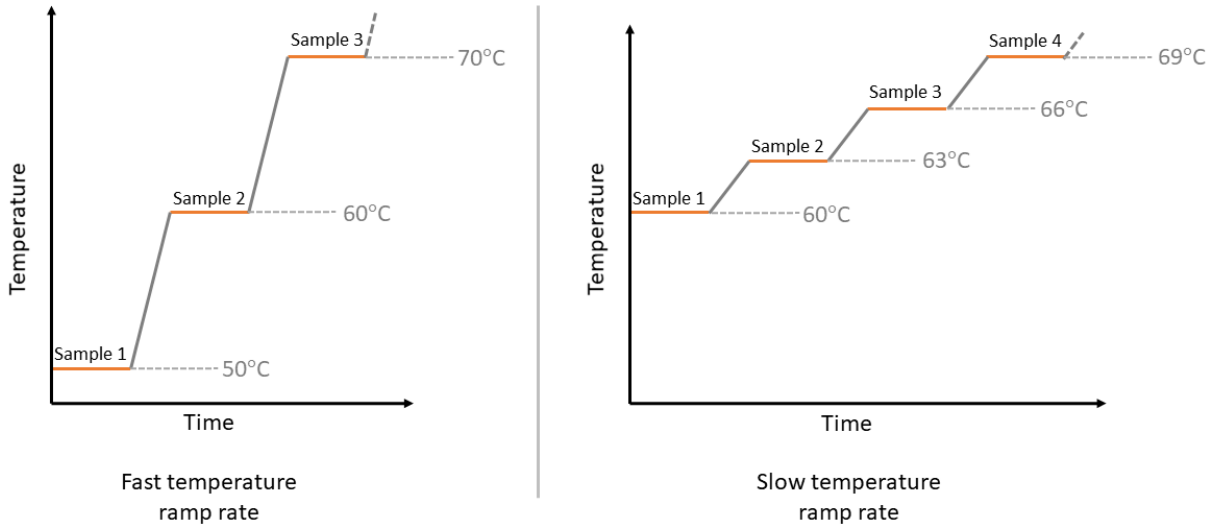

Figure 3-4: The experiment with fast a temperature ramp rate was performed with a resolution of 10°C (left panel), whereas the one with a slow ramp rate was done with a resolution of 3°C (right panel).

The experimental details regarding the procedure described in this sub-section are given in Table 3-2.

Table 3-2: Experimental details from the experiments for tuning the kinetics of $Pt(acac)_2$ and $Pd(acac)_2$.

Nominal comp.	$Pt(acac)_2$/ [mg]	$Pd(acac)_2$/ [mg]	PVP10/ [mg]	Type of solvent	Solvent/ [mL]	T_{pre}/ [°C]	t_{pre}/ [min]	No. of samples[2]
Pure Pd[1]	—	61	222	EG	20	120	15	17
Pure Pt[1]	79	—	222	EG	20	120	15	15
Pure Pd[1]	—	61	2223	EG	20	120	15	9
Pure Pt[1]	79	—	2223	EG	20	120	15	12
Pure Pd[3]	—	61	222	1,4-BD	20	150	15	14
Pure Pt[3]	79	—	222	1,4-BD	20	150	15	23
Pure Pd[1]	—	61	2223	1,4-BD	20	150	15	13
Pure Pt[1]	79	—	2223	1,4-BD	20	150	15	14
Pure Pd	—	61	222	1,2-BD	20	150	15	13
Pure Pt[1]	79	—	221	1,2-BD	20	150	15	14
Pure Pd	—	61	222	1,3-PD	20	120	15	13
Pure Pt	79	—	222	1,3-PD	20	120	15	18

[1] Experiment repeated with large and small temperature increments

[2] Withdrawn from the solution in the experiment with small temperature increments

[3]Did not need experiment with large temp. increments, because of previous experiences with the system

3.4 Modified $Pt_{1-x}Pd_x$ Polyol Synthesis

During the propagation of the project attempts were made to manipulate the element distribution of NPs with nominal composition $Pt_{0.50}Pd_{0.50}$ to promote Pt@Pd core@shell rather than Pd@Pt. The strategy was to first synthesize Pt-core NPs, followed by growth of the Pd-shell on the cores. The procedure was inspired by the works of Long et al. [92].

Five experiments (M1-5) were done containing three sequences, and the details regarding each of these are summarized in Table 3-3.

Preparation of Pt Core-Nanoparticles (Sequence 1)

The Pt-core was first synthesized following the standard polyol route (section 3.2), except half the amounts of reactants were used, maintaining the same concentrations. After the 2 h reaction time had passed, the dark brown Pt suspension was cooled to below 50°C with continuous stirring at 1500 rpm.

Preparation of Pd Precursor Solution (Sequence 2)

First 10 mL 1,4-butanediol with 1 mmol PVP10 were mixed and heated following the preheating step in the standard polyol method (3.2). After this step, the solution was cooled to below 50°C before 0.1 mmol $Pd(acac)_2$ was added. To homogenize the solution, it was stirred for 20 min at 1500 rpm.

Preparation of Pt@Pd Core@Shell Nanoparticles (Sequence 3)

To form the Pd-shell, the solution of $Pd(acac)_2$ was introduced into the colloidal suspension of Pt NPs, followed by heating up the system again to temperatures between 70-220°C for precipitating Pd. The reaction time in the Pd growth-step was varied between 2 and 6 hours. A schematic illustration of the reaction conditions for the five experiments is presented in Figure 3-5.

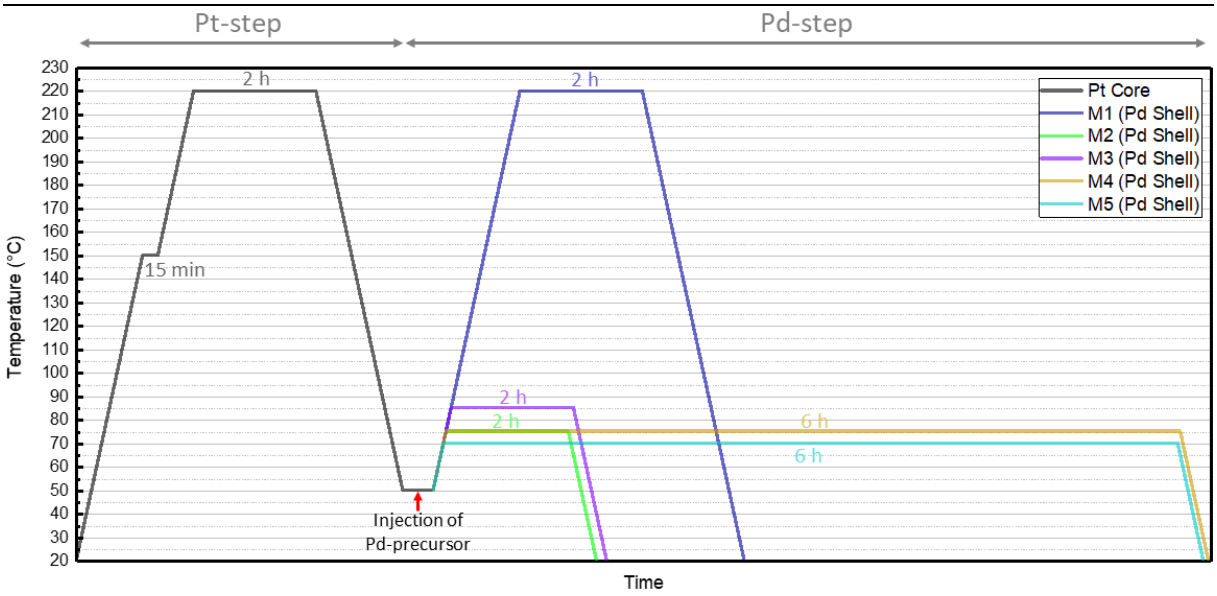

Figure 3-5: Schematic illustration of reaction conditions in the modified $Pt_{1-x}Pd_x$ polyol synthesis. The gray line to the left (Pt-step) shows the conditions for production of the Pt core of the Pt-Pd NPs. The colored lines on the right-hand side (Pd-step) refer to the various conditions used for producing the Pd shell.

The experimental details concerning the experiments in this sub-section are listed in Table 3-3.

Table 3-3: Overview of the experimental details regarding the modified $Pt_{1-x}Pd_x$ polyol synthesis. T_{rxn} refers to the reaction temperature in main-step of the syntheses, and t_{rxn} is the dwell time in this step.

Component	$Pt(acac)_2$ [mg]	$Pd(acac)_2$ [mg]	PVP10 [mg]	1,4-BD [mL]	T_{rxn} [°C]	t_{rxn} [hrs]
Pt-core	39	—	111	10	220	2
Pd-shell	—	31	111	10	70, 75, 85, 220	2, 6

3.5 Characterization

Several characterization techniques were used throughout this thesis. The technical details regarding instrumentation as well as sample preparation is described in this section.

3.5.1 Electron Microscopy

Many samples were analyzed with SEM, STEM and TEM throughout the work of this thesis, and the sample preparation procedure of these samples, is described in this section.

A typical sample for electron microscopy was prepared by diluting washed NPs in either chloroform, ethanol, methanol or ethylene glycol, followed by sonication (1-5 min). A drop of the homogeneous suspension was then put on a carbon coated copper grid (holey carbon, 300 square mesh) from Innovative Microscopy Supplies. This technique was used for SEM- and TEM-samples. Sample grids containing Pd were put in a glove box to dry.

Scanning Electron Microscopy

The SEM-instrument that was used was of the type Hitachi SU8230 Ultra High Resolution Cold FE-SEM (Figure 3-6). Typically, the STEM-detector was used for the samples in this thesis, but in some cases also the SE-detector. Plasma cleaning (30 sec; 20 watt) of the samples was done prior to measurement to minimize carbon contamination during measurement.

Figure 3-6: HITACHI SU8230 Ultra High Resolution Cold FE-SEM that was used in this thesis.

NP-Size Measurements

The procedure that was employed for measuring the size of NPs in this thesis, is described in this section.

A software called imageJ [93] was used to analyze electron microscopy images of NP samples to measure the particle sizes. The images that are analyzed with this software must have a *scalebar*, as shown at point *A* in Figure 3-7. The scalebar was measured such that the program could calculate the number of pixels corresponding to the real distance in nanometers. In this way, a line drawn in the program could measure the NP-sizes. The particles were measured individually. In the measurement of a particle, the line was drawn over its largest extension. This is illustrated at point *B* in the figure. Particles that were very overlapping were not measured.

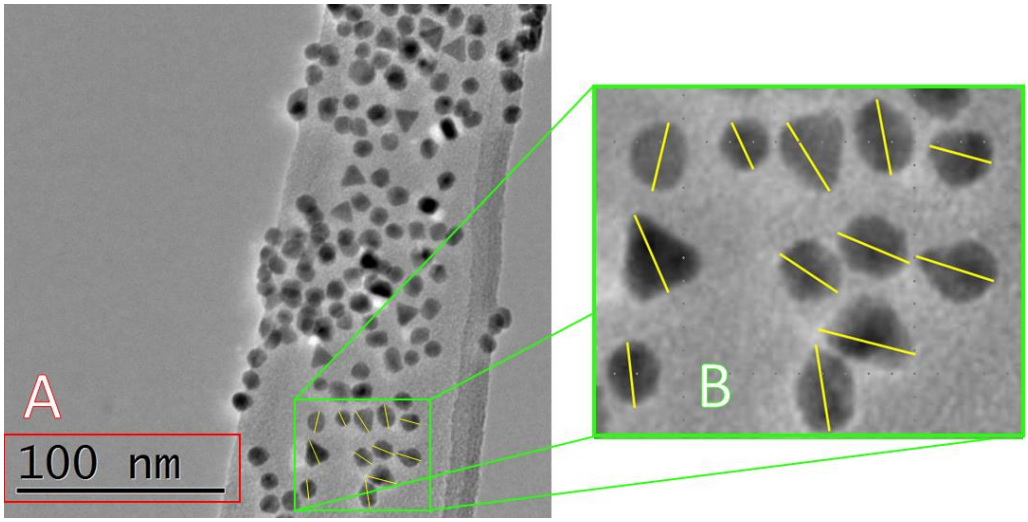

Figure 3-7: Illustration of particle size measurements. Note that this figure is made for illustrative purposes only, and is not from an actual measurement. The accuracy in the positioning of the yellow lines seen here is not representative of the measured samples in this thesis.

When particle sizes are reported by the measurements that are performed in this thesis, the notation is $\overline{D} = \pm 1\sigma$, where $\overline{D}$ is the average largest extension of the particles and σ is the standard deviation.

Histograms were made based on the SEM- and TEM-images. For the SEM-images, each of the recorded histograms are based on a dataset of only 50 NPs. In the case of the TEM-images, the number of measured particles were 250. The number of bins in the histogram is equal to the nearest integer of $\sqrt{n}$, where n is the number of particles measured.

Transmission Electron Microscopy

Two different TEM instruments have been used in this work.

A Jeol 2100F TEM operating at an acceleration voltage of 200 kV was used for the HAADF-STEM, TEM and EDX elemental mapping characterization techniques used in this thesis. This applies to the results in section 4.3 and 4.4.1. The EDX elemental mapping was performed with the software AZtec [94].

A Jeol JEM-ARM200F double C_s-corrected TEM equipped with a FEG, a STEM unit and an HAADF detector was used at acceleration voltage of 200 kV for HAADF-STEM-EDX analysis. This TEM was used to obtain the results in section 4.2.2. Samples on TEM grids were plasma cleaned for 45 s using a Gatan Solarus model 950 plasma cleaner at 25 W under 20 sccm Ar.

3.5.2 Powder X-ray Diffraction

Powder XRD was used in this thesis for determination of the cubic unit cell dimensions, i.e. the a-axis, for the current nanoparticle samples. In the preparation of the XRD sample, colloidal NPs (dispersed in ethanol) were transferred to a small mortar and a small portion of a Si NIST standard was added. This mixture was finely ground. During this procedure some of the solvent will evaporate, thereby concentrating the suspension. The suspension was thereafter transferred to a single crystal Si sample holder, and dispersed evenly as a thin layer of the surface.

The adopted experimental conditions for the powder XRD-measurements are given in Table 3-4. A Ge (111) monochromator was used in combination with the copper anode, assuring only monochromatic Cu $K_{\alpha 1}$radiation, 1.5406 Å. Two measurement series were carried out in line using the exact same sample and sample holder without any physical manipulation. The measurement parameters for the first run was optimized for small nanoparticles, whereas the second run was optimized for measuring the XRD profile of the highly crystalline Si NIST standard. The unit cell dimension for the Si standard was 5.43086.

Table 3-4: Conditions for powder XRD-measurements in this thesis.

Run optimized for:	Step size [°]	Time per step [s]	2θ scan range [°]	Anode (Cu $K_{\alpha 1}$) wavelength [Å]
NIST standard (Si)	0.016	19.20	30-95	1.54060
Nanoparticles	0.100	1152.00		

The instrument used was a Bruker D8 Discover, and has Bragg-Brentano geometry.

Determination of the unit cell dimensions (a-axis for the cubic NPs) was done by means of the Rietveld method (section 2.5.2), using the TOPAS [95] software package for refinements.

The following input parameters were required for the TOPAS refinements:

- X-ray wavelength
- File containing information about diffractometer and detector
- Approximate values of a-axis, space groups, atomic coordinates (for Pt and Pd)
- Peak shape function and useful starting values for its free variables

In TOPAS, the following parameters were refined according to the Rietveld method: a-axis, particle size, background, height displacement and zero point error. The height displacement and zero point error for a given NP sample was kept constant during the refinement, and to the exact values obtained in the parallel measurement for the Si NIST standard.

The uncertainties calculated by the program reflect *mathematical* uncertainty associated with counting statistics and the least square approach. It is established in our research group that this number needs to be multiplied by a factor of 4 to reflect the real uncertainty.

Synchrotron X-ray Diffraction

Powder XRD patterns were measured at the Swiss-Norwegian Beamline BM31 at the European Synchrotron Radiation Facility in Grenoble, France. $Pt_{1-x}Pd_x$ samples (NP powder) were packed in sealed borosilicate glass capillaries (diameter 0.5 mm). The capillaries were rotated during measurement.

The wavelength in the experiments was 0.50277 Å as determined from a Si powder calibrant. A 2D Mar345 image plate detector was used. The 2D data were integrated by using the PyFAI software. The instrumental background as well as the background scattering from the capillary was measured, and subtracted during the subsequent data analysis.

The whole powder pattern fitting (WPPF) method was used in order to reveal structural details of the measured samples. All WPPF calculations were done by using the Discus software [96] and the refinements used the evolutionary algorithm incorporated in Diffev program [96]. The following parameters were varied in the refinement of the crystal structure the nanoparticles: unit cell dimensions, temperature displacement factors, composition, Pt/Pd atom substitution and distribution, and anisotropic particle size. Possible stacking faults and the nanoparticle size distribution were also considered.

The model used in the refinement assumed ellipsoidal particle shape, Gaussian distribution of particle sizes and stacking faults along [111] in the cubic unit cell.

3.6 Preparation of 1 wt.% $Pt_{1-x}Pd_x/Al_2O_3$ and $Pt_{1-x}Rh_x/Al_2O_3$ Catalysts

Three catalysts were prepared by a postdoc in our research group with selected members of $Pt_{1-x}Pd_x/Al_2O_3$ with a metal loading of 1 wt.% noble metal on **γ**-alumina. A reference Pt/Al_2O_3 catalyst (Pt bought from Sigma-Aldrich) was also prepared. The steps involved in the production of these are described in this section, and summarized in Figure 3-8.

Free standing $Pt_{1-x}Pd_x$ NPs were first synthesized via our standard polyol synthesis (section 3.2) and re-dispersed in chloroform. A yield of 70% was assumed, with losses through e.g. the washing procedure and not full conversion of precursor to product. The 30% product loss was compensated for to reach the targeted metal loading of 1 wt.% on alumina.

As-received boehmite was heat treated in an alumina crucible for 4 hours at 800°C in air to convert it to γ-Al_2O_3 (70-90 m^2/g). In the next step, the support material was dispersed by mixing with chloroform followed by sonication (60 min).

Following this, the NPs were deposited on the γ-Al_2O_3 by mixing the nanoparticle suspension with the alumina-suspension with stirring (48 hours) in a sealed container. After mixing, the solvent was evaporated in room temperature, yielding a grey powder of NPs/γ-Al_2O_3.

The NPs/γ-Al_2O_3 powder was then transferred to an alumina crucible and calcined in a fixed bed furnace at 400°C for 10 hours in an atmosphere of air to remove organic compounds.

Before catalytic testing of the $Pt_{1-x}Pd_x/Al_2O_3$ and $Pt_{1-x}Rh_x/Al_2O_3$ catalysts were performed, the respective catalyst powders were pressed into tablets and grained into granules of 0.2-0.4 mm in size.

A schematic illustration of the procedure is given as a flow-diagram in Figure 3-8.

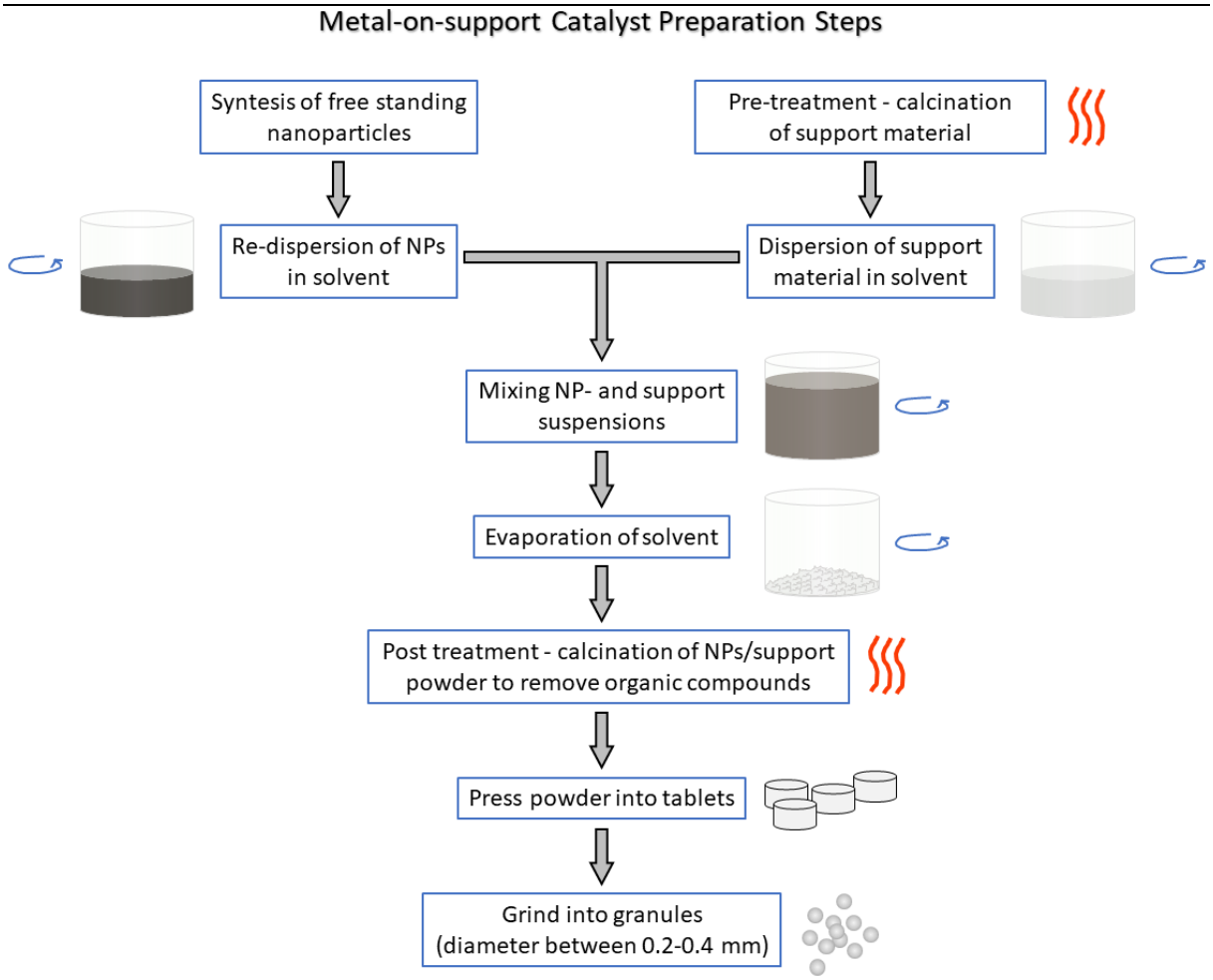

Figure 3-8: Schematic illustration of the procedure for producing a metal-on-support catalyst by deposition of free standing nanoparticles that is followed in this thesis. The blue arrows indicate that stirring was performed in the respective step.

3.7 Catalyst Testing

The catalytic testing of the $Pt_{1-x}Pd_x/Al_2O_3$ catalysts were performed by YARA International, Herøya.

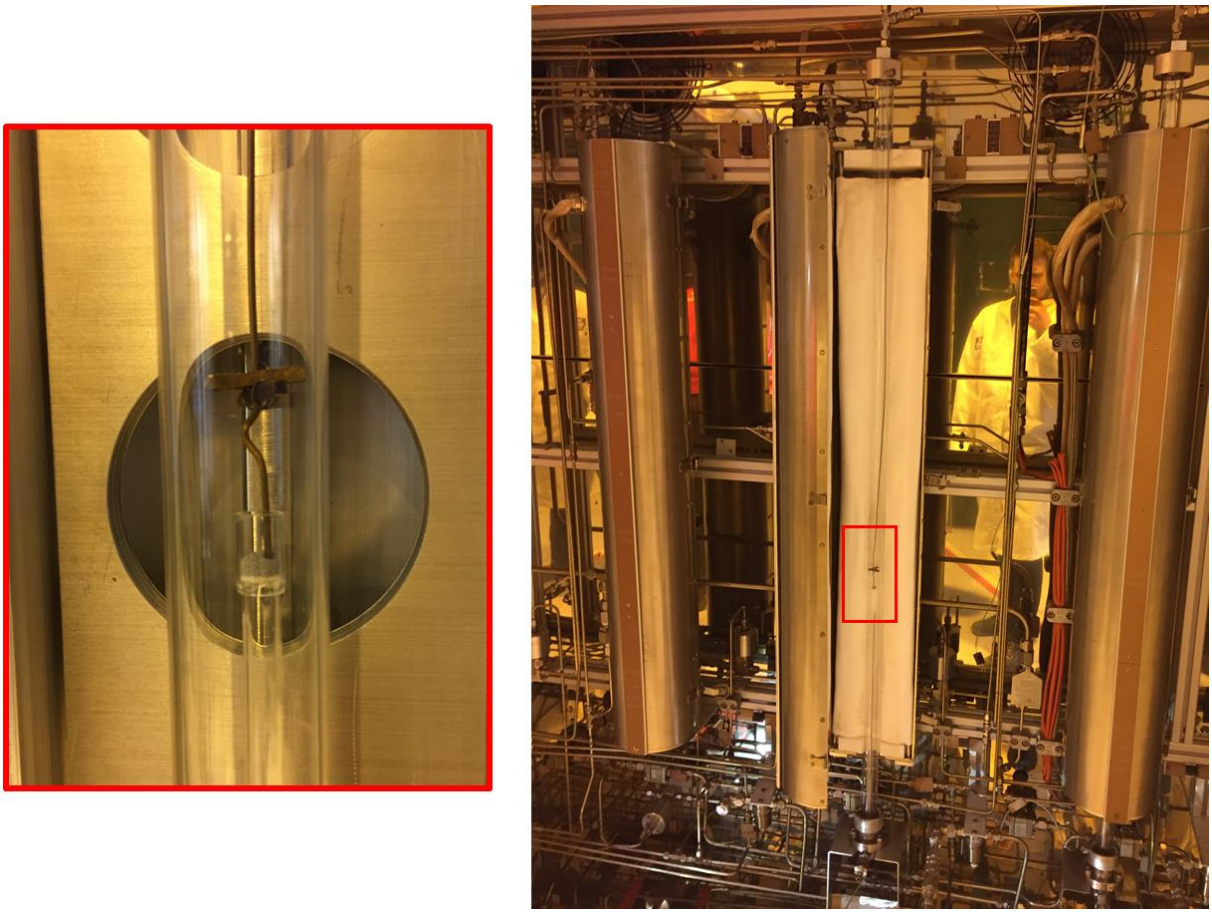

Figure 3-9: The catalytic testing reactor at YARA. In the image on the left-hand side is the sample shown in close-up. The image to the right shows how the quartz reactor is connected to the system supplying gas flow. The sample is also indicated in a red square in this image.

Activity-selectivity tests of the $Pt_{1-x}Pd_x/Al_2O_3$ catalysts for the intermediate temperature NH_3 oxidation reaction were performed in a quartz tubular fixed bed reactor with inner diameter of 8 mm and 4 mm bed height (Figure 3-9). Typically, 0.110-0.150 g catalyst (grain size 0.2-0.4 mm) was used in each experiment (see Table 3-5 for details). Effluent was analyzed with respect to NH_3, NO, NO_2 and N_2O using IR spectroscopy (Quantum Cascade Laser (QCL) technology). N_2 formed during the oxidation process was calculated with basis in analyzed quantities of the other N-based species in the effluent [$N_2 = (NH_{3,in} - NH_{3,out} - NO_{out} - NO_{2,out} - 2\times N_2O_{out})/2$].

The gas flow rate was 4.2 NL/min (GHSV = 1 260 000 h^{-1}, 20 ºC and 1 atm) and gas composition 95% N_2, 5% O_2 and 450 ppm NH_3. The temperature program applied in the experiments is shown in Figure 3-10.

The turnover frequency is identified as the number of reactant molecules (NH_3) converted to products over one active site per second. In this study each Pt/Pd atom on the outer surface of the $Pt_{1-x}Pd_x$ nanoparticles are considered as one active site. Experimental input needed for calculating the number of active sites are nanoparticle size and quantity of noble metal on the catalyst. Details connected to the calculations are given in the theory section.

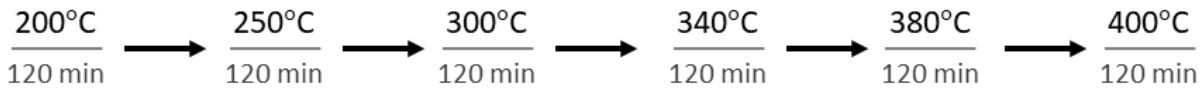

Figure 3-10: Temperature program for catalyst testing at YARA, showing temperature at each step and dwell time.

Table 3-5: Masses of the $Pt_{1-x}Pd_x/Al_2O_3$ (x = 0, 0.10, 0.50) catalysts prepared in-house, and reference catalyst supplied from Sigma-Aldrich that were used in the catalytic testing.

Pt/Al_2O_3 [g]	$Pt_{0.90}Pd_{0.10}/Al_2O_3$ [g]	$Pt_{0.50}Pd_{0.50}/Al_2O_3$ [g]	(Ref.) Pt/Al_2O_3 [g]
0.1330	0.1445	0.1398	0.1131

4 Results

In this chapter, all of the results gathered throughout the thesis are presented.

4.1 Synthesis of $Pt_{1-x}Pd_x$ Nanoparticles

The thesis work was initiated by starting out to synthesize some selected PtPd based NPs with nominal composition $Pt_{1-x}Pd_x$ (x = 0; 0.25; 0.50; 0.75; 1) adopting our standard polyol protocol described in section 3.2. Table 4-1 gives an overview of nominal compositions synthesized.

All synthesized samples were analyzed by means of PXRD and the obtained powder X-ray diffractograms are reported in Figure 4-1.

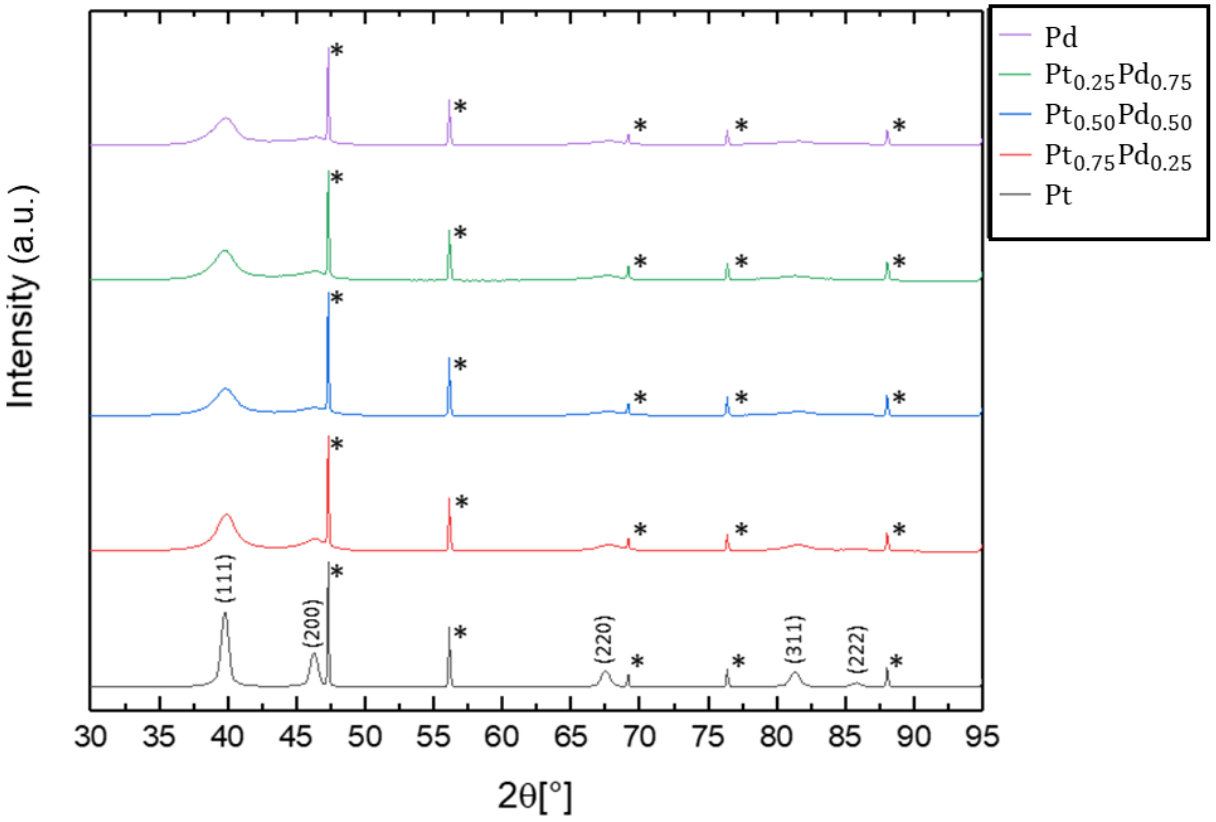

Figure 4-1: PXRD diffractograms of the $Pt_{1-x}Pd_x$ (x = 0, 0.25, 0.50, 0.75, 1.00) NP-samples. The star-markings refers to the signal originating from the silicon reference. Diffraction peaks originating from the PtPd NPs are assigned with Miller indices corresponding to a ccp type structure.

Careful inspection of the diffractograms show that all samples are phase pure, containing a single-phase crystallizing with a cubic close packed structure (ccp) due to the presence of only the (111), (200), (220), (311) and (222) hkl-planes. Finding the $Pt_{1-x}Pd_x$ NPs to take a ccp

structure is expected as the two end members Pt and Pd are reported to be ccp [35],[34]. The difference in intensity between the obtained diffractograms of the various samples may be due to variations in sample preparation quality (e.g. more sample present yielding higher intensity). It is also noted that the pure Pt NPs give less peak broadening than the bimetallic compositions and pure Pd. This can indicate differences in particle size and/or other effects causing strain in the lattice.

For more careful PXRD analysis, the unit cell dimension (a-axis) was refined for all samples using TOPAS software [95] following the procedure described in detail in section 3.5.2.

As a start, the powder diffractograms obtained for the end members Pt and Pd were refined. The refinements gave a = 3.9228 $\pm$0.0009 Å and a = 3.928 $\pm$0.004 Å for Pt and Pd, respectively. Corresponding bulk values of Pt and Pd are 3.9242 Å [35] and 3.8907 Å [34]. For comparison, Bundli [13] and Papa et al. [23] found the a-axis of Pt NPs synthesized via the polyol route to be 3.92 Å (NP size = 16 $\pm$5 nm) and 3.917 Å (NP size = 4.9 nm), respectively, which is in line with our findings. In contrast, Teranishi et al. [42] report the a-axis of Pt to be in the range 3.9157 – 3.9366 Å depending on particle size (see Table 1-3, section 1.4). In the case of Pd, no studies are reported on a-axis determinations of NPs obtained by the polyol route, but Pd NPs are reported to be in the range 3.90-3.98 Å, depending on the particle size (see Table 1-3, section 1.4) [43],[44],[45]. Our results fall into the reported range of obtained a-axis values of NPs, but we do not find the expected trend valid for corresponding bulk materials; i.e. that Pt is expected to have a slightly larger a-axis than Pd.

The remaining bimetallic samples were analyzed following two approaches for calculating the a-axes in the NPs; (a) assuming that only a single phase (Pt-Pd solid solution) was present in the NPs, (b) assuming two phases (Pt and Pd, respectively) as a basis for the calculations. Both strategies were tested as our a-axis values of Pt and Pd were found to be very similar (see above) and the extensive peak broadening would not allow us to easily identify distinct peak splitting in case the scenario of a two-phase mixture was valid (b). The results from the Rietveld refinements of the bimetallic compositions showed that the two-phase scenario is not statistically valid and was therefore rejected for further analysis.

The a-axis values obtained from approach (a) are included in Table 4-1. From Table 4-1 it becomes clear that the refinements of the PXRD data are not very sensitive to monitor compositional changes in the $Pt_{1-x}Pd_x$ NPs. Within uncertainty the a-axis for the various

nominal compositions are similar. No reported a-axis values were found for bimetallic PtPd NPs; therefore, we are unable to evaluate our findings in view of literature.

With basis in the alarming spread in reported a-axis values for Pd NPs together with the non-conclusive trend obtained for the bimetallic PtPd compositions, a more elaborated discussion on PXRD analysis of metallic NPs will begiven in section 5.

Table 4-1: All of the experiments performed in this sub-chapter. XRD results: The a-axes are shown for the Pt and Pd separately (assuming both these two phases exist in the sample), and the resulting a-axes found by assuming only one phase (Pt-Pd) is present. The uncertainties given here are only the mathematical uncertainty originating from the refinement.

Nominal composition	**Experimental details**		**XRD (single phase)**
	$Pt(acac)_2$ [mg]	$Pd(acac)_2$ [mg]	a-axis [Å]
Pt	79	—	3.9228 ±0.0009
$Pt_{0.75}Pd_{0.25}$	59	15	3.915 ±0.003
$Pt_{0.50}Pd_{0.50}$	39	31	3.920 ±0.004
$Pt_{0.25}Pd_{0.75}$	20	46	3.928 ±0.004
Pd	—	61	3.928 ±0.004

4.2 Kinetics of the Precursors $Pt(acac)_2$ and $Pd(acac)_2$ in the Polyol Synthesis

Our initial results with basis in x-ray diffraction analysis of selected members in the series $Pt_{1-x}Pd_x$ NPs (section 4.1) indicated lack of formation of a Pt-Pd solid solution. Based on this, we decided to explore the reactivity of $Pt(acac)_2$ and $Pd(acac)_2$ toward NP formation in more detail by studying relative color changes of the suspensions during the propagation of the reaction in combination with evaluation of nanoparticle formation by means of SEM imaging. Change in color of the suspension is taken as the signature of that the metal precursor is reduced and nucleation and growth of NPs take place. See experimental details in section 3.3.1.

4.2.1 $Pt_{1-x}Pd_x$ Nanoparticle Formation Reaction Kinetics in 1,4-Butanediol - Standard Synthesis

As a start two experiments were performed to demonstrate the difference in reactivity of $Pt(acac)_2$ and $Pd(acac)_2$ in 1,4-butanediol. Two individual syntheses of pure Pt and Pd NPs were thus conducted at standard conditions (0.2 mmol metal; metal/PVP = 1/10; 20 mL 1,4-butanediol) with one exception: The temperature of the main step was set to 200°C rather than 220°C as it could potentially lead to a higher temporal resolution in the color changes, enabling easier differentiation between the kinetics of the two precursors. Samples were taken out at different *time points (0-9)* during the course of the reaction; see Figure 4-2.

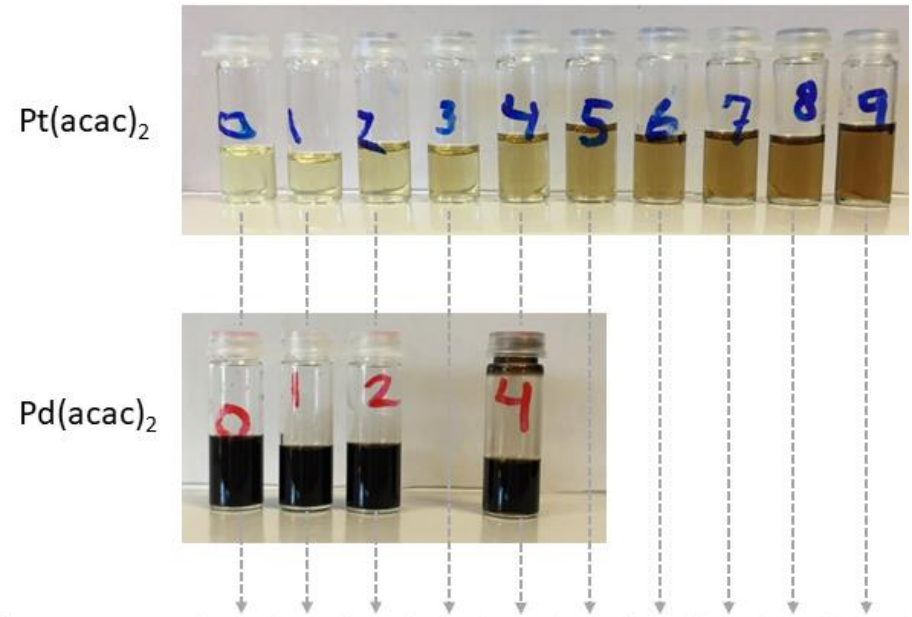

Sample	0	1	2	3	4	5	6	7	8	9
Time [min.]	15.0	0.0	3.5	6.0	10.0	15.0	22.5	30.0	40.0	55.0
Temperature [°C]	150	200	200	200	200	200	200	200	200	200

Figure 4-2: Color change at different time points (0-9) during the reaction of $Pt(acac)_2$ to form Pt NPs (top) and $Pd(acac)_2$ to form Pd NPs (bottom). The *Time* refers to the time passed after reaching the indicated temperature.

The results clearly document that the reactivity of the two metal precursors in 1,4-butanediol is very different. The color of the $Pt(acac)_2$ solution shown in Figure 4-2 is changing *gradually* from the color of unreacted precursor in solution which has been at 150°C for 15 minutes (*sample 0*), through the samples, until 55 minutes into the reduction reaction at 200°C (*sample 9*). It can be seen from this figure that the change in color appears approximately in *sample 2-3,* indicating that particles start to form in a visible quantity after dwelling 3-4 minutes at the targeted reaction temperature of 200°C. On the other hand, in the case of the $Pd(acac)_2$ solution, it is visually fully transformed to a blackish state already at the end of the preheating temperature of 150°C.

In order to document that the change in color is the signature of NP formation, and to roughly *map at what time* this took place, *three more experiments were conducted* using standard synthesis condition at 220°C. These experiments consisted of three respective syntheses of NPs with different nominal compositions; Pd, $Pt_{0.50}Pd_{0.50}$ and Pt. According to the procedure described in section 3.3.1, samples for STEM-images were taken out at five time points (P1-5). In Figure 4-3 Figure 4-4, Figure 4-5 and Figure 4-6 are representative STEM-images with their corresponding histograms for Pd, $Pt_{0.50}Pd_{0.50}$, and Pt at the different time points of the synthesis reported. For facilitating the comparison of NP formation for the three compositions, the mean particle size of each composition including the particle size distribution is plotted versus time point in Figure 4-7. By comparing the obtained STEM-images from the three syntheses and the color experiments described above, it became evident that the reaction kinetics of $Pd(acac)_2$ is significantly faster than that of $Pt(acac)_2$. The STEM-images shows clearly that when only the $Pd(acac)_2$ precursor is used, fully developed NPs (~10-11 nm) was observed already at the beginning of the preheating step at 150°C. In the case where only the $Pt(acac)_2$ precursor was used, no observable NP formation took place before at the end of the preheating step. These nanoparticles were about 4 nm and they reached full size first at approximately 2 h reaction time at 220°C. The $Pt_{0.50}Pd_{0.50}$ case gave an intermediate situation, however more similar to that observed for Pd.

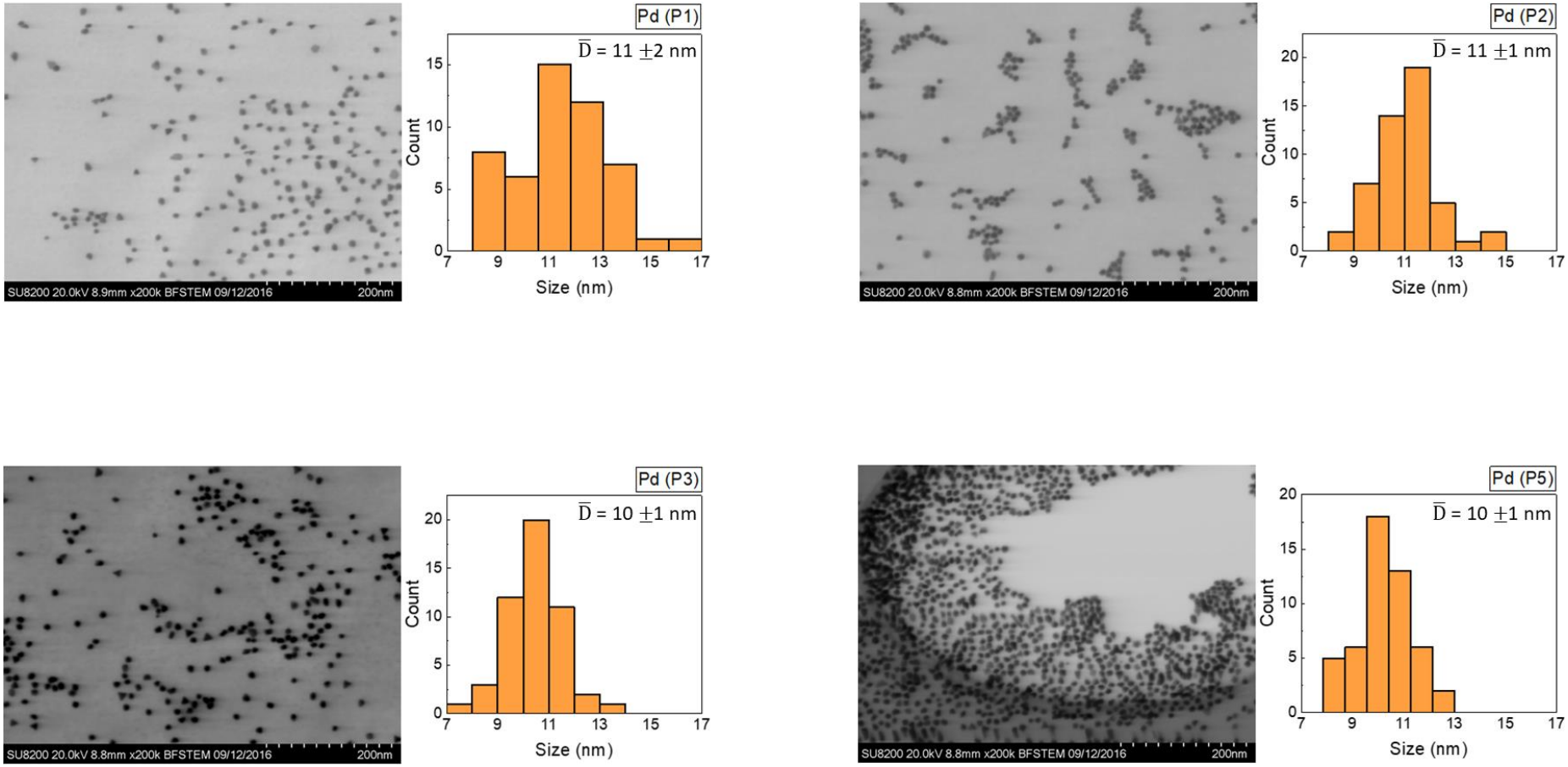

Figure 4-3: STEM-images and corresponding histograms of pure Pd NPs at time points P1-3 and P5.

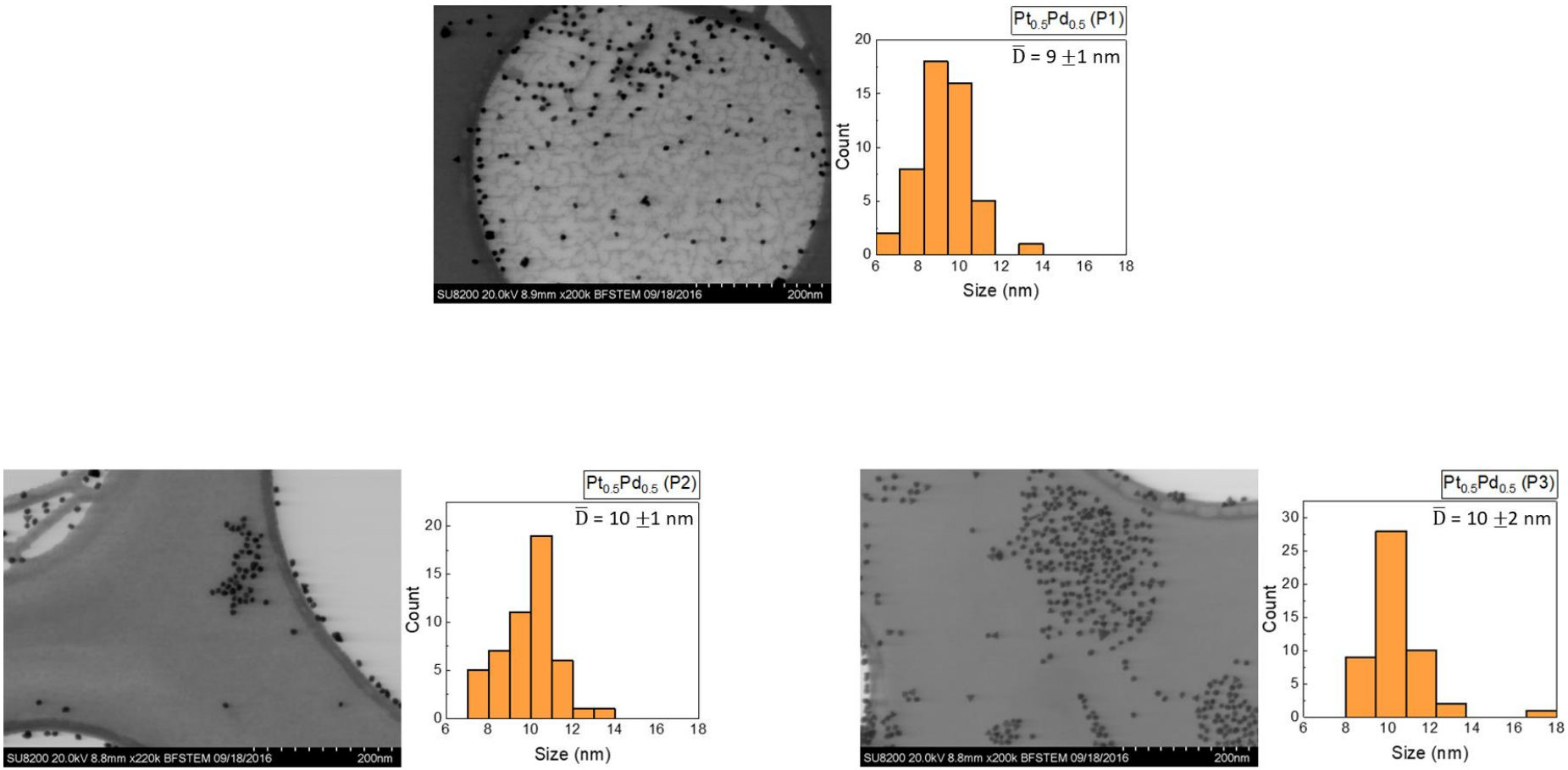

Figure 4-4: STEM-images and corresponding histograms of $Pt_{0.50}Pd_{0.50}$ NPs at time points P1-3.

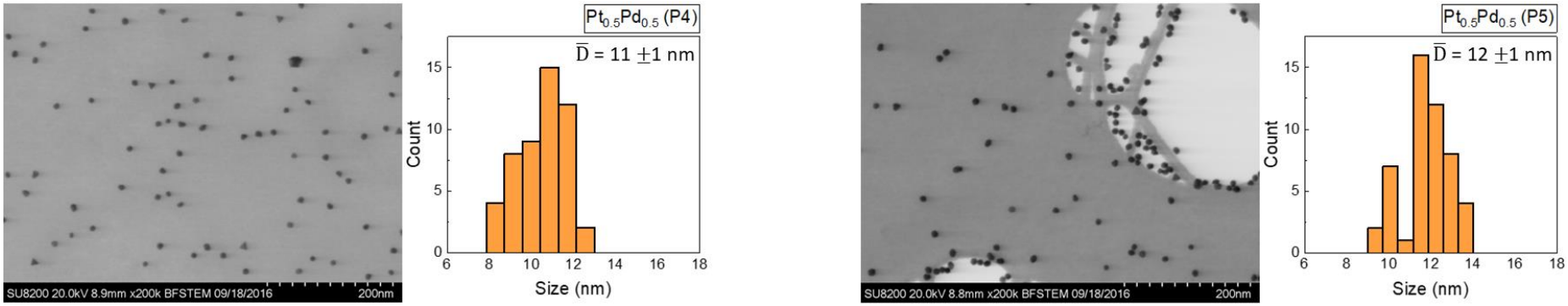

Figure 4-5: STEM-images and corresponding histograms of $Pt_{0.50}Pd_{0.50}$ NPs at time points P4-5.

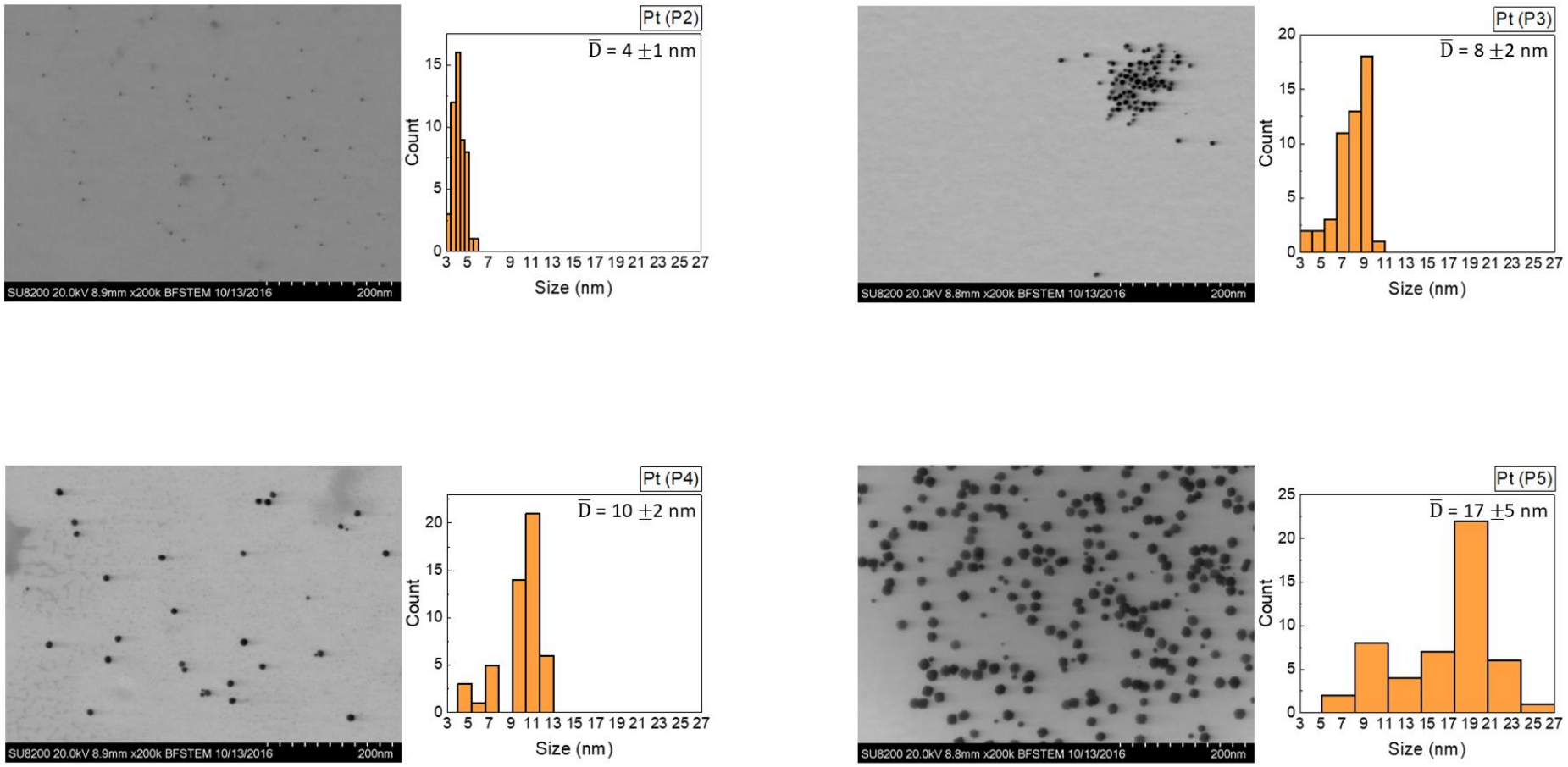

Figure 4-6: STEM-images and corresponding histograms of pure Pt NPs at time points P2-5.

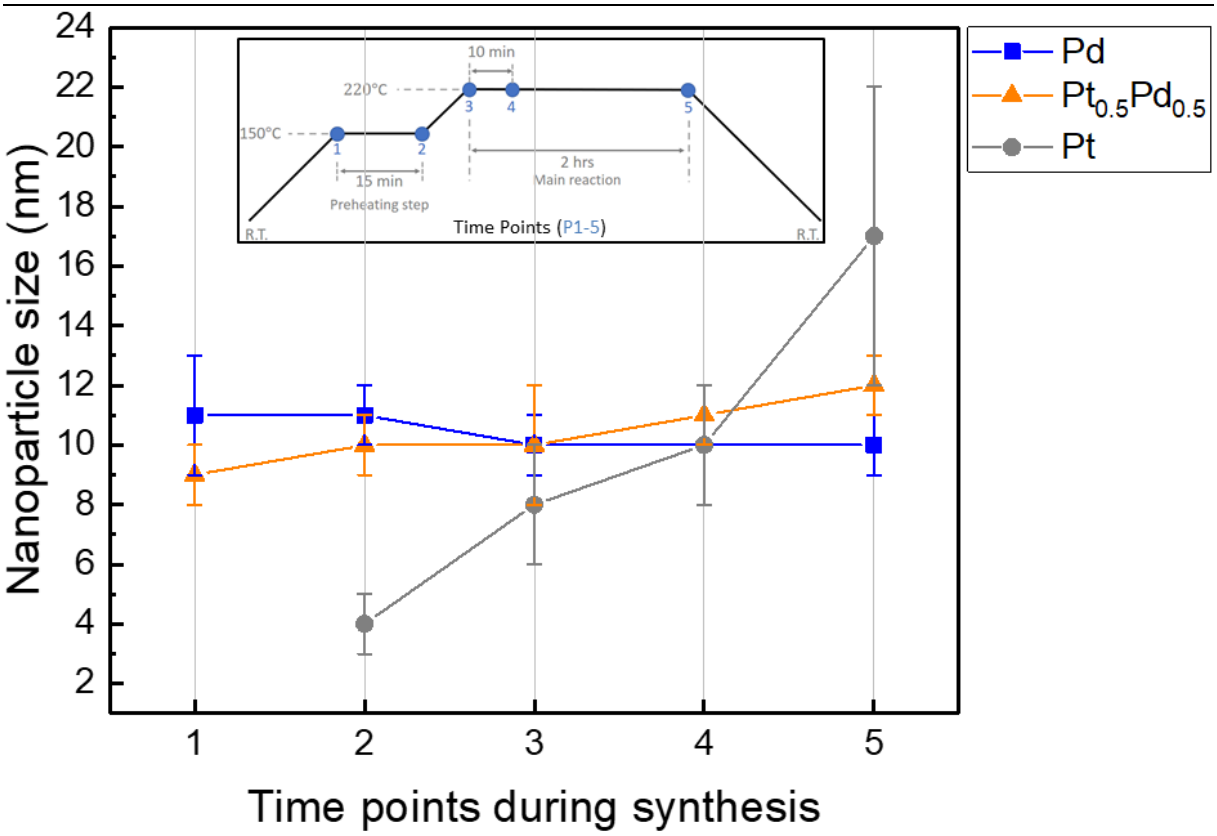

Figure 4-7: Mean nanoparticle size including the size distribution for Pt-Pd nanoparticles with nominal compositions Pd, $Pt_{0.50}Pd_{0.50}$ and Pt plotted versus time point in the synthesis. The insert is showing the five time points with respect to time and temperature during synthesis.

4.2.2 Element Distribution in $Pt_{0.50}Pd_{0.50}$ NPs – Standard Synthesis

Electron Microscopy and Energy Dispersive X-ray Analysis

The kinetics experiments described in section 4.2.1 and the initial XRD results obtained for selected members in the $Pt_{1-x}Pd_x$ series as described in section 4.1 opens up the question on how the element distribution is in the bimetallic $Pt_{1-x}Pd_x$ NPs synthesized following our standard polyol synthesis protocol. For this reason, we decided to perform selected HAADF-STEM-EDX analyses of NPs with nominal composition $Pt_{0.50}Pd_{0.50}$ synthesized at standard conditions.

The results from the TEM investigations are reported in Figure 4-8. From the HAADF-STEM images it can be observed that the particles have a darker core and brighter edges. Contrast in HAADF-STEM images has its origin in atomic number (Z), and the intensity is proportional to Z^2 [97]. As Pt (Z=78) is a heavier element than Pd (Z= 46), and thus scatter electrons more strongly, giving higher intensity in the image. Therefore, the HAADF-STEM results indicate that the distribution is Pd@Pt core@shell. For further affirmation of the chemical composition, EDX-elemental mapping was performed in parallel and the results are presented in Figure 4-8. It is evident from the elemental mapping that the concentration of Pt is higher in the outer rim of the particles than in in the core, and the case is opposite for Pd.

The HAADF-STEM-EDX analysis clearly document that the elemental distribution in the nanoparticles is Pd@Pt core@shell. The nanoparticles are synthesized by a simultaneous reduction method, but still the result is core@shell NPs. The elemental distribution seen in the experiments in this section are comparative to the findings of Zhou et al. [14]. They synthesized Pd@Pt core@shell NPs by the same simultaneous reduction method, and although this was in a different chemical system, they found that the elemental distribution originated from the difference in reduction kinetics of the two Pt- and Pd- precursors.

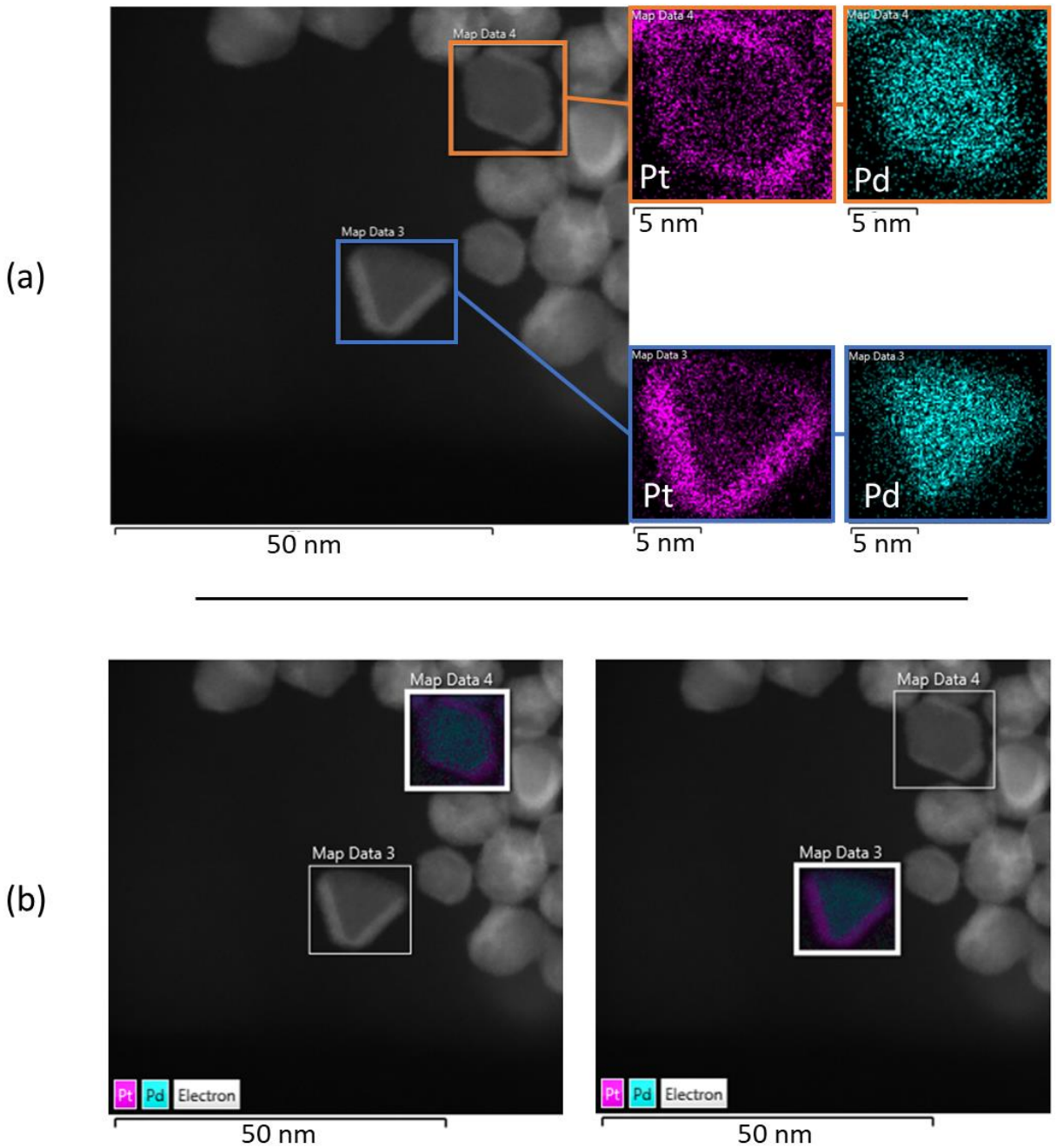

Figure 4-8: HAADF-STEM-images of $Pt_{0.50}Pd_{0.50}$ NPs with 2 h reaction time; (a) Two particles (orange and blue squares) were selected for EDX elemental mapping. (b) The Pd- and Pt- EDX-mapping signals are overlapped, showing the elemental distribution clearly.

Synchrotron Powder X-ray Diffraction

Two $Pt_{0.50}Pd_{0.50}$ nanoparticle samples were synthesized by the standard polyol synthesis (section 3.2), however, with one exception to the standard protocol: One of the samples was aged at 24 hours, instead of the standard time of 2 hours, with the objective to clarify whether increased reaction time may result in a Pt-Pd solid solution in the NPs rather than maintaining the core shell feature. Both samples were measured and analyzed according to a Whole Powder Pattern Fitting approach (experimental details in section 3.5.2). Data treatment was done by dr. W. Slawinski.

Two approaches were followed in the fitting process; (a) the refinement was done assuming solid solution and Gaussian size distribution; (b) the refinement was done based on the assumption of core@shell element distribution and Gaussian size distribution. The R-value associated with each of these two approaches are summarized in Table 4-2 for both samples.

Table 4-2: Results from the whole powder pattern fitting with R-values describing how well the fitted pattern correspond to the experimental pattern with respect to the given assumptions in the refinement.

Sample, aging time [hour]	Assumption of element distribution	Assumption of size distribution type	R-value
2	Solid solution	Gaussian	0.0192
	Core@shell	Gaussian	0.0161
24	Solid solution	Gaussian	0.0248
	Core@shell	Gaussian	0.0251

The obtained results point in the direction that the 2-hour aged sample has a core@shell element distribution, whereas the 24-hour sample was a Pt-Pd solid solution. This is indicated by the R-values listed in Table 4-2. The lowest R-value for the 2-hour sample results is obtained when the element distribution in the particles is core@shell, with an R-value of 0.0161. On the other hand, for the 24-hour sample the lowest R-value correspond to the assumption of solid solution, at R = 0.0248. However, the difference in R-factor to that of a core@shell model is probably not significant. In both of these cases a Gaussian size distribution was assumed. It should be noted that the small differences in the R-values means that the obtained results should not be considered as absolutely conclusive with respect to the element distribution.

Figure 4-9 and Figure 4-10 shows measured and fitted PXRD patterns.

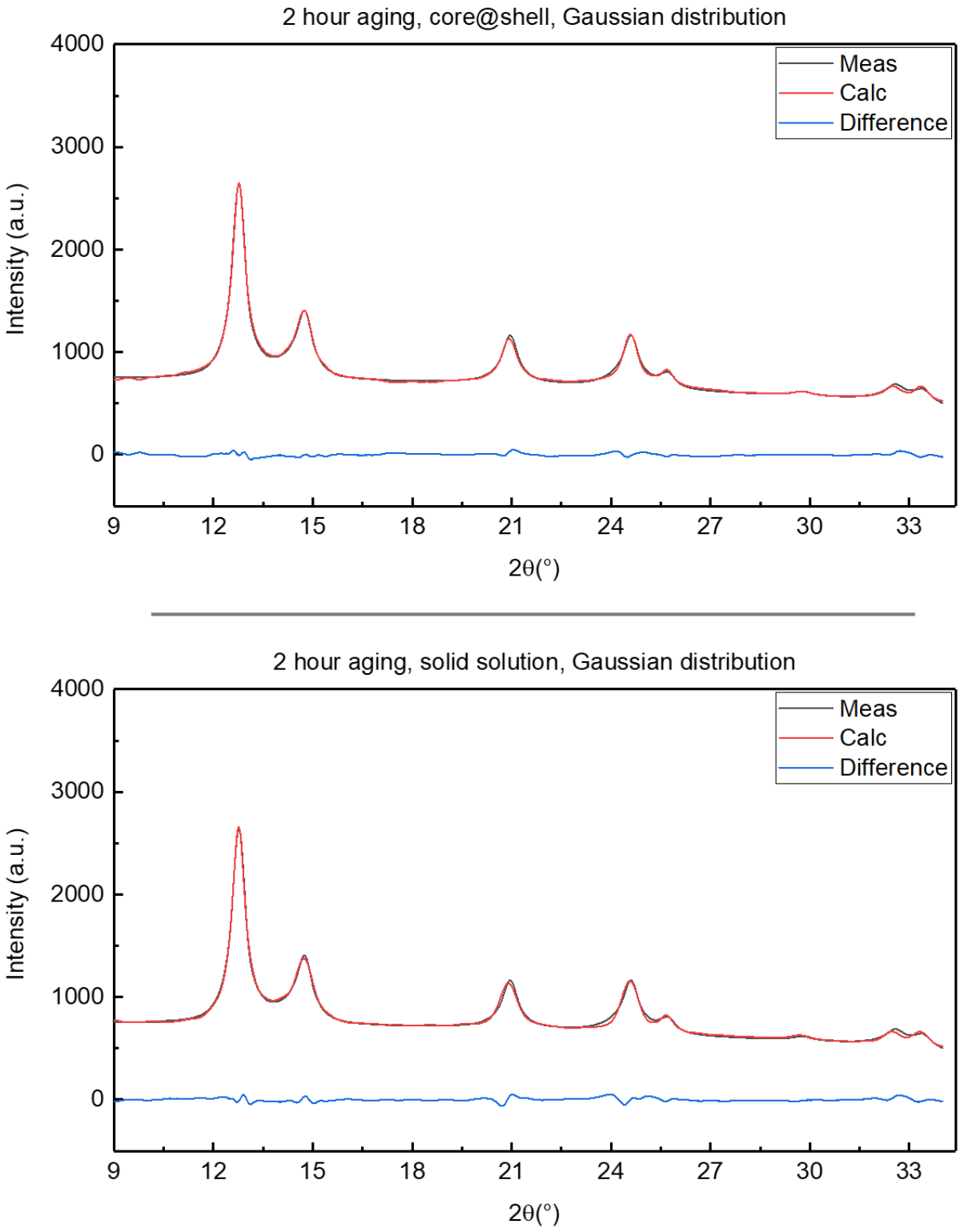

Figure 4-9: Diffractograms for the 2-hour samples showing the measured (black) and calculated (red) pattern with the difference between them (blue).

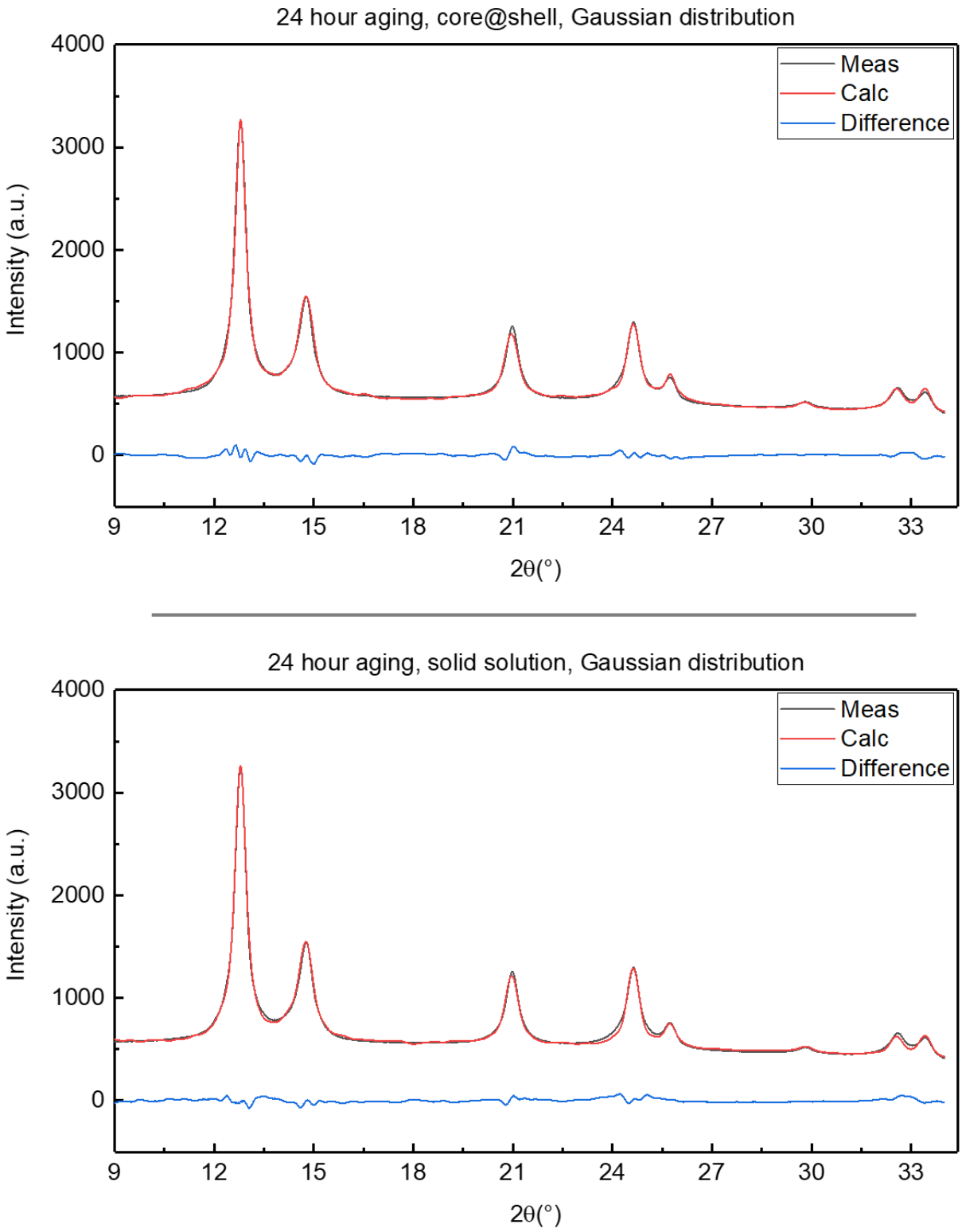

Figure 4-10: Diffractograms for the 24-hour samples showing the measured (black) and calculated (red) pattern with the difference between them (blue).

4.2.3 Tuning the Reduction Kinetics of $Pt(acac)_2$ and $Pd(acac)_2$

The previous kinetics experiment results (section 4.2.1), the elemental distribution results (section 4.2.2) and results obtained in the Pt-Rh system from a previous master student in our research group [13] motivated an attempt to tune the kinetics of the $Pt(acac)_2$ and $Pd(acac)_2$ precursors such that their relative reduction kinetics would become more similar. Based on this we decided to explore the effect of using various polyalcohols and tuning the metal/surfactant ratio had on the NP formation kinetics. The experimental details are described in section 3.3.2, and all performed experiments are reported in table Table 4-3.

As outlined in the experimental section each experiment was performed twice; first a quick heating of the suspension to get an approximate idea about at which temperature the NP nucleation takes place. In the second test, the ramping is slowed down in the temperature region the nucleation is expected to take place. By visual inspection we define the nucleation temperature (T_{Nucl}) to be at the temperature we visually observe a color change in the suspension. This is the origin of the reported temperatures in Table 4-3.

As we performed many such experiments, in the following the details for one series will be described in detail; $Pt(acac)_2$ and $Pd(acac)_2$ using ethylene glycol as solvent and using two different metal/PVP ratios of 1/10 and 1/100. Corresponding detailed results for all other solvents are reported in the appendix (9.1.1), and a summary is given in Table 4-3 at the end of this section.

Figure Figure 4-11 gives an overview of the color change in the samples when pulled out from the reaction mixture at selected temperatures during the heating, and Figure 4-12 reports STEM-images of the observed NPs collected at the temperature marked in red in the overview.

Note that the nucleation temperature does not in all cases coincide with the exact nucleation temperature (first appearance of color change).

With basis in the observed color change in the samples and the SEM-images of the particles of the same samples it becomes clear that $Pd(acac)_2$ transforms in ethylene glycol to nanoparticles at ~74-78°C independently of the metal/PVP ratio. Correspondingly for $Pt(acac)_2$ the reaction take place at ~175°C, also independently of the metal/PVP ratio. I.e. the reaction kinetics was not altered by changing the metal/PVP -ratio.

Similar observations were found when exploring the reactivity in the various other solvent (1,4-butanediol; 1,2-butanediol; 1,3-propanediol); appendix 9.1.1, Table 4-3.

An extra note should be added at this point. It can be observed from the photographs that not all of the $Pd(acac)_2$ precursor was fully dissolved at the starting temperature. In the case of $Pt(acac)_2$, this was not observed. Residues of undissolved $Pd(acac)_2$ precursor can potentially affect the nucleation temperature for $Pd(acac)_2$, but as the temperature in the solution increased, much more of the precursor dissolved. However, we assume potentially undissolved Pd-precursor present when approaching T_{Nucl} do not influence the conclusions. Therefore, we summarize that the main finding from this series of experiments is that we were not able to alter the reaction kinetics for either one of the metal precursors by varying parameters as type of solvent and metal/PVP ratio. This is in contrast to what Bundli found for the Pt-Rh system [13].

Pd(acac)$_2$ - Metal : PVP = 1: 10

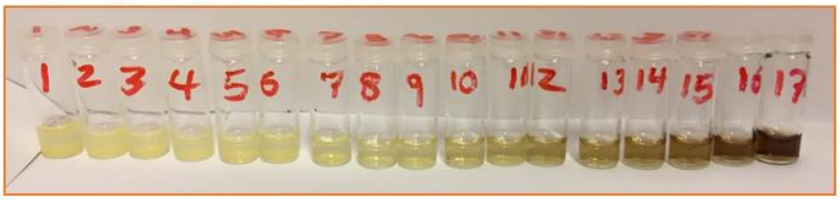

Sample	1	2	3	4	5	6	7	8	9	10	11	12	13	14	15	16	17
T [°C]	47	50	53	56	59	62	65	68	71	74	77	80	83	86	89	92	95

Pd(acac)$_2$ - Metal : PVP = 1: 100

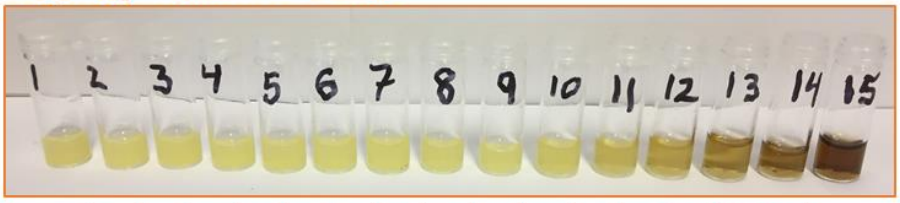

Sample	1	2	3	4	5	6	7	8	9	10	11	12	13	14	15
T [°C]	45	48	51	54	57	60	63	66	69	72	75	78	81	84	87

Pt(acac)$_2$ - Metal : PVP = 1: 10

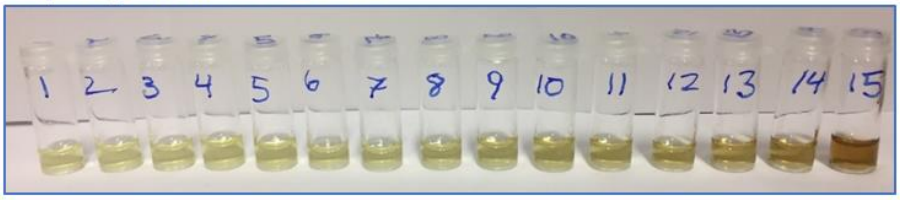

Sample	1	2	3	4	5	6	7	8	9	10	11	12	13	14	15
T [°C]	148	151	154	157	160	163	166	169	172	175	178	181	184	187	190

Pt(acac)$_2$ - Metal : PVP = 1: 100

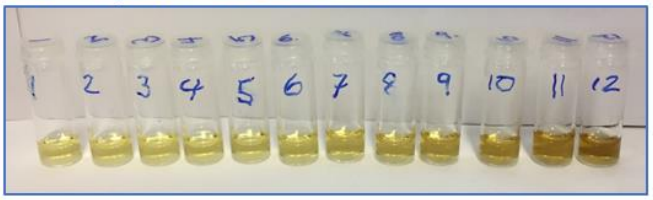

Sample	1	2	3	4	5	6	7	8	9	10	11	12
T [°C]	148	151	154	157	160	163	166	169	172	175	178	181

Figure 4-11: Color change in samples where ethylene glycol was used as solvent, pulled out at given temperatures (T), with the red highlight corresponding to the STEM images for each respective sample.

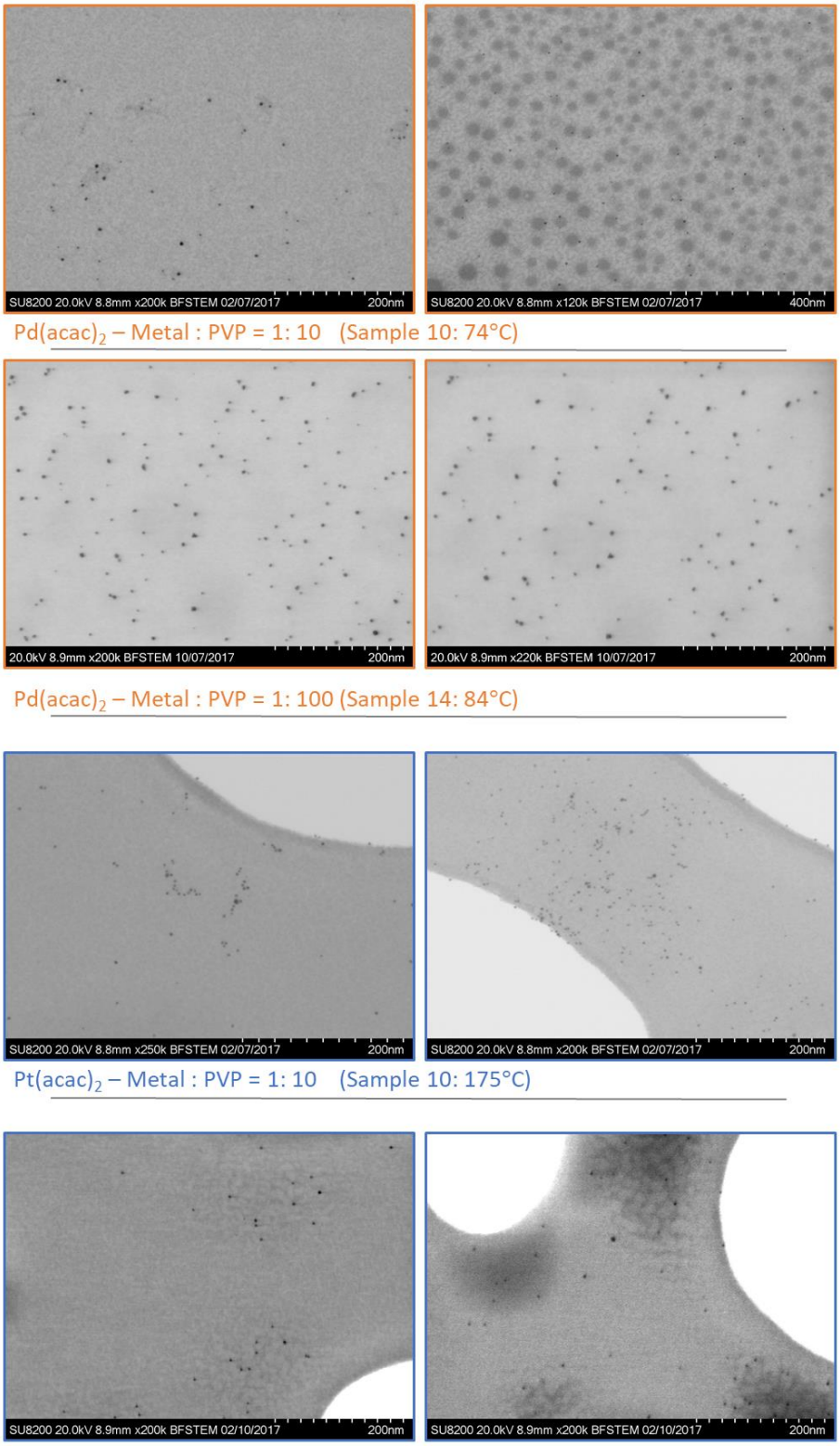

Figure 4-12: STEM-images documenting the formation of Pt and Pd NPs at ~T_{Nucl} from $Pt(acac)_2$ and $Pd(acac)_2$ respectively in ethylene glycol with indicated ratios of metal/PVP.

Table 4-3: Overview of all the experiments performed in this sub-chapter with reported nucleation temperatures.

Solvent	Metal : PVP	T_N of $Pd(acac)_2$ [°C]	T_N of $Pt(acac)_2$ [°C]
EG	1 : 10	74	175
EG	1 : 100	78	172
1,4-BD	1 : 10	77	189
1,4-BD	1 : 100	77	182
1,2-BD	1 : 10	72	178
1,3-PD	1 : 10	78	172

All of the experiments except those with 1,4-BD as solvent were repeated twice.

4.3 Modified $Pt_{1-x}Pd_x$ Polyol Synthesis

Since the attempt of tuning the reduction kinetics of the $Pt(acac)_2$ and $Pd(acac)_2$ precursors proved unsuccessful (results in section 4.2.3), a two-step approach was followed in the pursuit to produce bimetallic Pt-Pd NPs with reversed configuration. Pt@Pd core@shell NPs (Pt core and Pd shell). In the first step core-Pt NPs was synthesized, and in the second step Pd was intended to nucleate and grow onto the core-NPs to form the shell. To find the optimal conditions for Pd to nucleate on the Pt NP core-NPs the effect of varying temperature and reaction time in the Pd-growth step was investigated. The experimental procedure is described in section 3.4. The nominal composition in the bimetallic NPs in all experiments (M1-5) was $Pt_{0.50}Pd_{0.50}$. Figure 4-13 is included to visualize the experimental variations with respect to synthesis temperatures and times of the five syntheses (M1-5) for the Pd growth step. STEM-images of the washed $Pt_{0.50}Pd_{0.50}$ NP products after ended synthesis are presented in Figure 4-14.

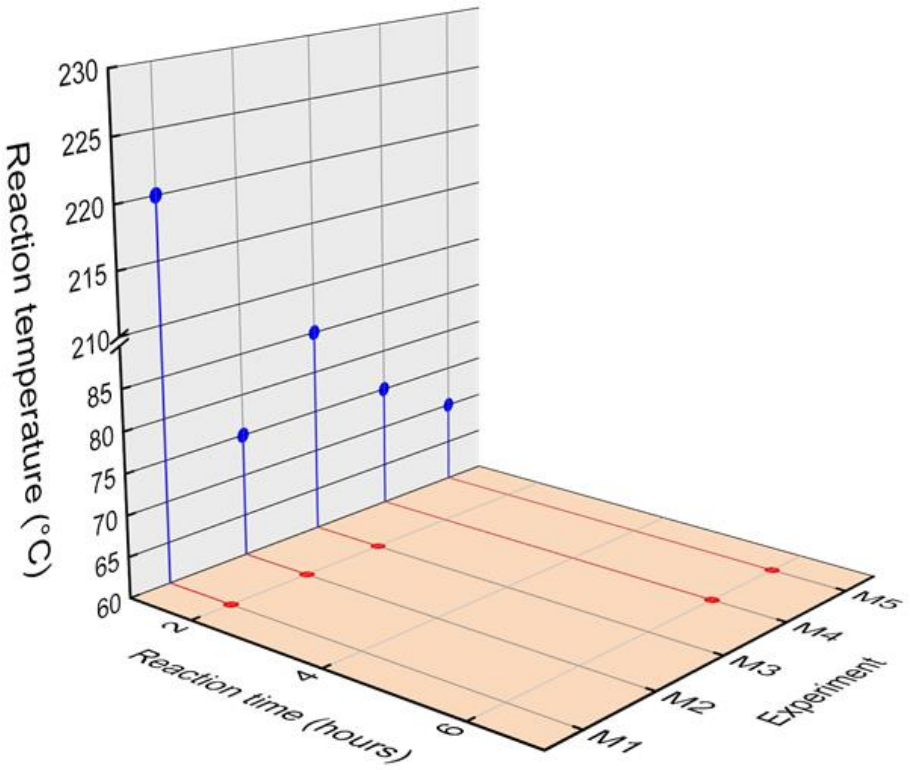

Figure 4-13: Overview of reaction conditions in the Pd-growth step for experiments M1-5.

With basis in the STEM-images in Figure 4-14, the following can be said about experiments M1-5: The size distribution in experiment M1 is very broad, ranging from 6-19 nm (Figure 4-14), and the procedure was therefore discarded. In experiment M2 the results show a narrower size distribution, but in the washing procedure of these NPs the color of the eluent after the first centrifugation was very similar to the color of the $Pd(acac)_2$ solution, indicating minor or no nucleation of Pd (Figure 4-14). For this reason, the procedure was also discarded. A bimodal size distribution is obvious from a brief look at the images from experiment M3 (Figure 4-14). The presence of small NPs suggested that homogeneous nucleation of Pd may have taken place during the reaction, however this does not rule out the possibility of nucleation of Pd on the Pt-core NPs as well. The procedure was dismissed because of the presence of the small NPs. In experiment M4 (Figure 4-14) the results also show a bimodal size distribution even though a lower temperature was used during the growth step, and the method was therefore not accepted either. The lower temperature was chosen to decrease the tendency for homogeneous nucleation of Pd, and to promote controlled growth of Pd onto the preformed Pt NPs, inspired by Zhang et al. [98]. In experiment M5 (Figure 4-14) a bimodal size distribution was still the outcome of the methodology, and to check if Pd was in fact nucleating as small separate NPs and on the Pt core-NPs this sample was investigated in further detail. These results are presented in the following.

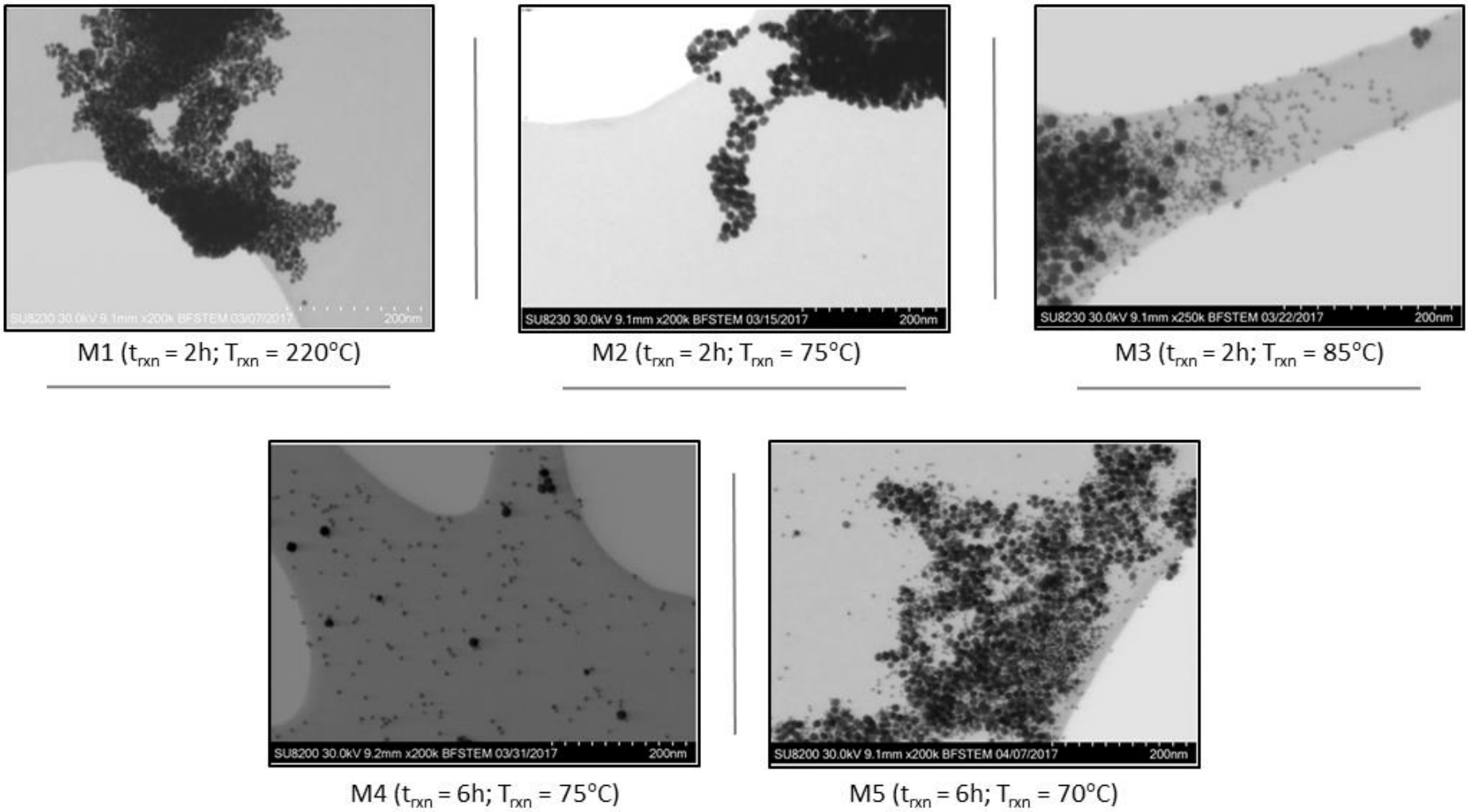

Figure 4-14: STEM-images of the washed NP-product from experiments M1-5. The reaction time and -temperature in the Pd-growth step are given in parentheses.

In Figure 4-15, SE-SEM and TEM-images of the nanoparticles of sample M5 are shown. It can be seen from the SEM images that the smaller NPs tend to accumulate in the proximity of the larger ones. Also, their shapes may indicate that a process of coalescence is taking place. A more close-up perspective on this is given by the TEM-images.

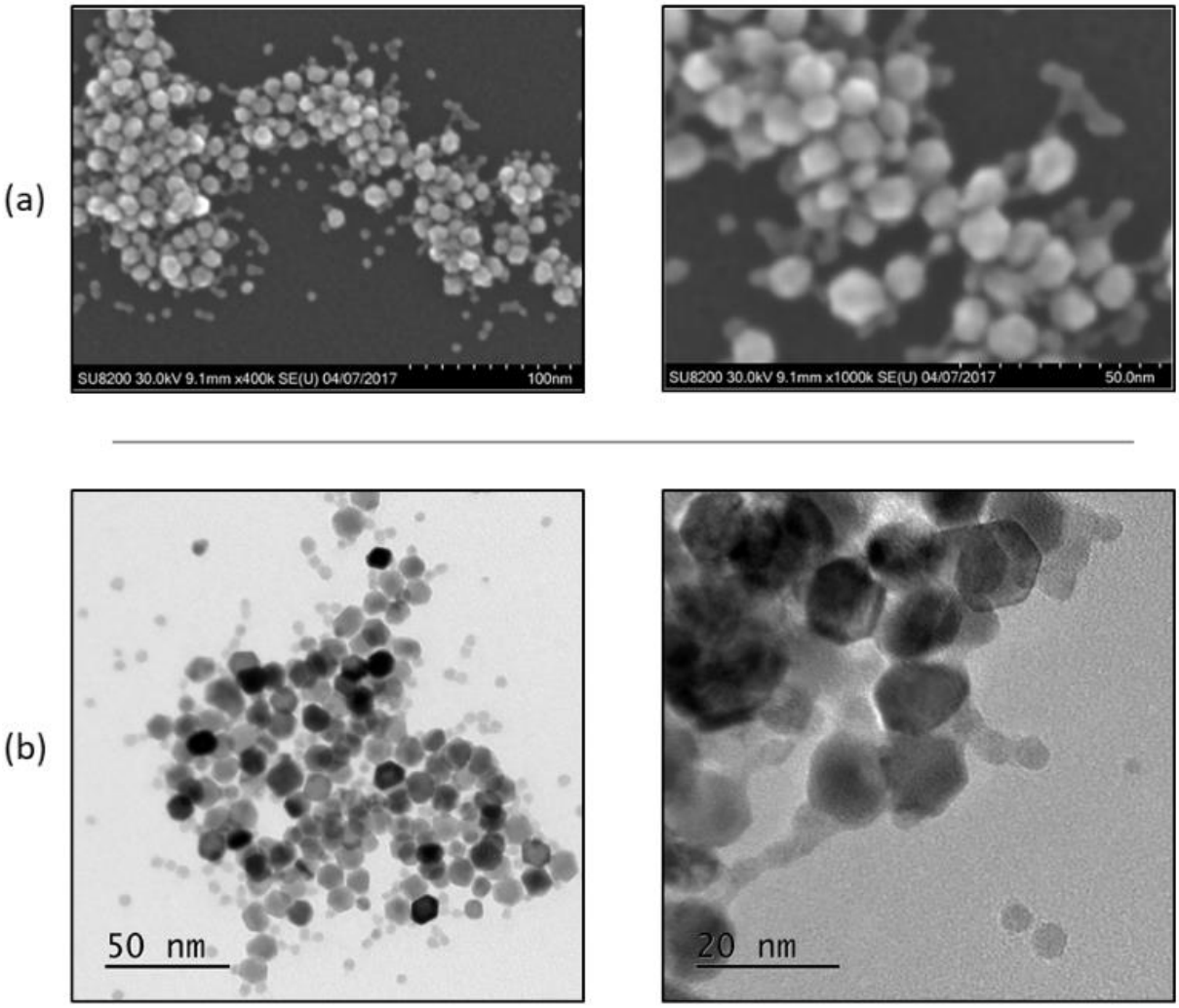

Figure 4-15: (a) SE-SEM-images of the NPs from experiment M5. (b) Conventional TEM-images of the same NPs.

Elemental mapping and quantitative analysis with EDX was also performed on the sample to investigate the elemental composition of the small and large NPs, to verify if the small particles were composed of pure Pd, and to see if Pd had nucleated on the large Pt-core nanoparticles. The EDX elemental map in Figure 4-16 and the quantitative analysis (Table 4-4) shows that the small nanoparticles are composed of pure Pd, whereas in the large ones the final composition is approximately $Pt_{0.10}Pd_{0.90}$. Because of drift in the electron beam during the recording of the

element maps, it cannot be stated if the element distribution is e.g. core@shell or solid solution, however as the EDX data was collected from isolated particles, the calculated composition should reflect the mean composition in the particle.

The EDX elemental map (Figure 4-16), TEM and SEM results (Figure 4-15), along with the quantitative EDX analysis (Table 4-4) indicate that Pd is homogeneously nucleating to form the small Pd NPs under the synthesis conditions in experiment M5. Since these results also show that Pd is present in the larger Pt core-NPs, it may imply that Pd has also nucleated heterogeneously on these particles or become incorporated by another mechanism.

In summarizing the findings for this series of experiments, it becomes clear that in order to achieve controlled growth of Pd onto the preformed Pt nanoparticles in this system of reactants, the temperature and reaction time in the growth step of the shell must be finely tuned. The results points in the direction that the reaction temperature in this step should be low to decrease the tendency for homogeneous nucleation of Pd. A prolonged reaction time is then needed for the shell to grow. This picture fits well the statement of Zhang et al. [98], in that the growth rate of the shell in the core@shell NPs should be slow to achieve the heterogeneous nucleation.

Table 4-4: Quantitative EDX analysis based on indicated areas in Figure 4-16 for small and large NPs in the bimodal size distribution.

NP-size	Spectrum (map)	Line Type	Atomic %
Small	Pd	L – series	100
	Pt	M – series	0
Large	Pd	L – series	10
	Pt	M – series	90

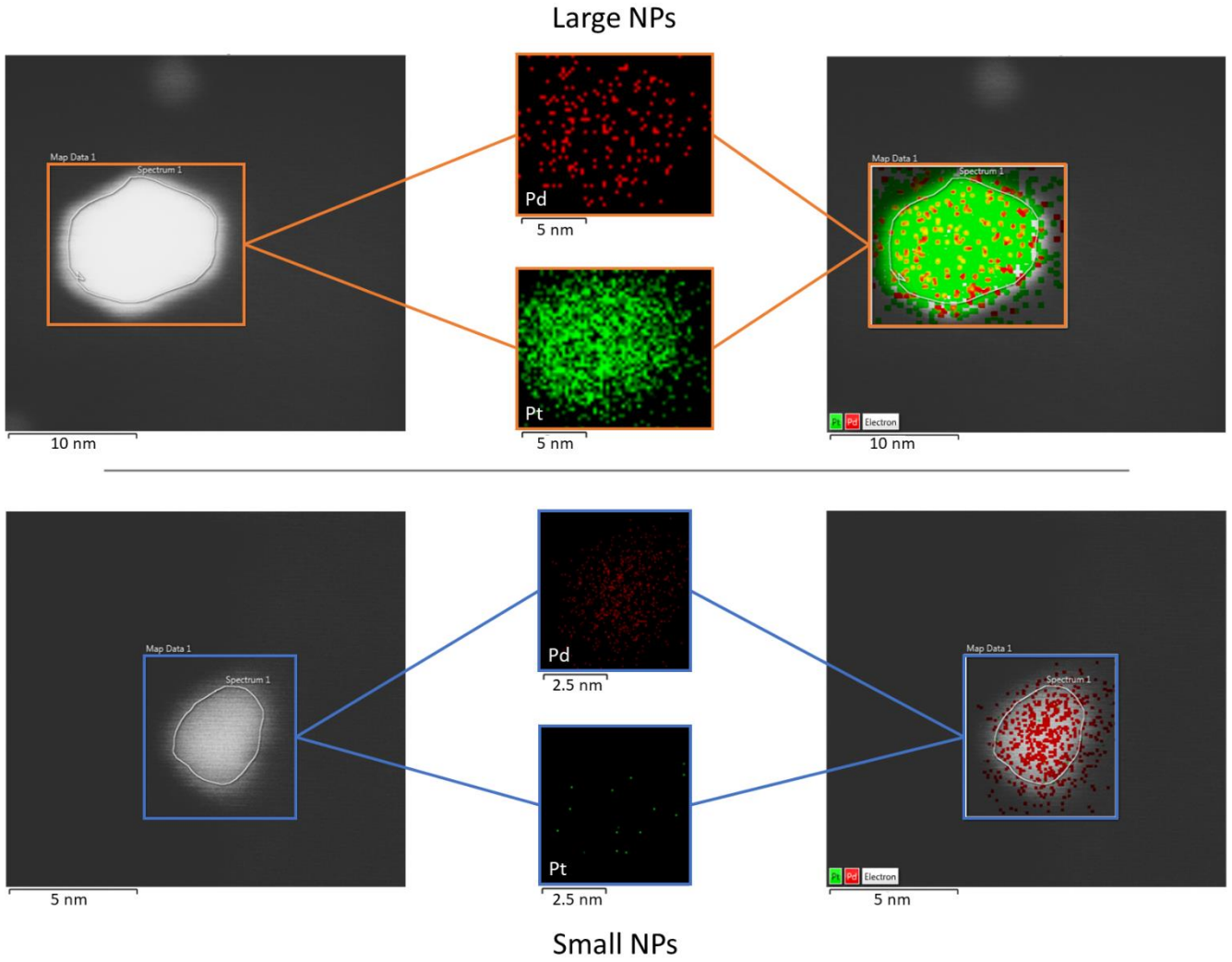

Figure 4-16: EDX elemental mapping on large (top) and small (bottom) nanoparticles in experiment M5. On the left-hand side is HAADF-STEM-images of the particles selected for EDX analysis with indicated area for the quantitative analysis of elemental composition. To the right is an overlay of the EDX element map.

4.4 $Pt_{1-x}Pd_x/Al_2O_3$ Catalysts for Intermediate Temperature NH_3 Oxidation

In the current thesis, one of the main goals has been to convert free-standing $Pt_{1-x}Pd_x$ NPs into metal-on-support catalysts and test their suitability as intermediate temperature NH_3 oxidation catalysts. In the following results obtained with respect to the materials aspects of the catalysts before and after catalytic testing are described together with the catalytic testing results (activity toward NH_3 oxidation and product selectivity).

4.4.1 Characterization of 1 wt.% $Pt_{1-x}Pd_x/Al_2O_3$ Catalysts

Three catalysts with compositions $Pt_{1-x}Pd_x/Al_2O_3$ (x = 0, 0.10, 0.50) and targeted metal loadings of 1 wt.% on alumina were prepared by a postdoc in our research group by following the protocol developed by Muri [15]. See section 3.6 for details. A reference 1 wt.% Pt/Al_2O_3 catalyst supplied from Sigma-Aldrich was included. An overview of the four catalysts is given in Table 4-5.

Step 1 in the catalyst preparation protocol is to synthesize the free-standing $Pt_{1-x}Pd_x$ NPs by the standard polyol method (section 3.2). The obtained products from the syntheses were analyzed by PXRD and TEM to determine the a-axes and particle size distributions, respectively. PXRD analysis showed the samples to be phase pure, giving only rise to Bragg peaks that could be assigned to a ccp type structure (similar PXRD patterns as reported in Figure 4-1).

The refined a-axes of the free-standing nanoparticles of the three different nominal compositions were furthermore found to be similar within uncertainty; Table 4-5.

Nanoparticles from each synthesis batch were subsequently analyzed by TEM with the purpose to map the nanoparticle size distribution. A droplet of re-dispersed NP suspension was deposited onto a carbon TEM grid and dried overnight prior to analysis. TEM-images of the three compositions were obtained applying the bright field technique (section 2.5.1), and representative images are reported in Figure 4-17 together with the histograms showing the particle size distribution. The histograms (Figure 4-17) were made based on the measured diameter of 250 NPs for x = 0 and 0.10, and 145 NPs for x = 0.50. The pure Pt NPs ($\overline{D}$ = 17.4 $\pm$2.5 nm) (a) have a larger size and broader size distribution than the $Pt_{0.90}Pd_{0.10}$ ($\overline{D}$ = 10.1 $\pm$ 1.7 nm) (b) and $Pt_{0.50}Pd_{0.50}$ ($\overline{D}$ = 10.7 $\pm$1.3 nm) NPs (c). With respect to morphology/faceting,

all three compositions show multi-faceted particles, which corresponds to what Bundli [13] found in the Pt-Rh system using the same synthesis procedure.

Step 2 of the preparation of the catalysts is to deposit the free-standing $Pt_{1-x}Pd_x$ NPs onto the Al_2O_3 support targeting for 1 wt.% $Pt_{1-x}Pd_x/Al_2O_3$. Critical aspects of this step are to (a) obtain a real noble metal loading close to the targeted value of 1 wt.%, and (b) obtain a catalyst with well dispersed NPs.

The noble metal loading as well as the relative molar ratio between Pt and Pd in the deposited NPs were analyzed by ICP-MS. Samples were sent to an external laboratory for analysis, but the subsequent evaluation of the received data is done in-house and reported in Table 4-5. From the evaluation of the ICP-MS data it became clear that the nominal compositions of the bimetallic $Pt_{1-x}Pd_x$ (x = 0.10 and 0.50) nanoparticles are different from the real values; one being enriched in Pt, whereas the other with a lower Pt content relative to the nominal compositions.

Furthermore, the real noble metal loadings (wt.%) were calculated to be 0.83 wt.% $Pt_{0.66}Pd_{0.34}/Al_2O_3$, 0.64 wt.% $Pt_{0.82}Pd_{0.18}/Al_2O_3$ and 0.55 wt.% Pt/Al_2O_3, all showing less noble metal deposited than what targeted for. The reference catalyst supplied via Sigma-Aldrich give a metal loading of 1.03 wt.% Pt/Al_2O_3, which is in good agreement with its specifications.

Bright field TEM-images of the as-synthesized catalysts are reported in Figure 4-18 (upper row). As imaging in bright field mode use the transmitted electron beam to form the image, contrast is a result of sample thickness, crystallographic direction and atomic number (section 2.5.1). Under the conditions that sample thickness is the same, the noble metal nanoparticles should show up as dark spots in the images. In the cases of Pt/Al_2O_3 and $Pt_{0.90}Pd_{0.10}/Al_2O_3$ (Figure 4-18) it is difficult to conclude if the dark areas represent the noble metal NPs or if they are contrast from sample thickness or crystallography. In the case of $Pt_{0.50}Pd_{0.50}/Al_2O_3$ and the reference catalyst Pt/Al_2O_3, individual NPs are visible in the form of dark spots. Corresponding bright field TEM-images were collected for the catalysts after being tested for intermediate temperature NH_3 oxidation with the purpose to evaluate if the as-deposited noble metal NPs underwent any sintering during testing. The images are reported in Figure 4-18 (lower row). Again, it is difficult to state conclusively if the deposited noble metal NPs are well dispersed, and not sintered. However, in the continuation it is assumed the NPs are well dispersed and that no major sintering is taking place during the catalytic testing due to the mild testing conditions (T < 450°C).

Table 4-5: Overview of $Pt_{1-x}Pd_x/Al_2O_3$ (x = 0.50; 0.10; 0) and reference Pt/Al_2O_3 catalysts before catalytic testing. The targeted metal loading was 1 wt.% metal on alumina.

Target composition	**Support**	Free standing nanoparticles: a-axis (PXD); particle size (TEM); chemical composition (ICP-MS)		Finished catalyst before catalytic testing: Metal loading (ICP-MS); chemical composition (ICP-MS)	
		a-axis [Å]	**Particle size with distribution [nm]**	**Metal loading [metal wt.%/Al_2O_3]**	**Chemical composition**
Pt (reference)	γ-Al_2O_3	—	—	1.0	Pt
Pt	γ-Al_2O_3	3.9228 ±0.0009	17.4 ±2.5	0.55	Pt
$Pt_{0.90}Pd_{0.10}$	γ-Al_2O_3	3.915 ±0.001	10.1 ±1.7	0.64	$Pt_{0.82}Pd_{0.18}$
$Pt_{0.50}Pd_{0.50}$	γ-Al_2O_3	3.920 ±0.004	10.7 ±1.3	0.83	$Pt_{0.66}Pd_{0.34}$

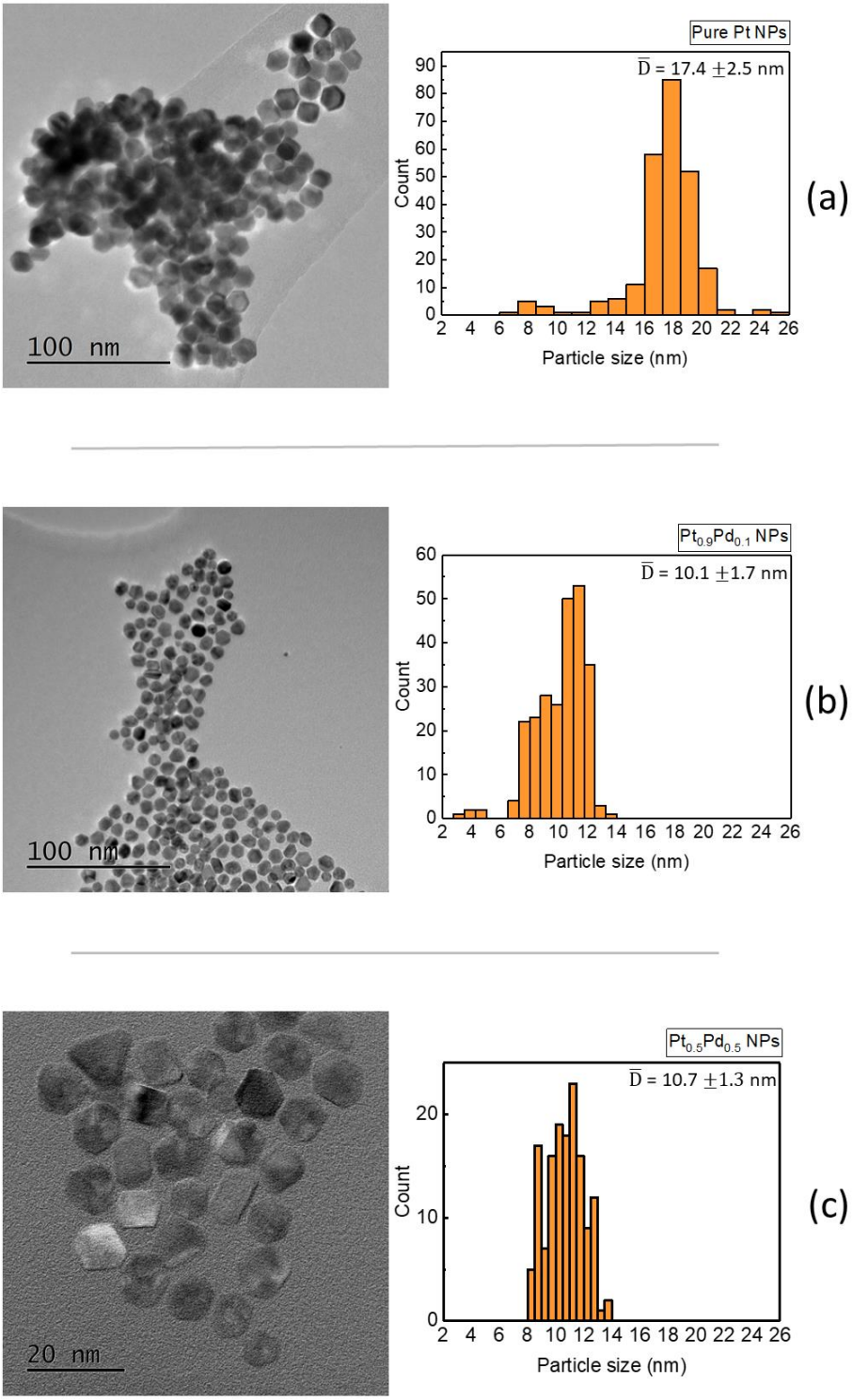

Figure 4-17 : Bright field TEM-images and corresponding histograms of free-standing $Pt_{1-x}Pd_x$ NPs with compositions: (a) x = 0, (b) x = 0.10 and (c) x = 0.50.

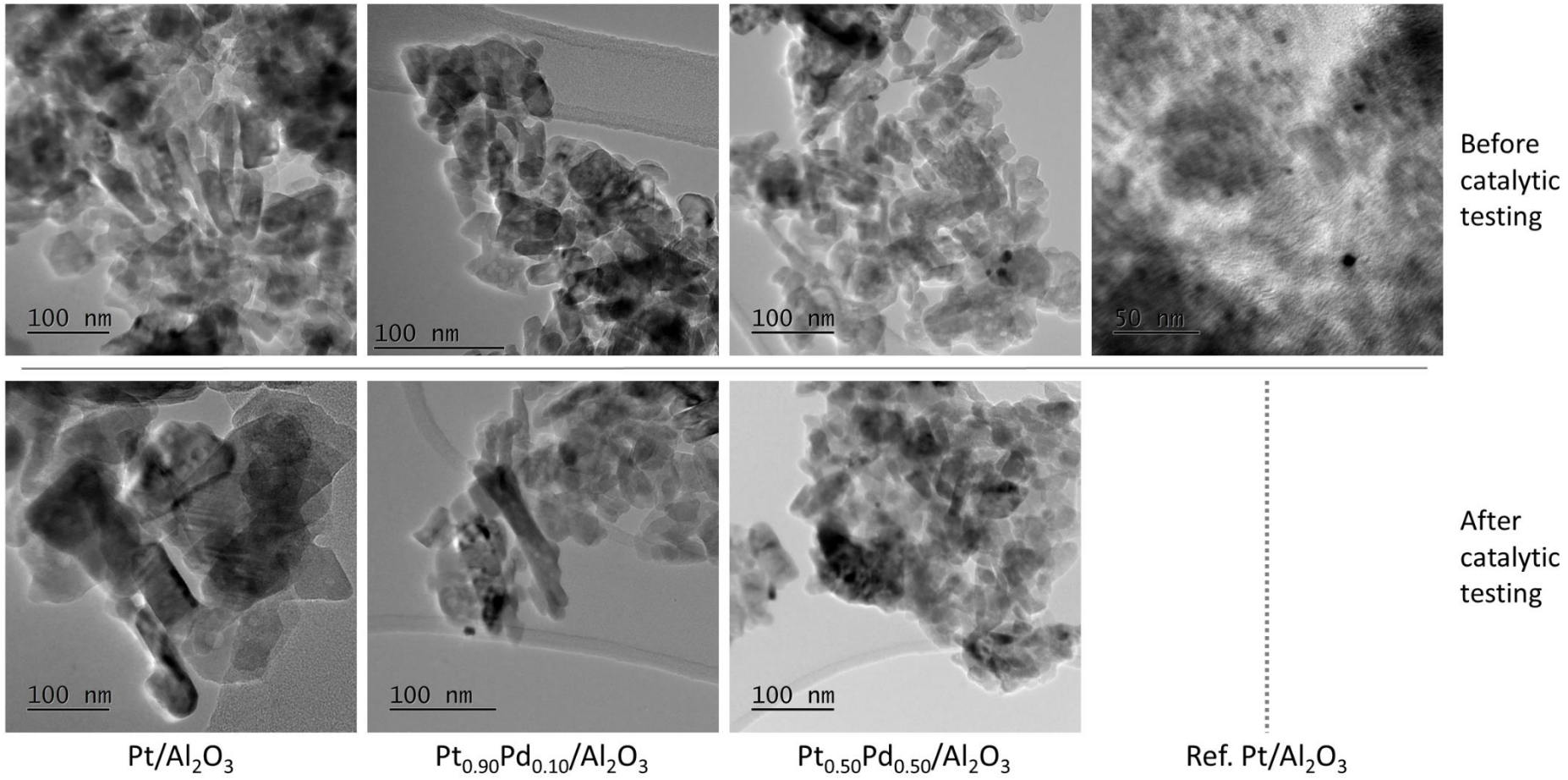

Figure 4-18: Bright field TEM-images of the as-prepared catalysts before and after catalytic testing. The upper row shows the catalysts before testing, and the lower row shows after testing. The compositions indicated in the lower images are equal in the image directly above.

4.4.2 Catalytic Reactor Testing

The three as-prepared $Pt_{1-x}Pd_x/Al_2O_3$ (x = 0, 0.10, 0.50) catalysts described in section 4.4.1 were tested together with the Pt/Al_2O_3 reference catalyst purchased from Sigma-Aldrich for intermediate temperature NH_3 oxidation in a fixed bed reactor at YARA International, Herøya. The catalysts were exposed to a reaction mixture containing 450 ppm NH_3, 5% O_2 in rest N_2 at increasing increments of temperature (200-400°C) with a fixed dwell time (2 hour) at each step to investigate their capacity toward NH_3 oxidation. N_2 is the preferred reaction product for the current investigation (see section 1.3) whereas NO_x and N_2O are undesired. A detailed description of the experimental conditions is given in section 3.7. In the following, the catalysts will be evaluated with respect to NH_3 conversion, turnover frequency (TOF) and product selectivity.

The results obtained with respect to NH_3 conversion (%) versus temperature for the four catalysts are reported in Figure 4-19. From Figure 4-19 it can be noted that the reference catalyst is converting NH_3 100 % already at 250°C. The three in-house prepared catalysts are internally behaving very similarly, and none of them give full NH_3 conversion (%) in the explored temperature interval. At the maximum testing temperature of 400°C, the catalysts convert ~65-75% NH_3.

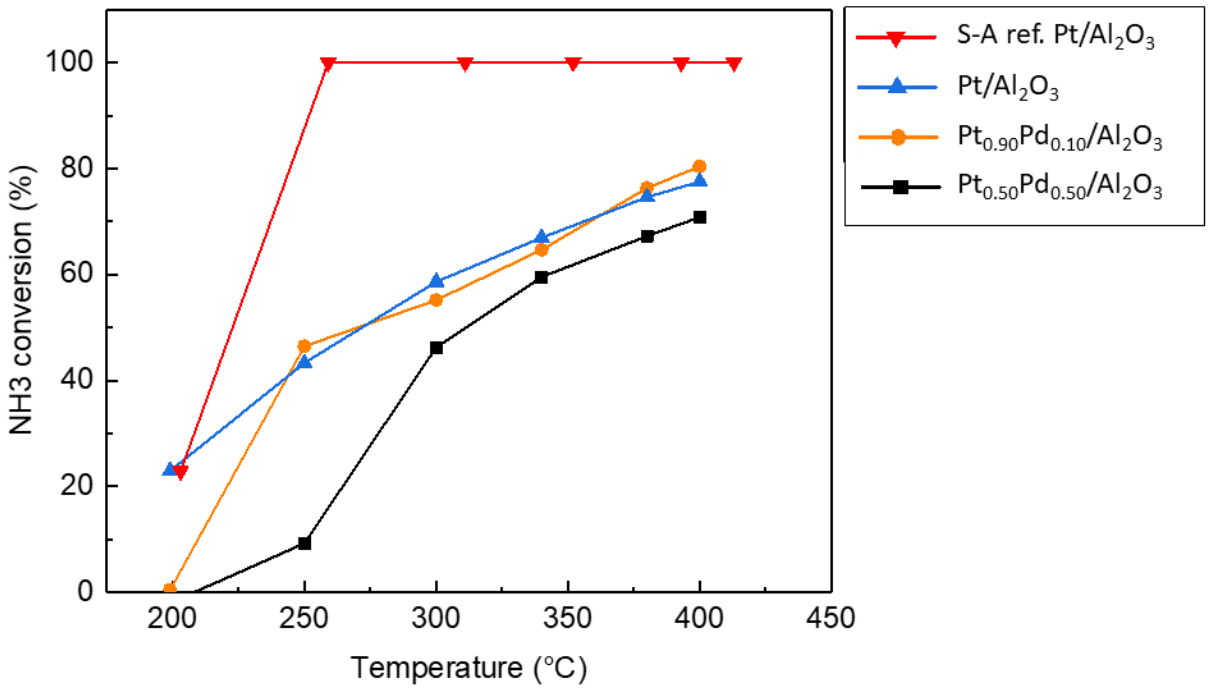

Figure 4-19: NH_3 conversion (%) versus temperature for the in-house prepared $Pt_{1-x}Pd_x/Al_2O_3$ (x = 0, 0.10, 0.50) catalysts and Pt/Al_2O_3 reference catalyst supplied by Sigma-Aldrich. Test conditions: 450 ppm NH_3, 5% O_2 in rest N_2. Total flow 4.2 NL/min.

The NH_3 conversion data presented in Figure 4-19 may be misleading with respect to evaluating catalyst activity. A better approach to extract information on catalyst activity is via the turnover frequency (TOF), which gives a direct measure of the number of NH_3 molecules an active site converts to a product species per second. The TOF values for the catalysts tested in this work can be calculated on basis of knowledge on exact noble metal-loading, mean nanoparticle size and the NH_3 conversion at a fixed temperature (for details on calculations, see section 2.4.2 and appendix 9.1.3). In the current work we have used the mean NP sizes as obtained from the free-standing NPs (Table 4-5), the real catalyst compositions as determined by ICP-MS (Table 4-5) as well as we are ass assuming that the particles do not sinter during the testing. NH_3 conversion data are taken at 200°C and 400°C as the Pt/Al_2O_3 reference catalyst is converting NH_3 100% at 400°C and only the two pure Pt catalysts are active at 200°C. The results from the TOF calculations are reported in Table 4-6. For the sake of clarity, the essential input data for obtaining the TOF values are included to the table (although already reported in various sections above).

Comparing TOF at 400°C for $Pt_{1-x}Pd_x/Al_2O_3$ (x = 0, 0.10, 0.50) show that Pt/Al_2O_3 is superior to the two Pd substituted variants with respect to activity. On the other hand, the two Pd substituted variants appear to have very similar activity at 400°C. Furthermore, by including TOF values at 200°C it can be observed that the Pt/Al_2O_3 reference catalyst is less active than the in-house Pt/Al_2O_3 variant.

Table 4-6: Calculated TOF (s^{-1}) for all catalysts.

	Pt/Al_2O_3	$Pt_{0.90}Pd_{0.10}/Al_2O_3$	$Pt_{0.50}Pd_{0.50}/Al_2O_3$	(Ref.) Pt/Al_2O_3
$\bar{D}$ [nm]	17.4 ±2.5	10.1 ±1.7	10.7 ±1.3	~5
Metal loading	0.55 wt.%	0.64 wt.%	0.83 wt.%	1.0 wt.%
Mass catalyst [g]	0.1330	0.1445	0.1398	0.1131
$NH_{3,400°C}$ [%]	78	80	71	100
$NH_{3,200°C}$ [%]	23	1	0	23
$TOF_{3,400°C}$ [s^{-1}]	21	9.4	6.6	NA
$TOF_{3,200°C}$ [s^{-1}]	6.3	NA	NA	1.2

NA: Not applicable

When oxidizing NH_3 with O_2, NH_3 may convert to N_2, NO_x and N_2O. for application toward NH_3 slip catalysis the desired product is N_2. For this reason, an important criterion in the catalyst evaluation is the selectivity toward N_2 (S_{N_2}). The selectivities toward N_2O, NO_x and N_2 when converting ammonia by oxidation at intermediate temperatures for our $Pt_{1-x}Pd_x/Al_2O_3$ catalysts are plotted versus composition in Figure 4-20. Here, the selectivities are shown at two selected ranges of ammonia conversion (43-46%; 65-67%). The selectivity data for both conversion ranges show clearly that Pt/Al_2O_3 has a significantly higher S_{N_2} than the two Pd substituted variants.

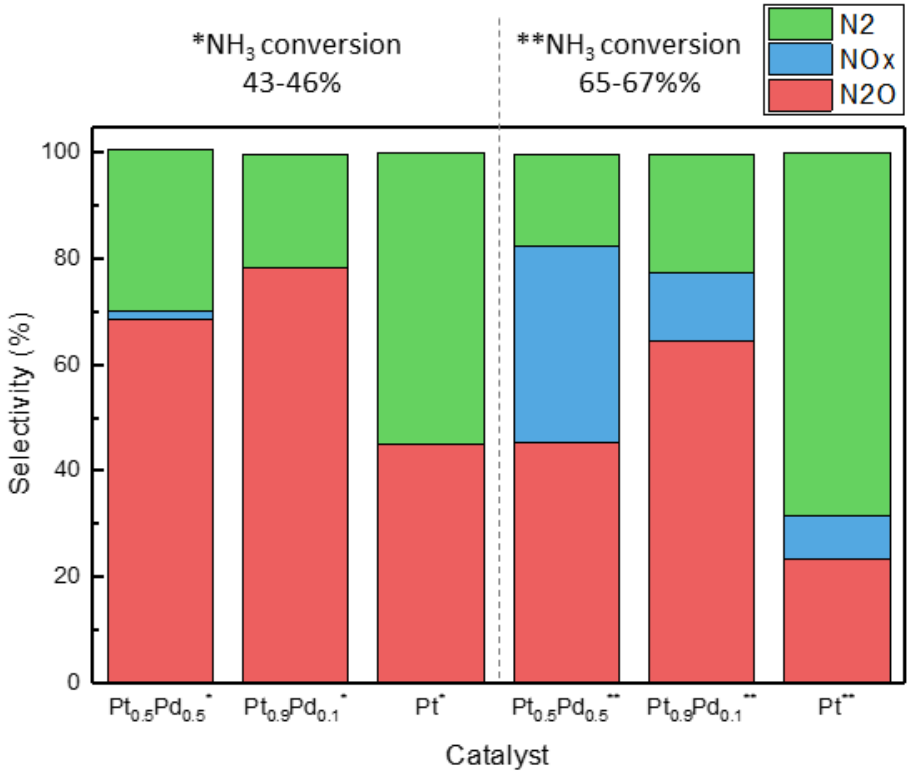

Figure 4-20: Selectivity for N_2, NO_x and N_2O for the respective catalysts for intermediate temperature NH_3 oxidation. The three bars to the left of the stippled vertical line (marked with one star) are for values of ammonia conversion between 43-46%, and to the right of the line are selectivities for values of conversion between 65-67%.

In the case of the Pt/Al_2O_3 reference catalyst, it is slightly more complicated to evaluate the selectivities relative to the catalysts made in-house, as it goes from being close to inactive at 200°C to 100% active at 250°C. Based on this, the selectivity data at all temperatures are

reported in Figure 4-21. From the data reported in Figure 4-21, it can be observed that S_{N_2} selectivity is not favored when NH_3 conversion is 100% and/or at temperatures above 250°C.

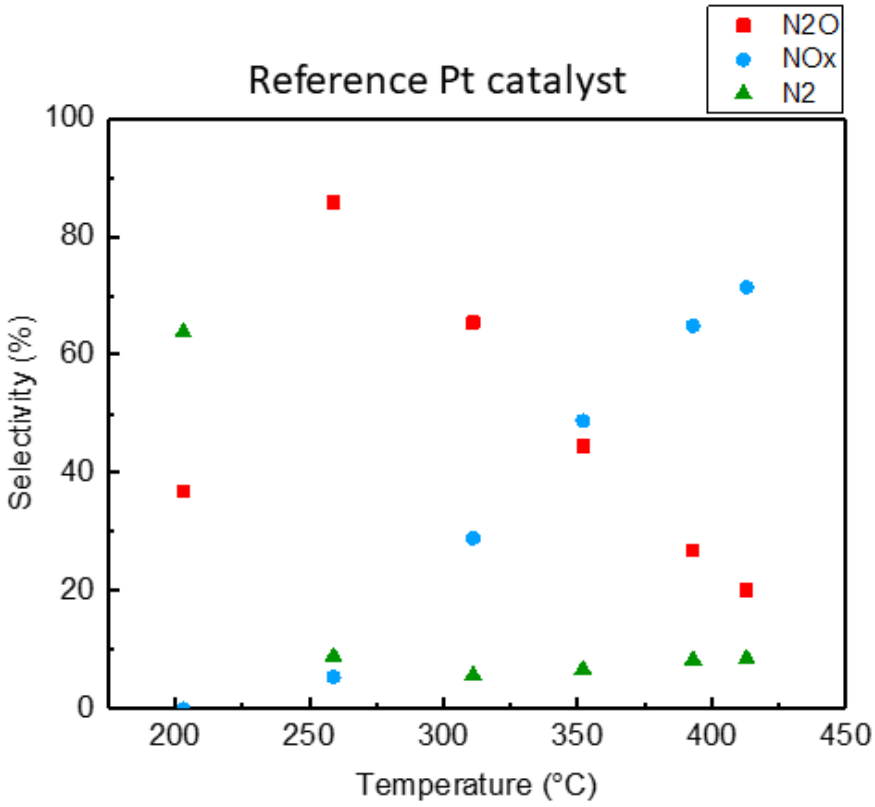

Figure 4-21: Selectivity toward N_2O, NO_x and N_2 for intermediate temperature NH_3 oxidation versus temperature (200-425°C) for the reference Pt/Al_2O_3 catalyst.

With basis in the results obtained from the NH_3 conversion data, TOF calculations as well as selectivity analysis, it is tempting to conclude that the in-house made Pt/Al_2O_3 catalyst has superior performance toward intermediate temperature than the Pd substituted variants. This will be elaborated further in the discussion section, bringing in also information from the materials characterization.

5 Discussion

The aim of the current master project was to undertake a first screening of $Pt_{1-x}Pd_x$ NP synthesis by means of the polyol route and to explore their potential as NH_3 oxidation catalysts at intermediate temperatures. As our research group did not have any previous experience with the $Pt_{1-x}Pd_x$ NP system, it was of key importance to discuss synthesis and characterization research strategies and to draw parallels between different types of experiments to understand how the results are interconnected. Three topics will be considered in detail. These are:

- Strategic aspects of bimetallic nanoparticle synthesis
    - Reaction kinetics of metal precursors
    - Element distribution as a result of kinetics and thermodynamics

- Structural aspects and chemical composition of as-synthesized $Pt_{1-x}Pd_x$ nanoparticles
    - Evaluation of refined unit cell dimensions
    - Evaluation of element distribution in bimetallic samples
    - Evaluation of suitability of powder X-ray diffraction versus TEM

- Feasibility of $Pt_{1-x}Pd_x$ nanoparticles for NH_3 oxidation catalysis
    - Metal composition of nanoparticles
    - Analysis of metal distribution on support in relation to TOF calculations

5.1 Strategic Aspects of Bimetallic Nanoparticle Synthesis

With applications in mind, it is of key importance to be able to control (and document through characterization) the metal distribution in bimetallic nanoparticles. Two approaches can be followed in the synthesis of bimetallic nanoparticles; either a simultaneous- or successive reduction method. Simultaneous reduction of the two different metal precursors is expected to facilitate formation of nanoparticles having a solid solution if the reaction if the reaction kinetics of the metal precursors are similar, whereas the successive reduction approach would promote core-shell nanostructuring. I.e., in the case of the Pt-Pd system we would expect three possible configurations; $Pt_{1-x}Pd_x$ solid solution, Pd@Pt core@shell or Pt@Pd core@shell.

In our work on producing $Pt_{1-x}Pd_x$ NPs it became clear quite early that our standard polyol protocol for simultaneous reduction (section 3.2), produced Pd@Pt core@shell NPs (section 4.2.2). The core-shell structure was documented via the HAADF-STEM and EDX elemental mapping (section 4.2.2). In order to understand the reason for the core-shell formation, kinetics experiments were performed to identify the relative difference in reaction kinetics for nanoparticle formation between the $Pt(acac)_2$ and $Pd(acac)_2$ precursors. It became obvious that the as-synthesized $Pt_{1-x}Pd_x$ nanoparticles are formed with a Pd@Pt core@shell structure, since Pd is precipitated as nanoparticles already in the pre-heating step of 150°C, whereas Pt first start to precipitate when almost all Pd is reacted. It is well known that the reaction kinetics of metal precursors can be tuned by the type of solvent and by the ratio between metal precursor and surfactant [13]. We therefore tested if we could trim the reactivity of the two metal precursors to become more similar or reversed by using different polyalcohols (ethylene glycol, 1,4-butanediol, 1,2-butanediol and 1,3-propanediol) and by varying the quantity of added surfactant (PVP), with metal/PVP ratios of 1/10 and 1/100. A more similar reaction kinetics would promote a solid solution whereas a reverse reaction kinetics would promote an inverse core-shell structure; Pt@Pd core@shell. Our experiments showed that the reactivity of $Pd(acac)_2$ in all cases were very fast compared to that of $Pt(acac)_2$. This finding is surprising since Bundli [13] was able to manipulate the reaction kinetics of $Pt(acac)_2$ relative to $Rh(acac)_3$ by tuning the same parameters. Another parameter, not explored by us so far, is to change the metal precursor source. We here take notice of the work of Long et al. who reports successful synthesis of the reverse configuration, Pt@Pd core@shell NPs by the successive reduction of H_2PtCl_6 and Na_2PdCl_4, although in a different polyol system [21]. At circumstances where the reaction kinetics of the two selected precursors hardly can be sufficiently tuned, a solid solution can be obtained by an alternative approach where the nanoparticles are aged in the reaction medium and thereby allowing atomic level mixing by post diffusion in the solid particles. The current experimental results obtained by means of powder X-ray diffraction and the "Whole Powder Pattern Fitting" method for $Pt_{0.50}Pd_{0.50}$ bimetallic nanoparticles indicate that Pt and Pd are mixed at the atomic level after aging for 24 hours at 220°C (section 4.2.2). This result is encouraging, as post treatment of the as-synthesized nanoparticles then appears as a powerful tool to tune the type of elemental nanostructuring. This being said, atomic mixing in form of a solid solution by means of aging at elevated temperatures will only occur if this configuration is the preferred thermodynamic state. According to the phase diagram for bulk Pt-Pd (section 1.4), Pt and Pd should give a two-phase situation for a sample with nominal composition $Pt_{0.50}Pd_{0.50}$. However, cross-overs in stability are frequently seen when going from bulk to the

nanometer scale, and it could well be the case that a solid solution is thermodynamically the most stable configuration for $Pt_{1-x}Pd_x$ particles at the nanometer scale. Finally, a possible route to achieve reverse elemental nanostructuring would be to nucleate and grow the slow component first and thereafter add the second component and allow it to nucleate on the existing NP surfaces. This approach was also explored in the current thesis, whereof Pt was first nucleated followed by Pd deposition (section 4.3). Preliminary TEM analyses confirm that both Pt and Pd are present in the particles, however the quality of the data analysis does not allow us to conclude fully if we have a reverse core-shell structure (Pd@Pt core@shell) or if Pt is diffusing towards the core Pd component and forming a solid solution.

In order to synthesize bimetallic nanoparticles with a specific element distribution, care must be taken in the planning of the experiments. The reactivity of the metal precursors, type of solvent, concentration of surfactant together with stepwise or simultaneous reduction steps and post annealing are all key parameters to control and utilize to achieve the targeted product. In addition, to be in position to document the elemental nanostructuring in the obtained products, special care with respect to the characterization work must be taken (see5.2). In brief, we have successfully produced $Pt_{1-x}Pd_x$ solid solution, Pd@Pt core@shell and possibly Pt@Pd core@shell particles by:

- Exploring the relative reaction kinetics of metal precursors. Optimize for similar or different reaction kinetics to obtain the desired nanostructuring (solid solution versus core-shell) by varying solvent, metal precursor and metal precursor – surfactant ratio

- Consider an aging step for homogenization of as-synthesized nanoparticles

- Combining powder X-ray diffraction and TEM analyses for determination of type of nanostructuring

5.2 Structural Aspects and Chemical Composition of As-Synthesized $Pt_{1-x}Pd_x$ Nanoparticles

In the current work, both powder X-ray diffraction and TEM (HAADF-STEM and EDX) were utilized for chemical analysis of the synthesized $Pt_{1-x}Pd_x$ particles.

According to powder X-ray diffraction, all synthesized $Pt_{1-x}Pd_x$ samples are phase pure; no extra Bragg peaks were observed relative to those indexed according to the ccp type structure of the metallic nanoparticles (Figure 4-1).

Rietveld refinements for the end members Pt and Pd gave a = 3.9228 ± 0.0009 Å and a = 3.928 ± 0.004 Å, respectively. The a-axis for Pt, is in good agreement with other reports for particles in the nanometer scale as well as bulk sample values (see Table 1-2 and Table 1-3), however, we note that deviations are reported by Teranishi et al. [42] for very small particles, i.e. 2-3 nm. In the case of Pd, the picture is slightly more complicated. Our obtained value of a = 3.928 ± 0.004 Å falls into the range of reported values for Pd (3.90-3.98) for nanoparticles, but is significantly larger than that of bulk Pd (3.891 Å); see Table 1-2 and Table 1-3. Jeon et al. [44] suggest that the unit cell is sensitive to the size of the Pd nanoparticle; i.e. there is a finite size effect. The comparison of reported unit cell dimensions of a compound from different laboratories ought to be straightforward, but is frequently more complicated, and in particular so for the lesser well defined nano sized materials. One may then question how the data analysis is done, what type of instrumentation was used for collecting the X-ray diffraction data as well as how the sample quality is. Different research groups may have synthesized the material by different routes, which in turn may have created different types and amounts of imperfections in the particles. All this adds uncertainty, and it is likely that the spread we see in the reported a-axis can partly be explained by such factors.

In the study of Muri [15], the a-axis versus Rh content (x) for $Pt_{1-x}Rh_x$ followed a nice Vegard law correlation, whereof the end members Pt and Rh had a ~ 3.92 Å and a ~ 3.81 Å, respectively. Bundli [13] confirmed later that the $Pt_{1-x}Rh_x$ NPs formed a solid solution by means of TEM. In the case of our bimetallic $Pt_{1-x}Pd_x$ particles any evaluation by means of the Vegard law approach gives no meaning. Firstly, by carefully looking into the reported a-axis values for the $Pt_{1-x}Pd_x$ series (Table 4-1) obtained by the standard polyol route, we see that the a-axis is within uncertainty not affected by the degree of Pd substitution (x). With only powder X-ray diffraction data at hand, it is difficult to conclude as the end member Pd also behaves

unexpectedly (see above). For this reason, TEM and kinetic experiments must be brought into consideration. The experiments on monitoring the kinetics of the two metal precursors [($Pt(acac)_2$ and $Pd(acac)_2$] clearly revealed that the reaction kinetics of Pd is faster than that of Pt when using standard polyol conditions (4.2.1). This implies that these synthesis conditions facilitate a Pd@Pt core@shell structure. To verify the real element distribution in the synthesized nanoparticles HAADF-STEM and EDX was applied (4.2.2), which indeed documented that the nanoparticles have a Pd@Pt core@shell structure. In order to correctly obtain structural information of bimetallic $Pt_{1-x}Pd_x$ NP samples from the powder X-ray diffraction data, such information must be implemented into the model and "whole powder pattern fitting" (WPPF) is necessary with basis in high quality diffraction data, and like here, collected at a large-scale facility such as the Swiss-Norwegian Beam Lines, ESRF, Grenoble. This implies that many structural aspects should be considered in the data modelling: Pt-Pd distribution throughout the particle; Pt-Pd molar ratio; particle size and size distribution; degree of stacking disorder and possibly also anisotropic particle shape along with unit cell dimensions and temperature displacement factors. In the current work this approach was adopted for two samples, both synthesized by the standard polyol approach but aged for 2 and 24 hours, respectively. The WPPF analysis of the sample aged for 2 hours indicated a core-shell model in accordance with HAADF-STEM and EDX data, whereas the results for the sample aged for 24 h pointed in direction of a solid solution (4.2.2).

A concluding remark to the structural analysis of bimetallic nanoparticles is that powder X-ray diffraction and the TEM methods should go hand in hand. Traditionally PXRD is considered to be a very strong tool for characterization of crystal structure aspects of materials, but in cases such as the bimetallic $Pt_{1-x}Pd_x$ nanoparticles the most correct description is obtained by combining information from the two techniques. It should also be added that the kinetics experiments added valuable information for the structural evaluation of these particles.

5.3 Feasibility of $Pt_{1-x}Pd_x$ Nanoparticles for NH_3 Oxidation Catalysis

Three $Pt_{1-x}Pd_x/Al_2O_3$ (x = 0, 0.10, 0.50) catalysts were prepared in-house, and a reference Pt/Al_2O_3 catalyst was bought from Sigma-Aldrich. These were tested towards suitability for intermediate temperature NH_3 oxidation (4.4.2). It was concluded in section 4.4.2 that Pd had a negative effect on the reaction of ammonia oxidation towards N_2 as the product. Furthermore, it was found that the Pt/Al_2O_3 (prepared in-house) performed better than the rest of the tested catalysts at intermediate temperatures, based both on TOF calculations and with respect to selectivity toward N_2 yield. All three in-house made catalysts performed better than the reference catalyst supplied by Sigma-Aldrich. Interestingly, it was also observed that the catalytic activity and N_2 selectivity for $Pt_{0.90}Pd_{0.10}/Al_2O_3$ and $Pt_{0.50}Pd_{0.50}/Al_2O_3$ were similar. The bimetallic $Pt_{1-x}Pd_x$ (x = 0.1, 0.5) NPs used in the preparation of the catalysts are of the type Pd@Pt core@shell as documented through the HAADF-STEM, EDX and kinetic analysis (see e.g. 5.2). This implies that the two catalysts have similar surfaces, and as the catalysis take place only on the top atomic layer(s), it is expected that the two samples perform in the same way. One may speculate why Pt/Al_2O_3 performs slightly better than $Pt_{0.90}Pd_{0.10}/Al_2O_3$ and $Pt_{0.50}Pd_{0.50}/Al_2O_3$. According to EDX mapping of $Pt_{0.50}Pd_{0.50}$ NPs (Figure 4-8) there is some Pd in the Pt shell, and it is therefore tempting to state that Pd has a poisoning/inhibiting effect on the ammonia oxidation reaction. In order to verify this statement, some further experiments should be conducted. A final note; for the PtPd system the alloying did not have a positive influence on the catalysis. However, within the ASCAT project, some PtRh based $Pt_{1-x}Rh_x/Al_2O_3$ catalysts were tested for the same oxidation reaction. For NPs in the PtRh system, it is observed that adding some Rh to the Pt has a positive effect both with respect to TOF and N_2 selectivity [99]. Currently, we have no mechanistic explanation to the different behaviour between the PtPd system and the PtRh system.

Turnover frequency (TOF) is an important parameter to evaluate catalyst activity as it gives a direct measure of number of molecules (ammonia) that is converted per unit time per active site on the catalyst. However, the derived TOF value is especially sensitive to one assumption that has been made, i.e. the size of the active nanoparticles during the catalytic reaction at elevated temperatures. In the current study the size of the free-standing nanoparticles (before deposited on Al_2O_3) were used as a measure of the NP size during catalysis (Figure 4-17). The reason for this choice is that the bright field TEM images of the supported catalysts (used during catalysis)

do not provide details on the noble metal dispersion and hence not on any minor sintering that possibly could take place during catalysis (Figure 4-18). A firmer conclusion on the TOF calculations could probably be achieved by imaging the catalysts in HAADF-STEM mode, which will give very good atomic number contrast. In a HAADF-STEM image the PtPd NPs would appear as bright spots since Pt and Pd have much higher atomic numbers than the constituents of Al_2O_3.

6 Conclusions

A standard polyol approach was followed to produce phase pure $Pt_{1-x}Pd_x$ NPs in 1,4-butanediol in the presence of PVP in the current work. The nanoparticle formation reaction kinetics in the synthesis was analyzed in multiple experiments, revealing a significant difference in reactivity between the Pt- and Pd precursors used in the synthesis method. Furthermore, it was concluded that it was not possible to tune the reaction kinetics of the two precursors by using a different polyalcohol or tuning the metal precursor/surfactant ratio.

HAADF-STEM with complementary EDX elemental mapping studies was performed on $Pt_{0.50}Pd_{0.50}$ NPs to explore the elemental distribution in samples produced by the standardized polyol approach. The $Pt_{0.50}Pd_{0.50}$ NPs had a Pd@Pt core@shell elemental distribution when the aging time in the synthesis was 2 h. Another experiment was performed in addition, to explore whether an increased aging time would facilitate diffusion of the metallic species, forming a solid solution. In this case, the same synthesis conditions were used, except the increased aging time of 24 h. Our results based on synchrotron X-ray diffraction, points in the direction that solid solution was achieved for $Pt_{1-x}Pd_x$ NPs, however these results are not fully conclusive, as the similar behavior of Pt and Pd in the X-ray beam poses severe challenges in the data treatment with the "Whole Powder Pattern Fitting method".

The standard polyol approach is a simultaneous reduction method, and in this scenario the conclusion is that the metal precursor reaction kinetics plays an imperative role in the determination of the elemental distribution in the nanoparticle products.

Further, we reached great lengths towards tuning the elemental distribution in nanoparticles with nominal composition $Pt_{0.50}Pd_{0.50.}$ This was done by modifying the standard synthesis protocol, altering the methodology from a simultaneous reduction to a successive reduction method. The outline of the experiment was that Pd was first reduced followed by Pt (the reverse

situation as described above). TEM analysis showed that both elements were present in the particles. Due to lack of resolution it was not possible to conclude if the particles had a Pt@Pd core@shell or solid solution configuration.

Through the current work, we have shown that when producing bimetallic nanoparticles, two different methodologies can be used; a simultaneous reduction- or successive reduction method. For a wise choice between these two methods, a preliminary screening of the relative reaction kinetics of the two metal precursors should be performed. HAADF-STEM with complementary EDX elemental mapping has also been shown to be a very good characterization method of the bimetallic nanoparticles, as it provides information about elemental distribution on an atomic scale. With this characterization method it is easy to conclude on the elemental distribution in the nanoparticles.

It has been shown that routine powder X-ray diffraction characterization method is not necessarily capable of providing conclusive results for bimetallic nanoparticles, with respect to determination of composition from the unit cell dimension (a-axis). This is particularly critical if the nanoparticles have a core-shell structure rather than a solid solution. In the case of a core-shell situation one of the constituents may not contribute to the diffraction pattern due to being too thin or give a significant peak boarding which is merged with the background. In such situations it becomes difficult to extract exact crystallographic information, and diffraction data of high quality are requested together with detailed additional information on the sample to provide a good analysis using e.g. the "Whole Powder Pattern Fitting" analysis. In this context it should also be added that unit cell dimensions are reported to undergo "finite size effect", which in turn complicates structural data analysis.

$Pt_{1-x}Pd_x/Al_2O_3$ metal-on-support catalysts have been tested at YARA International, Herøya. It was found that our Pt/Al_2O_3 catalyst prepared in-house showed promising catalytic activity and selectivity toward N_2 in oxidation reaction of ammonia. Although Pd has been proven to exist mainly in the core and less in the shell of the core@shell $Pt_{1-x}Pd_x/Al_2O_3$ catalysts, we have shown that when Pd was incorporated into the supported NPs, it had a negative effect towards conversion of NH_3 to N_2.

The material characterization of the $Pt_{1-x}Pd_x/Al_2O_3$ catalysts is in need for optimization to facilitate easier detection of the metal NPs on the support material. Via bright field TEM-imaging performed on the as-prepared catalysts, the alumina support material gave rise to diffraction contrast which could be mistaken for metallic nanoparticles. In this case, the bright

field imaging technique might not be the optimal choice to determine the distribution and appearance of the supported nanoparticles. A suggested alternative or complementary imaging technique in this regard, is HAADF-STEM imaging. The contrast in this imaging technique is highly dependent on atomic number (Z-contrast) of the specimen, and should neglect misleading contrast-forming effects associated with bright field TEM-imaging, such as e.g. diffraction contrast.

7 Perspectives

In the current work we have used both simultaneous and stepwise reduction to facilitate different PtPd nanostructuring. In the modified polyol method, stepwise reduction was applied to form Pt@Pd NPs. This part of the study could be developed further to achieve clearer results. It would be interesting to investigate the effect of diluting the reactants on the overgrowth of Pd on the Pt-seeds. A lower concentration of Pd in the solution surrounding the Pt-seeds might better facilitate controlled overgrowth, as the situation in this scenario is closer to thermodynamic equilibrium. In our case, we saw that too rapid Pd-precursor reaction kinetics can push the system far away from equilibrium conditions, leading to the formation of small NPs of pure Pd by burst nucleation. The goal is to consume all of the Pd in the form of overgrowth on the Pt-seeds. Another approach that may be able to solve this problem is to perform a series of experiments screening different types of metal precursors with respect to their relative reaction kinetics. The elemental distribution in the product-NPs can in this manner be tuned by combining precursors with different relative reaction kinetics. The nanostructuring should be documented by means of high-quality HAADF-STEM-EDX analysis.

Synchrotron powder X-ray diffraction (SXRD) experiments were performed on $Pt_{0.50}Pd_{0.50}$ NPs synthesized in 1,4-butanediol with the presence of PVP according to a standardized polyol method in the current work. Careful analysis of the data collected on a sample aged for 2 h by means of the "Whole Powder Pattern Fitting" method indicated a core@shell structure as documented through high-quality HAADF-STEM-EDX analysis. When the aging time was 24 h, the "Whole Powder Pattern Fitting" results hinted at a Pt-Pd solid solution in the NPs instead. HAADF-STEM-EDX measurements for this composition are unfortunately lacking due to instrumental errors, and their results are still pending. More importantly it would be of great interest to explore and develop on the combined SXRD – "Whole Powder Pattern Fitting"

strategy toward analysis of such nanostructures. In such a scenario, more optimized nanostructures for SXRD should be provided (significant atomic number contrast and different atomic radii of the constituents). Among the noble metal systems our group work on, Pt-Rh stand out as a prime candidate. Indeed, the analysis should go hand in hand with HAADF-STEM-EDX analysis.

In order to obtain a more complete understanding of the role of Pd in the $Pt_{1-x}Pd_x/Al_2O_3$ catalysts that were produced, a Pd/Al_2O_3 catalyst must be prepared. This can also give insight to whether it is worth also investigating $Pt_{1-x}Pd_x/Al_2O_3$ catalysts with Pt@Pd (core@shell) element distribution for oxidation of ammonia. In a broader prospective, the role of Pd substitution should be compared with other substituents as Rh and explanations for different behavior should be searched for.

8 Literature

1. Xiong, Y. and X. Lu, *Metallic Nanostructures From Controlled Synthesis to Applications*. 2015. p. XI, 301 p. 196 illus., 137 illus. in color. online resource.
2. Sun, S., *Chemical Synthesis of Monodisperse Magnetic Nanoparticles for Sensitive Cancer Detection.* Journal of Inorganic and Organometallic Polymers and Materials, 2014. **24**(1): p. 33-38.
3. Wikipedia. *Cuboctahedron*. [Image] [cited 2017 28.09]; Image of cuboctahedron]. Available from: https://en.wikipedia.org/wiki/Cuboctahedron.
4. Chakravarty, C., P.G. Debenedetti, and F.H. Stillinger, *Lindemann measures for the solid-liquid phase transition.* The Journal of Chemical Physics, 2007. **126**(20): p. 204508.
5. Sigma-Aldrich. *Quantum Dots*. [cited 2017 04.10]; Available from: http://www.sigmaaldrich.com/technical-documents/articles/materials-science/nanomaterials/quantum-dots.html.
6. MIT. *Nanoclusters*. [cited 2017 05.10]; Available from: http://nanocluster.mit.edu/research.php.
7. *Magnetic iron oxide nanoparticles for MR contrast agents*. [cited 2017 04.10]; Available from: http://bme240.eng.uci.edu/students/08s/ykim30/02.htm.
8. *MENA3000 Lectures spring 2015*.
9. Zacharaki, E., *Burst nucleation by hot injection for size controlled synthesis of ε-cobalt nanoparticles.* Chemistry Central Journal, 2016. **10**(10): p. 11.
10. Reyes-Coronado, D., et al., *Phase-Pure TiO2 Nanoparticles: Anatase, Brookite and Rutile*. Vol. 19. 2008. 145605.
11. Somorjai, G.A. and C. Aliaga, *Molecular Studies of Model Surfaces of Metals from Single Crystals to Nanoparticles under Catalytic Reaction Conditions. Evolution from Prenatal and Postmortem Studies of Catalysts.* Langmuir, 2010. **26**(21): p. 16190-16203.
12. Ghosh Chaudhuri, R. and S. Paria, *Core/Shell Nanoparticles: Classes, Properties, Synthesis Mechanisms, Characterization, and Applications.* Chemical Reviews, 2012. **112**(4): p. 2373-2433.
13. Bundli, S.A., *Syntese og karakterisering av Pt1-xRhx nanopartikler. Kolloidal partikkelsyntese, røntgendiffraksjon og elektronmikroskopi*, in *Department of Physics, Faculty of Mathematics and Natural Sciences*. 2016, University of Oslo.
14. Zhou, M., et al., *Quantitative Analysis of the Reduction Kinetics Responsible for the One-Pot Synthesis of Pd–Pt Bimetallic Nanocrystals with Different Structures.* Journal of the American Chemical Society, 2016. **138**(37): p. 12263-12270.
15. Muri, M.E., *Synthesis and characterization of free standing Pt-Rh nanoparticles, and 2wt. % Pt0.70Rh0.30/Al2O3 and 20 wt. % Co1-xRex/Al2O3 (0.00 $\leqslant x \leqslant$ 0.15) metal-on-support catalysts*, in *Department of Physics, Faculty of Mathematics and Natural Sciences*. 2015, University of Oslo.
16. Gupta, D., et al., *A low temperature hydrogen sensor based on palladium nanoparticles.* Sensors and Actuators B: Chemical, 2014. **196**(Supplement C): p. 215-222.
17. Wang, Y., et al., *Shape-Controlled Synthesis of Palladium Nanocrystals: A Mechanistic Understanding of the Evolution from Octahedrons to Tetrahedrons.* Nano Letters, 2013. **13**(5): p. 2276-2281.
18. Hei, H., et al., *Controlled Synthesis and Characterization of Nobel Metal Nanoparticles.* Soft Nanoscience Letters, 2012. **Vol.02No.03**: p. 7.
19. Lee, Y.-W., S.-E. Oh, and K.-W. Park, *Highly active Pt–Pd alloy catalyst for oxygen reduction reaction in buffer solution.* Electrochemistry Communications, 2011. **13**(12): p. 1300-1303.
20. Lee, Y.-W., et al., *Glycerol-mediated synthesis of Pd nanostructures with dominant {111} facets for enhanced electrocatalytic activity.* Catalysis Communications, 2011. **15**(1): p. 137-140.

21. Long, N.V., et al., *Synthesis and characterization of Pt–Pd alloy and core-shell bimetallic nanoparticles for direct methanol fuel cells (DMFCs): Enhanced electrocatalytic properties of well-shaped core-shell morphologies and nanostructures.* International Journal of Hydrogen Energy, 2011. **36**(14): p. 8478-8491.
22. Long, N.V., et al., *Effects of heat treatment and poly(vinylpyrrolidone) (PVP) polymer on electrocatalytic activity of polyhedral Pt nanoparticles towards their methanol oxidation.* Colloid and Polymer Science, 2011. **289**(12): p. 1373-1386.
23. Papa, F., et al., *Morphology and chemical state of PVP-protected Pt, Pt–Cu, and Pt–Ag nanoparticles prepared by alkaline polyol method.* Journal of Nanoparticle Research, 2011. **13**(10): p. 5057.
24. Chen, Y., et al., *Controlled synthesis of palladium icosahedra nanocrystals by reducing H2PdCl4 with tetraethylene glycol.* Colloids and Surfaces A: Physicochemical and Engineering Aspects, 2009. **348**(1): p. 145-150.
25. Li , C., et al., *Controllable Polyol Synthesis of Uniform Palladium Icosahedra: Effect of Twinned Structure on Deformation of Crystalline Lattices.* Angewandte Chemie International Edition, 2009. **48**(37): p. 6883-6887.
26. Han, S.-B., et al., *Platinum nanocube catalysts for methanol and ethanol electrooxidation.* Electrochemistry Communications, 2008. **10**(7): p. 1044-1047.
27. Park, J.Y., et al., *Tuning of Catalytic CO Oxidation by Changing Composition of Rh−Pt Bimetallic Nanoparticles.* Nano Letters, 2008. **8**(2): p. 673-677.
28. Tao, F., et al., *Reaction-Driven Restructuring of Rh-Pd and Pt-Pd Core-Shell Nanoparticles.* Science, 2008. **322**(5903): p. 932.
29. Song, H., et al., *Pt Nanocrystals: Shape Control and Langmuir−Blodgett Monolayer Formation.* The Journal of Physical Chemistry B, 2005. **109**(1): p. 188-193.
30. Xiong, Y., et al., *Kinetically Controlled Synthesis of Triangular and Hexagonal Nanoplates of Palladium and Their SPR/SERS Properties.* Journal of the American Chemical Society, 2005. **127**(48): p. 17118-17127.
31. Gao, F., et al., *A Review on Selective Catalytic Reduction of NOx by NH3 over Mn–Based Catalysts at Low Temperatures: Catalysts, Mechanisms, Kinetics and DFT Calculations.* Catalysts, 2017. **7**(7).
32. Zhang, Q., et al., *In situ DRIFTS studies on CuO-Fe2O3 catalysts for low temperature selective catalytic oxidation of ammonia to nitrogen.* Applied Surface Science, 2017. **419**(Supplement C): p. 733-743.
33. ASM. *ASM Alloy Phase Diagram Database*. [Image] [cited 2017 28.09]; Pd-Pt binary phase diagram]. Available from: http://mio.asminternational.org/apd/index.aspx.
34. Webelements. *Palladium: crystal structures*. [cited 2017 02.10]; Lattice parameters of Pd]. Available from: https://www.webelements.com/palladium/crystal_structure.html.
35. Webelements. *Platinum: crystal structures*. [cited 2017 06.10]; Lattice parameters of Pt]. Available from: https://www.webelements.com/platinum/crystal_structure.html.
36. Gibaud, A., et al., *An X-ray scattering study of Pt1−xVx alloys.* Journal of Alloys and Compounds, 2009. **484**(1): p. 168-171.
37. Manoun, B., et al., *Thermal Expansion of Polycrystalline Ti3SiC2 in the 25°–1400°C Temperature Range.* Journal of the American Ceramic Society, 2005. **88**(12): p. 3489-3491.
38. Arblaster, J.W., *Crystallographic Properties of Platinum.* Platinum Metals Review, 1997. **41**(1): p. 12-21.
39. Arblaster, J.W., *Crystallographic Properties of Palladium.* Platinum Metals Review, 2012. **56**(3): p. 181-189.
40. Thiebaut, S., et al., *Structural and thermodynamic properties of the deuterium-palladium solid solutions systems: D2-[Pd(Pt), Pd(Rh), Pd(Pt, Rh)].* Journal of Alloys and Compounds, 1995. **231**(1): p. 440-447.
41. Moysan, I., et al., *Pd–Pt alloys: correlation between electronic structure and hydrogenation properties.* Journal of Alloys and Compounds, 2001. **322**(1): p. 14-20.

42. Teranishi, T., et al., *Size Control of Monodispersed Pt Nanoparticles and Their 2D Organization by Electrophoretic Deposition.* The Journal of Physical Chemistry B, 1999. **103**(19): p. 3818-3827.
43. Teranishi, T. and M. Miyake, *Size Control of Palladium Nanoparticles and Their Crystal Structures.* Chemistry of Materials, 1998. **10**(2): p. 594-600.
44. Jeon, Y.T. and G.H. Lee, *Magnetism of the fcc Rh and Pd nanoparticles.* Journal of Applied Physics, 2008. **103**(9): p. 094313.
45. Shinohara, T., T. Sato, and T. Taniyama, *Surface Ferromagnetism of Pd Fine Particles.* Physical Review Letters, 2003. **91**(19): p. 197201.
46. Salas, G., R. Costo, and M.d.P. Morales, *Chapter 2 - Synthesis of Inorganic Nanoparticles*, in *Frontiers of Nanoscience*, M.d.l.F. Jesus and V. Grazu, Editors. 2012, Elsevier. p. 35-79.
47. Hiemenz, P.C. and R. Rajagopalan, *Principles of colloid and surface chemistry*. 3rd ed. 1997, New York: Marcel Dekker. xix, 650 p.
48. Hunter, R.J., *Introduction to modern colloid science*. 1st ed. 1993, Oxford ; New York: Oxford University Press. viii, 338 p.
49. Hornyak, G.L., *Introduction to nanoscience & nanotechnology*. 2009, Boca Raton: CRC Press. xxxiv, 1593 p.
50. Morrison, I.D. and S. Ross, *Colloidal dispersions : suspensions, emulsions, and foams*. 2002, New York: Wiley. xxvii, 616 p.
51. Mullin, J.W., *Crystallization*. 4th ed. 2001, Oxford ; Boston: Butterworth-Heinemann. xv, 594 p.
52. JuliyaK. *Critical Radius Illustration*. [Image] 2008 [cited 2017 22.05-17]; Image showing interfacial and volume free energy, critical radius]. Available from: https://commons.wikimedia.org/wiki/File:Critical_radius.jpg.
53. JuliyaK. *Wikimedia commons*. [Image] 2008 23.02-2015 [cited 2017 23.05-2017]; Comparison of the free energy barrier for heterogeneous and homogeneous nucleation]. Available from: https://commons.wikimedia.org/wiki/File:Hethomnucdifference.JPG.
54. Ingham, B., et al., *How Nanoparticles Coalesce: An in Situ Study of Au Nanoparticle Aggregation and Grain Growth.* Chemistry of Materials, 2011. **23**(14): p. 3312-3317.
55. Atkins, P.W., *Shriver & Atkins' inorganic chemistry*. 5th ed. 2010, Oxford ; New York: Oxford University Press. xxiv, 824 p.
56. Polte, J., *Fundamental growth principles of colloidal metal nanoparticles - a new perspective.* CrystEngComm, 2015. **17**(36): p. 6809-6830.
57. Sau, T.K. and A.L. Rogach, *Nonspherical Noble Metal Nanoparticles: Colloid-Chemical Synthesis and Morphology Control.* Advanced Materials, 2010. **22**(16): p. 1781-1804.
58. Commons, W. [Image] [cited 2017 17.08]; Figure of octahedron shape]. Available from: https://commons.wikimedia.org/wiki/File:Octahedron.jpg.
59. Commons, W. [Image] [cited 2017 17.08]; Image of truncated octahedron]. Available from: https://commons.wikimedia.org/wiki/File:Truncatedoctahedron.jpg.
60. Metals, S.S.o.f. [Figure] [cited 2017 18.08]; Figures used from this site (crystallographic planes in fcc structure; (111), (110) and (100)]. Available from: http://www.chem.qmul.ac.uk/surfaces/scc/scat1_2.htm.
61. Iqbal, P., J.A. Preece, and P.M. Mendes, *Nanotechnology: The "Top-Down" and "Bottom-Up" Approaches*, in *Supramolecular Chemistry*. 2012, John Wiley & Sons, Ltd.
62. Natelson, D., *Nanostructures and nanotechnology*. 2015, Cambridge: Cambridge University Press. x, 630 pages.
63. Ataee-Esfahani, H. and S.E. Skrabalak, *Manipulating the architecture of Pd@Pt nanostructures through metal-selective capping agent interactions.* Chemical Communications, 2016. **52**(71): p. 10783-10786.
64. van Embden, J., A.S.R. Chesman, and J.J. Jasieniak, *The Heat-Up Synthesis of Colloidal Nanocrystals.* Chemistry of Materials, 2015. **27**(7): p. 2246-2285.
65. Schubert, U. and N. Hüsing, *Synthesis of inorganic materials*. 3rd completely rev. and enlarged ed. 2012, Weinheim: Wiley-VCH. xxii, 370 p.

66. Biacchi, A.J. and R.E. Schaak, *The Solvent Matters: Kinetic versus Thermodynamic Shape Control in the Polyol Synthesis of Rhodium Nanoparticles.* ACS Nano, 2011. **5**(10): p. 8089-8099.
67. Toshima, N., *Inorganic Nanoparticles for Catalysis*, in *Inorganic Nanoparticles*. 2010, CRC Press. p. 475-509.
68. Fievet, F., et al., *Homogeneous and heterogeneous nucleations in the polyol process for the preparation of micron and submicron size metal particles.* Solid State Ionics, 1989. **32**: p. 198-205.
69. Dong, H., Y.C. Chen, and C. Feldmann, *Polyol synthesis of nanoparticles: status and options regarding metals, oxides, chalcogenides, and non-metal elements.* Green Chemistry, 2015. **17**(8): p. 4107-4132.
70. Murphy, C.J., T.K. Sau, and A.L. Rogach, *Complex-shaped metal nanoparticles : bottom-up syntheses and applications*. 2012, Weinheim: Wiley-VCH. xxiii, 558 p.
71. Bock, C., et al., *Size-Selected Synthesis of PtRu Nano-Catalysts: Reaction and Size Control Mechanism.* Journal of the American Chemical Society, 2004. **126**(25): p. 8028-8037.
72. Atkins, P.W. and J. De Paula, *Atkins' Physical chemistry*. Tenth edition. ed. 2014, Oxford ; New York: Oxford University Press. xxv, 1008 pages.
73. Database, P.P. *Polymer Properties Database*. [Webpage] 2015 [cited 2017 15.05-2017]; Available from: http://polymerdatabase.com/polymer%20physics/Chi%20%20Temp%20dependence.html.
74. Koczkur, K.M., et al., *Polyvinylpyrrolidone (PVP) in nanoparticle synthesis.* Dalton Transactions, 2015. **44**(41): p. 17883-17905.
75. Thomas, J.M. and W.J. Thomas, *Principles and practice of heterogeneous catalysis*. 1997, Weinheim ; New York: VCH. xxiii, 669 p.
76. Ponec, V.r. and G.C. Bond, *Catalysis by metals and alloys*. Studies in surface science and catalysis. 1995, Amsterdam ; New York: Elsevier. x, 734 p.
77. Jia, C.-J. and F. Schuth, *Colloidal metal nanoparticles as a component of designed catalyst.* Physical Chemistry Chemical Physics, 2011. **13**(7): p. 2457-2487.
78. Santos, P.S., H.S. Santos, and S.P. Toledo, *Standard transition aluminas. Electron microscopy studies.* Materials Research, 2000. **3**: p. 104-114.
79. Williams, D.B. and C.B. Carter, *Transmission electron microscopy : a textbook for materials science*. 2nd ed. 2008, New York: Springer.
80. Jeol. *Scanning Electron Microscope A to Z, Basic Knowledge For Using The SEM*. [User Guide] [cited 2017 21.08]; User Guide for the SEM]. Available from: https://www.jeol.co.jp/en/applications/pdf/sm/sem_atoz_all.pdf.
81. Hitachi, *Let's Familiarize Ourselves with the SEM!*, H.H.-T. Corporation, Editor. 2013: Tokyo, Japan.
82. Flewitt, P.E.J. and R.K. Wild, *Physical methods for materials characterisation*. Third edition. ed. Series in materials science and engineering. 2017, Boca Raton, FL: CRC Press, Taylor & Francis Group. pages cm.
83. JEOL. *JEM-2100F Field Emission Electron Microscope*. [Figure] [cited 2017 30.09]; Image of TEM]. Available from: https://www.jeol.co.jp/en/products/detail/JEM-2100F.html.
84. ETH, Z. *Imaging and Diffraction in the TEM (schematic)*. [Figure] [cited 2017 30.07]; Schematic illustration of the TEM]. Available from: http://www.microscopy.ethz.ch/TEMED.htm.
85. Tanaka, N., *Electron nano-imaging : basics of imaging and diffraction for TEM and STEM*. 2017, Tokyo, Japan: Springer.
86. Misture, S.T. and R.L. Snyder, *X-ray Diffraction A2 - Buschow, K.H. Jürgen*, in *Encyclopedia of Materials: Science and Technology (Second Edition)*, R.W. Cahn, et al., Editors. 2001, Elsevier: Oxford. p. 9799-9808.
87. Rayner-Canham, G. and T. Overton, *Descriptive inorganic chemistry*. 5th ed. 2010, New York: W.H. Freeman.
88. Tilley, R.J.D., *Understanding solids : the science of materials*. 2nd edition. ed. 2013, Chichester, West Sussex, United Kingdom: Wiley, John Wiley & Sons Inc. xx, 556 pages.

89. EESemi. *EDX Analysis and WDX Analysis*. [Figure] [cited 2017 29.09]; K, L, M, N shells in relation to x-ray generation]. Available from: http://eesemi.com/edxwdx.htm.
90. Pecharsky, V.K. and P.Y. Zavalij, *Fundamentals of powder diffraction and structural characterization of materials*. 2nd ed. 2009, New York: Springer. xxiii, 741 p.
91. Mittemeijer, E.J. and U. Welzel, *Modern diffraction methods*. 2013, Weinheim: Wiley-VCH. xxvi, 528 p.
92. Long, N.V., et al., *Shape-controlled synthesis of Pt–Pd core–shell nanoparticles exhibiting polyhedral morphologies by modified polyol method.* Acta Materialia, 2011. **59**(7): p. 2901-2907.
93. ImageJ. *ImageJ*. [cited 2017 26.09-17]; Available from: http://imagej.net/Welcome.
94. Oxford-Instruments. *EDS Software- AZtecEnergy*. [cited 2017 06.10]; Software for EDX analysis]. Available from: https://www.oxford-instruments.com/products/microanalysis/energy-dispersive-x-ray-systems-eds-edx/eds-for-sem/eds-software-aztec.
95. Bruker. *TOPAS Software*. [cited 2017 03.10]; Software for XRD analysis]. Available from: https://www.bruker.com/products/x-ray-diffraction-and-elemental-analysis/x-ray-diffraction/xrd-software/topas.html.
96. Proffen, T. and R.B. Neder, *DISCUS: a program for diffuse scattering and defect-structure simulation.* Journal of Applied Crystallography, 1997. **30**(2): p. 171-175.
97. Midgley, P.A., et al., *Z-contrast HAADF-STEM Tomography.* Microscopy and Microanalysis, 2003. **9**(S02): p. 178-179.
98. Zhang, J., et al., *Versatile Strategy for Precisely Tailored Core@Shell Nanostructures with Single Shell Layer Accuracy: The Case of Metallic Shell.* Nano Letters, 2009. **9**(12): p. 4061-4065.
99. Dhak, P., *Private communication*. 2017.

9 Appendix

9.1 Results

The results that did not fit into the main text of the thesis are given in this appendix.

9.1.1 Tuning the Reduction Kinetics of $Pt(acac)_2$ and $Pd(acac)_2$

$Pd(acac)_2$ in 1,4-butanediol (metal/PVP = 1/10)

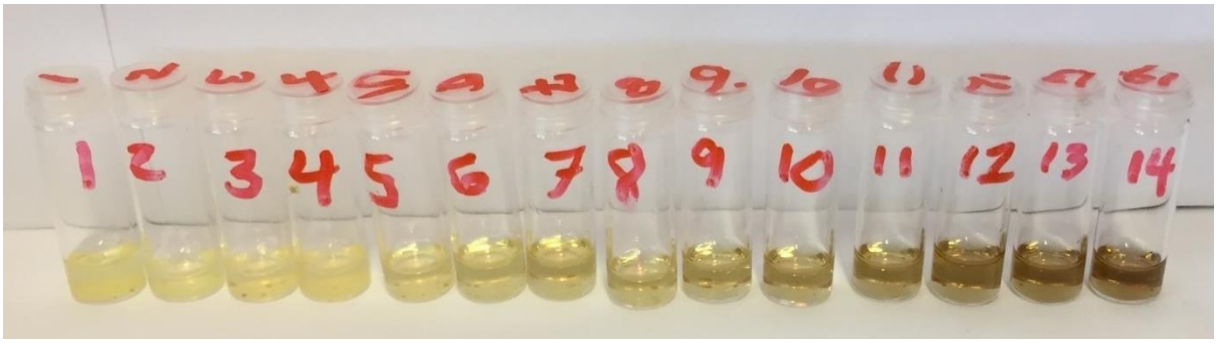

Figure 9-1: $Pd(acac)_2$ in 1,4-BD, with metal : PVP = 1 : 10.

Table 9-1: The samples from Figure 9-1 and their corresponding temperatures (T) at which they were pulled out of the synthesis solution are presented in this table. The sample highlighted in red corresponds to the STEM-image.

Sample	**1**	**2**	**3**	**4**	**5**	**6**	**7**	**8**	**9**	**10**	**11**	**12**	**13**	**14**
T/[°C]	50	53	56	59	62	65	68	71	74	77	80	83	86	89

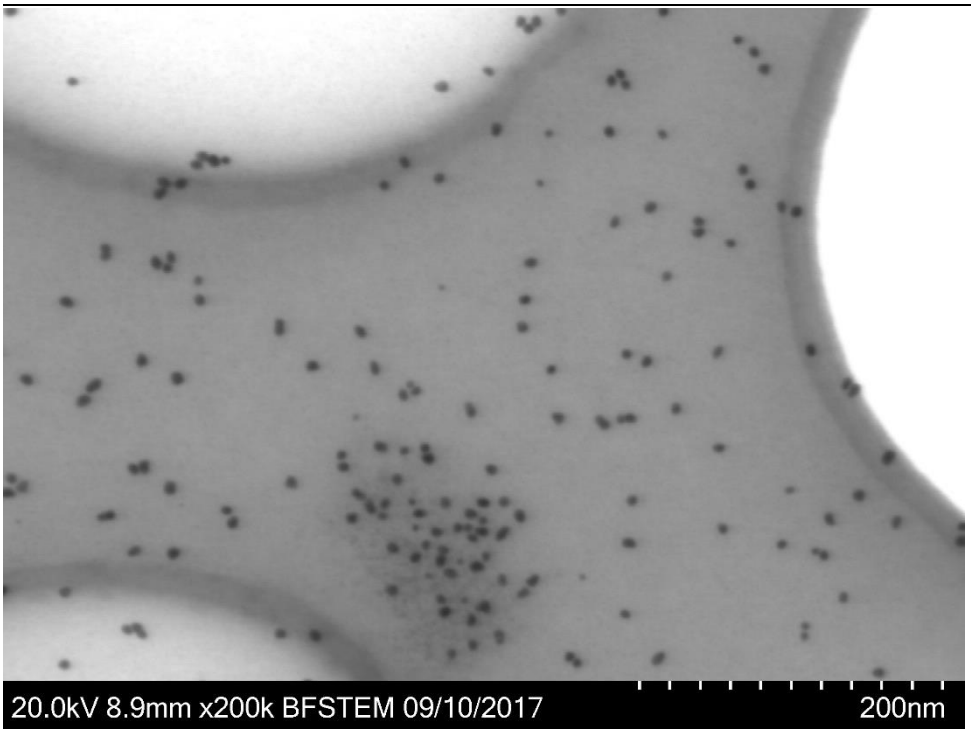

Figure 9-2: $Pd(acac)_2$ in 1,4-BD, with metal : PVP = 1 : 10.

$Pt(acac)_2$ in 1,4-butanediol (metal/PVP = 1/10)

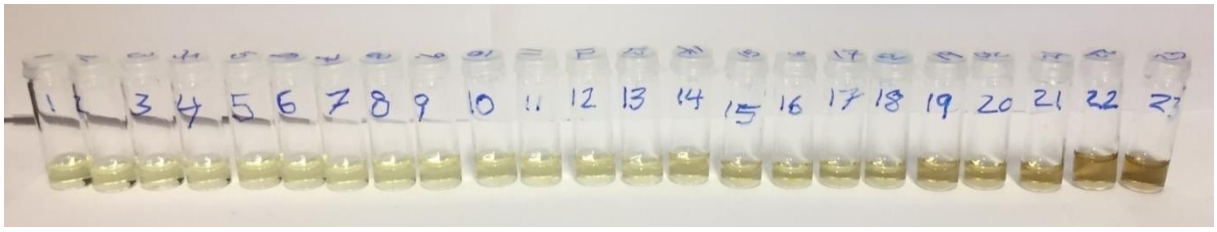

Figure 9-3: $Pt(acac)_2$ in 1,4-BD, with metal : PVP = 1 : 10.

Table 9-2: The samples from Figure 9-3 and their corresponding temperatures (T) at which they were pulled out of the synthesis solution are presented in this table. The sample highlighted in red corresponds to the STEM-image.

Sample	**1**	**2**	**3**	**4**	**5**	**6**	**7**	**8**	**9**	**10**	**11**	**12**	**13**	**14**
T/[°C]	150	153	156	159	162	165	168	171	174	177	180	183	186	189
Sample	**15**	**16**	**17**	**18**	**19**	**20**	**21**	**22**	**23**					
T/[°C]	192	195	198	201	204	207	210	213	216					

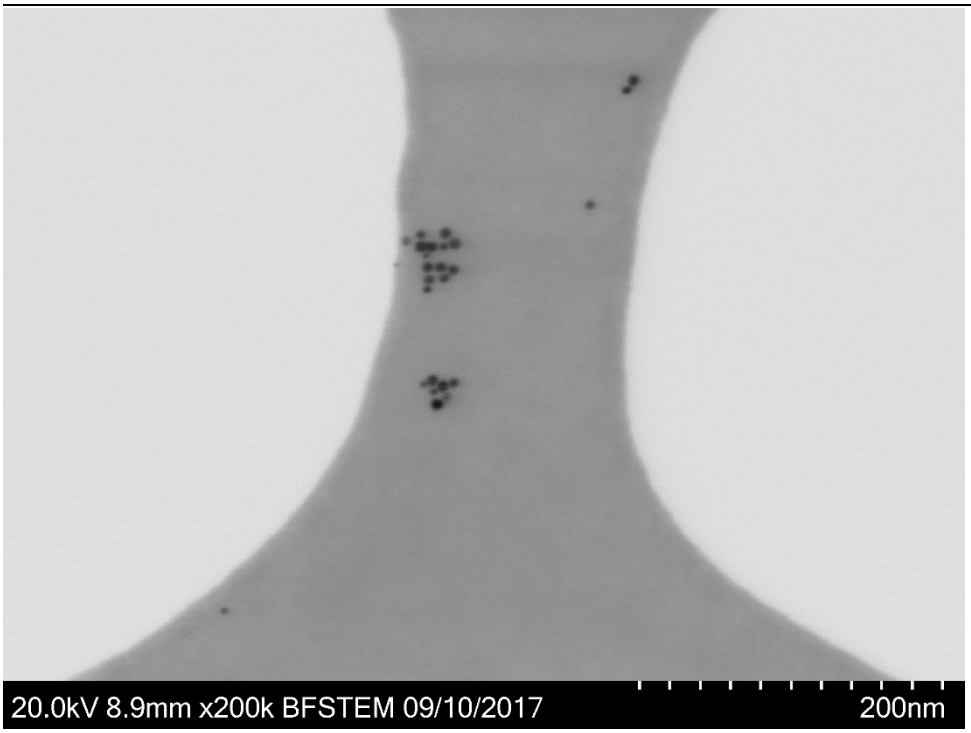

Figure 9-4: $Pt(acac)_2$ in 1,4-BD, with metal : PVP = 1 : 10.

$Pd(acac)_2$ in 1,4-butanediol (metal/PVP = 1/100)

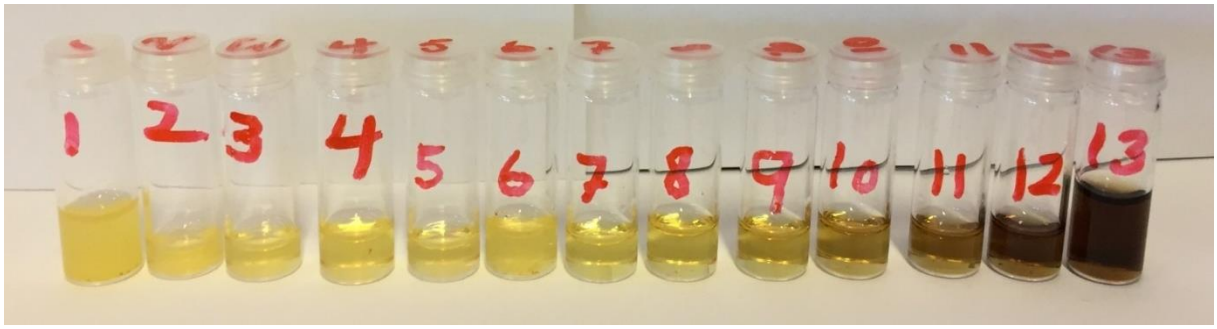

Figure 9-5: $Pd(acac)_2$ in 1,4-BD, with metal : PVP = 1 : 100.

Table 9-3: The samples from Figure 9-5 and their corresponding temperatures (T) at which they were pulled out of the synthesis solution are presented in this table. The sample highlighted in orange also has a complementary STEM-sample.

Sample	**1**	**2**	**3**	**4**	**5**	**6**	**7**	**8**	**9**	**10**	**11**	**12**	**13**
T/[°C]	40	50	53	56	59	62	65	68	71	74	77	80	83

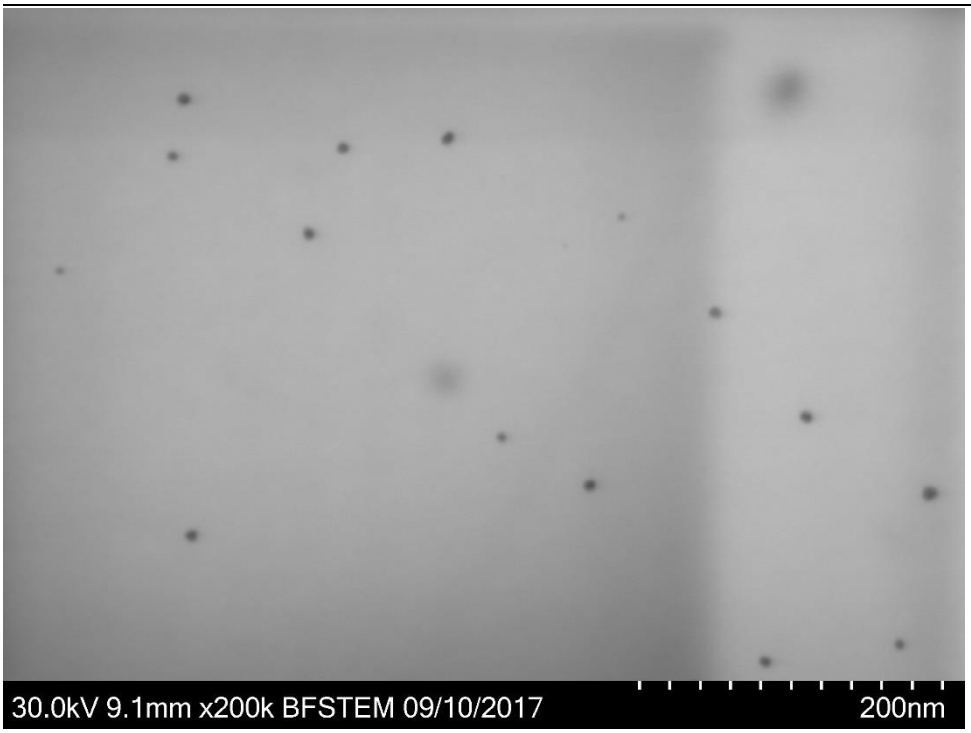

Figure 9-6: $Pd(acac)_2$ in 1,4-BD, with metal : PVP = 1 : 100.

$Pt(acac)_2$ in 1,4-butanediol (metal/PVP = 1/100)

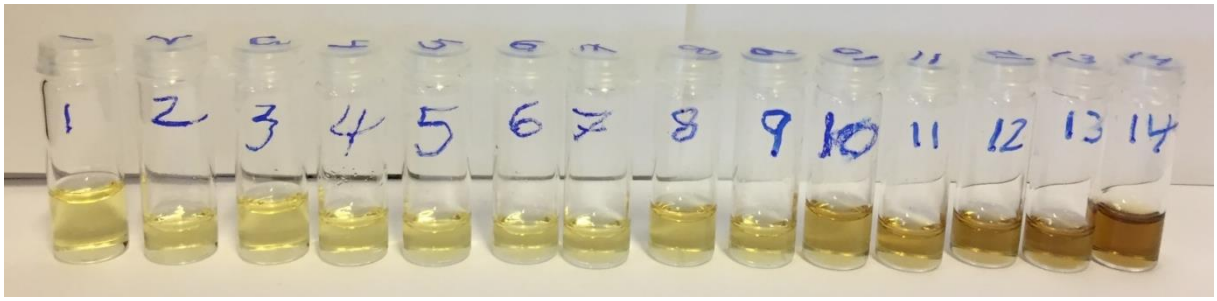

Figure 9-7: $Pt(acac)_2$ in 1,4-BD, with metal : PVP = 1 : 100.

Table 9-4: The samples from Figure 9-7 and their corresponding temperatures (T) at which they were pulled out of the synthesis solution are presented in this table. The sample highlighted in red corresponds to the STEM-image.

Sample	**1**	**2**	**3**	**4**	**5**	**6**	**7**	**8**	**9**	**10**	**11**	**12**	**13**	**14**
T/[°C]	130	140	150	160	170	173	176	179	182	185	188	191	194	197

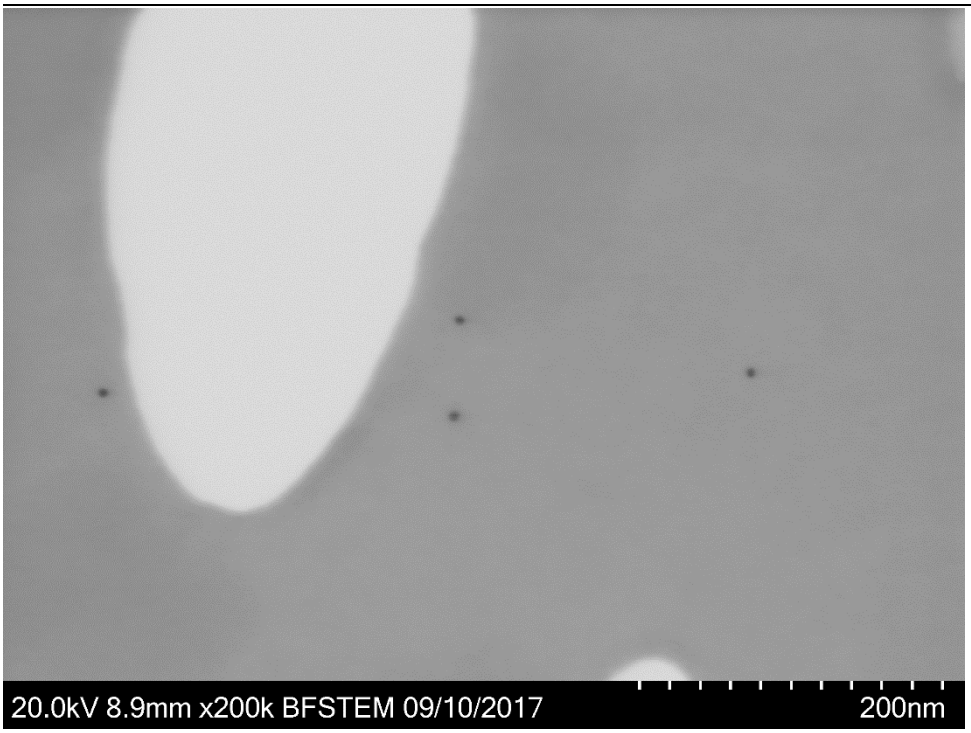

Figure 9-8: $Pt(acac)_2$ in 1,4-BD, with metal : PVP = 1 : 100.

$Pd(acac)_2$ in 1,2-butanediol (metal/PVP = 1/10)

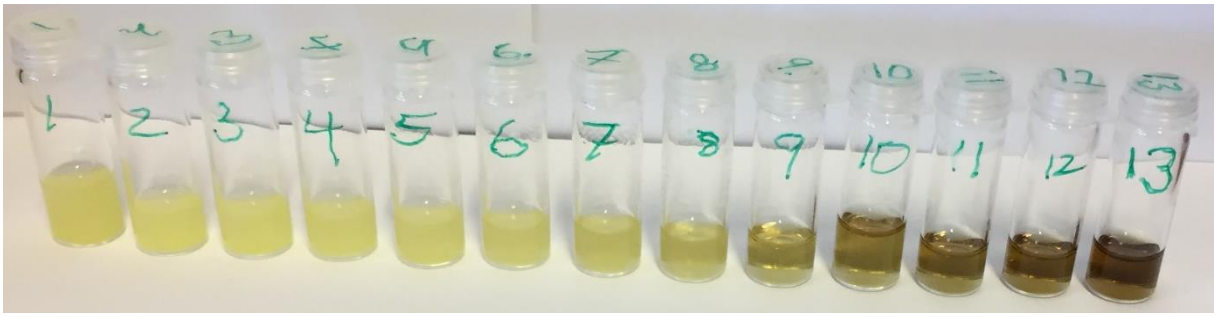

Figure 9-9: $Pd(acac)_2$ in 1,2-BD, with metal : PVP = 1 : 10.

Table 9-5: The samples from Figure 9-9 and their corresponding temperatures (T) at which they were pulled out of the synthesis solution are presented in this table. The sample highlighted in red corresponds to the STEM-image.

Sample	**1**	**2**	**3**	**4**	**5**	**6**	**7**	**8**	**9**	**10**	**11**	**12**	**13**
T/[°C]	50	53	54	57	60	63	66	69	72	75	78	81	84

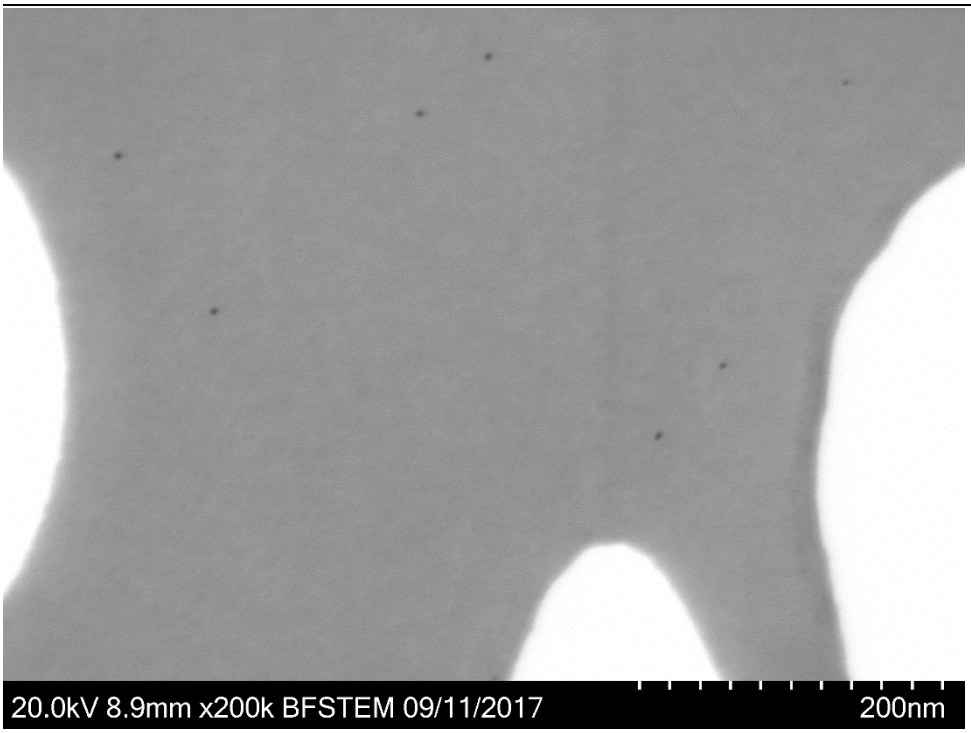

Figure 9-10: $Pd(acac)_2$ in 1,2-BD, with metal : PVP = 1 : 10.

$Pt(acac)_2$ in 1,2-butanediol (metal/PVP = 1/10)

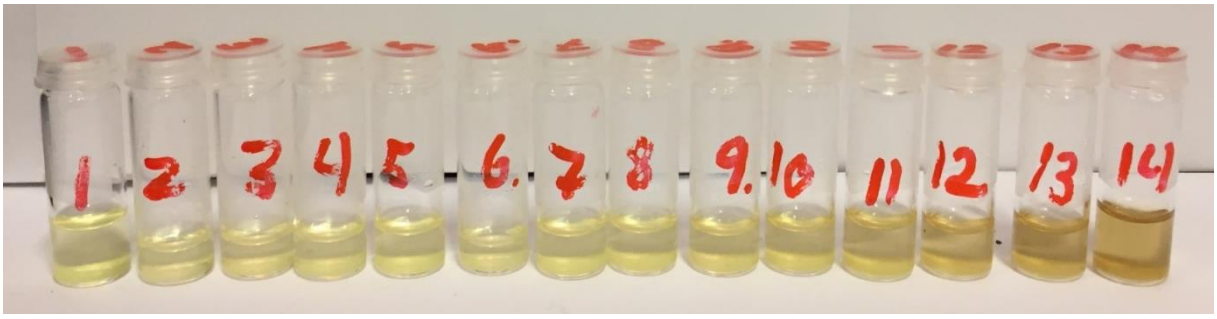

Figure 9-11: $Pt(acac)_2$ in 1,2-BD, with metal : PVP = 1 : 10.

Table 9-6: The samples from Figure 9-11 and their corresponding temperatures (T) at which they were pulled out of the synthesis solution are presented in this table. The sample highlighted in red corresponds to the STEM-image.

Sample	**1**	**2**	**3**	**4**	**5**	**6**	**7**	**8**	**9**	**10**	**11**	**12**	**13**	**14**
T/[°C]	140	150	160	163	166	169	172	175	178	181	184	187	190	193

Figure 9-12: $Pt(acac)_2$ in 1,2-BD, with metal : PVP = 1 : 10.

$Pd(acac)_2$ in 1,3-propanediol (metal/PVP = 1/10)

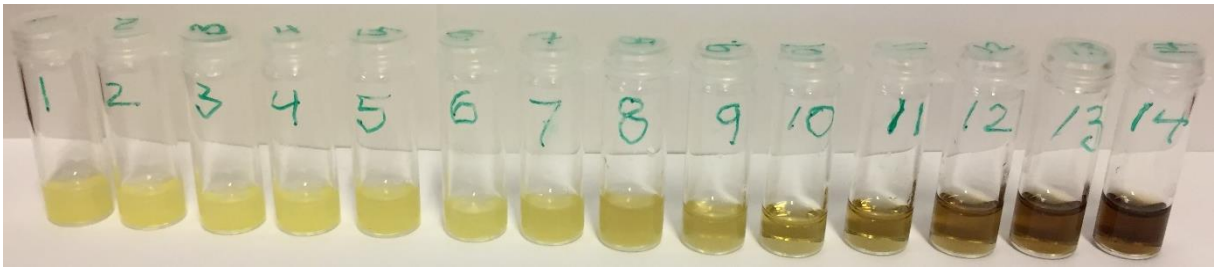

Figure 9-13: $Pd(acac)_2$ in 1,3-PD, with metal : PVP = 1 : 10.

Table 9-7: The samples from Figure 9-13 and their corresponding temperatures (T) at which they were pulled out of the synthesis solution are presented in this table. The sample highlighted in red corresponds to the STEM-image.

Sample	**1**	**2**	**3**	**4**	**5**	**6**	**7**	**8**	**9**	**10**	**11**	**12**	**13**
T/[°C]	51	54	57	60	63	66	69	72	75	78	81	84	87

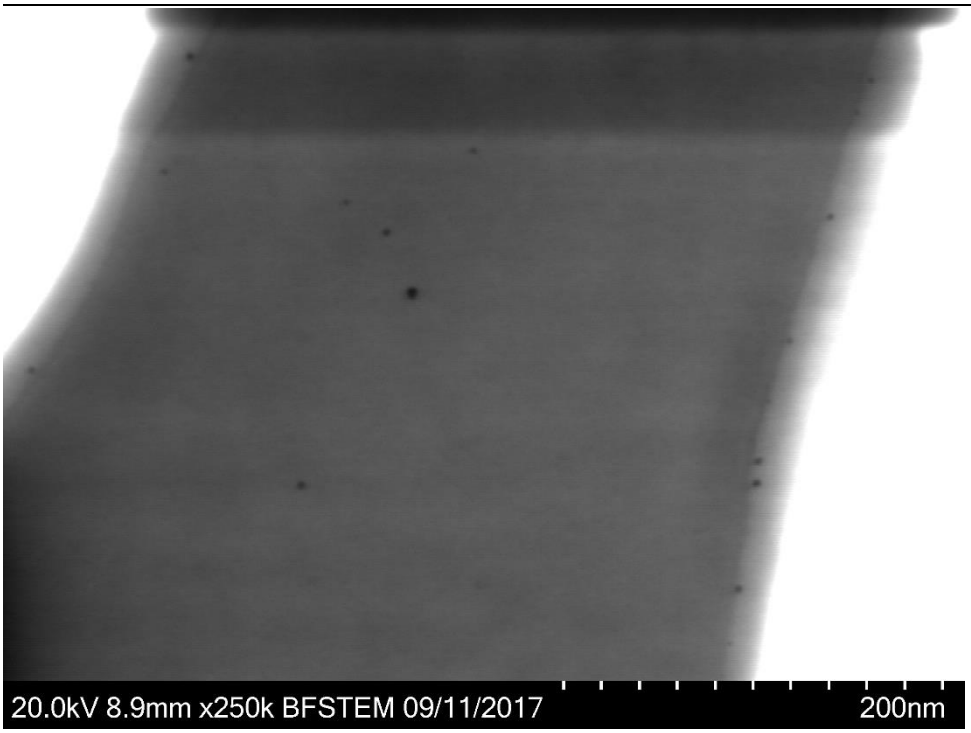

Figure 9-14: $Pd(acac)_2$ in 1,3-PD, with metal : PVP = 1 : 10.

$Pt(acac)_2$ in 1,3-propanediol (metal/PVP = 1/10)

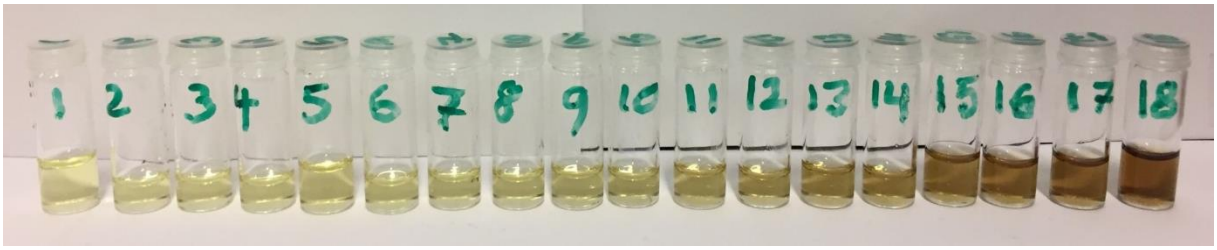

Figure 9-15: $Pt(acac)_2$ in 1,3-PD, with metal : PVP = 1 : 10.

Table 9-8: The samples from Figure 9-15 and their corresponding temperatures (T) at which they were pulled out of the synthesis solution are presented in this table. The sample highlighted in orange also has a complementary STEM-sample.

Sample	**1**	**2**	**3**	**4**	**5**	**6**	**7**	**8**	**9**	**10**	**11**	**12**	**13**	**14**
T/[°C]	140	150	160	163	166	169	172	175	178	181	184	187	190	193
Sample	**15**	**16**	**17**	**18**										
T/[°C]	196	199	202	205										

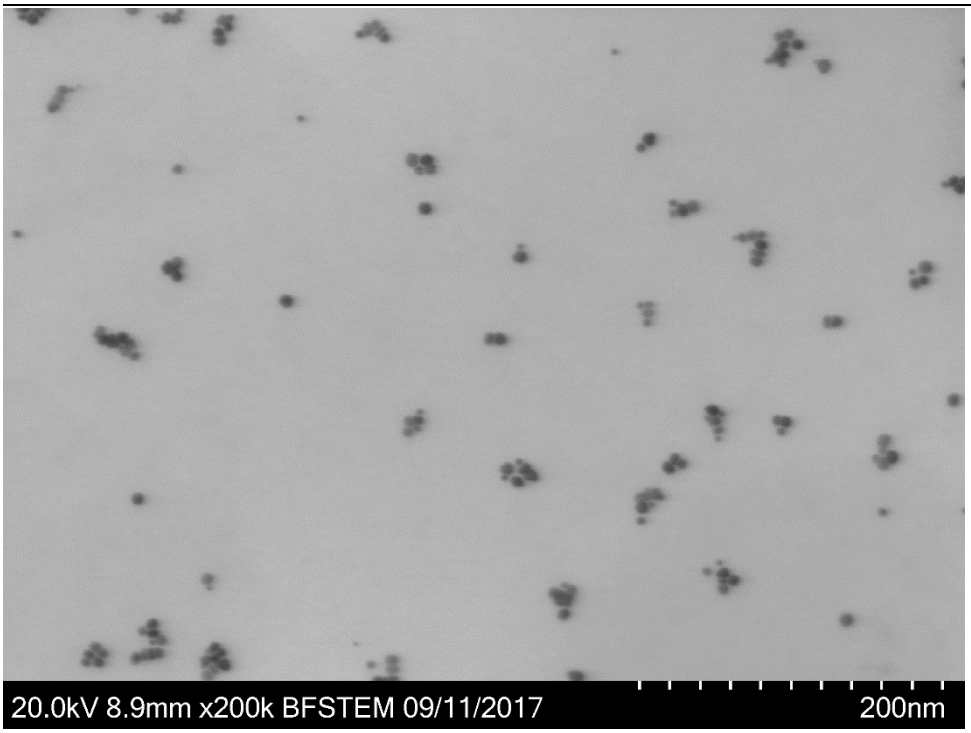

Figure 9-16: $Pt(acac)_2$ in 1,3-PD, with metal : PVP = 1 : 10.

9.1.2 Size Distribution of Free Standing Pd Nanoparticles

Histograms were made based on TEM-images of pure Pd NPs synthesized by the standard polyol method (section 3.2), in addition to the $Pt_{1-x}Pd_x$ (x = 0.50; 0.10; 0) NPs presented in section 4.4.1. The pure Pd NP-results are shown in

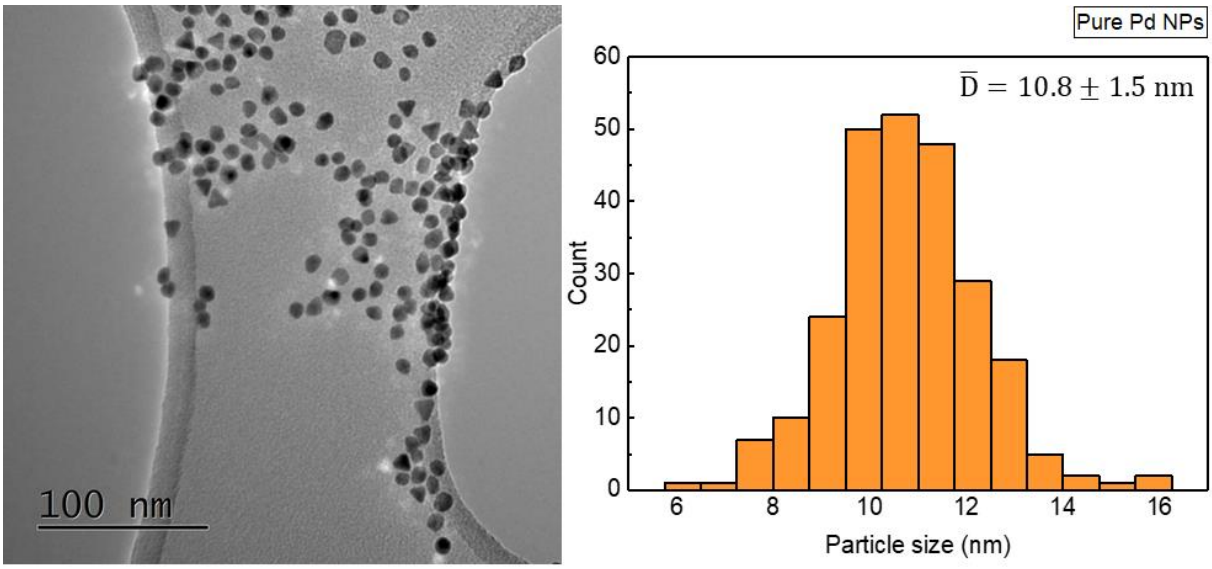

Figure 9-17: TEM-image and histogram of pure Pd NPs as synthesized by the standard polyol method.

9.1.3 Calculation of Turnover Frequency

The Excel sheets attached in the following show the calculation of TOF at 200°C and 400°C.

	Pt/Al2O3	Pt90Pd10/Al2O3	Pt50Pd50/Al2O3	Ref.Pt/Al2O3		n(NH3)/t [mol/s]	1,40502E-06
Mass of catalyst [g]	0,133	0,1445	0,1398	0,1131			
Wt.% ICP (Pt) [%]	0,56	0,57	0,64	0,97		Standartd p [bar]	1,013
Wt.% ICP (Pd) [%]	0	0,07	0,18	0			
Mass of Pt in catalyst [g]	0,0007448	0,00082365	0,00089472	0,00109707		V/t [L/s]	0,0000315
Mass of Pd in catalyst [g]	0	0,00010115	0,00025164	0			
Volume Pt if all reduced [cm^3]	3,47226E-05	3,83986E-05	4,17119E-05	5,11455E-05		R [Lbar/Kmol]	0,083145
Volume Pd if all reduced [cm^3]	0	8,41304E-06	2,09299E-05	0			
Volume total metal [cm^3]	3,47226E-05	4,68116E-05	6,26418E-05	5,11455E-05		T [K]	273,15
Average NP diameter [cm]	0,00000174	0,00000101	0,00000107	0,0000005			
Volume of 1 NP [cm^3]	2,75833E-18	5,39464E-19	6,41431E-19	6,54498E-20		Density Pd [g/cm^3]	12,023
Number of Pt NPs	1,25883E+13	8,67743E+13	9,76594E+13	7,81445E+14			
Surface area all Pt NPs [cm^2]	119,7331404	278,0889687	351,2622757	613,7454545		Density Pt [g/cm^3]	21,45
Surface area 1 Pt atom [cm^2]	3,84845E-15	3,84845E-15	3,84845E-15	3,84845E-15			
Total number of surface Pt atoms	3,1112E+16	7,226E+16	9,12737E+16	1,59479E+17		Na [mol^-1]	6,02214E+23
NH3 conversion	0,23	0,01	0	0,23			
NH3 flow [mL/s]	0,0315	0,0315	0,0315	0,0315		Pt atomic radius [cm]	1,75E-08
n(NH3)/second [mol/s]	1,40502E-06	1,40502E-06	1,40502E-06	1,40502E-06			
TOF [s^-1]	6,3	0,1	0,0	1,2			
TOF*1000	**6 255**	**117**	**-**	**1 220**			

	Pt/Al2O3	Pt90Pd10/Al2O3	Pt50Pd50/Al2O3	Ref.Pt/Al2O3		n(NH3)/t [mol/s]	1,40502E-06
Mass of catalyst [g]	0,133	0,1445	0,1398	0,1131			
Wt.% ICP (Pt) [%]	0,56	0,57	0,64	0,97		p [bar]	1,013
Wt.% ICP (Pd) [%]	0	0,07	0,18	0			
Mass of Pt in catalyst [g]	0,0007448	0,00082365	0,00089472	0,00109707		V/t [L/s]	0,0000315
Mass of Pd in catalyst [g]	0	0,00010115	0,00025164	0			
Volume Pt if all reduced [cm^3]	3,47226E-05	3,83986E-05	4,17119E-05	5,11455E-05		R [Lbar/Kmol]	0,083145
Volume Pd if all reduced [cm^3]	0	8,41304E-06	2,09299E-05	0			
Volume total metal [cm^3]	3,47226E-05	4,68116E-05	6,26418E-05	5,11455E-05		T [K]	273,15
Average NP diameter [cm]	0,00000174	0,00000101	0,00000107	0,0000005			
Volume of 1 NP [cm^3]	2,75833E-18	5,39464E-19	6,41431E-19	6,54498E-20		Density Pt [g/cm^3]	21,45
Number of Pt NPs	1,25883E+13	8,67743E+13	9,76594E+13	7,81445E+14			
Surface area all Pt NPs [cm^2]	119,7331404	278,0889687	351,2622757	613,7454545		Density Pd [g/cm^3]	12,023
Surface area 1 Pt atom [cm^2]	3,84845E-15	3,84845E-15	3,84845E-15	3,84845E-15			
Total number of surface Pt atoms	3,1112E+16	7,226E+16	9,12737E+16	1,59479E+17		Na [mol^-1]	6,02214E+23
NH3 conversion	0,78	0,8	0,71	1			
NH3 flow [mL/s]	0,0315	0,0315	0,0315	0,0315		Pt atomic radius [cm]	1,75E-08
n(NH3)/second [mol/s]	1,40502E-06	1,40502E-06	1,40502E-06	1,40502E-06			
TOF [s^-1]	21	9,4	6,6	5,3			
TOF*1000	**21 213**	**9 368**	**6 582**	**5 306**			